1985

Synthesis and characterization of some reduced ternary and quaternary molybdenum oxide phases with strong metal-metal bonds

Kwang-Hwa Lii
Iowa State University

INFORMATION TO USERS

This reproduction was made from a copy of a manuscript sent to us for publication and microfilming. While the most advanced technology has been used to photograph and reproduce this manuscript, the quality of the reproduction is heavily dependent upon the quality of the material submitted. Pages in any manuscript may have indistinct print. In all cases the best available copy has been filmed.

The following explanation of techniques is provided to help clarify notations which may appear on this reproduction.

1. Manuscripts may not always be complete. When it is not possible to obtain missing pages, a note appears to indicate this.

2. When copyrighted materials are removed from the manuscript, a note appears to indicate this.

3. Oversize materials (maps, drawings, and charts) are photographed by sectioning the original, beginning at the upper left hand corner and continuing from left to right in equal sections with small overlaps. Each oversize page is also filmed as one exposure and is available, for an additional charge, as a standard 35mm slide or in black and white paper format.*

4. Most photographs reproduce acceptably on positive microfilm or microfiche but lack clarity on xerographic copies made from the microfilm. For an additional charge, all photographs are available in black and white standard 35mm slide format.*

***For more information about black and white slides or enlarged paper reproductions, please contact the Dissertations Customer Services Department.**

Lii, Kwang-Hwa

SYNTHESIS AND CHARACTERIZATION OF SOME REDUCED TERNARY AND QUATERNARY MOLYBDENUM OXIDE PHASES WITH STRONG METAL-METAL BONDS

Iowa State University PH.D. 1985

PLEASE NOTE:

In all cases this material has been filmed in the best possible way from the available copy. Problems encountered with this document have been identified here with a check mark __✓__.

1. Glossy photographs or pages __✓__
2. Colored illustrations, paper or print _____
3. Photographs with dark background __✓__
4. Illustrations are poor copy _____
5. Pages with black marks, not original copy _____
6. Print shows through as there is text on both sides of page _____
7. Indistinct, broken or small print on several pages __✓__
8. Print exceeds margin requirements _____
9. Tightly bound copy with print lost in spine _____
10. Computer printout pages with indistinct print _____
11. Page(s) _____ lacking when material received, and not available from school or author.
12. Page(s) _____ seem to be missing in numbering only as text follows.
13. Two pages numbered _____. Text follows.
14. Curling and wrinkled pages _____
15. Dissertation contains pages with print at a slant, filmed as received _____
16. Other _____

_____

_____

University
Microfilms
International

Synthesis and characterization of some reduced ternary and quaternary molybdenum oxide phases with strong metal-metal bonds

by

Kwang-Hwa Lii

A Dissertation Submitted to the
Graduate Faculty in Partial Fulfillment of the
Requirements for the Degree of
DOCTOR OF PHILOSOPHY

Department: Chemistry
Major: Inorganic Chemistry

Approved:

Signature was redacted for privacy.

In Charge of Major Work

Signature was redacted for privacy.

For the Major Department

Signature was redacted for privacy.

For the Graduate College

Iowa State University
Ames, Iowa

1985

TABLE OF CONTENTS

LIST OF TABLES

LIST OF FIGURES

GENERAL INTRODUCTION

Prior to 1979, the only examples of reduced ternary molybdenum oxides with strongly metal-metal bonded clusters were $M^{II}_2Mo_3O_8$ (M^{II} = Mg, Mn, Fe, Co, Ni, Zn or Cd) (1). These compounds contain triangles of molybdenum atoms joined by Mo-Mo bonds. The discovery of $NaMo_4O_6$ (2) along with $Ba_{0.62}Mo_4O_6$ (3) not only greatly expanded our vision of chemistry but also signaled a large number of new structures in this family. The $NaMo_4O_6$ structure is comprised of infinite metal cluster chains based on M_6X_{12} building blocks, which was unprecedented among metal oxide systems. The average oxidation state of Mo in $NaMo_4O_6$ is 2.75. Subsequently, an oxide hollandite, $Ba_{1.14}Mo_8O_{16}$ (3), containing regular and distorted rhomboidal cluster units was discovered. This interesting hollandite is also the first example of oxides having tetranuclear cluster units. All the compounds mentioned above have been obtained at or below 1100°C in sealed molybdenum or fused silica tubes for a few days. More recent examples were $Sc_{0.75}Zn_{1.25}Mo_4O_7$, and $Ti_{0.5}Zn_{1.5}Mo_4O_7$ (4) which can be regarded as closest-packing of molybdenum metal cluster chains with the ternary metal cations at the octahedral or tetrahedral sites in the narrow channels created by the infinite chains. The former compound was discovered during attempts to grow single crystals of $ScZnMo_3O_8$ at considerably higher reaction

temperature (ca. 1450°C). This discovery has encouraged us to undertake a synthetic program aimed at uncovering new structure types by solid-state reactions in the temperature interval from 1100 to 1500°C. Higher reaction temperatures have been proved to be particularly useful for obtaining single crystals suitable for x-ray structure analysis. The experiments at higher temperature have led to the discovery of three new structure types. One of them contains three different types of molybdenum metal cluster chains (SECTION 3), the second one contains infinite octahedral cluster chains running in two orthogonal directions (SECTION 5), and the third structure type consists of unidirectional octahedral cluster chains which are "diluted" with the ternary metal cations (SECTION 6). A further research on the oxide hollandites led to two new compounds containing tetranuclear cluster units (SECTION 1). SECTION 2 presents two compounds which are isomorphous with $NaMo_4O_6$. A comprehensive study of a series of compounds having the $Sc_{0.75}Zn_{1.25}Mo_4O_7$ structure is included in SECTION 4. An interesting spinel phase is also briefly discussed in SECTION 6.

Explanation of Dissertation Format

This dissertation consists of six sections, each of which is written in a form suitable for publication in a technical journal. Although references cited in the general introduction are found at the end of the dissertation, each section contains an independent listing of references and notes which are cited in that section.

SECTION 1. SYNTHESES, CRYSTAL STRUCTURES, AND BONDINGS OF TWO NEW HOLLANDITE PHASES CONTAINING DISCRETE TETRANUCLEAR MOLYBDENUM METAL CLUSTERS: $Na_{0.35}BaMo_8O_{16}$ AND $Li_{0.34}BaMo_8O_{16}$

INTRODUCTION

Tetranuclear early transition metal clusters can be classified into five different types: tetrahedron, butterfly, square, rectangle, and rhomboid. Examples for each type of cluster are briefly described below.

MMo_4S_8 (M = Al, Ga), $GaMo_4Se_8$, $Mo_4S_4X_4$ (X = Cl, Br, I) (1,2), $MMo_2Re_2S_8$ (M = Fe, Co, Ni, Cu) (3), $GaMo_4X_nX'_{8-n}$ (X, X' = S, Se, Te) (4), $GaNb_4X_8$ (X = S, Se), $GaTa_4Se_8$, and $Nb_4Se_4I_4$ (5) consist of tetrahedral transition metal cluster units. All of them adopt the very interesting spinel structure in which the transition metals are at octahedral sites and the ternary metal cations are at tetrahedral sites. A butterfly cluster can be formed by removing any two adjacent metal atoms from an octahedron. Two of the examples are $(Bu_4N)_2Mo_4I_{11}$ (6), and $Mo_4(OPr^i)_8Br_4$ (7). Interestingly enough, the analogous compound, $Mo_4(OPr^i)_8Cl_4$ (7), contains a square planar molybdenum cluster unit which can be thought as a fragment formed by removing any two trans-molybdenum atoms from an octahedron. Rectangular clusters have been found in lots of compounds such as $Mo_4Cl_8(PR_3)_4$ (R = C_2H_5 or C_4H_9) (8), and $W_4Cl_8(PBu^n{}_3)_4$ (9). Regular and distorted rhomboids can be formed by squeezing along any one of the face diagonals of square and rectangle, respectively. MNb_4X_{11} (M = Rb, Cs; X = Cl, Br) (10) contain regular rhomboidal cluster units, but $W_4(OEt)_{16}$ (11) consists of distorted rhomboidal cluster

units. However, the surprising and puzzling oxide, $Ba_{1.14}Mo_8O_{16}$ (12), adopts the hollandite structure and is built up from two nonequivalent chains containing, respectively, regular and distorted rhomboidal cluster units. This interesting compound is also the first example of oxides containing tetranuclear cluster units.

Based on the Mo-Mo bond distances in $Ba_{1.14}Mo_8O_{16}$ the regular and distorted rhomboidal metal clusters can be formulated as $Mo_4O_8^{2-}$, and $Mo_4O_8^{0.28-}$, respectively. A total of about eight electrons are involved in the Mo-Mo bonding orbitals for the distorted cluster unit. The distorted cluster is less reduced compared to the regular one. Therefore, it might be possible to reduce the relatively electron-deficient clusters in $Ba_{1.14}Mo_8O_{16}$ by inserting some smaller cations such as Li^+ or Na^+ into the tunnels in which the barium ions sites are only partially occupied. It is also very interesting to study the interplay among several factors, such as the number of metal cluster electrons and the interactions between oxygens and molybdenum atoms or even ternary metal cations, which govern the observed crystal structure and the extent of distortion in the clusters.

This type of tunnel structure was first found for the hollandite group of minerals $A_xMn_8O_{16}$ (13) where A is one of the ions Ba^{2+}, K^+, or Pb^{2+}. If the cubic sites in the large tunnels are filled the ternary compound has the formula $A_2M_8O_{16}$. This appears to be the case for $K_2Mo_8O_{16}$ (14). A

few reactions were conducted in an attempt to prepare $NaBaMo_8O_{16}$ and $LiBaMo_8O_{16}$. However, the inserted small cations are so small that they are not likely to be at the center of the cubes. Nonstoichiometric compounds with complicated superstructures were obtained. This section describes the syntheses, single crystal structures, and bonding of two new hollandites containing rhomboidal molybdenum metal clusters, $Na_{0.35}BaMo_8O_{16}$ and $Li_{0.34}BaMo_8O_{16}$.

EXPERIMENTAL AND RESULTS

Materials

Sodium molybdate dihydrate (Fisher Certified A.C.S.) was dehydrated by drying at 120°C under dynamic vacuum overnight. Anhydrous lithium molybdate (98.5 %) was obtained from Alfa products. It was also heated at 120° under dynamic vacuum overnight. Because both compounds are hygroscopic, they were stored over P_4O_{10}. Barium molybdate was prepared by mixing an aqueous solution of $BaCl_2.2H_2O$ (Baker Analyzed Reagent, 99.6 %) with an aqueous solution containing the stoichiometric quantity of sodium molybdate dihydrate. The white precipitate was filtered, washed with water, and then dried at 120°C under dynamic vacuum overnight. Molybdenum trioxide (99.9 %) and molybdenum metal (99.99 %) were obtained from Baker Chemical Co. and Aldrich Chemical Co., respectively.

Syntheses and Analyses

$Na_{0.35}BaMo_8O_{16}$

This compound was discovered in a mixture resulting from the reaction of Na_2MoO_4, $BaMoO_4$, MoO_3, and Mo in 3:6:20:19 mole ratio ($NaBaMo_8O_{16}$). The reactants were weighed with an analytical balance in air, but ground together in a mortar in the dry box. The loose powder was electron beam welded in an

evacuated copper tube which, in turn, was sealed in an evacuated quartz tube, and then heated at 1000°C for six days. Small, black, columnar crystals were grown in the reaction product. The typical size was about 0.04 x 0.04 x 0.2 mm. The product was washed with water before taking an x-ray powder pattern. A Guinier x-ray powder pattern of the bulk product indicated that it essentially contained a compound whose structure was closely related to that of $Ba_{1.14}Mo_8O_{16}$, but with higher crystal symmetry. Weak lines due to MoO_2 and Mo(?) were also observed in the powder pattern. Six crystals were selected and analyzed by the electronmicroprobe method. The analytical results showed that Na, Ba, and Mo were present and no other elements were observed. The Na:Ba:Mo ratio of the crystals was found to be 0.3: 1.01(2): 8.00. A more accurate sodium to barium ratio was obtained by dissolving the product in aqua regia and analyzed by atomic absorption spectroscopy. It was found that Na:Ba mole ratio was 0.35: 1.00. These analytical results were consistent with the single crystal x-ray diffraction data. Later, it was found that the product containing very little MoO_2 could be obtained by reacting stoichiometric quantities of Na_2MoO_4, $BaMoO_4$, MoO_3, and Mo under similar reaction conditions.

$\underline{Li}_{0.34}\underline{BaMo}_8\underline{O}_{16}$

This compound was also discovered from a reaction mixture consisting of Li_2MoO_4, $BaMoO_4$, MoO_3, and Mo in 3:6:20:19 mole

ratio. The reaction conditions were essentially the same as those for $Na_{0.35}BaMo_8O_{16}$. But much bigger, black, columnar crystals were grown in the product. The product was washed with water before taking an x-ray powder pattern. A Guinier x-ray powder pattern of the bulk product showed that this compound was also related to $Ba_{1.14}Mo_8O_{16}$, but with even higher crystal symmetry than $Na_{0.35}BaMo_8O_{16}$. Lines due to MoO_2 were also observed in the powder pattern. The Ba:Mo mole ratio obtained by electronmicroprobe analysis was found to be 1.06(2): 8.00. The lithium to barium mole ratio was also obtained by dissolving the product in aqua regia and analyzed by atomic absorption spectroscopy. The Li:Ba mole ratio was found to be 0.34: 1.00. Therefore, the compound was formulated as $Li_{0.34}BaMo_8O_{16}$. The pure compound could be prepared by reacting a stoichiometric amount of Li_2MoO_4, $BaMoO_4$, MoO_3, and Mo under similar reaction conditions.

Preliminary Film Work and X-ray Powder Diffraction

$Na_{0.35}BaMo_8O_{16}$

Most of the crystals in the product were either multiple crystals or too small to be used for single crystal x-ray structure determination. Many had to be selected before a satisfactory crystal was obtained. A crystal of dimensions 0.06 x 0.06 x 0.3 mm was selected for indexing and data collection based on the quality of the axial oscillation

picture. The oscillation photograph indicated that the repeat distance along the needle direction was equal to 5.70 A. This length is comparable to the c-length of $Ba_{1.14}Mo_8O_{16}$. However, the first-layer reflections were weaker than zero and second-layer reflections. No superlattice reflections were observed on the axial oscillation photograph. Because there was a mirror plane perpendicular to the oscillation axis, the compound must belong to the monoclinic or higher crystal system.

An Enraf Nonius Delft Guinier camera was used to obtain all x-ray powder diffraction patterns. National Bureau of Standard Si powder was mixed with all samples as an internal standard. Cu $K\alpha_1$ (λ = 1.54056 A) was used for calculating the observed d-spacings and unit cell parameters of all samples.

The x-ray powder pattern of $Na_{0.35}BaMo_8O_{16}$ was indexed on the basis of a monoclinic unit cell. Some of the diffraction peaks were strong and broad because a few peaks were so closely spaced that they were hardly resolved. The d-spacings and relative intensities are tabulated in Table 1.1. A least-squares fit of the peak positions of 50 sharp reflections gave the following cell parameters: a = 10.283(1), b = 5.7303(5), c = 10.222(1) A, β = 90.308(9)^o.

$\underline{Li}_{0.34}\underline{BaMo}_8\underline{O}_{16}$

A columnar crystal of dimensions 0.05 x 0.05 x 0.36 mm was selected. Its axial oscillation picture, zero and first-layer

Table 1.1. X-ray powder data for $Na_{0.35}BaMo_8O_{16}$

d-spacings[a]	intensities	d-spacings	intensities
7.26(1)	m	1.8474(8)	w
7.22(1)	m	1.8173(8)	w
5.728(8)	w	1.8069(8)	w
5.133(7)	s	1.7893(7)	w
5.107(7)	s	1.7622(7)	vs, br
4.492(5)	vw	1.7565(7)	m-s
3.825(4)	m	1.7515(7)	w
3.809(4)	m	1.7134(7)	s
3.629(3)	m	1.7034(7)	s
3.613(3)	m	1.6681(6)	vw
3.584(3)	w	1.6645(6)	vw
3.569(3)	w	1.6455(6)	w
3.234(3)	vs, br	1.6273(6)	w
2.865(2)	vvw	1.6147(6)	w
2.757(2)	w	1.5902(6)	m
2.665(2)	w	1.5857(6)	s
2.569(2)	m	1.5809(6)	w
2.554(2)	m	1.5329(5)	vw
2.428(1)	vs, br	1.5297(5)	vw
2.410(1)	m	1.5148(5)	s, br
2.300(1)	w-m	1.5004(5)	w
2.291(1)	m	1.4971(5)	w
2.283(1)	w-m	1.4329(4)	s
2.231(1)	w	1.4242(4)	w
2.220(1)	w	1.4201(4)	vw
2.197(1)	m-s	1.4057(4)	vw
2.191(1)	m-s	1.4010(4)	s
2.145(1)	vw	1.3949(4)	s
2.017(1)	w, br	1.3800(4)	m
2.007(1)	w	1.3671(4)	w
1.9430(9)	w	1.3521(4)	w
1.9094(8)	w		
1.8811(8)	vs, br		
1.8749(8)	vs, br		

[a]Cu $K\alpha_1$ (λ = 1.54056 A) was used for calculating the observed d-spacings.

Weissenberg pictures were taken. The oscillation picture (Fig. 1.1) showed two very weak, closely spaced superlattice reflections suggesting a very large supercell along the c axis (needle direction). The repeat distance along the oscillation axis can be calculated according to Eq. 1:

$$d = \frac{n \times \lambda}{\sin \tan^{-1} \frac{y_n}{R}} \qquad \text{Eq. 1}$$

where n is the nth layer line on a photograph, λ is the wavelength of the x-ray (1.5418 A), y_n is the distance from zero layer line to the nth layer line, and R is the film radius. Eq. 2 with appropriate values substituted can be easily derived from the above equation.

$$\frac{n'}{n} = \frac{\sin \tan^{-1}(y_n'/30.2)}{\sin \tan^{-1}(y_n/30.2)} \qquad \text{Eq. 2}$$

Substituting y_n values for those two very weak superlattice reflections on the oscillation photograph, n'/n ratio was equal to 1.125. The possible solutions for n' and n are: $n' = n + 1$, $n = 8$; $n' = n + 2$, $n = 16$; ...., etc. Therefore, the repeat distance in the tunnel direction for the smallest supercell is 48.91 A which is 17 times the subcell c constant (2.8794(6) A). Interestingly enough, the axial oscillation picture did not reveal any reflections which corresponded to doubling the subcell c constant. This interesting and complicated superstructure will be further discussed in later

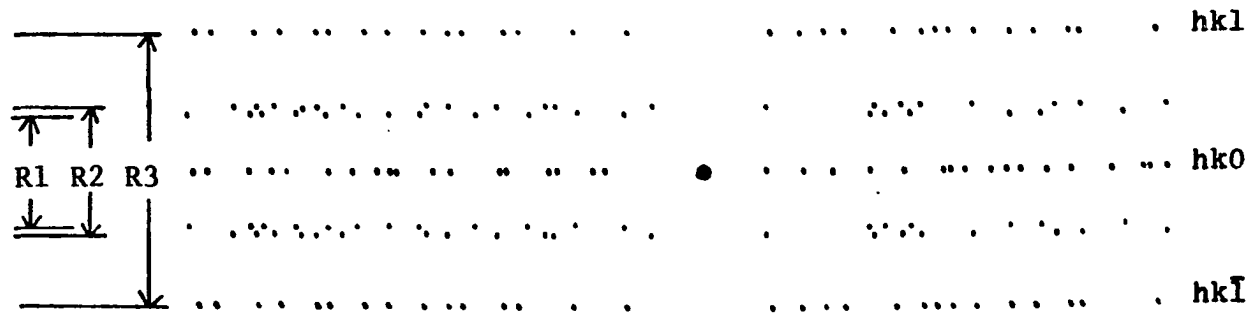

Fig. 1.1. An axial oscillation photograph along the tetragonal c axis. The indexed planes represent the regular Bragg scattering due to the periodic framework. The scattering between these planes reflects a superstructure due to a three-dimensional long-range order of the cations in the tunnel. R1 = 15.74 mm, R2 = 17.88 mm, and R3 = 38.22 mm.

sections.

The zero and first-layer Weissenberg photographs gave the following information: a = b = 10.45 A, 4/m symmetry, hk0 reflections(h + k = 2n), and hkℓ reflections (h + k + ℓ = 2n). No superlattice reflection was observed along either the a or b direction.

Many columnar crystals were selected, washed with water to remove adherent small particles, dried, ground into powder, and mixed with NBS silicon powder as an internal standard. All of the diffraction peaks on the Guinier powder pattern could be indexed based on a tetragonal unit cell. A few very weak reflections were due to superlattice reflections. The d-spacings, relative intensities, and hkℓ values are listed in Table 1.2.

X-ray Single Crystal Data Collection for $Na_{0.35}BaMo_8O_{16}$

The crystal was mounted in a 0.3 mm Lindemann glass capillary with a small amount of silicone grease. Its needle direction was nearly collinear with the ϕ-circle axis. A four-circle diffractometer designed and built in Ames Laboratory (15) was used for indexing and intensity data collection. The orientation matrix of the crystal was calculated by using an automatic indexing program (16) that uses reflections taken from several ω-oscillation pictures as input. The observed systematic absences of h0ℓ (h = 2n + 1)

Table 1.2. X-ray powder data for $Li_{0.34}BaMo_8O_{16}$[a]

d-spacing (A)	intensity	hkℓ
7.23(1)	w-m	110
5.113(6)	s	200[b]
4.329(4)	vw	---[b]
3.718(3)	w	---[b]
3.664(3)	vw	---[b]
3.613(3)	m	220
3.232(2)	vs	130
2.772(2)	vw	101
2.553(1)	w	400
2.435(1)	vs	211
2.406(1)	w-m	330
2.283(1)	w-m	420
2.199(1)	m	301
2.0188(9)	w	321
2.0028(9)	w	510
1.8783(8)	vs	411[b]
1.8118(8)	vw	---[b]
1.8050(7)	vw	440
1.7521(7)	m	530[b]
1.7397(6)	w	---[b]
1.7019(6)	s	600
1.6659(6)	vw	501
1.6137(5)	vw	620
1.5842(5)	s	521[b]
1.4983(5)	w	---[b]
1.4510(4)	vw	161
1.4402(4)	w	002
1.4164(4)	vw	460
1.3953(4)	m-s	541
1.3845(4)	vw	202
1.3458(4)	vw	361
1.3408(4)	vw	730
1.3156(3)	w	132
1.3018(3)	vw	701
1.2616(3)	w	271
1.2545(3)	vw	402
1.2349(3)	vw	332

[a]Cu $K\alpha_1$ (1.54056 A) was used to calculate observed d-spacings. A least-squares fit of peak positions of subcell reflections gave the following unit cell parameters: a = b = 10.213(1) A, c = 2.8794(6) A, $\alpha = \beta = \gamma = 90^{\circ}$.

[b]These are superlattice reflections. If they are included in the calculation, then the cell constants become a = b = 10.214(2)A, c = 48.91(2)A (xn), $\alpha = \beta = \gamma = 90^{\circ}$.

and N(z) distribution (17) of the entire data set (excluding systematic absences) indicated the nonstandard space group P2/a. Unit cell parameters determined from 20 accurately centered high-angle ($2\theta = 28^{o} - 40^{o}$) reflections were a = 14.475(7) A, b = 5.732(1) A, c = 10.231(5) A, $\beta = 134.70(3)^{o}$. In order to show the relationship to other hollandite structures, the space group was transformed into P2/n so that the interaxial angle β was as near 90^{o} as possible. The unit cell parameters became: a = 10.289(2) A, b = 5.732(1) A, c = 10.231(3) A, $\beta = 90.28(2)^{o}$. Intensity data were corrected for absorption, and for Lorentz and polarizaion effects. Numerical details of the diffraction data and the structure refinement are provided in Table 1.3.

Solution and Refinement of $Na_{0.35}BaMo_8O_{16}$

The data set could be well-averaged in 2/m symmetry (R = 2.2%). The four symmetry-unrelated Mo atoms were located by solving the Patterson map. The atomic scattering factors were taken from reference (18) for neutral atoms and molybdenum and barium atoms were corrected for the real and imaginary parts of anomalous dispersion. A full matrix least-squares refinement on the molybdenum positional parameters resulted in an unweighted R = 0.308. At this point, an electron density map revealed large peaks at the twofold special positions 2e(1/4, y, 3/4; 3/4, -y, 1/4). Two barium atoms were then

Table 1.3. Crystallographic data for $Na_{0.35}BaMo_8O_{16}$

---

crystal system: monoclinic
space group: P2/n
a = 10.289(2) A
b = 5.732(1) A
c = 10.231(3) A
β = 90.28(2)°
V = 603.4(2) A^3
Z = 2
d(calcd) = 6.436 g/cm^3
crystal size: 0.06 x 0.06 x 0.30 mm
absn coeff: 112.2 cm^{-1}
refln used for empirical aborption correction (hkℓ, 2Θ, T_{max}/T_{min}): $1\bar{4}\bar{1}$, 29.25°, 1.084
radiation: Mo Kα (λ = 0.71034 A)
monochromator: oriented graphite
scan type: ω-scan
automatic background detn, max scan half width: 0.5 degree
std reflns: 3 measured every 75 reflns; no significant decay
reflns measd: hkℓ, $\bar{h}\bar{k}\ell$, $\bar{h}k\bar{\ell}$, $h\bar{k}\bar{\ell}$ octants
max 2Θ: 60°
reflns collected: 3433 collected, 2871 observed ($I > 3\sigma(I)$)
no. of unique reflns with $I > 3\sigma(I)$: 1754
no. of parameters refined: 124
R = 0.067[a]
R_w = 0.076[b]
quality-of-fit indicator: 1.014[c]

---

[a] $R = \Sigma||F_o| - |F_c||/\Sigma|F_o|$.

[b] $R_w = [\Sigma w(|F_o|-|F_c|)^2/\Sigma w|F_o|^2$; $w = 1/\sigma^2(|F_o|)$.

[c] Quality of fit = $[\Sigma w(|F_o|-|F_c|)^2/(N(observns)-N(parameters))]^{1/2}$.

placed at two of these special positions and a refinement of barium multipliers and all atomic positional parameters converged at R = 0.180. Oxygen atoms were located from a difference map and a refinement of all Mo, O, and Ba positional and isotropic thermal parameters gave R = 0.10. A full anisotropic refinement gave R = 0.072 and R_w = 0.110. At this point, a difference map revealed small peaks at the twofold special positions 2e. They were probably due to sodium ions. A least-squares refinement including the sodium multipliers and anisotropic thermal parameters converged at R = 0.068 and R_w = 0.105. Then, the data set was reweighted in 30 overlapping groups sorted according to F_o. A final full-matrix least-squares refinement, varying barium and sodium occupancy factors, positional and isotropic thermal parameters of sodium, and positional and anisotropic thermal parameters of all other atoms, converged at R = 0.067 and R_w = 0.076. The stoichiometry of this compound ($Na_{0.34(3)}Ba_{1.048(6)}Mo_8O_{16}$) obtained from the single crystal x-ray diffraction data was in reasonably good agreement with the analytical results. The largest residual electron density (2.7e/A^3) lay 0.58 Å from the sodium position in the tunnel. The sodium atom was isotropically refined because of the negative temperature factors and large B22 value (ca. 11) in the anisotropic refinement. The residual electron densities around the molybdenum atoms were smaller, ranging from 1.0 to 2.0 e/A^3. The positional and thermal parameters are listed in Tables 1.4

and 1.5, respectively. Tables 1.6 and 1.7 tabulated bond distances and bond angles, respectively.

The unit cell is nearly metrically tetragonal and might be described in the tetragonal space group P4/n. However, the coordinate transformations led to a set of atomic coordinates that were not compatible with the symmetry of P4/n. Furthermore, the data set was transformed and averaged in 4/m symmetry, but 60 reflections with $|I_o-I(ave)| > 6.0\sigma I$ were eliminated from the data averaging. Perhaps the best evidence that the cell is better described in monoclinic symmetry comes from its Guinier powder pattern. About 75 lines ranging from $2\Theta = 12^o$ to 80^o could be measured and indexed in the monoclinic space group. Some reflections such as 400 and 004 were clearly observed as two separate peaks on the Guinier powder pattern. If the lattice does have the 4-fold symmetry, then those peaks should not split. Therefore, all the above evidence confirm the monoclinic space group.

X-ray Single Crystal Data Collection for $Li_{0.34}BaMo_8O_{16}$

The same crystal was mounted in a similar way in a 0.3 mm Lindemann glass capillary with its needle direction nearly collinear with the ϕ-circle axis. The same diffractometer and similar procedures were used for indexing and intensity data collection. Because the superlattice reflections were so weak that they could not be detected by the diffractometer in the

Table 1.4. Positional parameters for $Na_{0.35}BaMo_8O_{16}$

atom	multiplier	x	y	z	$B(A^2)^a$
Ba1	0.236(3)	0.75	0.7969(6)	0.75	2.02
Ba2	0.288(3)	0.75	0.4213(5)	0.75	2.13
Na	0.17(2)	0.75	0.093(5)	0.75	2.1
Mo1	1.0	0.9195(1)	0.8849(2)	0.43035(9)	0.71
Mo2	1.0	0.9005(1)	0.3351(2)	0.42424(9)	0.71
Mo3	1.0	0.9209(1)	0.6553(2)	0.1029(1)	0.76
Mo4	1.0	0.92771(9)	0.1008(2)	0.0823(1)	0.65
O1	1.0	0.0825(8)	0.882(1)	0.7187(8)	0.74
O2	1.0	0.5957(8)	0.615(1)	0.9430(9)	0.98
O3	1.0	0.7209(7)	0.875(1)	0.4183(8)	0.49
O4	1.0	0.5525(9)	0.620(2)	0.5940(9)	1.2
O5	1.0	0.9193(8)	0.119(1)	0.8826(8)	0.81
O6	1.0	0.7093(8)	0.377(1)	0.4191(8)	0.75
O7	1.0	0.6186(8)	0.109(1)	0.9170(8)	0.68
O8	1.0	0.9183(8)	0.617(1)	0.2894(8)	0.68

[a]The isotropic equivalent thermal parameter is defined as $B = 4/3\,[a^2\beta_{11} + b^2\beta_{22} + c^2\beta_{33} + 2ab(\cos\gamma)\beta_{12} + 2ac(\cos\beta)\beta_{13} + 2bc(\cos\alpha)\beta_{23}]$.

Table 1.5. Thermal parameters[a] for $Na_{0.35}BaMo_8O_{16}$

atom	B11	B22	B33	B12	B13	B23
Ba1	1.2(1)	4.0(2)	0.94(9)	0.0	0.17(7)	0.0
Ba2	1.12(8)	4.4(1)	0.87(8)	0.0	0.09(5)	0.0
Mo1	0.95(4)	0.51(4)	0.66(4)	-0.02(3)	0.13(3)	-0.09(2)
Mo2	0.92(4)	0.60(4)	0.62(3)	-0.07(3)	0.11(3)	-0.10(3)
Mo3	0.83(4)	0.62(4)	0.83(4)	-0.01(3)	-0.02(3)	0.04(3)
Mo4	0.72(4)	0.53(4)	0.72(4)	0.14(2)	0.05(3)	-0.20(2)
O1	0.9(3)	0.5(3)	0.9(3)	0.2(2)	0.3(2)	-0.2(2)
O2	0.9(3)	0.6(3)	1.4(3)	0.0(2)	-0.1(3)	0.3(2)
O3	0.3(3)	0.7(3)	0.6(3)	-0.1(2)	-0.1(2)	0.1(2)
O4	1.7(4)	0.8(3)	0.9(3)	0.5(3)	-0.1(3)	0.0(2)
O5	0.8(3)	0.7(3)	0.9(3)	-0.3(2)	0.0(2)	0.3(2)
O6	0.9(3)	0.5(3)	1.0(3)	-0.5(2)	0.1(2)	0.1(2)
O7	0.7(3)	0.8(3)	0.6(3)	0.2(2)	0.1(2)	0.3(2)
O8	1.3(3)	0.5(3)	0.3(3)	-0.1(2)	0.2(2)	-0.1(2)
Na	isotropic temperature factor (B): 2.1(4)					

[a]The general thermal parameter expression used is $\exp[-1/4(B_{11}h^2a^{*2} + B_{22}k^2b^{*2} + \ldots + 2B_{23}klb^*c_*)]$.

Table 1.6. Bond distances (Å) in $Na_{0.35}BaMo_8O_{16}$

more-distorted cluster(A)		less-distorted cluster (B)	
	Mo-Mo and Mo-O distances		
Mo3-Mo4'	2.828(2)	Mo1-Mo1'	2.547(2)
Mo4-Mo4'	2.532(2)	Mo1-Mo2'	2.684(2)
Mo3-Mo4[a]	2.564(2)	Mo1-Mo2[a]	2.589(2)
Mo3-Mo4[b]	3.185(2)	Mo1-Mo2[b]	3.158(2)
Mo3-O3	1.941(8)	Mo1-O1'	2.030(8)
Mo3-O8'	1.922(8)	Mo1-O3	2.046(8)
Mo3-O6	2.091(8)	Mo1-O8	2.103(8)
Mo3-O4'	2.075(9)	Mo1-O2	2.025(9)
Mo3-O4	2.045(10)	Mo1-O7'	2.054(8)
Mo3-O5'	2.095(8)	Mo1-O7	2.063(8)
Mo4-O5'	2.045(8)	Mo2-O1'	1.927(8)
Mo4'-O5'	2.045(9)	Mo2-O7	2.089(8)
Mo4'-O4	2.058(9)	Mo2-O2'	2.039(9)
Mo4'-O6'	2.121(8)	Mo2-O2	2.201(9)
Mo4'-O1'	2.041(8)	Mo2-O6	1.984(8)
Mo4'-O3'	2.007(8)	Mo2-O8	2.135(8)
	Ba-O and Na-O distances		
Ba1-O2	2.746(9)	Ba2-O2	2.771(9)
Ba1-O4	2.774(10)	Ba2-O4	2.817(10)
Ba1-O5	2.875(9)	Ba2-O5	2.806(8)
Ba1-O7	2.821(8)	Ba2-O7	2.822(8)
Na-O5	2.212(8)	Na-O7	2.185(8)

[a]Intracluster bond distances.

[b]Intercluster bond distances.

Table 1.7. Bond angles (deg) in $Na_{0.35}BaMo_8O_{16}$

more distorted clusters (A)		less distorted cluster (B)	
	intrachain bond angles		
Mo4-Mo4'-Mo3	67.39(5)	Mo1-Mo1'-Mo2	59.25(5)
Mo4'-Mo4-Mo3'	56.85(6)	Mo2-Mo1-Mo1'	63.01(5)
Mo4-Mo3'-Mo4'	55.77(4)	Mo1-Mo2-Mo1'	57.74(4)
Mo4'-O5-Mo3'	76.5(3)	Mo1-O7-Mo2	77.1(3)
Mo4'-O5-Mo4	76.5(3)	Mo2-O7-Mo1'	80.75(3)
Mo4-O5-Mo3'	86.2(3)	Mo1-O7-Mo1'	76.44(3)
Mo4'-O3'-Mo3'	81.0(3)	Mo1-O1'-Mo2	81.7(3)
Mo4-O4'-Mo3'	87.1(4)	Mo2-O2'-Mo1'	82.7(3)
Mo3'-O4-Mo3	102.2(4)	Mo2-O2-Mo1	99.9(4)
Mo3'-O4-Mo4'	100.8(4)	Mo2-O2-Mo2'	100.5(4)
Mo3'-O6'-Mo4'	98.2(4)	Mo2-O8-Mo1	96.4(3)
	interchain bond angles		
Mo3-O3-Mo1	141.0(4)	Mo1-O8-Mo3	126.8(4)
Mo3-O6-Mo2	137.0(4)	Mo1-O1-Mo4	135.7(4)
Mo4-O3-Mo1	138.0(4)	Mo2-O8-Mo3	136.7(4)
Mo4-O6-Mo2	124.6(4)	Mo2-O1-Mo4	142.6(4)

indexing procedure, the orientation matrix for the smallest subcell was obtained. Then, the orientation matrix was deliberately changed and the intensity data were collected on a bigger unit cell, a = b = 10.213 A, c = 2 x 2.879 A, $\alpha = \beta = \gamma = 90^{o}$. Later it was found that all of the reflections with odd ℓ values had weak intensities and very poor peak profiles. The data set showed 4/m symmetry and the following extinction condition: hk0, h + k = 2n + 1. Therefore, the space group P4/n (no. 85) was selected. The intensity data were corrected for Lorentz and polarization effects. An absorption correction was not made because the intensity fluctuation in a ϕ-scan was small.

Solution and Refinement of $Li_{0.34}BaMo_8O_{16}$

The data set was averaged in 4/m symmetry (R = 3.3 %). Ten reflections were eliminated, but nine of them had odd ℓ indices. The molybdenum atoms which were at 8h (x,y,0) special positions could be located by either the Patterson method or the Direct method. A least-squares refinement on the molybdenum positional parameters gave R = 35%. An electron density map revealed two strong and very much elongated peaks at the 2c special position. Two barium atoms were then included in a refinement with the barium multipliers and all positional parameters varied. The R factor dropped to 26%. At this point, the oxygen atoms could be easily located

from an electron density map. A refinement of all Mo, O, and Ba positional and anisotropic thermal parameters resulted in R = 12%. A difference map showed large residual electron densities at both the molybdenum ($7e/A^3$) and barium ($11e/A^3$) positions. Each of the two barium sites was about 50% occupied by a very much elongated barium ion (e.g., B33 = 11 B11 for Ba1). This poor refinement result and the axial oscillation photograph strongly suggested that those weak reflections should not be included in the data set. Therefore, those reflections with odd ℓ values were deleted and the repeat distance along the c axis and ℓ values were halved.

The new data set showed the extinction condition for body-centering. The space group became I4/m (no. 87) which also has been observed as the space group for many hollandites. The molybdenum atom was located by the Patterson-superposition method. One barium atom and two oxygen atoms were located on a subsequent electron density map. A refinement varying positional and anisotropic thermal parameters of all atoms converged at R = 6.2% and R_w = 10.9%. Because the B33 value (3.00 A^2) for the molybdenum atom was a little too large, the structure was then refined with the molybdenum atom off the mirror plane. A few more cycles of least-squares refinement with alternately fixed temperature factors and z coordinate of the molybdenum atom gave R = 4.5% and R_w = 7.4%. At this point, Hamilton test (19) was applied to check the

significance of the changes in R factors when the second model was used. It was found that R_w(model 1)/R_w(model 2) = 1.47 which greatly exceeded the value (ca. 1.03) obtained by interpolation in the Hamilton's table for α(level of significance) = 0.01. On the other hand, the second refinement gave lower e.s.d.'s for both positional and thermal parameters. Therefore, we could assert with a very high probability of being correct that the decrease in R factors was significant. The oxygens should closely follow the Mo atom distortion so that the Mo-O bond distances were correct. The structure was then refined with the intrachain oxygen atom (O1) off the mirror plane, but catastrophic results ensued. Therefore, the oxygen atom was still placed on the mirror plane. The data set was reweighted in six groups sorted according to F_o. A final full-matrix least-squares refinement, varing positional and anisotropic temperature factors of Ba and O atoms but with alternately fixed z coordinate and temperature factors for the Mo atom converged at R = 0.042, and R_w = 0.060. The molybdenum atom only shifted slightly off (0.11 A) the mirror plane and its B33 value decreased a little bit to 2.25 A^2. An electron difference map showed the maximum residual electron density (< 0.9 e/A^3) in the tunnel and residual electron density (< |-0.7 e/A^3|) at molybdenum positions. Because the scattering factor for lithium atom is very samll, no attempt was made to locate the lithium atomic position. The crystallographic data for

this complicated structure is listed in Table 1.8. Positional, thermal parameters, bond distances, and bond angles are tabulated in Tables 1.9, 1.10, 1.11, and 1.12, respectively.

Table 1.8. Crystallographic data for $Li_{0.34}BaMo_8O_{16}$

---

crystal system: tetragonal
space group: I4/m (no. 87)
a = b = 10.213(1) A
c = 2.8794(6) A
V = 300.4(1) A
Z = 1
d(calcd) = 6.433 g/cm^3
crystal size: 0.05 x 0.05 x 0.36 mm
absn coeff: 112.2 cm^{-1}
radiation: Mo Kα (λ = 0.71034 A)
monochromator: oriented graphite
scan type: ω-scan
automatic background detn, max scan half width: 0.5 degree
std reflns: 3 measured every 75 reflns; no significant decay
reflns measd: hkℓ, $\bar{h}\bar{k}\ell$ octants
max 2θ: 60^o
no. of unique reflns with I > 3σ(I): 250
no. of parameters refined: 24
R = 4.2%[a]
R_w = 6.0%[b]
quality-of-fit indicator: 0.930[c]

---

[a] $R = \Sigma||F_o| - |F_c||/\Sigma|F_o|$.

[b] $R_w = [\Sigma w(|F_o|-|F_c|)^2/\Sigma w|F_o|^2$; $w = 1/\sigma^2(|F_o|)$.

[c] Quality of fit = $[\Sigma w(|F_o|-|F_c|)^2/(N(observns)-N(parameters))]^{1/2}$.

Table 1.9. Positional parameters for $Li_{0.34}BaMo_8O_{16}$

atom	multiplier	x	y	z	$B(A^2)^a$
Ba	0.0625	0.5	0.5	0.1190(9)	1.55
Mo	0.5	0.67613(6)	0.15821(8)	0.5370(8)	1.81
O1	0.5	0.1432(7)	0.1804(7)	0.0	2.0
O2	0.5	0.1679(5)	0.4631(5)	0.0	0.92

[a]The isotropic equivalent thermal parameter is defined as $B = 4/3\ [a^2\beta_{11} + b^2\beta_{22} + c^2\beta_{33} + 2ab(\cos\gamma)\beta_{12} + 2ac(\cos\beta)\beta_{13} + 2bc(\cos\alpha)\beta_{23}]$.

Table 1.10. Thermal parameters[a] for $Li_{0.34}BaMo_8O_{16}$

atom	B11	B22	B33	B12	B13	B23
Ba	0.63(4)	0.63	4.0(2)	0.0	0.0	0.0
Mo	0.76(4)	2.04(4)	2.25(6)	0.38(2)	-0.32(4)	-1.08(5)
O1	2.5(3)	3.2(3)	1.0(2)	2.1(2)	0.0	0.0
O2	0.8(2)	1.0(2)	0.9(2)	-0.2(1)	0.0	0.0

[a]The general thermal parameter expression used is $\exp[-1/4(B11h^2a^{*2} + B22k^2b^{*2} + ... + 2B23klb^*c^*)]$.

Table 1.11. Bond distances (A) in $Li_{0.34}BaMo_8O_{16}$

Mo1-Mo1'''	2.699(2)	
Mo1-Mo1'	2.662(4)[a]	
	3.097(4)[b]	
Mo1-Mo1''	2.804(1)	
Mo1'-Mo1''	2.922(3)[b]	
Mo1-O1	2.137(5)	
Mo1-O1'	2.032(7)	
Mo1-O1''	1.985(6)	
Mo1-O2	2.105(4)	
Mo1-O2'	1.997(5)	
Mo1-O2''	1.950(4)	
Ba-O1	2.952(6)	(4X)
	2.596(7)	(4X)

[a]Intracluster distance.

[b]Intercluster distance.

Table 1.12. Bond angles (deg) in $Li_{0.34}BaMo_8O_{16}$

Mo1''-Mo1-Mo1'''	57.81(9)
Mo1'-Mo1-Mo1'''	63.08(8)
Mo1-Mo1'-Mo1'''	59.11(8)
O2-Mo1-O2''	88.5(3)
O2-Mo1-O2'	91.0(3)
O2-Mo1-O1	86.2(2)
O2-Mo1-O1''	176.3(2)
O2-Mo1-O1'	85.3(2)
O2''-Mo1-O2'	95.6(2)
O2''-Mo1-O1	174.6(2)
O2''-Mo1-O1''	94.8(2)
O2''-Mo1-O1'	89.5(2)
O2'-Mo1-O1	85.9(2)
O2'-Mo1-O1''	90.1(2)
O2'-Mo1-O1'	173.7(1)
O1-Mo1-O1''	90.4(2)
O1-Mo1-O1'	88.8(2)
O1''-Mo1-O1'	93.3(2)

DESCRIPTION OF THE STRUCTURES

$Na_{0.35}BaMo_8O_{16}$

Fig. 1.2 is the structure of $Na_{0.35}BaMo_8O_{16}$ as viewed down the monoclinic b axis. It consists of molybdenum-oxide cluster chains extended parallel to the b axis. Four chains are linked together via the sp^2 type of oxygen atoms to form channels in which sodium and barium ions are located. But there are only two different types of chains each of which is composed of one type of discrete rhomboidal molybdenum metal cluster units. Both of the metal cluster units have $\bar{1}$ symmetry. Therefore, each cluster contains two different molybdenum atoms; the apical atoms which are each bonded to two other molybdenum atoms and six oxygen atoms and the waist atoms which are each bonded to three molybdenum and six oxygen atoms (Figs. 1.3 and 1.4). Both cluster units are distorted, but one is apparently much more distorted than the other. The extent of distortion for each of these two cluster units is intermediate between the regular and distorted cluster units in $Ba_{1.14}Mo_8O_{16}$. This aspect will be further discussed in "Discussion" section. In the following, the more distorted cluster and the less distorted cluster will be called clusters A and B, respectively.

As in $Ba_{1.14}Mo_8O_{16}$ oxygen atoms can also be divided into four different types: type I, intrachain capping oxygens

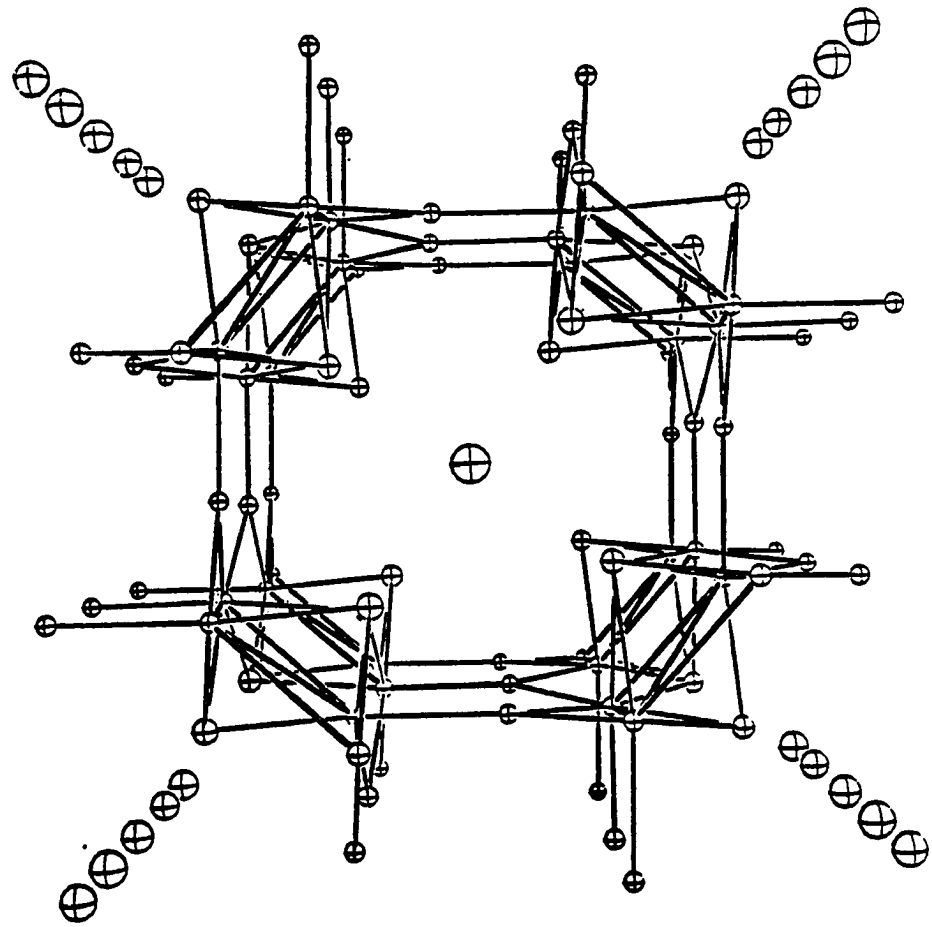

Fig. 1.2. Three-dimensional view of the $Na_{0.35}BaMo_8O_{16}$ structure as seen along the monoclinic b axis. The fifty percent probability isotropic thermal ellipsoids are shown.

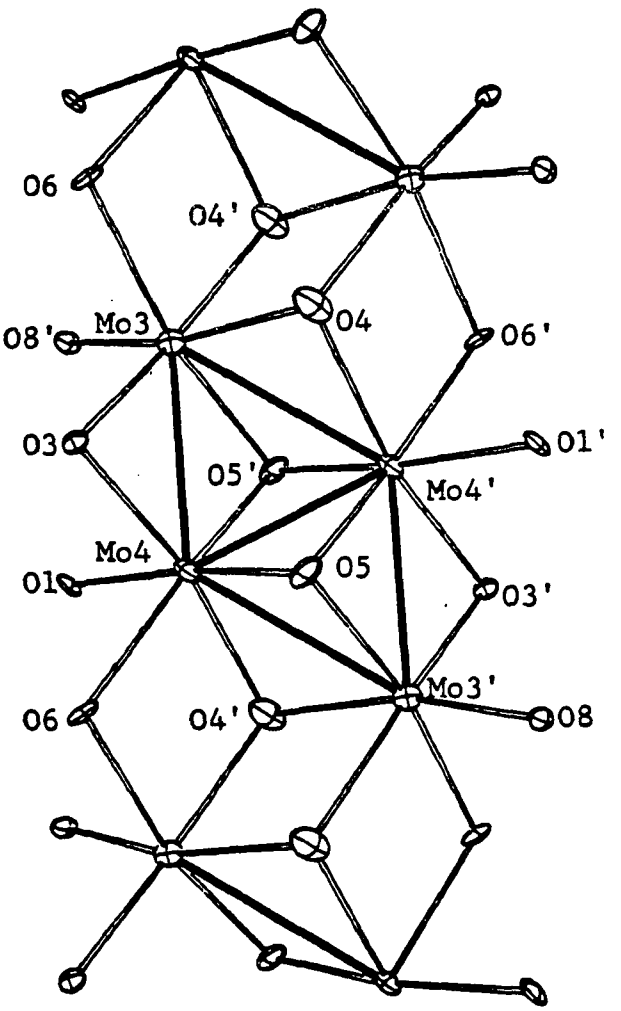

Fig. 1.3. A section of one metal-oxide chain containing the "more distorted" molybdenum metal clusters in $Na_{0.35}BaMo_8O_{16}$. Mo-Mo bonds are represented by solid black lines. Fifty percent probability anisotropic thermal ellipsoids are shown.

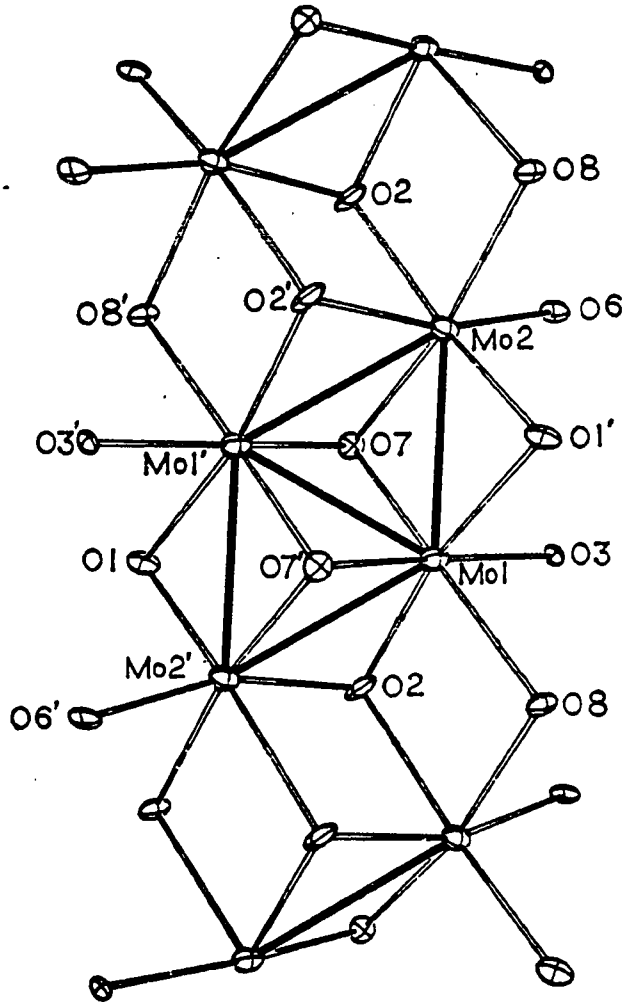

Fig. 1.4. A section of one metal-oxide chain containing the "less distorted" molybdenum metal clusters in $Na_{0.35}BaMo_8O_{16}$. Mo-Mo bonds are represented by solid black lines. Fifty percent probability anisotropic thermal ellipsoids are shown.

(05,07); type II, intrachain bridging oxygens (02, 04) which are doubly bridging on an edge of a cluster and singly bonded to an apical atom in a neighboring cluster; type III, interchain bridging oxygens (06, 08) which connect two intrachain clusters and an apical atom in an adjacent chain; type IV, interchain bridging oxygens (01, 03) which are bridging on an edge of a cluster unit and bonded to a waist atom in an adjacent chain.

Fig. 1.5 is a view perpendicular to the b axis showing the oxygen coordination around the two barium ions and one possible position of the sodium ion. All of the sites in the tunnel are fractionally occupied. The distances between the ternary metal cations are so short (Na-Ba1 = 1.67, Na-Ba2 = 1.91, Ba1-Ba2 = 2.154 Å) that such pairs cannot occur together in a unit cell. Ba1 and Ba2 is each coordinated by eight intrachain oxygen atoms (type I and II) and the site for Ba2 is slightly favored as shown by the occupancy factors of 0.288(3)(= 57.6%) for Ba2 and 0.236(3)(= 47.2%) for Ba1. Both barium ion sites in $Na_{0.35}BaMo_8O_{16}$ are located between four linked pairs of molybdenum-oxide clusters. However, one of the barium ion sites in $Ba_{1.14}Mo_8O_{16}$ is disordered, consisting of two inversion-related positions within a distorted rectangular box. In $Na_{0.35}BaMo_8O_{16}$, the distances of O-Ba1 range from 2.746 to 2.875 A, and d(O-Ba2) range from 2.771 to 2.882 A. The shorter distances involve oxygen atoms, O2 and O4, which bridge two separate clusters within a chain and are

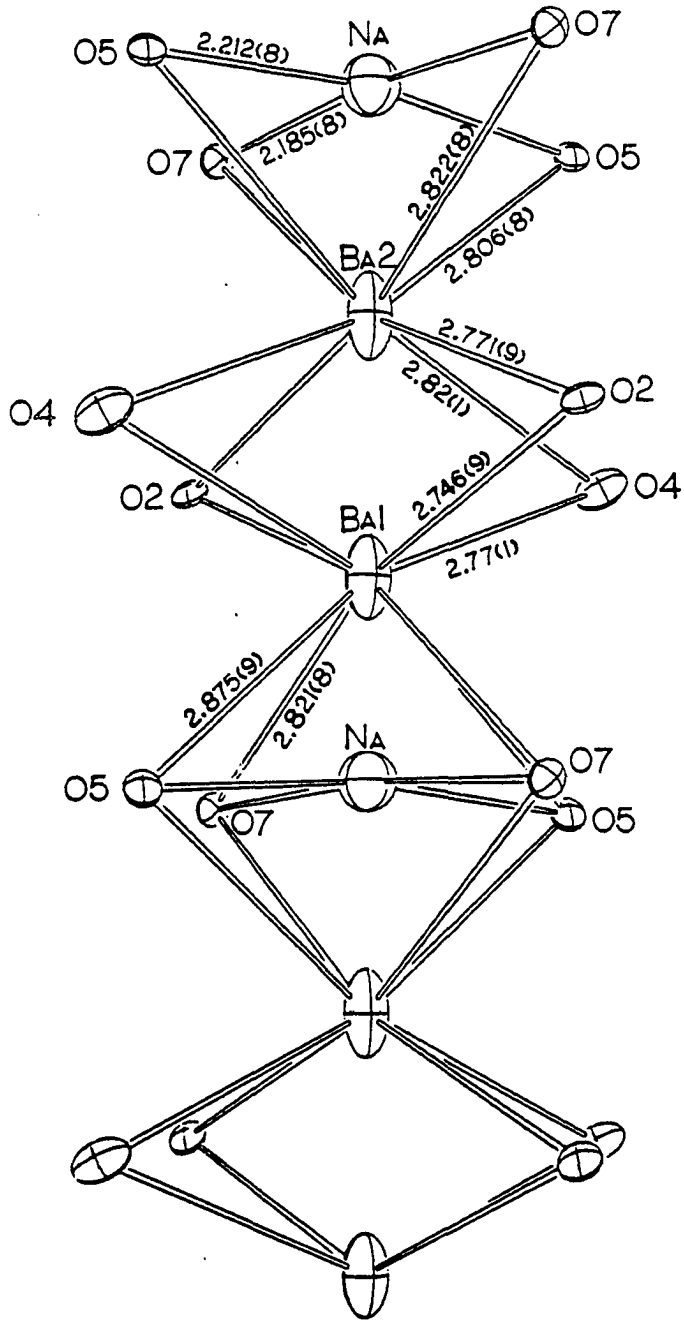

Fig. 1.5. A view perpendicular to the monoclinic b axis of $Na_{0.35}BaMo_8O_{16}$ showing the oxygen coordinations around barium and sodium ion sites

located closer to the plane of molybdenum atoms. However, in $Ba_{1.14}Mo_8O_{16}$ the corresponding barium-oxygen distances are the longest. The sodium ions are coordinated by four intrachain capping oxygen atoms (type I) which are nearly on a plane. The Na^+ is a little off (0.14 A) the plane and is thus in a slightly distorted square-planar symmetry. Na-O bond distances are 2.212 and 2.185 A which seem too short when effective ionic radii (20) for Na^+ (c. n. = 4) and O^{2-} (c. n. = 4) are used to predict the Na-O (= 2.37 A) bond length. This aspect will be further discussed later. The large B22 thermal parameter of the sodium ion in the anisotropic least-squares refinement probably indicates that the sodium ion is disordered among several sites. No superlattice reflections were observed on the axial oscillation picture along the crystallographic b axis suggesting that sodium and barium ions occupy some possible sites in the tunnel, but without 3-dimensional ordering.

$Li_{0.34}BaMo_8O_{16}$

This compound also adopts the very interesting hollandite structure. The crystal is tetragonal indicating only one type of molybdenum metal-oxide chain in the lattice. An axial oscillation picture along the tetragonal c axis did not reveal any reflections corresponding to the doubling of the c constant. This observation implies two possibilities: 1. the

molybdemum atoms are equally spaced, 2. molybdenum atoms are still clustered in each chain in a similar way as $Na_{0.35}BaMo_8O_{16}$, but metal clusters in one chain are not ordered along the c direction in the lattice. According to what we have observed in the $Na_{0.35}BaMo_8O_{16}$, and $Ba_{1.14}Mo_8O_{16}$ compounds, the second possibility seems more likely. The appearance of two very closely spaced superlattice reflections on the oscillation photograph was probably caused by the ordering of barium ions in the tunnel. The crystal structure was refined based upon the above assumption. The second model requiring the molybdenum atom off the mirror plane gave better results from least-squares refinement (vide supra).

The rhomboidal molybdenum metal cluster in $Li_{0.35}BaMo_8O_{16}$ (Fig. 1.6) is distorted and its extent of distortion is also intermediate between the distorted and regular cluster units in $Ba_{1.14}Mo_8O_{16}$. But there are two obvious differences from other analogous compounds. Firstly, the Mo(waist)-Mo(waist) bond distance in this lithium-containing compound is appreciably longer. Secondly, the intercluster distances within one chain become a lot shorter.

In the subcell refinement, there are only two types of oxygen atoms: intrachain (O1) and interchain (O2) oxygens. The barium ion site is 50% occupied. The two mirror-plane related barium ions are only about 0.22 A apart. The barium ions are ordered in the tunnel in a complicated way such that the repeat distance along the tunnel direction is 48.91(2) A.

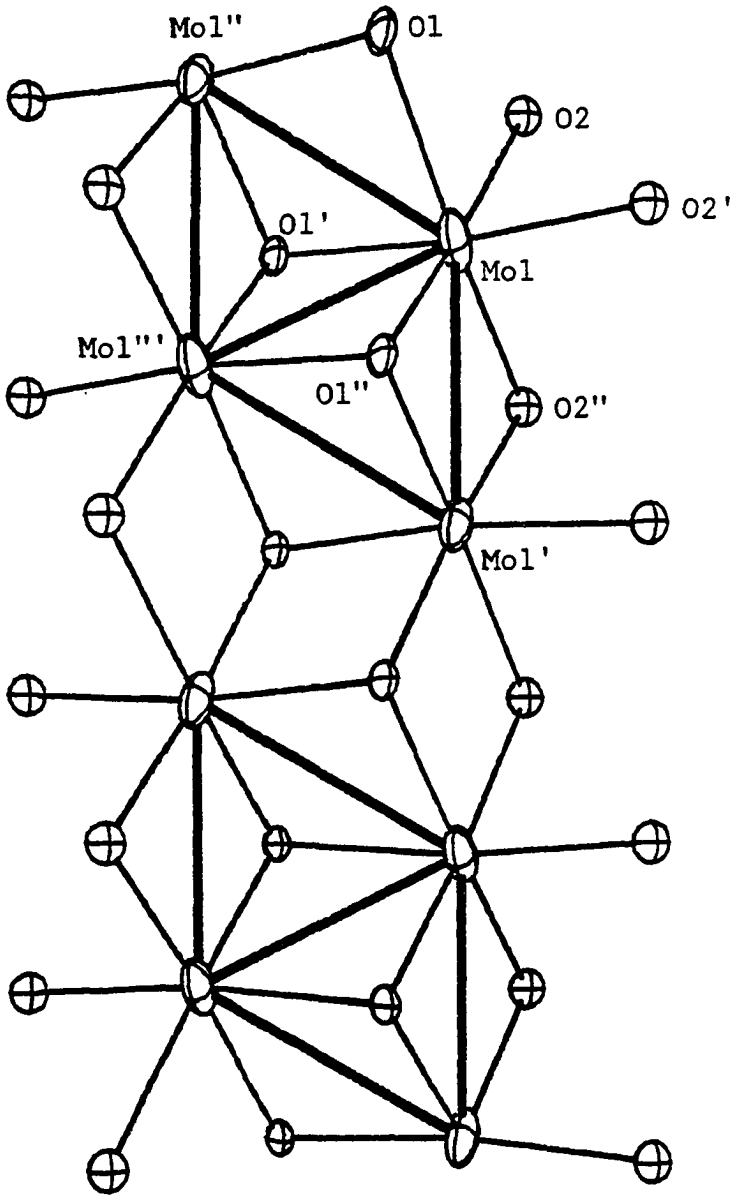

Fig. 1.6. A section of one metal-oxide chain containing the molybdenum metal clusters in $Li_{0.34}BaMo_8O_{16}$. Mo-Mo bonds are represented by solid black lines

Each barium ion is coordinated by eight intrachain oxygen atoms in a square prismatic arrangement. The relatively large temperature factor for the intrachain oxygen (O1) is probably connected with the clustering of the molybdenum atoms.

DISCUSSION

According to the reaction condition and the reactants used it is expected that molybdenum dioxide would be one of the phases formed in the initial stage of the reaction. Molybdenum dioxide adopts the very interesting distorted rutile structure in which molybdenum atoms are paired. Fig. 1.7 shows an ideal rutile structure consisting of strings of cation-occupied, edge-shared anion octahedra parallel to the tetragonal c axis. Each string shares corners with four neighboring strings to give a body-centered tetragonal cation array. Also discernible in the figure are the small, square channels running along the c direction. Cox et al. (21) have studied the lithiation of several rutile phases. The lithium is believed to be incorporated into the vacant channels of MoO_2 to form $LiMoO_2$, but the resulting compound is best described as distorted NiAs structure rather than rutile structure. The barium ion is of course too large to be inserted into the channel without changing the rutile structure drastically. It is possible to imagine a transformation as shown in Fig. 1.8. This rutile-hollandite transformation requires a cooperative jump of the cations into neighboring sites followed by an adjustment of the Mo-O bonds to convert the primitive tetragonal packing (PTP) to the hollandite structure. The latter structure was regarded as an intergrowth of PTP and HCP (hexagonal close packing) by David

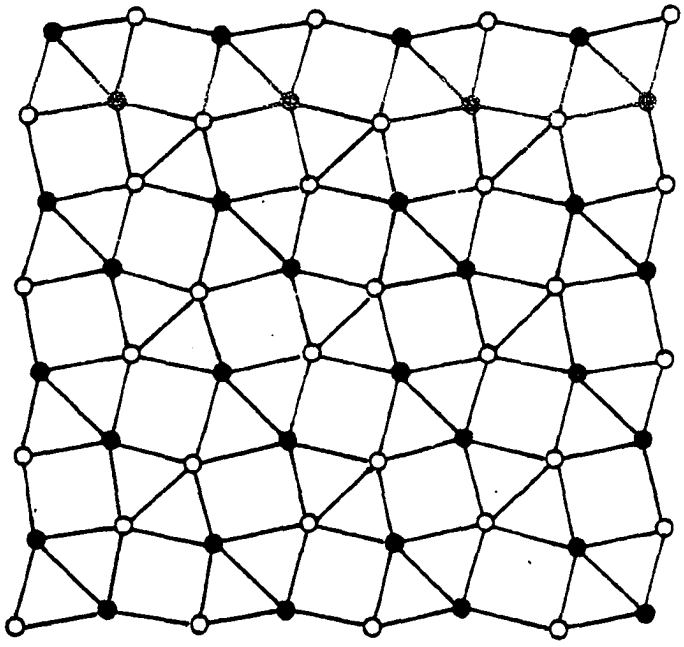

Fig. 1.7. Projection of rutile down the unique c-axis. Filled and empty circles represent oxygen atoms at z = 0 and z = 1/2 respectively

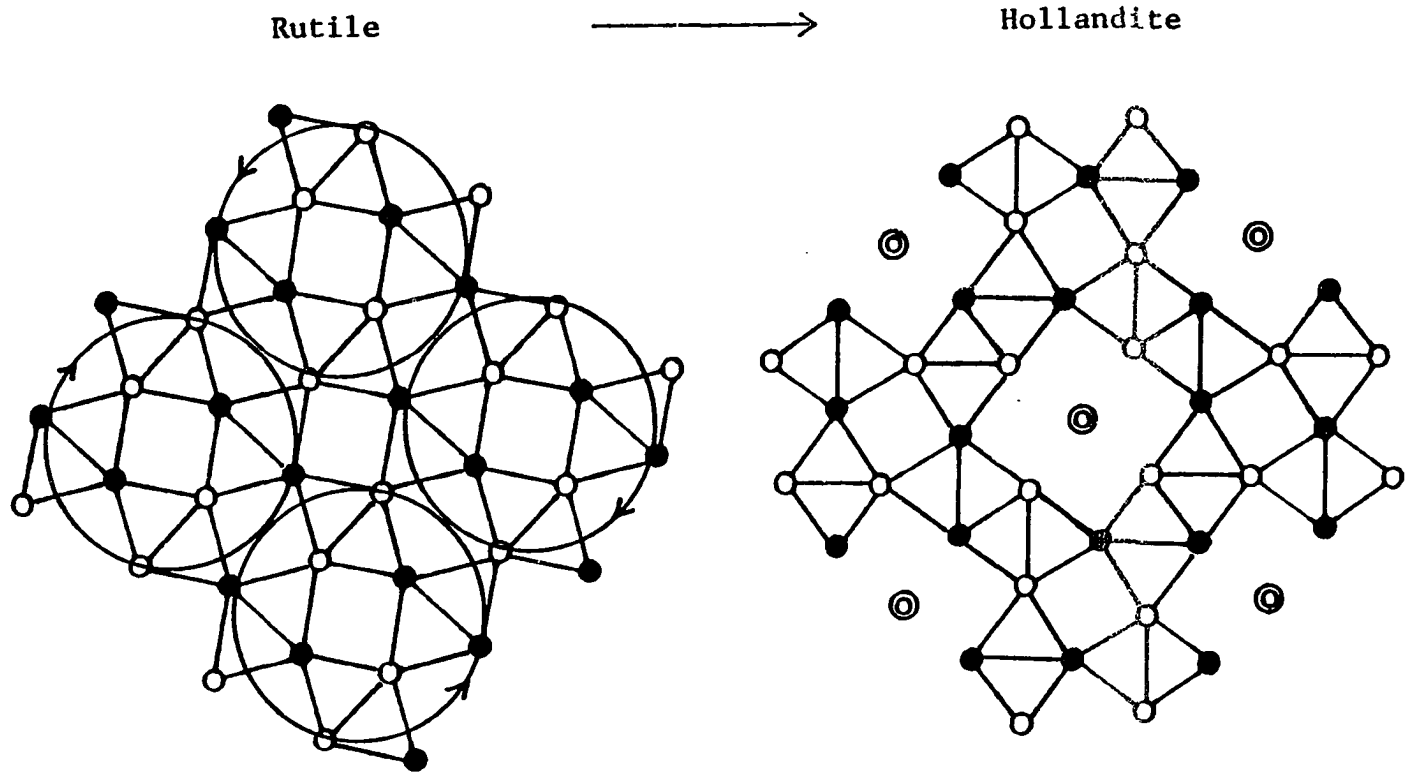

Fig. 1.8. Rutile-hollandite transformation. Filled and empty circles represent oxygen atoms at z = 0 and z = 1/2 respectively. Double circles are the ternary metal cations in the tunnels

et al. (22). Then, much bigger tunnels are created in which big cations such as barium and potassium can be inserted.

Different and related transformations were found in other systems, such as PTP-HCP and rutile-spinel transformations (23). We can also imagine a new layer structure with the ternary metal cations between the $(MoO_2)_n$ layers. This rutile-$CdCl_2$ transformation (Fig. 1.9) also requires a cooperative jump of metal cations to the neighboring sites with an adjustment of Mo-O bonds so that the anion arrays are no longer corrugated as in PTP. The transformation may go through an intermediate structure which was mentioned in a recent paper (22). This idea has found experimental support by the recent discovery of a new ternary molybdenum oxide (24), Li_xMoO_2, in which the oxygen anions are in cubic close packing. The rutile structure may also transform into the CdI_2 type structure via the intermediate structure (Fig. 1.9). This idea is also experimentally supported by the discovery of a high pressure form of β'-PtO_2 (25) with the rutile structure. Two other known polymorphs are the ambient pressure phase α-PtO_2 (26) with the CdI_2 structure and the high pressure phase β-PtO_2 (27, 28) adopting the $CaCl_2$ structure. In fact, the $CaCl_2$ structure is an orthorhombic modification of the rutile structure. The anion in the $CaCl_2$ structure has a better approximation to close packing. In other words, the anion arrays in $CaCl_2$ are nearly straight lines rather than corrugated as in the rutile structure.

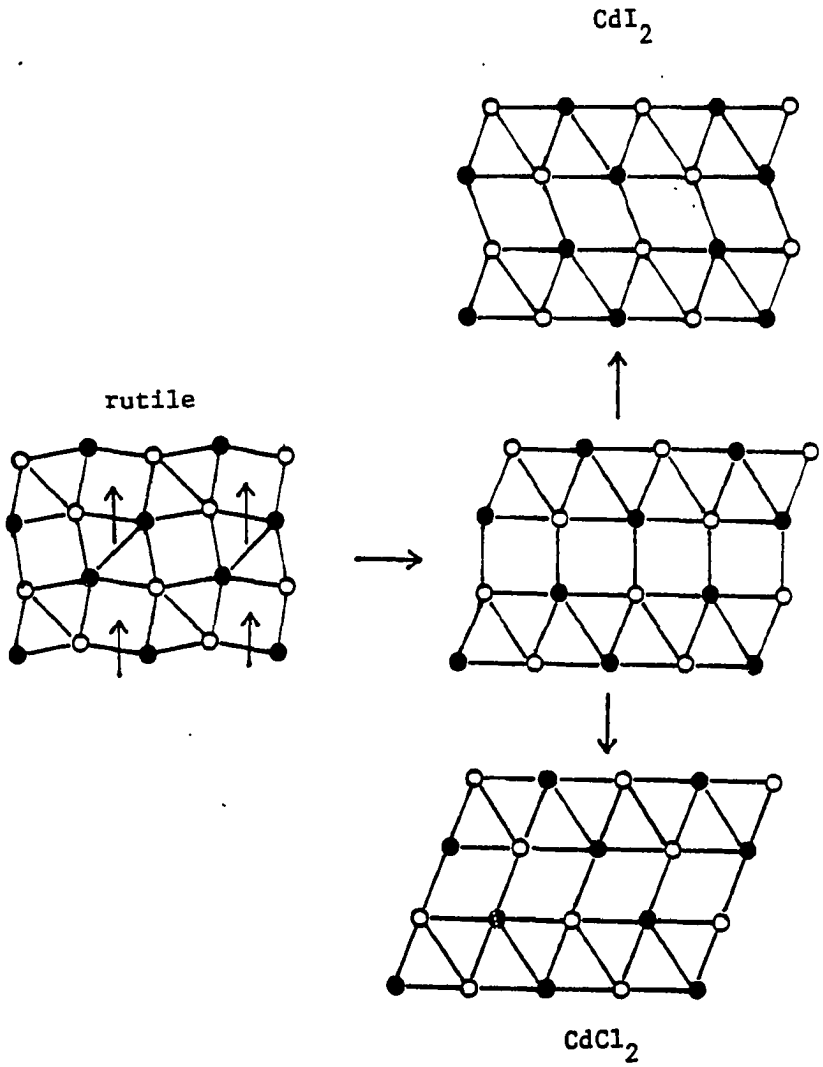

Fig. 1.9. Rutile-CdI_2 and rutile-$CdCl_2$ transformations. Filled and empty circles represent oxygen atoms at z = 0 and z = 1/2 respectively. The arrows indicate the cooperative jumps of the cations to the nearest-neighbor sites. The transformation may go through an intermediate structure which was mentioned in the paper by David et al. (22)

Therefore, one may conclude that at high pressure α-PtO_2 (CdI_2 structure) transforms into the densest phase β'-PtO_2 (rutile structure). One may also speculate that β-PtO_2, which has an intermediate density, can be converted to β'-PtO_2.

One of the most important features of this hollandite structure is that each molybdenum oxide chain consists of tetranuclear molybdenum metal clusters. These two new compounds, along with $Ba_{1.14}Mo_8O_{16}$ and $K_2Mo_8O_{16}$, are the only examples known so far. Very interestingly, the sodium-containing compound contains two different types of cluster units which are essentially the same as those in $K_2Mo_8O_{16}$. Although the compounds $Li_{0.34}BaMo_8O_{16}$, $Na_{0.35}BaMo_8O_{16}$, and $Ba_{1.14}Mo_8O_{16}$ have about the same metal cluster electrons (MCE), their rhomboidal clusters distort differently. Therefore, it is speculated that MCE is not the only factor governing the distortion of the metal clusters when different cluster chains are compared. The interaction between the ternary cation and the intrachain oxygen atoms might also be important (vide infra). The Mo-Mo bond distances for these four compounds are tabulated in Table 1.13.

Cotton and Fang (29) have performed molecular orbital calculations on the hypothetical cluster, $[Mo_4(OH)_{16}]^{-2}$, of C_{2h} symmetry. Their calculation results are shown in Fig. 1.1). The five molecular orbitals ($14b_u + 12a_u + 14a_g + 15a_g + 12b_g$) are strongly involved in Mo-Mo bonding. These five orbitals are filled in the hypothetical ion and significantly

Table 1.13. Molybdenum-molybdenum bond distances(A) in four hollandite structures containing rhomboidal Mo metal clusters

	$Na_{0.35}BaMo_8O_{16}$	$K_2Mo_8O_{16}$	$Ba_{1.14}Mo_8O_{16}$	$Li_{0.34}BaMo_8O_{16}$
	(cluster A)	(cluster A)	(distorted)	
[a]R_1	2.828(2)	2.837(2)	2.847(1)	2.804(1)
R_2	2.564(2)	2.565(2)	2.546(1)	2.662(4)
R_3	2.532(2)	2.527(3)	2.560(1)	2.699(2)
	(cluster B)	(cluster B)	(regular)	
R_1	2.684(2)	2.697(2)	2.616(1)	
R_2	2.589(2)	2.596(2)	2.578(1)	
R_3	2.547(2)	2.551(3)	2.578(1)	

[a]R_1, R_2, and R_3 are defined as below:

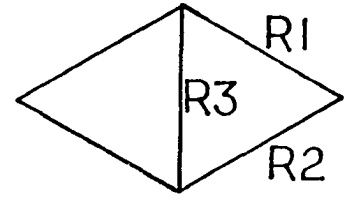

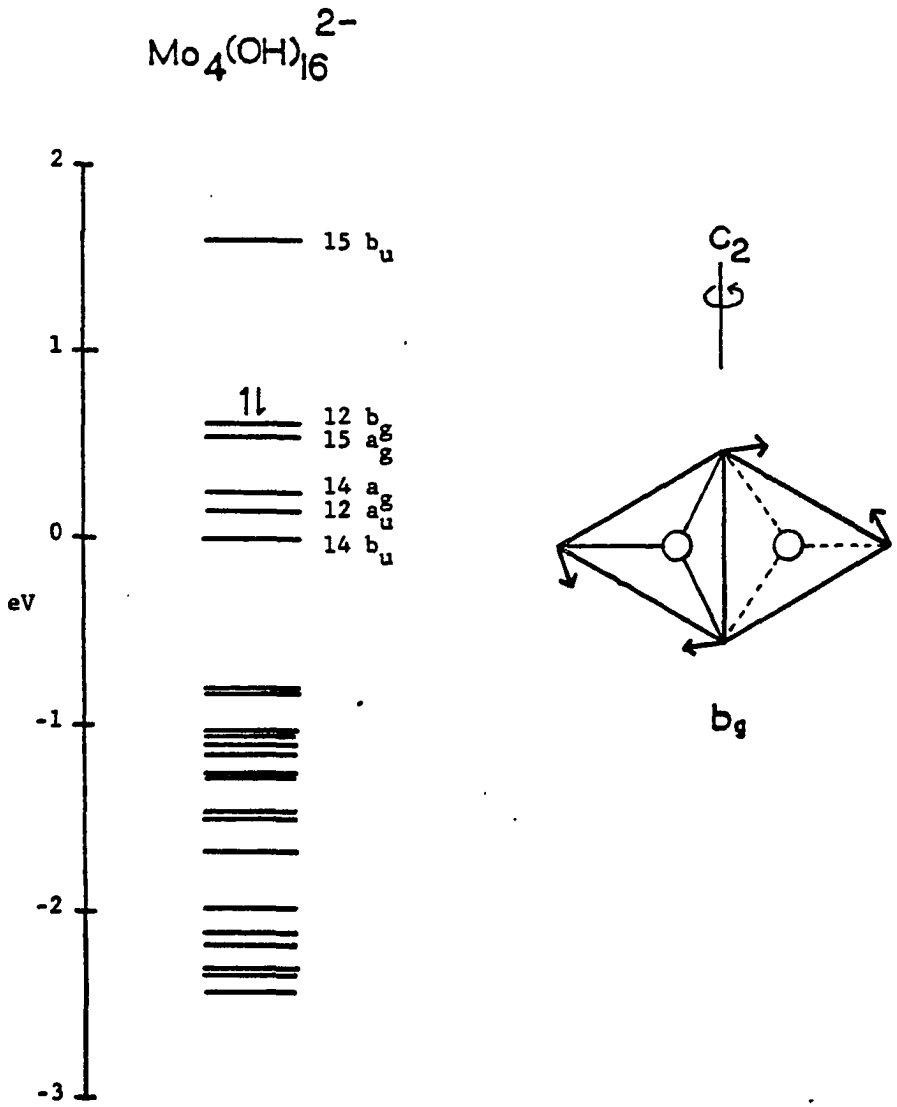

Fig. 1.10. A partial energy level diagram for the hypothetical ion, $[Mo_4(OH)_{16}]^{-2}$. (From Cotton, F. A.; Fang, A. J. Am. Chem. Soc. 1982, 104, 113.)

contribute to the five Mo-Mo single bonds in the rhomboidal cluster. Because $12b_g$ and $15a_g$ are very close in calculated energy, the HOMO of this cluster is either the $12b_g$ or the $15a_g$ orbital. If two electrons are lost from the HOMO, then the cluster has a totally symmetric (A_g) ground state with a very low-lying excited state of B_g symmetry. Because the direct product of A_g and B_g is B_g, we expect the second-order Jahn-Teller distortion to take the form of a b_g normal vibration. There is only one b_g vibration and it leads to exactly the same type of distortion as observed in the molecular compound $W_4(OEt)_{16}$ (11).

Let us take a look at our compounds. The $Ba_{1.14}Mo_8O_{16}$ compound consists of two types of cluster units. One is almost regular and the other one is very distorted. According to the MO calculation, the regular cluster unit has about 10 electrons, and the very distorted cluster only has about 8.28 (ave.) electrons available for Mo-Mo bonding. Therefore, it is likely that the second-order Jahn Teller distortion occurs in the latter clusters. Interestingly enough, the sodium and potassium-containing compounds have almost identical cluster units. Both clusters are more distorted than the regular clusters, but less distorted than the distorted cluster in the $Ba_{1.14}Mo_8O_{16}$ compound. This implies that cluster A on the average has less electrons available for Mo-Mo bonding than cluster B. In other words, the MCE in cluster A is a little higher than 8.28, and the MCE in cluster B is a little less

than 10 so that a little distortion occurs. But the reason why these two compounds are different from the $Ba_{1.14}Mo_8O_{16}$ compound is not very clear. It is more difficult to predict the extent of distortion in the lithium-containing compound based on the MO calculation because the intercluster Mo-Mo distance is a lot shorter so that the above argument may not be applicable.

In order to know more about the oxidation states of the molybdenum atoms and charge distribution between the clusters, the following approach was made. Recently, Bart and Ragaini (30) applied the molybdenum-oxygen bond-strength bond-length relationship $s = (d/1.882)^{-6.0}$ of Brown and Wu (31) to a variety of oxomolybdenum configurations. In the equation s = bond strength of an Mo-O bond in valence units, d = Mo-O bond length, and the quantities 1.882(Mo-O bond length of unit strength) and -6.0 are fitted parameters. Application of the analytical expression gave results for the cation bond valence sums which were in good agreement with the formal oxidation states for many compounds. They also pointed out that molybdenum cation-cation interaction did not influence the results of the calculation. Thus, we can use the Mo-O bond-strength bond-length relationship to estimate the oxidation states of Mo atoms, and the charge distributions between the cluster units. The calculation results for the above four compounds are summarized in Table 1.14. The estimated standard deviations are given in parentheses and they are

Table 1.14. Assessment of oxidation states for Mo and charge distributions in four hollandite structures containing rhomboidal Mo metal clusters

compound	cluster	oxidation state	charge on Mo_4O_8
$Na_{0.35}BaMo_8O_{16}$	A	apex: 3.94(4)	
		waist: 3.58(4)	-0.94(8)
	B	apex: 3.74(3)	
		waist: 3.57(3)	-1.38(7)
			total: -2.3(1)
$K_2Mo_8O_{16}$	A	apex: 3.99(5)	
		waist: 3.54(4)	-0.94(9)
	B	apex: 3.74(5)	
		waist: 3.53(4)	-1.46(9)
			total: -2.4(1)
$Ba_{1.14}Mo_8O_{16}$	distorted	apex: 4.03(3)	
		waist: 3.61(3)	-0.72(6)
	regular	apex: 3.66(3)	
		waist: 3.51(2)	-1.66(5)
			total: -2.38(8)
$Li_{0.34}BaMo_8O_{16}$		apex: 3.84(3)	
		waist: 3.84(3)	-0.64(5)
			total: -1.28(7)

obtained by including the standard deviation (1σ) of the Mo-O bond lengths in bond-strength bond-length calculations.

The summation of negative charge on each cluster unit in either $Na_{0.35}BaMo_8O_{16}$ or $Ba_{1.14}Mo_8O_{16}$ is compatible, within 2σ, with its stoichiometry. The calculation result for $K_2Mo_8O_{16}$ is a little off. But the calculated charge for the $Li_{0.34}BaMo_8O_{16}$ compound is much too low. The apical molybdenum atom is expected to have a higher oxidation state because it is only bonded to two molybdenum atoms. In the $Li_{0.34}BaMo_8O_{16}$ compound, both apex and waist molybdenum atoms have the same oxidation state probably because the intercluster Mo(apex)-Mo(apex) bond distance becomes a lot shorter. Molybdenum atoms of cluster A in either the sodium or potassium-containing compound have lower oxidation states than the corresponding atoms of the distorted cluster unit in $Ba_{1.14}Mo_8O_{16}$. These results agree with the observed extent of distortions. Consistent results are also obtained for cluster B and regular cluster unit. The major difference in the oxidation states is at the apical molybdenum atom. For example, in $Na_{0.35}BaMo_8O_{16}$ the estimated oxidation state of the apical atom in cluster A is a lot higher than the corresponding one in B. The difference may trace back to the very long Mo2-O2 bond length. O2 is one of the type II intrachain oxygen atoms which are bonded to the barium ions. The O2-Ba bond distances (2.746 and 2.771 A) are so short that O2 is pulled away from the apical molybdenum atom (Mo2) in

cluster B. Therefore, the oxidation state of Mo2 becomes much lower. These compounds exhibit intriguing interplay among the number of metal cluster electrons, Mo-O interaction, and the interaction between oxygen and the ternary metal cations.

The bond-length bond-strength calculation was also applied to the Ba-O bonds in the three different barium-containing compounds. The equation (31) used in the calculation was:

$$s = \left(\frac{d(Ba\text{-}O)}{2.297}\right)^{-7.0}$$

The calculation results are listed below with the calculated valences in the parentheses: $Na_{0.35}BaMo_8O_{16}$, Ba1(2.00), Ba2(1.98); $Ba_{1.14}Mo_8O_{16}$, Ba1(2.14), Ba2(2.59); $Li_{0.34}BaMo_8O_{16}$, Ba(2.39). The results are excellent for the sodium-containing compound, but poor for the other two compounds. Both the $Li_{0.34}BaMo_8O_{16}$ and $Ba_{1.14}Mo_8O_{16}$ compounds revealed superlattice reflections on the axial oscillation pictures, while the sodium-containing compound did not. These experimental observations might be important in rationalizing the above discrepancies because the averaged x-ray structure obtained without including the superlattice reflections in the intensity data set might give inaccurate Ba atomic positions. This argument is reflected in the puzzling Ba-O bond distances: $Ba_{1.14}Mo_8O_{16}$, Ba1-O (2.885 to 2.677 A), Ba2-O (3.440 to 2.506 A); $Li_{0.34}BaMo_8O_{16}$, Ba-O (2.952 to 2.596 A). In contrast, the Ba-O bond distance ranges in the sodium-containing compound are much smaller (2.875 to 2.746 A for

Ba1; 2.822 to 2.771 A for Ba2). Estimation results are often poor when very distorted coordination polyhedra are involved. Such cases are annoying from the viewpoint of predicting valence state successfully.

As described earlier the sodium ion in $Na_{0.35}Mo_8O_{16}$ is involved in 4-fold coordination of a very unusual type. Furthermore, the Na-O bond distances seem a little shorter when bond lengths in other compounds with sodium in low coordination are compared. For example, d(^{IV}Na-O) = 2.401 A in Na_2O (32), d(^{IV}Na-O) = 2.22 - 2.59 A (ave. 2.37 A) in $Na_5P_3O_{10}$ (phase I) (33), d(^{IV}Na-O) = 2.30 - 2.41 A (ave. 2.36 A) in $NaOH.H_2O$ (34), and d(^{IV}Na-O) = 2.319 - 2.539 A (ave. 2.39 A) in Na_6ZnO_4 (35). McGuire and O'Keeffe (32) recently discussed the anomalously long Na-O bond distance in Na_2O and attributed it to cation-cation interactions. Because the nonbonded interactions might invalidate the strict applicability of bond-strength bond-length relationships, they excluded those cation-rich compounds in their analysis and obtained the following equation:

$$s = \left(\frac{d(Na\text{-}O)}{1.592}\right)^{-4.16}$$

Substituting the Na-O bond distances into the above equation we obtain $\Sigma s = 1.04$. Based on this very satisfactory result and the good agreement between the occupancy factor and the chemical analysis one can conclude that the sodium ions in

$Na_{0.35}BaMo_8O_{16}$ are located at unusual, nearly square-planar sites with reasonably short Na-O bond distances.

There is good prospect for other solid state compounds adopting the hollandite structure. For example, the surprising compound $Mo_4N_2(OPr^i)_{12}$ (36), recently prepared by Chisholm consists of a zig-zag chain with one short (2.55 A) and two long (2.92 A) Mo-Mo bond distances. This six-electron cluster can be regarded as a distorted rhomboid with two very long (3.8 A) parallel sides. Thus, a particularly fascinating prospect is the preparation of an isoelectronic compound such as $Ba_2Nb_8O_{16}$ in which the barium ions may fully occupy the possible sites in the tunnel formed by four infinite metal-oxide chains containing zig-zag Nb-Nb bonds.

REFERENCES

1. Perrin, C.; Chevrel, R.; Sergent, M. C. R. Acad. Sci. Ser. C. 1975, 280, 949.

2. Perrin, C.; Chevrel, R.; Sergent, M. C. R. Acad. Sci. Ser. C. 1975, 281, 23.

3. Perrin, C.; Chevrel, R.; Sergent, M. J. Solid State Chem. 1976, 19, 305.

4. Yaich, H. B.; Jegaden, J. C.; Potel, M.; Chevrel, R.; Sergent, M.; Berton, A.; Chaussy, J.; Rastogi, A. K.; Tournier, R. J. Solid State Chem. 1984, 51, 212.

5. Yaich, H. B.; Jegaden, J. C.; Potel, M.; Sergent, M.; Rastogi, A. K.; Tournier, R. J. Less-Common Metals 1984, 102, 9.

6. Stensvad, S.; Helland, B. J.; Babich, M. W.; Jacobson, R. A.; McCarley, R. E. J. Am. Chem. Soc. 1978, 100, 6257.

7. Chisholm, M. H.; Errington, R. J.; Folting, K.; Huffman, J. C. J. Am. Chem. Soc. 1982, 104, 2025.

8. Ryan, T. R.; McCarley, R. E. Inorg. Chem. 1982, 21, 2072.

9. McCarley, R. E.; Ryan, T. R.; Torardi, C. C. Am. Chem. Soc. Symp. Ser. No. 155, 41-60, 1981.

10. Broll, A.; Simon, A.; von Schnering, H.-G.; Schafer, H. Z. Anorg. Allg. Chem. 1969, 367, 1.

11. Chisholm, M. H.; Huffman, J. C.; Kirkpatrick, C. C.; Leonelli, J.; Folting, K. J. Am. Chem. Soc. 1981, 103, 6093.

12. Torardi, C. C.; McCarley, R. E. J. Solid State Chem. 1981, 37, 393.

13. Bystrom, A.; Bystrom, A. M. Acta Cryst. 1950, 146, 3.

14. Torardi, C.; Calabrese, J. C. Inorg. Chem. 1984, 23, 3281.

15. Rohrbaugh, W. J.; Jacobson, R. A. Inorg. Chem. 1974, 13, 2535.

16. Jacobson, R. A. J. Appl. Crystallogr. 1976, 9, 115.

17. Howells, E. R.; Phillips, D. C.; Rogers, D. Acta Crystallogr. 1950, 3, 210.

18. Hanson, H. P.; Herman, F.; Lea, J. D.; Skillman, S. Acta Crystallogr. 1964, 17, 1040.

19. Hamilton, W. C. Acta Crystallogr. 1965, 18, 502.

20. Shannon, R. D. Acta Crystallogr. 1976, A32, 751.

21. Cox, D. E.; Cava, R. J.; McWhan, D. B.; Murphy, D. W. J. Phys. Chem. Solids, 1982, 43, 657.

22. David, W. I. F.; Bruce, P. G.; Goodenough, J. B. J. Solid Chem. 1983, 50, 235.

23. David, W. I. F.; Thackeray, M. M.; Bruce, P. G.; Goodenough, J. B. Mat. Res. Bull. 1984, 19, 99.

24. Aleandri, L. E.; McCarley, R. E. unpublished research, Department of Chemistry, Iowa State University, Ames, Iowa, 1985.

25. Fernandez, M. P. H.; Chamberland, B. L. J. Less-Common Metals 1984, 99, 99.

26. Hoekstra, H. R.; Siegel, S; Gallagher, F. X. Adv. Chem. Ser. 1971, 98, 39.

27. Muller, O.; Roy, R.; J. Less-Common Metals 1968, 16, 129.

28. Shannon, R. D. Solid State Commun. 1968, 6, 139.

29. Cotton, F. A.; Fang, A. J. Am. Chem. Soc. 1982, 104, 113.

30. Bart, J. C. J.; Ragaini, V. Inorg. Chimica Acta 1979, 36, 26.

31. Brown, I. D.; Wu, K. K. Acta Crystallogr. 1976, B32, 1957.

32. McGuire, N. K.; O'Keeffe, M. J. Solid State Chem. 1984, 54, 49.

33. Corbridge, D. E. C. Acta Crystallogr. 1960, 13, 263.

34. Wunderlich, P. J. A. Acta Crystallogr. 1957, 10, 462.

35. Von Kastner, P.; Hopper, R. Z. Anorg. Allg. Chem. 1974, 409, 69.

36. Chisholm, M. H. private communication to R. E. McCarley, 1985.

SECTION 2. SYNTHESES, CRYSTAL STRUCTURES, AND PHYSICAL PROPERTIES OF TWO TERNARY MOLYBDENUM OXIDES HAVING THE $NaMo_4O_6$ STRUCTURE TYPE: $InMo_4O_6$ AND $Pb_{0.77}Mo_4O_6$

INTRODUCTION

Compounds containing octahedral metal cluster chains may be divided into two different types on the basis of their building blocks, namely the M_6X_8 and the M_6X_{12} clusters. Both condensed systems have a diverse collection of structure types and compounds.

Chains based on M_6X_8 clusters may be subdivided into two groups: octahedra sharing trans faces and octahedra sharing trans edges. The former group is well-exemplified by the well-known Chevrel phases. These compounds can be formulated as $Mo_{3n+3}X_{3n+5}$, where X and n denote chalcogenides and the number of M_6 octahedra. The end member for this type of condensation was discovered in MMo_3X_3 (M = Li - Cs, In, Tl, Ag) (1 - 5). Infinite chain compounds containing trans edge-linked M_6X_8 octahedra were found in the prototype compounds Gd_2Cl_3 (6) and Sc_7Cl_{10} (7).

Chains based on 6-12 type building blocks were not only discovered in reduced binary lanthanide halides but also in reduced ternary and quarternary molybdenum oxides. The first member of the oxide system is $NaMo_4O_6$ (8). It is more electron-rich (13 e/Mo_4) and more tightly bound than the analogous lanthanide halides. The repeat distance along the cluster chain direction is considerably less than those in the halides. The sodium ions in $NaMo_4O_6$ occupy sites in channels formed by four metal oxide cluster chains cross-linked by

metal-oxygen bonds. The sodium ion is coordinated by eight oxygen atoms which form a square box compressed along the tunnel direction. The structure of $NaMo_4O_6$ was unprecedented among metal oxide systems. Its discovery along with $Ba_{0.62}Mo_4O_6$ (9) signaled a large number of new structures in this family. Experiments have been designed to synthesize analogous compounds with different ternary metal cations in the square box. The reasons are twofold. First, one may be able to vary the number of metal cluster electrons in order to know the upper limit of m.c.e.s. per Mo_4O_6 cluster unit. Second, different ternary metal cations may modify the physical properties or the structure types dramatically.

This section describes the syntheses, single crystal structures, spectroscopic and physical properties studies of two infinite chain compounds containing trans edge-shared M_6X_{12} type clusters, $InMo_4O_6$ and $Pb_{0.77}Mo_4O_6$.

EXPERIMENTAL AND RESULTS

Materials

Molybdenum tubing was obtained from Thermo-Electron Corp. (99.97%), molybdenum metal powder from Aldrich Chemical Co. (99.99%), molybdenum trioxide from Baker Chemical Co. (99.9%), In_2O_3 powder from Apache Chemicals Inc. (99.95%), indium metal shot from Alfa Products (99.99%), and lead metal powder from Fisher (Certified A. C. S.). Lead molybdate was prepared by mixing an aqueous solution of sodium molybdate (Fisher Certified A. C. S.) with an aqueous solution containing the stoichiometric quantity of lead nitrate (Baker's Analyzed Reagent). The white precipitate was filtered, washed thoroughly with water, and dried at 125°C under dynamic vacuum overnight.

Syntheses and Analyses

$\underline{InMo_4O_6}$

The title compound was first discovered by Larry Brough in the product of the following reaction:

$$3\ In_2O_3 + 11\ MoO_3 + 13\ Mo \xrightarrow[\text{Mo tube}]{\text{1300C, 7 days}} 6\ \text{"}InMo_4O_7\text{"}$$

There were two new phases in the product. One occurred as chunky and the other as needle-like crystals. Unfortunately,

most crystals of the former one were found to be twinned. Electron microprobe analysis gave Mo to In ratios of about 3.0. Its x-ray powder pattern was considerably more complicated than that for $InMo_4O_6$, suggesting a larger unit cell or a lower crystal symmetry. The powder pattern of the chunky crystals has not been fully indexed yet. Most of the needle-like crystals in the product were very small. A significant quantity of MoO_2 was also found in the reaction product. A needle-like crystal was selected and indexed on a four-circle diffractometer. The indexing results indicated that it had the $NaMo_4O_6$ structure type.

Bigger needles and chunks were obtained by reacting a mixture of In_2O_3, MoO_3, and Mo in mole ratio of 1: 3: 5 (i.e., aiming at $InMo_4O_6$) in a molybdenum tube at 1350°C. A lot of molybdenum metal remained in the reaction product. Electron microprobe analyses on four needle-like crystals gave an In to Mo ratio of 0.252(5). Subsequently, a few more reactions to prepare pure $InMo_4O_6$ were conducted. It was found that pure product could not be obtained if In_2O_3 was used. Even though correct stoichiometry and different reaction conditions (1310 - 895°C; 6 - 28 days) were tried, the product always contained some second indium-containing compound.

In a specific reaction a pressed pellet containing a stoichiometric amount of In_2O_3, MoO_3, and Mo was placed in a zirconia crucible which was then sealed in a molybdenum tube. The reaction was conducted at 1310°C for 71 hrs. After

opening up the reaction container, it was found that lots of chunky and needle-like crystals deposited on both the molybdenum cap and the outer surface of the zirconia crucible. Evidently some interesting chemical transport reaction took place.

Indium metal was then used instead of In_2O_3 and pure $InMo_4O_6$ was finally obtained. Some of the reaction results are summarized as follows: 950°C, 13 d, fused silica tube, $InMo_4O_6$ and the second phase; 880°C, 13 d, fused silica tube, $InMo_4O_6$, MoO_2, and Mo; 895°C, 28 d, fused silica tube, $InMo_4O_6$ (x-ray pure). It seemed that higher reaction temperature (> 900°C) favored the formation of the second phase. Thus, a lower temperature and longer reaction time seemed necessary. Pure $InMo_4O_6$ prepared by this route gave sharp and strong x-ray powder diffraction pattern, but no crystal big enough for single crystal x-ray diffraction work was obtained. The crystal growth of $InMo_4O_6$ was carried out by heating the pure powder in an evacuated fused silica tube at 1200°C with a temperature gradient of about 30°C for a few days. Many needle-like crystals grew in the colder end of the tube. An x-ray powder pattern of the product showed that it was identical to the starting material. The reaction tube became opaque after the transport reaction. The transport reagent was probably H_2O although the fused silica tube was evacuated and flame-dried before being sealed.

Because reactions between $NaMo_4O_6$ and molten LiCl resulted

in a partial ion exchange of Na^+ by Li^+ (10), the possibility of ion exchanging indium with lithium was also considered. LiCl was dried at 175°C under dynamic vacuum for 12 hours. Pure $InMo_4O_6$ and excess LiCl were mixed in a dry box and then sealed in an evacuated fused silica tube. The reaction mixture was heated at 650°C for 20 hours. The product was washed with water, ethanol, and then air-dried. Guinier x-ray powder pattern of the product was the same as $InMo_4O_6$. A reaction at higher temperature (750°C) for a longer time (48 hours) was then conducted. Guinier x-ray powder pattern showed lines due to MoO_2, Mo metal, $InMo_4O_6$, and a few weak unidentified lines. The reason for MoO_2 and Mo formation was conjectured by Charlie Torardi (10).

Recently, new binaries Mo_9S_{11}, α- and β-$Mo_{15}Se_{19}$ and Mo_6X_6 (X = chalcogen) have been prepared by Potel et al. (11) via a low temperature route. These metastable phases were prepared by reacting the corresponding ternary phases with HCl(g) at about 500°C. Accordingly, the following reaction was conducted with the hope of preparing a new binary molybdenum oxide, Mo_4O_6.

$$InMo_4O_6 \xrightarrow[510\ C]{HCl(g)} \quad \text{(dashed arrow)}$$

HCl gas was dried by slowly passing through concentrated H_2SO_4 and a trap cooled by dry ice-acetone. The reaction was conducted for 4.5 hours. A small amount of white and dark-red material deposited in the cooler end of the reaction tube. A

Guinier x-ray powder pattern of the product in the hotter end was identical to $InMo_4O_6$. The colder end of the reaction tube immediately became blue after exposure to air, but the dark-red material looked unchanged. Evidently, indium ions in $InMo_4O_6$ cannot be easily removed or ion exchanged under the above reaction conditions without decomposition of the structure.

$\underline{Pb}_{0.77}\underline{Mo}_4\underline{O}_6$

Small needle-like crystals of the title compound were discovered in a reaction mixture resulting from the reaction of PbO, MoO_3, and Mo in 3: 5: 7 mole ratio (i.e., aiming at $PbMo_4O_6$). The reactants were sealed in a double quartz tube and then fired at 1000°C for 7 days. A Guinier powder pattern of the bulk product indicated that it contained some MoO_2, Mo, and a new phase which was isomorphous with $NaMo_4O_6$. The reaction product also contained some small lead beads. A purer product was obtained by reacting $PbMoO_4$, MoO_3, and Mo in 3: 2: 7 mole ratio ($PbMo_4O_6$) at lower temperature (940°C) for 10 days. The only observed impurity was some excess lead metal suggesting that the actual lead content per Mo_4O_6 unit was less than one. The stoichiometry of $Pb_{0.77}Mo_4O_6$ was determined from the x-ray single crystal diffraction data. Much bigger crystals were grown by heating the sample in an evacuated quartz tube at 1200°C with a temperature gradient of about 30°C for a few days. The quartz tube remained

transparent. The transport reagent in this case was probably also H_2O.

Preliminary Film Work and X-ray Powder Diffraction

$InMo_4O_6$

A crystal of dimensions 0.20 x 0.03 x 0.03 mm was selected for film work and intensity data collection. The axial oscillation picture and Weissenberg photographs confirmed its good crystal quality. The repeat distance along the oscillation axis (needle direction) was 2.86 A. No superlattice reflections were observed on the oscillation picture. There was a mirror plane perpendicular to the oscillation axis indicating that the crystal symmetry was monoclinic or higher. The Weissenberg photographs combined with the oscillation photographs gave the following information: 4/mmm Laue symmetry, 0k& reflections (k = 2n), and a = b = 9.66 A. The Guinier powder pattern could be well-indexed on the basis of P4/mbm space group. The indexing results are listed in Table 2.1.

$Pb_{0.77}Mo_4O_6$

Many crystals had to be selected before a satisfactory one was obtained. (The transport reaction mentioned above gave much better crystals, and one of these has been selected for studying the very interesting superstructure.) A very small

crystal of dimensions 0.10 x 0.02 x 0.02 mm was selected for intensity data collection. Its crystal quality was also checked by the film work. An axial oscillation picture along the needle direction showed one row of superlattice reflections between hk0 and hkl layer lines. Its position indicated that the supercell was four times larger in the c dimension. The superstructure will be discussed in detail later. The film work gave the following information: 4/mmm Laue symmetry, 0kℓ reflections (k = 2n), a = b = 9.60 A, c = 2.85 A (for subcell). Its Guinier powder pattern was indexed based on P4/mbm space group and the indexing results are tabulated in Table 2.2.

X-ray Single Crystal Data Collection for $InMo_4O_6$

Room temperature data

The crystal was mounted on the tip of a glass fiber with a small amount of epoxy resin. Its needle direction was nearly along the ϕ-circle axis. The Ames Laboratory four-circle diffractometer (13) was used for indexing and intensity data collection. The orientation matrix of the crystal was calculated by using the same program as described in the first section of this thesis. Unit cell parameters determined from 25 accurately centered high angle (2θ = 25 - 46°) reflections were a = b = 9.682(1) A, c = 2.8661(5) A, $\alpha = \beta = \gamma = 90°$ (wavelength (Mo Kα) = 0.71034 A). Intensity data were

Table 2.1. X-ray powder diffraction data for $InMo_4O_6$[a]

d-spacings (A) obsd.	d-spacings (A) calcd.	relative intensities obsd.	relative intensities calcd.	hkℓ
6.84(1)	6.846	m	34.4	110
4.835(6)	4.841	w	17.0	200
4.321(5)	4.330	vw	4.5	210
3.416(3)	3.423	w	10.0	220
3.055(2)	3.062	vs	100.0	310
2.864(2)	2.866	vw-w	4.6	001
2.680(2)	2.685	w	9.2	320
2.640(2)	2.644	vw	1.5	111
2.464(2)	2.466	s	32.4	201
2.416(2)	2.420	w	9.1	400
2.387(1)	2.390	s	66.3	211
2.343(1)	2.348	vw	3.6	410
2.278(1)	2.282	vw	2.4	330
2.162(1)	2.165	vw-w	5.4	420
2.152(1)		vvw		---[b]
1.958(1)	1.960	s	61.5	321
1.9333(9)	1.936	w	17.3	430
1.8957(9)	1.899	m-s	30.1	510
1.8469(8)	1.849	vw-w	5.0	401
1.7952(8)	1.798	w	8.7	520
1.7831(8)	1.785	w-m	15.5	331
1.7091(7)	1.712	m-s	24.5	440
1.6021(6)	1.604	vw	2.1	431
1.5806(6)	1.583	m-s	22.8	511
1.5208(5)	1.523	m	16.1	522
1.5094(5)	1.512	vw	2.8	540
1.4316(5)	1.433	m	9.7	002
1.4037(5)	1.406	vw	7.2	601
1.4007(4)	1.403	vw	4.2	112
1.3890(4)	1.392	m	17.0	611
1.3272(4)	1.330	vw	3.9	720
1.2968(4)	1.298	w	9.3	312
1.2871(4)	1.289	vw	5.1	630
1.2692(4)	1.271	vw, br	7.9	730
1.2630(3)	1.264	vw	3.1	322

[a]The calculated powder pattern was according to the low-temperature (-98°C) single crystal x-ray diffraction data. Intensities were calculated with a computer program (12). Cu $K\alpha_1$ (1.54056 A) was used to calculate observed d-spacings.

[b]This line could not be identified. Single crystal data collected on four-circle diffractometer showed that there was also a very weak peak at d = 2.144 A.

Table 2.2. X-ray powder diffraction data for $Pb_{0.77}Mo_4O_6$

d-spacings[a]		intensities[b]		
obsd.	calcd.	obsd.	calcd.	hkℓ[c]
6.82(1) A	6.7966	m	14.3	110
4.817(6)	4.8060	m	24.2	200
4.306(4)	4.2986	vw	3.6	210
3.402(3)	3.3983	m	12.6	220
3.041(2)	3.0396	vs	100.	310
2.836(2)	2.8424	vw	0.2	001
2.667(2)	2.6659	w	8.0	320
2.623(2)	2.6223	m	8.8	111
2.447(1)	2.4465	vw	1.8	201
2.402(1)	2.4030	vw	5.3	400
2.371(1)	2.3709	vs	53.7	211
2.332(1)	2.3312	vw	2.9	410
2.265(1)	2.2656	vw	1.3	330
2.181(1)	2.1803	w-m	7.4	221
2.150(1)	2.1493	vw	6.7	420
2.077(1)	2.0761	m	11.7	311
1.9442(8)	1.9445	s	45.7	321
1.8854(8)	1.8851	m	27.2	510
1.7860(7)	1.7849	w	6.4	520
1.7723(7)	1.7716	vw	1.2	331
1.7156(6)	1.7144	w	6.6	421
1.6993(6)	1.6992	s	20.4	440
1.5928(5)	1.5924	vw	1.3	431
1.5120(5)	1.5116	w-m	11.4	521
1.5012(5)	1.5011	vw	2.2	540
1.4215(4)	1.4212	w	4.4	002
1.3913(4)	1.3911	vw-w, br	5.0	112
1.3815(4)	1.3811	vw	11.2	611
1.2880(3)	1.2874	vw	2.4	312
1.2794(3)	1.2795	vw	3.2	631

[a] Cu $K\alpha_1$ (λ = 1.54056A) was used for calculating observed d-spacings.

[b] Some of the peaks were a little diffuse. The observed intensity for 611 reflection does not agree well with the calculated value. Calculated intensities were according to atomic positions obtained from single crystal data.

[c] It was indexed on the basis of the subcell.

corrected for absorption, and for Lorentz and polarization effects. The crystallographic data are listed in Table 2.3.

Low temperature data (-98°C)

The same crystal was transferred to a 0.3 mm Lindemann glass capillary with epoxy adhesive. Its needle direction was also nearly collinear with the ϕ-circle axis. The same diffractometer was used for indexing and data collection. In the whole period of indexing and data collection, the temperature was maintained between -96° and -99°C. The goniometer head and the glass capillary had to be cleaned frequently during the indexing and data collection procedures in order to remove some condensed frost. A program named L-scan was used to scan through 00ℓ, h00, and 0k0 reflections with the hope of detecting any superlattice reflections at low temperature. But no superlattice reflections were observed at -98°C. The same unit cell as for the room temperature crystal was obtained from the indexing program. Unit cell parameters obtained from 21 accurately centered high angle (2Θ = 24 - 46°) reflections were a = b = 9.6576(9) A, c = 2.8628(4) A, $\alpha = \beta = \gamma = 90°$ (wavelength (Mo Kα) = 0.70964 A). The graphite monochromator for the four-circle diffractometer was realigned so that a different radiation wavelength was used for calculating the unit cell constants. The unit cell parameters calculated from the peak positions in a room-temperature Guinier powder pattern were a = b = 9.6650(5) A, c = 2.8633(3)

A, $\alpha = \beta = \gamma = 90^{o}$ (wavelength (Cu $K\alpha_1$) = 1.54056 A). The accuracy of the unit cell constants from the room-temperature single crystal data is doubtful. The agreement between the Guinier powder data and the low-temperature single crystal data is much better, but it seems that there is a slight shrinkage in a or b dimension at low temperature. The low-temperature intensity data were also corrected for absorption, and for Lorentz and polarization effects. The crystallographic data are tabulated in Table 2.4.

Solution and Refinement of $InMo_4O_6$

Room temperature structure

The intensity data set showed 4/mmm Laue symmetry and the extinction condition k = 2n for 0kℓ reflections. Therefore, the space group P4/mbm was selected. The data set was averaged in 4/mmm symmetry (R = 5.7% based on F_o) without any reflection being eliminated, but with relatively poor agreement factor. In the initial stage of least-squares refinement, individual isotropic temperature factors were assumed, and all the structural parameters for Mo and oxygen were assigned initial values equal to those for $NaMo_4O_6$. The indium positions were found in an electron density map, but the map clearly showed a region of electron density elongated along the c axis, consisting of only one strong and elongated peak at z = 0.0. Only one indium atom at the (0,0,0) special

Table 2.3. Crystallographic data for $InMo_4O_6$ (r.t.)

---

crystal system: tetragonal
space group: P4/mbm
a = b = 9.6650(5) A[a]
c = 2.8633(3) A
V = 267.47(3) A^3
Z = 2
d(calcd) = 7.385 g/cm^3
crystal size: 0.20 x 0.03 x 0.03 mm
absn coeff: 132.2 cm^{-1}
refln used for empirical absorption correction (hkℓ, 2Θ, T_{max}/T_{min}): $00\bar{2}$, 28.64°, 1.718
radiation: Mo Kα
monochromator: oriented graphite
scan type: ω-scan
automatic background detn, max scan half width: 0.5 degree
std reflns: 3 every 75 reflns; no significant decay
reflns measd: hkℓ, $\bar{h}\bar{k}\ell$, $\bar{h}k\bar{\ell}$, $h\bar{k}\bar{\ell}$
max 2Θ: 55°
reflns collected: 1571 collected, 1459 observed ($I > 3\sigma(I)$)
no. of unique reflns with $I > 3\sigma(I)$: 203
no. of parameters refined: 24
R = 0.035[b]
R_w = 0.048[c]
quality-of-fit indicator: 1.82[d]

---

[a]The cell parameters were calculated from peak positions in a Guinier powder pattern.

[b]$R = \Sigma||F_o| - |F_c||/\Sigma|F_o|$.

[c]$R_w = [\Sigma w(|F_o|-|F_c|)^2/\Sigma w|F_o|^2$; $w = 1/\sigma^2(|F_o|)$.

[d]Quality of fit = $[\Sigma w(|F_o|-|F_c|)^2/(N(observns)-N(parameters))]^{1/2}$.

Table 2.4. Crstallographic data for $InMo_4O_6$ (-98°C)

---

crystal system: tetragonal
space group: P4/mbm
a = b = 9.6576(9) A
c = 2.8628(4) A
V = 267.01(5) A^3
Z = 2
d(calcd) = 7.398 g/cm^3
crystal size: 0.20 x 0.03 x 0.03 mm
absn coeff: 132.2 cm^{-1}
refln used for empirical absorption correction (hkℓ, 2Θ, T_{max}/T_{min}): $00\bar{2}$, 28.70°, 1.394
radiation: Mo Kα
monochromator: oriented graphite
scan type: ω-scan
automatic background detn, max scan half width: 0.5 degree
std reflns: 4 measured every 75 reflns; no significant decay
reflns measd: hkℓ, $\bar{h}\bar{k}\ell$
max 2Θ: 50°
reflns collected: 582 collected, 558 observed ($I > 3\sigma(I)$)
no. of unique reflns with $I > 3\sigma(I)$: 154
no. of parameters refined: 24
R = 0.026[a]
R_w = 0.034[b]
quality-of-fit indicator[c]: 1.32

---

[a] $R = \Sigma||F_o| - |F_c||/\Sigma|F_o|$.

[b] $R_w = [\Sigma w(|F_o|-|F_c|)^2/\Sigma w|F_o|^2]$; $w = 1/\sigma^2(|F_o|)$.

[c] Quality of fit = $[\Sigma w(|F_o|-|F_c|)^2/(N(observns)-N(parameters))]^{1/2}$.

position was included in the refinement. An anisotropic refinement including the indium atom multiplier gave R = 8.4% with a total population of 1.03(1) indium atom per Mo_4O_6 unit. However, the B33 thermal parameter of the indium atom was unusually large (10 x B11 or B22) when the indium atom was placed on the mirror plane. Therefore, a displacement of this atom from the mirror plane was allowed and the occupancy factor was also varied. A full anisotropic refinement gave R = 7.2%, and Rw = 9.0% with one indium atom (occupancy factor = 0.123(2)) per Mo_4O_6 unit. The B33 thermal parameter of the indium atom became much smaller (2 x B11 or B22). The interchain oxygen atom (O1) showed negative temperature factors. At this point, the structure factors showed a few strong low-angle reflections had Fo < Fc, which suggested a secondary extinction problem. Then, the isotropic secondary extinction coefficient was included as a variable in the least-squares refinement (14). A final full matrix least-squares refinement, varying the indium multiplier, positional and anisotropic thermal parameters of all atoms, converged at R = 3.5% and Rw = 4.8%. The multiplier for the indium atom (0.119(1)) was slightly lower than before. The value for the secondary extinction coefficient (k) = 6.2×10^{-5}. A difference Fourier synthesis map showed that the residual electron density was < $1.8e/A^3$ at Mo1(waist), < $1.5e/A^3$ at Mo2(apex) positions, and < $0.7e/A^3$ in the tunnel. The atomic scattering factors were taken from Hanson et al. (15) for

neutral atoms and those of In and Mo were corrected for the real and imaginary parts for anomalous dispersion. The positional, thermal parameters, and selected interatomic distances and bond angles are tabulated in Tables 2.5, 2.6, and 2.7, respectively.

Low temperature structure (-98°C)

The intensity data showed the same Laue symmetry and extinction conditions as those of room temperature data. The same space group (P4/mbm) was selected. The data set was then averaged in 4/mmm symmetry with a much better agreement factor (R = 3.9%). All of the positional parameters for Mo, oxygen, and In atoms were assigned initial values equal to those from room temperature data. An isotropic least-squares refinement including indium multiplier gave R = 6.4% and Rw = 8.7%. A final full matrix least-squares refinement, varying the indium multiplier, secondary extinction coefficient, positional and anisotropic thermal parameters of all atoms, converged at R = 2.6%, and Rw = 3.4%. The multiplier for the indium atom (0.124(1)) was in a very good agreement with the microprobe analysis result. Compared to the room temperature data the secondary extinction effect for the low temperature data ($k = 9 \times 10^{-6}$) is much reduced. The reduction of extinction effect at low temperature might be due to a very small temperature gradient near the crystal because Seiler and Dunitz (16) found that for certain molecular crystals, application of a

temperature gradient of the order of 20°C per cm during the intensity measurement led to a marked reduction in extinction. On the final difference map, the residual electron density map was < 1.7 e/A^3 at (0, 0, 1/2) (in the tunnel), and < |-0.9 e/A^3| at either one of the two molybdenum atoms. The positional parameters are given in Table 2.8, and thermal parameters in Table 2.9. Selected interatomic distances and bond angles are tabulated in Table 2.10.

Resistivity, Magnetic Susceptibility, and Photoelectron Spectroscopy Studies on $InMo_4O_6$

Resistivity study

A very long needle-like crystal (1.60 x 0.013 x 0.013 mm) was selected for electrical resistivity measurement. The measurement was along the needle axis (infinite chain direction) by means of four-probe technique. Four leads of Pt wire were fixed to 4 points on the needle-like crystal by using silver paint. These leads were then soldered to the copper posts of the resistivity cryostat. A constant alternating current generated by an oscillator passed through the crystal and a standard resistor (1 mΩ). A phase-sensitive AC voltage detector could be switched to measure the voltage across the standard resistor or the voltage between two leads connected to the crystal. The voltage across the resistor was checked periodically during the experiment to ensure an

Table 2.5. Positional parameters for $InMo_4O_6$ (r.t.)

atom	position	multiplier	x	y	z	B(A^2)[a]
Mo1	4g	0.25	0.60146(8)	0.10146	0.0	0.86
Mo2	4h	0.25	0.14309(8)	0.64309	0.5	1.15
O1	4h	0.25	0.2927(7)	0.7927	0.5	1.1
O2	8i	0.5	0.0435(7)	0.7577(8)	0.0	1.3
In	4e	0.119(1)	0.0	0.0	0.0965(7)	1.92

[a]The isotropic equivalent thermal parameter is defined as $B = 4/3\,[a^2\beta_{11} + b^2\beta_{22} + c^2\beta_{33} + 2ab(\cos\gamma)\beta_{12} + 2ac(\cos\beta)\beta_{13} + 2bc(\cos\alpha)\beta_{23}]$.

Table 2.6. Thermal parameters[a] for $InMo_4O_6$ (r.t.)

atom	B_{11}	B_{22}	B_{33}	B_{12}	B_{13}	B_{23}
Mo1	0.89(5)	0.89	0.78(6)	0.00(3)	0.0	0.0
Mo2	0.83(5)	0.83	1.76(7)	0.00(3)	0.0	0.0
O1	1.38(2)	1.38	0.6(3)	-0.3(3)	0.0	0.0
O2	1.7(3)	1.5(2)	0.6(2)	-0.1(2)	0.0	0.0
In	1.48(6)	1.48	2.8(2)	0.0	0.0	0.0

[a]The general thermal expression used is $\exp[-1/4(B_{11}h^2a^{*2} + B_{22}k^2b^{*2} + \ldots + 2B_{23}klb^*c^*)]$.

Table 2.7. Interatomic distances and angles in $InMo_4O_6$[a] (r.t.)

Interatomic Distances (A)			
Mo1a-Mo1b	2.773(1)	Mo1a-O2a	2.060(7)
Mo1a-Mo2	2.7925(9)	Mo1a-O1a	2.036(6)
Mo1a-Mo1c	2.8633(3)	Mo2-O1c	2.044(5)
Mo1a-Mo1d	3.9863(8)	Mo2-O2a	2.051(5)
Mo2-Mo2	2.8633(3)		
Mo2-M02	3.912(1)	O2a-O2e	2.8633(3)
O1a-O2a	2.857(8)	In-O	2.395(7)
O1c-O2a	2.822(8)		
O2a-O2b	2.93(1)		
Bond Angles (degree)			
Mo1a-Mo1b-Mo1d	90.0	O1a-Mo1a-O2a	88.4(2)
Mo1a-Mo2-Mo1b	59.54(2)	O2a-Mo1a-O2c	175.5(3)
Mo1a-Mo2-Mo1c	61.68(1)	O1c-Mo2-O2a	87.1(2)
Mo1b-Mo1a-Mo2	60.23(2)	O2a-Mo2-O2b	91.1(2)
Mo1c-Mo1a-Mo2	59.16(1)	O2a-Mo2-O2e	88.5(2)
Mo1a-O2a-Mo2	85.6(1)		
Mo1a-O1a-Mo1c	89.4(1)		

[a]Calculated using the following cell parameters: a = b = 9.6650(5) A, c = 2.8633(3) A, $\alpha = \beta = \gamma = 90^{o}$. The atom labels refer to Fig. 15.

Table 2.8. Positional parameters for $InMo_4O_6$ (l.t.)

atom	position	multiplier	x	y	z	B(A^2)[a]
Mo1	4g	0.25	0.60147(7)	0.10147	0.0	0.66
Mo2	4h	0.25	0.14307(8)	0.64307	0.5	0.96
O1	4h	0.25	0.2939(6)	0.7939	0.5	0.64
O2	8i	0.5	0.0431(6)	0.7581(7)	0.0	0.95
In	4e	0.124(1)	0.0	0.0	0.0987(7)	1.79

[a]The isotropic equivalent thermal parameter is defined as $B = 4/3\,[a^2\beta_{11} + b^2\beta_{22} + c^2\beta_{33} + 2ab(\cos\gamma)\beta_{12} + 2ac(\cos\beta)\beta_{13} + 2bc(\cos\alpha)\beta_{23}]$.

Table 2.9. Thermal parameters[a] for $InMo_4O_6$ (l.t.)

atom	B_{11}	B_{22}	B_{33}	B_{12}	B_{13}	B_{23}
Mo1	0.60(5)	0.60	0.87(5)	-0.04(3)	0.0	0.0
Mo2	0.57(5)	0.57	1.83(6)	-0.03(3)	0.0	0.0
O1	0.7(2)	0.7	0.6(3)	-0.3(3)	0.0	0.0
O2	1.4(3)	0.9(2)	0.7(2)	-0.2(2)	0.0	0.0
In	1.14(6)	1.14	3.1(2)	0.0	0.0	0.0

[a]The general thermal expression used is:
$\exp[-1/4(B_{11}h^2a^{*2} + B_{22}k^2b^{*2} + \ldots + 2B_{23}klb^*c^*)]$.

Table 2.10. Interatomic distances and angles in $InMo_4O_6$[a] (l.t.)

Interatomic Distances (A)			
Mola-Molb	2.772(1)	Mola-O2a	2.059(6)
Mola-Mo2	2.7907(9)	Mola-O1a	2.022(3)
Mola-Molc	2.8628(4)	Mo2-O1c	2.060(4)
Mola-Mold	3.9848(8)	Mo2-O2a	2.053(4)
Mo2-Mo2	2.8628(4)		
Mo2-Mo2	3.908(1)	O2a-O2e	2.8628(4)
O1a-O2a	2.845(7)	In-O	2.390(6)
O1c-O2a	2.835(7)		
O2a-O2b	2.935(12)		
Bond Angles (degree)			
Mola-Molb-Mold	90.0	O1a-Mola-O2a	88.4(2)
Mola-Mo2-Molb	59.56(2)	O2a-Mola-O2c	175.5(3)
Mola-Mo2-Molc	61.72(1)	O1c-Mo2-O2a	87.1(2)
Molb-Mola-Mo2	60.22(2)	O2a-Mo2-O2b	91.3(2)
Molc-Mola-Mo2	59.14(1)	O2a-Mo2-O2e	88.4(2)
Mola-O2a-Mo2	85.5(1)		
Mola-O1a-Molc	90.14(8)		

[a]Calculated using the following cell parameters: a = b = 9.6576(9) A, c = 2.8628(4) A, $\alpha = \beta = \gamma = 90^{o}$. The atom labels refer to Fig. 15.

essentially constant current passing through the crystal. The resistivity vs. temperature was obtained by collecting data on cooling the sample from room temperature to about $2^{o}K$. The cooling rate was maintained at about $1^{o}K/min$. The temperature was monitored with a Pt thermometer for temperature above 30 K and a germanium resistance thermometer for temperature below 30 K. The normalized resistivity $\rho(T)/\rho(r.t.)$ is calculated by dividing the voltage across the crystal as a function of temperature by the voltage at room temperature. The specific resistivity is calculated according to $\rho = V \times A / I \times L$, where V = voltage across the crystal, A = cross section of the crystal, I = current, and L = length of the crystal between two silver paint contacts. In Fig. 2.1, the normalized resistivity is plotted vs. temperature. The specific resistivity at room temperature is 2×10^{2} $\mu\Omega$-cm.

Magnetic susceptibility study

The sample was checked for purity by means of an x-ray powder pattern before the measurement. Magnetic susceptibility data were obtained using the Faraday technique from 420K to 4K on 0.2928 g of $InMo_4O_6$ powder by Dr. F. J. DiSalvo at AT & T Bell Laboratories. The sample was weakly paramagnetic at room temperature suggesting that it is metallic (Fig. 2.2). The observed susceptibility also showed a Curie tail at low temperature due to the presence of a little magnetic impurity. The data were fit to

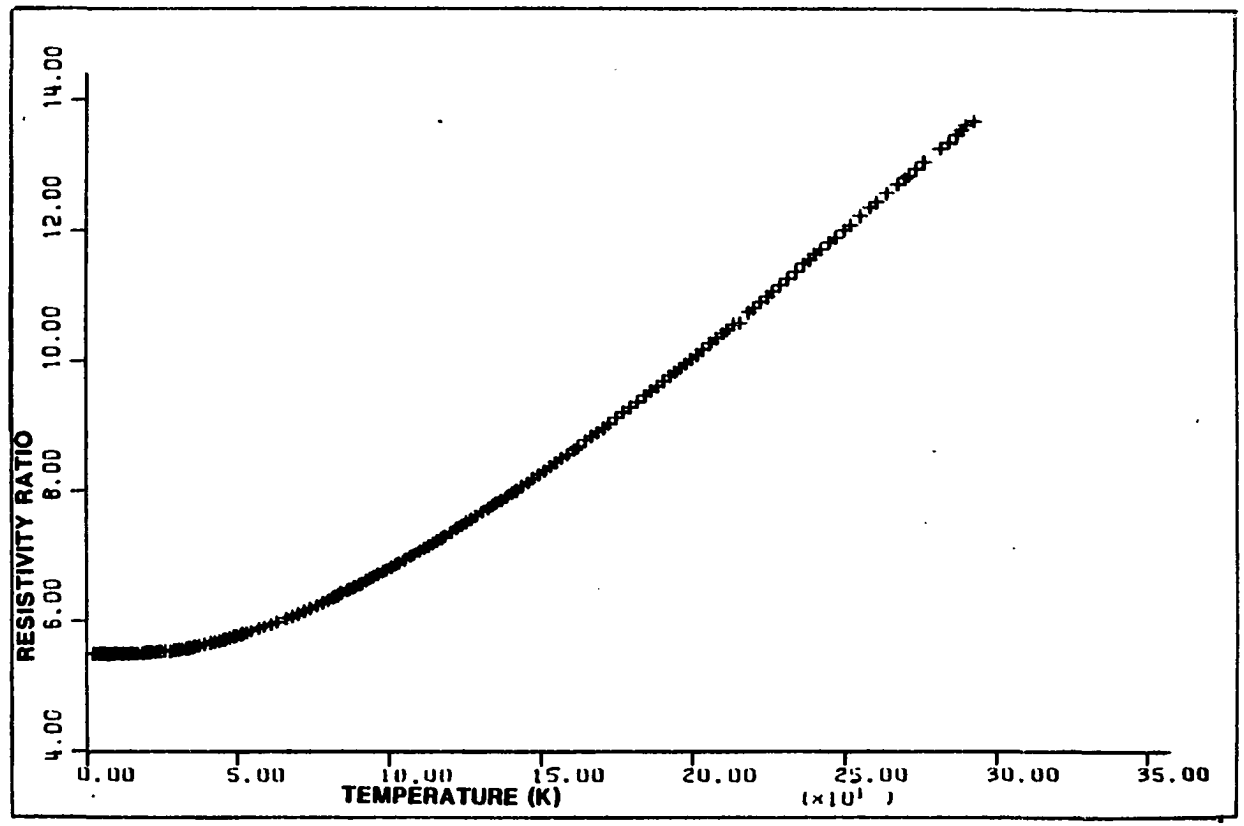

Fig. 2.1. Resistivity ratio ($\rho(T)/\rho(R.T.)$) vs temperature for $InMo_4O_6$. Electrical resistivities were measured along the needle axis

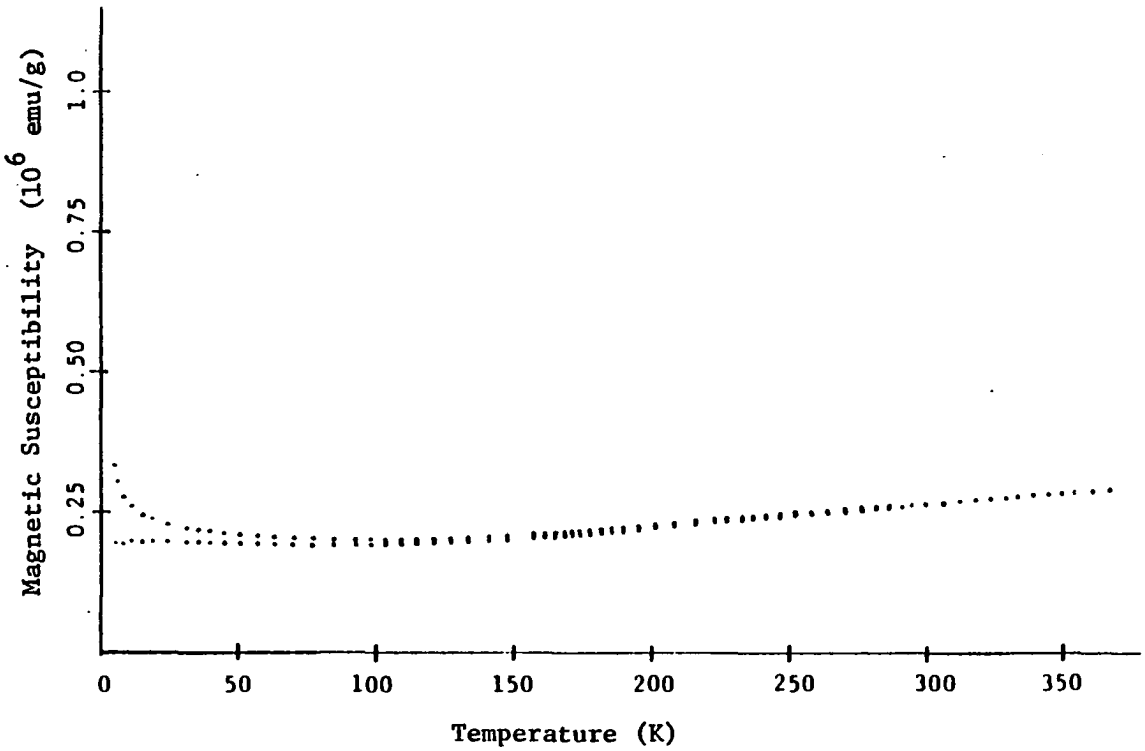

Fig. 2.2. Magnetic susceptibility of $InMo_4O_6$ powder is shown from 4.2 to 375°K. The lower curve represents the susceptibilities with the Curie contribution from impurities subtracted out.

$X_g = C/(T+\Theta) + X_o$ at low temperature. Then, the Curie contribution was subtracted at all temperatures to get intrinsic X which is shown in the lower curve. The magnetic susceptibility slightly increases with temperature and continues to 800K. This phenomenon will be further discussed in "Discussion" section. No anomalies indicative of a phase transition was observed in the temperature range.

Photoelectron spectroscopy study (core spectra)

The reaction tube was opened in a dry box which was attached directly to the sample chamber of an AEI ES200B photoelectron spectrometer. The oxygen content within the helium-filled dry box was maintained below 1 ppm during the sample preparation. The sample purity was checked by means of an x-ray powder pattern. The sample was spread on a piece of double-sided cellophane tape which was mounted on the sample holder. The core spectra were obtained by Mr. J. Anderegg by using Al Kα radiation (1486.6 eV) with minimum (4 x 4) slits but without a monochromater because of the weakness of the radiation. Fifty scans were made for Mo 3d and O 1s spectra, but twenty-five scans for the In 3d spectrum. Five hundred and twelve channels were utilized in each case. Binding energies (BE) of all the peaks were referenced to the C(1s) peak (BE = 285.0 eV) which originated from both the tape backing and adventitious carbon in the sample. The linewidth of the observed Cls peak (FWHM = 1.86 eV) indicated that the

correction was not referred to mixed standard signals. The corrected Mo 3d and In 3d XPS spectra are displayed in Fig. 2.3 and 2.4, respectively. The corrected oxygen 1s XPS spectrum (Fig. 2.5) shows a small shoulder on the high BE side of the peak.

The spectral data correction was accomplished with the APES computer program, developed in this laboratory (17). The corrections included smoothing of the data, base line adjustment, and a correction for inelastic scattering. The program is also able to fit the corrected spectral data with a linear combination of Gaussian and Lorentzian functions. The detailed procedure has been previously described (18). In Figs. 2.3, 2.4, and 2.5 points are not plotted, but smoothed curves are drawn with lowest level of smoothing. Computer deconvolution of the spectra into separate spectral components was attempted even though this did not appear to be necessary. Any one of the spectra could not be fit well by just one type of atom. The FWHM of the In peak (2.55 eV) is unusually large compared to some binary and ternary indium chlorides (FWHM = 1.5 - 2.1 eV) (19), very carefully cleaned indium metal foil (FWHM = 1.08 eV) (20), indium metal foil with oxidized surface (FWHM = 1.7 eV) (18), and In_2O_3 powder (FWHM = 1.6 eV) (18). The observed broadened In 3d peaks are puzzling because the reaction container was opened in a clean dry box and the sample purity was checked with an x-ray powder pattern. The Mo 3d spectrum (FWHM = 1.76 eV) indicates that it essentially

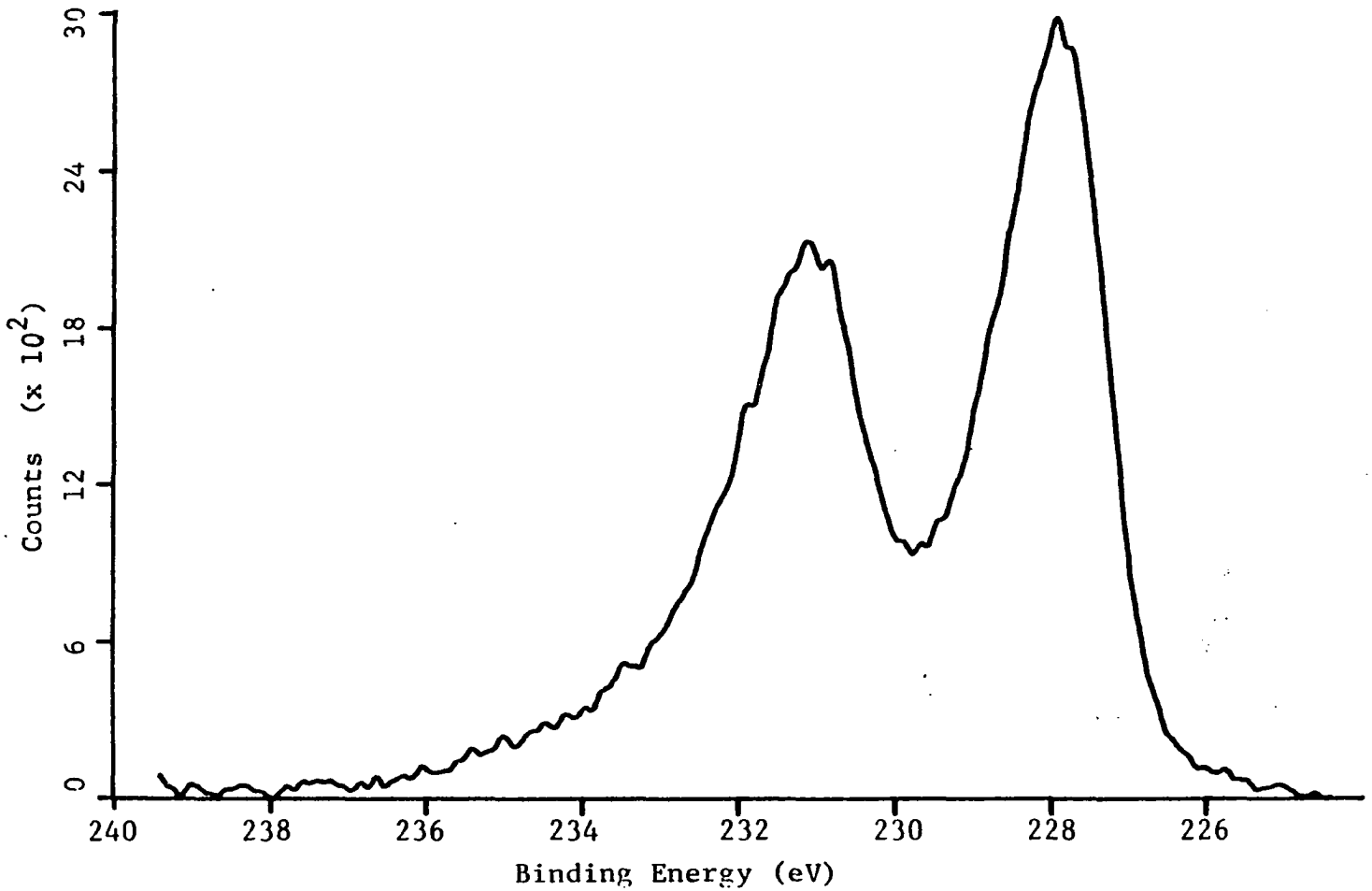

Fig. 2.3. Observed Mo 3d XPS spectrum of $InMo_4O_6$. The spectrum is referenced to the C(1s) peak

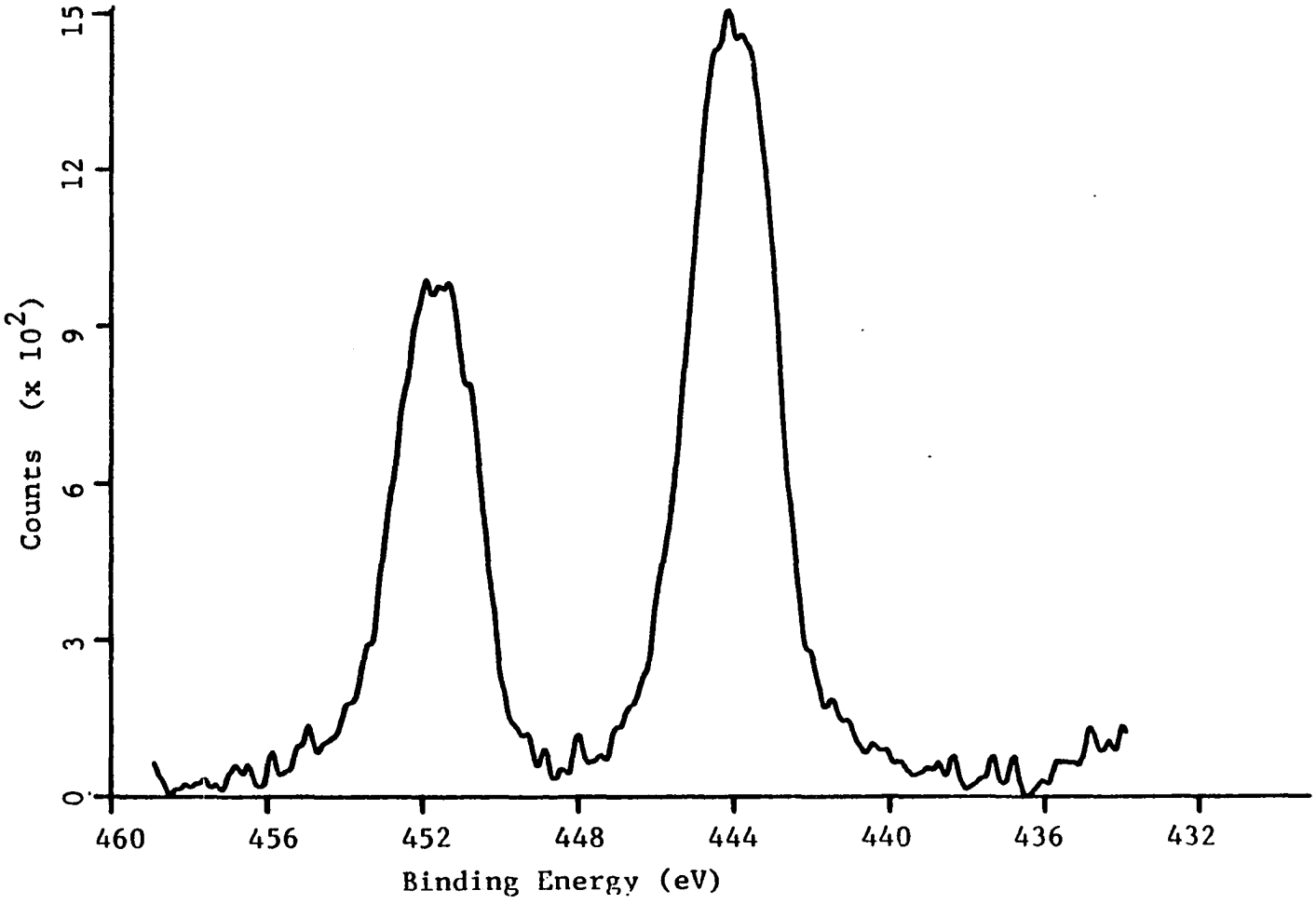

Fig. 2.4. Observed In 3d XPS spectrum of $InMo_4O_6$. The spectrum is referenced to the C(1s) peak

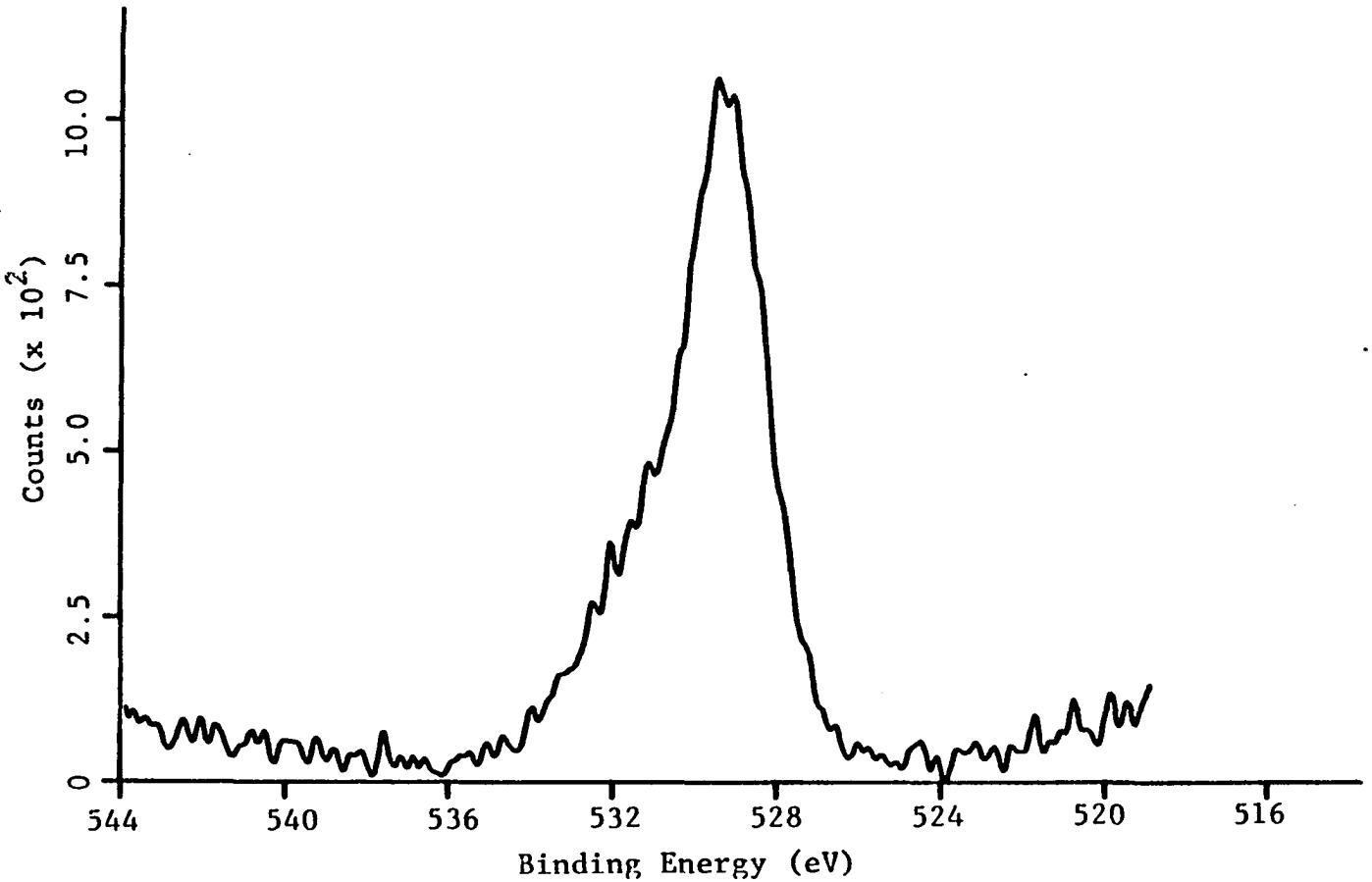

Fig. 2.5. Observed O 1s XPS spectrum of $InMo_4O_6$. The spectrum is referenced to the C(1s) peak

contains one type of Mo atom. No split peaks that could be associated with distinguishable apical and waist molybdenum atoms were detected in the spectrum. The binding energy for the low binding energy spin-orbit peak is 228.0 eV. However, the quality of fit to the spectral data with one type of Mo is not satisfactory. In fact, the spectrum shows a tail on the high binding energy side of the high binding energy spin orbit peak which could be due to the final state effects. Note also that the peak heights are in a ratio of 1.4 instead of 1.5 because both peaks show relaxation tails.

Photoelectron spectroscopy study (valence spectra)

A chunk of $InMo_4O_6$ from the same reaction product was crushed into powder just before the data collection. The exciting photon energies employed were 21.2 eV (HeI) and 1486.6 eV (Al Kα). For HeI spectra, the powder was pressed onto an indium foil which was mounted on a sample holder. The data were collected on the same spectrometer over the valence and conduction band regions by Mr. J. Anderegg at room temperature. Figs. 2.6 and 2.7 show the spectra excited with HeIα and unmonochromatized Al Kα radiations, respectively. The corresponding spectra for $NaMo_4O_6$ (21) are also shown in the figures for comparison. The rise in intensity on the left-hand side of the x-ray valence spectra for $InMo_4O_6$ is due to the intense In 4d core level which appears at around 18 eV of binding energy.

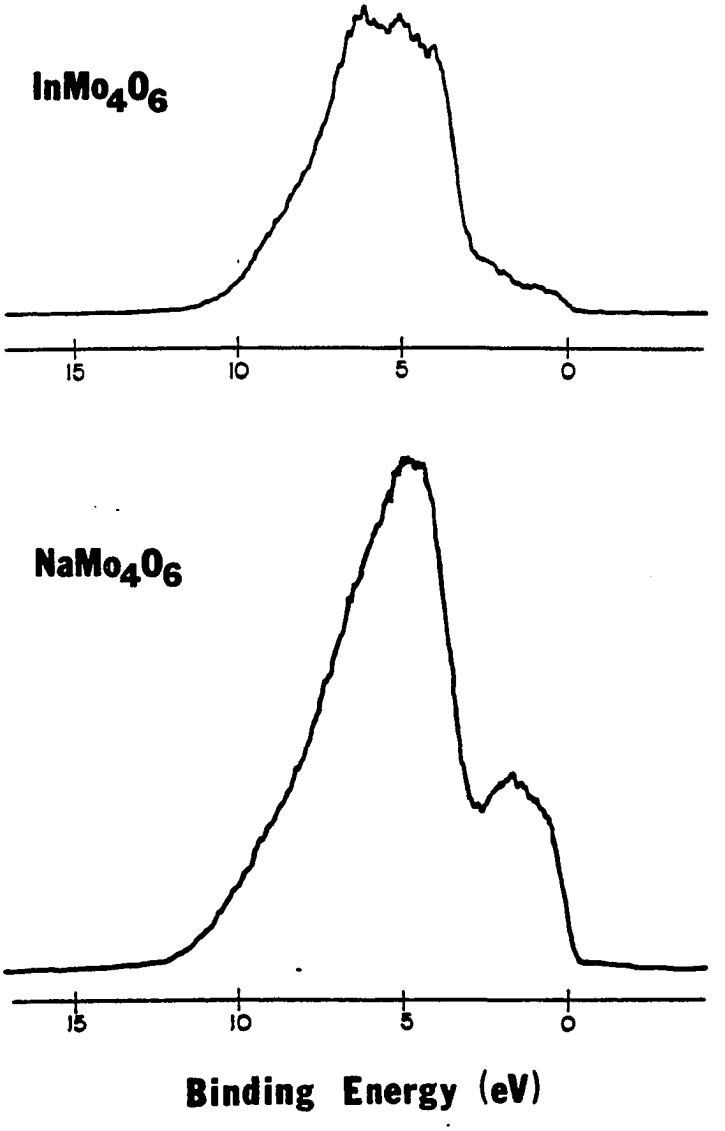

Fig. 2.6. HeI (hυ = 21.2 eV) photoelectron spectra of $InMo_4O_6$ and $NaMo_4O_6$ in the valence and conduction band region

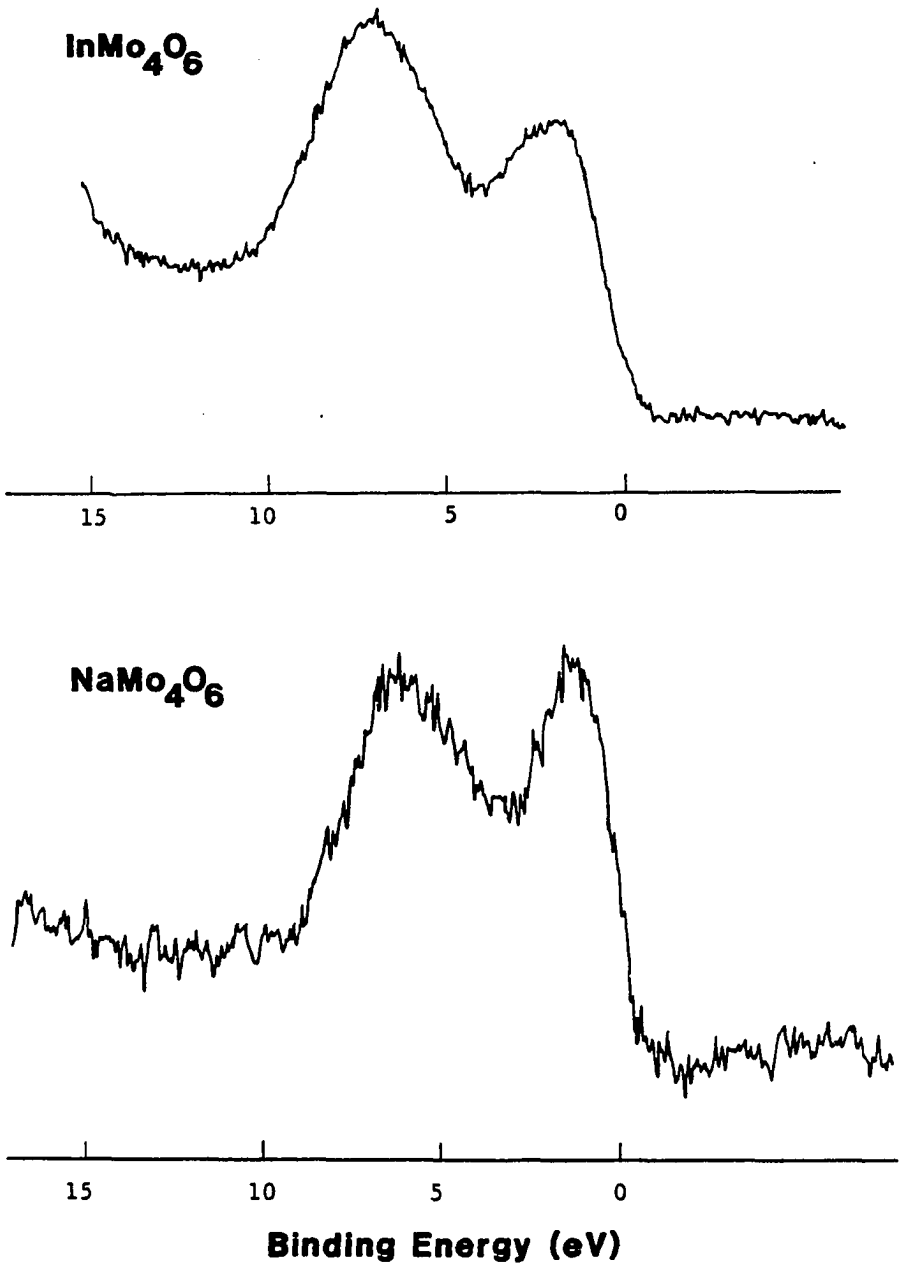

Fig. 2.7. X-ray (hυ = 1486.6 eV) photoelectron spectra of $InMo_4O_6$ and $NaMo_4O_6$ in the valence and conduction band region

X-ray Single Crystal Data Collection for $Pb_{0.77}Mo_4O_6$ Subcell

The crystal was mounted on the tip of a glass fiber with a small amount of epoxy resin. Its needle direction was also nearly along the ϕ-circle axis. A DATEX diffractometer was used for indexing and intensity data collection. The program which was described in SECTION I of this thesis was used to calculate the orientation matrix. The data set showed broader peak profiles compared to those of the indium analogue. The collected intensity data were relatively weak because the crystal used for data collection was very small. Unit cell parameters calculated from a Guinier powder pattern were used for later calculations. Intensity data were corrected for absorption, and for Lorentz and polarization effects. The crystallographic data are listed in Table 2.11.

Solution and Refinement of $Pb_{0.77}Mo_4O_6$ Subcell

The data set showed the same Laue symmetry and extinction conditions as those for $InMo_4O_6$. It was then averaged in 4/mmm symmetry without any reflection being eliminated. The poor agreement factor (R_{int} = 7.1% based on F_o) probably resulted because of the relatively weak intensities so that the internal consistency of the data set was statistically poorer. The initial positional parameters for Mo were

assigned the same values as those for $InMo_4O_6$. An electron density map was calculated using phases derived from the molybdenum positions. Two oxygen atoms were easily located on the map. The map showed a region of electron density centered about (0,0,1/2) and elongated parallel to the c axis. Refinement proceeded using the model with the lead atom on site 4e (0,0,z; 0,0,-z; 1/2,1/2,z; 1/2,1/2,-z). The lead atom shifted 0.45 A off the center of the unit cell. A final full-matrix least-squares refinement varying lead multiplier, positional and anisotropic temperature factors of all atoms converged at R = 3.3% and Rw = 3.9% with 0.77 lead atom (occupancy factor = 0.0965(10)) per Mo_4O_6 unit. In contrast to $InMo_4O_6$ the structure factors did not reveal a significant secondary extinction effect. The intrachain oxygen atom (O2) showed a negative temperature factor. The lead atom was elongated in c axis (tunnel direction) with B33 (=6.2 A^2) about 3 times B11 (=2.1 A^2), indicating some positional disorder in the tunnel direction. The residual electron density on the final difference map were from -2.7 to 1.8 e/A^3 in the tunnel, and < 1.3 e/A^3 near both Mo1(waist) and Mo2(apex) positions. The atomic scattering factors were also taken from Hanson et al. (13) for neutral atoms and those for Pb and Mo were corrected for anomalous dispersion. Tables 2.12 and 2.13 list positional and thermal parameters, respectively. Selected interatomic distances and bond angles are tabulated in Table 2.14. The apical molybdenum atom (Mo2)

had a larger B33 value (= 2.00 A^2, B11 = 0.66 A^2). Similar results were obtained in the other two analogous compounds $NaMo_4O_6$ (B33 = 1.45 A^2, B11 = 0.60 A^2) and $InMo_4O_6$ (B33 = 1.83 A^2, B11 = 0.57 A^2). In the case of $InMo_4O_6$, an attempt was made to refine the structure without constraining the apical molybdenum atom on the mirror plane. Catastrophic results ensued even though other atoms were alternately fixed in the refinement. Thus, a similar calculation on $Pb_{0.77}Mo_4O_6$ was not performed.

Solution of $Pb_{0.77}Mo_4O_6$ Supercell

As mentioned above the axial oscillation picture along the infinite chain direction showed one row of superlattice reflections at 3/4 r.l.u. (reciprocal lattice unit) between the hk0 and hkl layer lines. The superlattice reflections are sharp, indicating a three-dimensional ordering of the lead ions. However, a long-exposure oscillation photograph shows very faint, diffuse streaks between superlattice reflection points. These streaks are perpendicular to the c^* direction, suggesting that there is a slight extent of disorder in the a or b directions. A long-exposure rotation photograph (Fig. 2.8) using Mo Kα radiation shows superlattice reflections at the following positions (in r.l.u.) with their relative intensities in parentheses: 1/4(vvw), 2/4(vvw), 3/4(s), 5/4(w), 6/4(w), and 7/4(m).

Table 2.11. Crystallographic data for $Pb_{0.77}Mo_4O_6$

---

crystal system: tetragonal
space group: P4/mbm
a = b = 9.6119(5) A
c = 2.8424(3) A
V = 262.62(4) A^3
Z = 2
d(calcd) = 0.8087 g/cm^3
crystal size: 0.10 x 0.02 x 0.02 mm
absn coeff: 329.3 cm^{-1}
refln used for empirical absorption correction (hkℓ, 2Θ, T_{max}/T_{min}): $00\bar{2}$, 29.00°, 1.679
radiation: Mo Kα
monochromator: oriented graphite
scan type: w-scan
scan half width: 0.6 degree
std reflns: 3 measured every 50 reflns; no significant decay
reflns measd: hkℓ, $\bar{h}\bar{k}\ell$, $\bar{h}k\bar{\ell}$
max 2Θ: 55°
reflns collected: 1081 collected, 678 observed ($I > 3\sigma(I)$)
no. of unique reflns with $I > 3\sigma(I)$: 144
no. of parameters refined: 23
R = 0.033[a]
Rw = 0.039[b]
quality-of-fit indicator[c]: 1.054

---

[a] $R = \Sigma||F_o| - |F_c||/\Sigma|F_o|$.

[b] $R_w = [\Sigma w(|F_o|-|F_c|)^2/\Sigma w|F_o|^2]$; $w = 1/\sigma^2(|F_o|)$.

[c] Quality of fit = $[\Sigma w(|F_o|-|F_c|)^2/(N(observns)-N(parameters))]^{1/2}$.

Table 2.12. Positional parameters for $Pb_{0.77}Mo_4O_6$ subcell

atom	position	multiplier	x	y	z	$B(A^2)$[a]
Mo1	4g	0.25	0.6021(1)	0.1021	0.0	0.84
Mo2	4h	0.25	0.1435(1)	0.6435	0.5	0.76
O1	4h	0.25	0.293(1)	0.793	0.5	1.83
O2	8i	0.5	0.042(1)	0.763(1)	0.0	0.92
Pb	4e	0.0965(10)	0.0	0.0	0.341(1)	3.47

[a]The isotropic equivalent thermal parameter is defined as $B = 4/3\ [a^2\beta_{11} + b^2\beta_{22} + c^2\beta_{33} + 2ab(\cos\gamma)\beta_{12} + 2ac(\cos\beta)\beta_{13} + 2bc(\cos\alpha)\beta_{23}]$.

Table 2.13. Thermal parameters[a] for $Pb_{0.77}Mo_4O_6$ subcell

atom	B_{11}	B_{22}	B_{33}	B_{12}	B_{13}	B_{23}
Mo1	0.79(5)	0.79	0.96(9)	0.02(5)	0.0	0.0
Mo2	0.66(5)	0.66	2.0(1)	-0.02(5)	0.0	0.0
O1	1.7(5)	1.7	2.0(11)	-0.0(6)	0.0	0.0
O2	1.1(5)	-0.1(4)	2.0(7)	-0.1(3)	0.0	0.0
Pb	2.11(8)	2.11	6.2(3)	0.0	0.0	0.0

[a]The general thermal expression used is

$\exp[-1/4(B_{11}h^2a^{*2} + B_{22}k^2b^{*2} + \ldots + 2B_{23}klb^*c^*)]$.

Table 2.14. Interatomic distances and angles in $Pb_{0.77}Mo_4O_6$ subcell[a]

	Interatomic Distances (A)		
Mola-Molb	2.775(2)	Mola-02a	2.07(1)
Mola-Mo2	2.784(2)	Mola-01a	2.010(6)
Mola-Molc	2.8424(3)	Mo2-01c	2.036(9)
Mola-Mold	3.973(1)	Mo2-02a	2.070(7)
Mo2-Mo2	3.902(2)		
01a-02a	2.83(1)	02a-02e	2.8424(3)
01c-02a	2.82(1)	Pb-02	2.511(9) (4x)
02a-02b	3.00(2)		2.978(8) (4x)
	Bond Angles (degree)		
Mola-Molb-Mold	90.0	01a-Mola-02a	87.8(3)
Mola-Mo2-Molb	59.79(6)	02a-Mola-02c	173.8(6)
Mola-Mo2-Molc	61.39(3)	01c-Mo2-02a	86.7(3)
Molb-Mola-Mo2	60.10(3)	02a-Mo2-02b	92.9(4)
Molc-Mola-Mo2	59.30(3)	02a-Mo2-02e	86.7(4)
Mola-02a-Mo2	84.4(4)		
Mola-01a-Molc	90.0(4)		

[a]Calculated using the following cell parameters: a = b = 9.6119(5) A, c = 2.8424(3) A, $\alpha = \beta = \gamma = 90^{o}$. The atom labels are the same as those for $InMo_4O_6$.

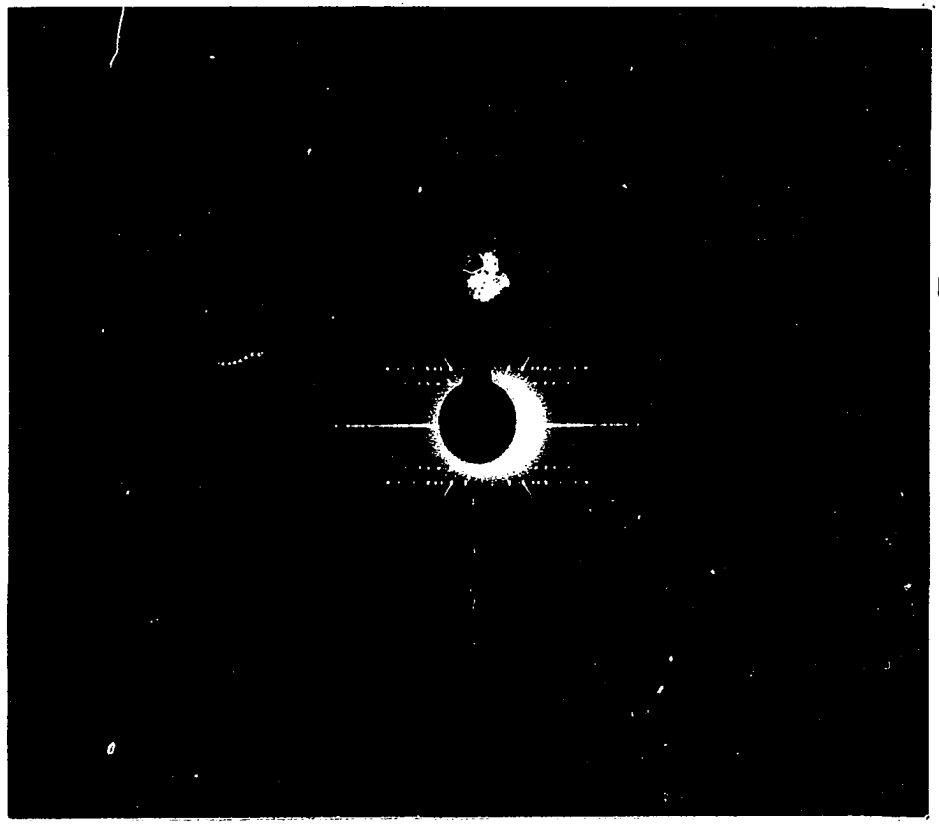

Fig. 2.8. A rotation photograph of $Pb_{0.77}Mo_4O_6$. The rotation axis is along the c direction. The indexed planes represent the Bragg scattering due to the molybdenum-oxide framework. The scattering between these planes are due to the three-dimensional ordering of the lead ions in the tunnel.

A comparison with the isomorphous compound $InMo_4O_6$ suggests that superlattice reflections originate from the ordering of the partially occupied lead ion sites. The crystal structure may be regarded as consisting of two sublattices. The molybdenum-oxide framework forms a sublattice of which the repeat distance in the c direction is 2.8424 A. A unit cell four times larger has to be used to describe the other sublattice formed by the lead ions. The supercell contains four sites, but there is on the average about one vacancy per supercell. Therefore, one is led to the supercell structure shown in Fig. 2.9. One lead atom is on the mirror plane ($z = 5/8$), and the other two lead atoms are at $(3/8 - \Delta z)$ and $(7/8 + \Delta z)$. The driving force for the displacement is probably because of the electrostatic repulsion between lead cations. The structure factor for this one-dimensional lattice can be calculated as follows:

$$F \propto \Sigma \cos (2\pi \ell z) + i \sin (2\pi \ell z)$$

$$\Sigma \cos 2\pi \ell z = [\cos 2\pi \ell(3/8 - \Delta z) + \cos 2\pi \ell(5/8) + \cos 2\pi \ell(7/8 + \Delta z)]$$

$$\cos \alpha + \cos \beta = 2 \cos [(\alpha+\beta)/2] \cos [(\alpha-\beta)/2]$$

$$\Sigma \cos 2\pi \ell z = 2 \cos 2\pi \ell[(3/8 - \Delta z + 7/8 + \Delta z)/2] \cos 2\pi \ell[(3/8 - \Delta z - 7/8 - \Delta z)/2] + \cos (5\pi \ell/4)$$

$$= 2 \cos (5\pi \ell/4) \cos \pi \ell(-1/2 - 2\Delta z) + \cos (5\pi \ell/4)$$

$$= [\cos (5\pi \ell/4)] [1 + 2 \cos 2\pi \ell(1/4 + \Delta z)]$$

Similarly, one obtains:

$$\Sigma \sin 2\pi \ell z = [\sin (5\pi \ell/4)] [1 + 2 \cos 2\pi \ell(1/4 + \Delta z)]$$

Thus, intensity $\propto F^2 \propto [1 + 2 \cos 2\pi\ell(1/4 + \Delta z)]^2$

In Fig. 2.10, the calculated intensities of the superlattice reflections are plotted vs. Δz for each ℓ value according to the above equation. The intensities of the superlattice reflections are very sensitive to the displacement parameter, Δz. On the basis of the observed relative intensities of the superlattice reflections on the rotation photograph, one can estimate Δz from the plot. It is approximately equal to 0.054. Δz becomes 0.22 (=0.054 x 4) if it is referred to a subcell. This estimated value agrees well with the least-squares refinement based on the subcell intensity data (Δz = 0.5 - 0.34 = 0.16). Because a third of the lead atoms are at the centers of the unit cells, the refined lead position shifts closer to the center with large B33 value in order to fit the elongated electron density. Therefore, there are two types of lead atoms. The first type of lead atom (Pb1) is at the center of a subcell and coordinated by eight oxygen atoms at the same distance (2.715 A). The second type of lead atom (Pb2) is about 0.62 A off the center and coordinated by eight oxygen atoms at two different distances (2.45 A, 3.09 A).

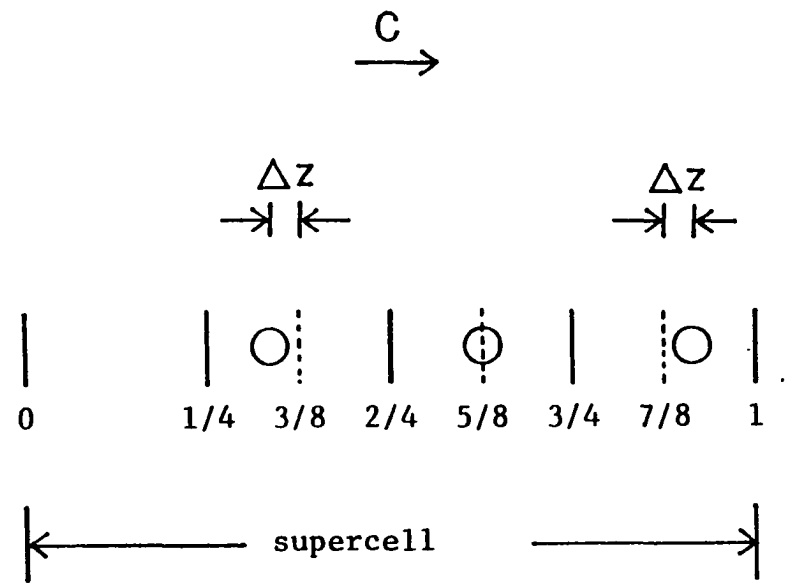

Fig. 2.9. A schematic diagram of a channel in $Pb_{0.77}Mo_4O_6$ showing a supercell parallel to the c axis. The displacement parameter Δz is used in a model calculation (see text)

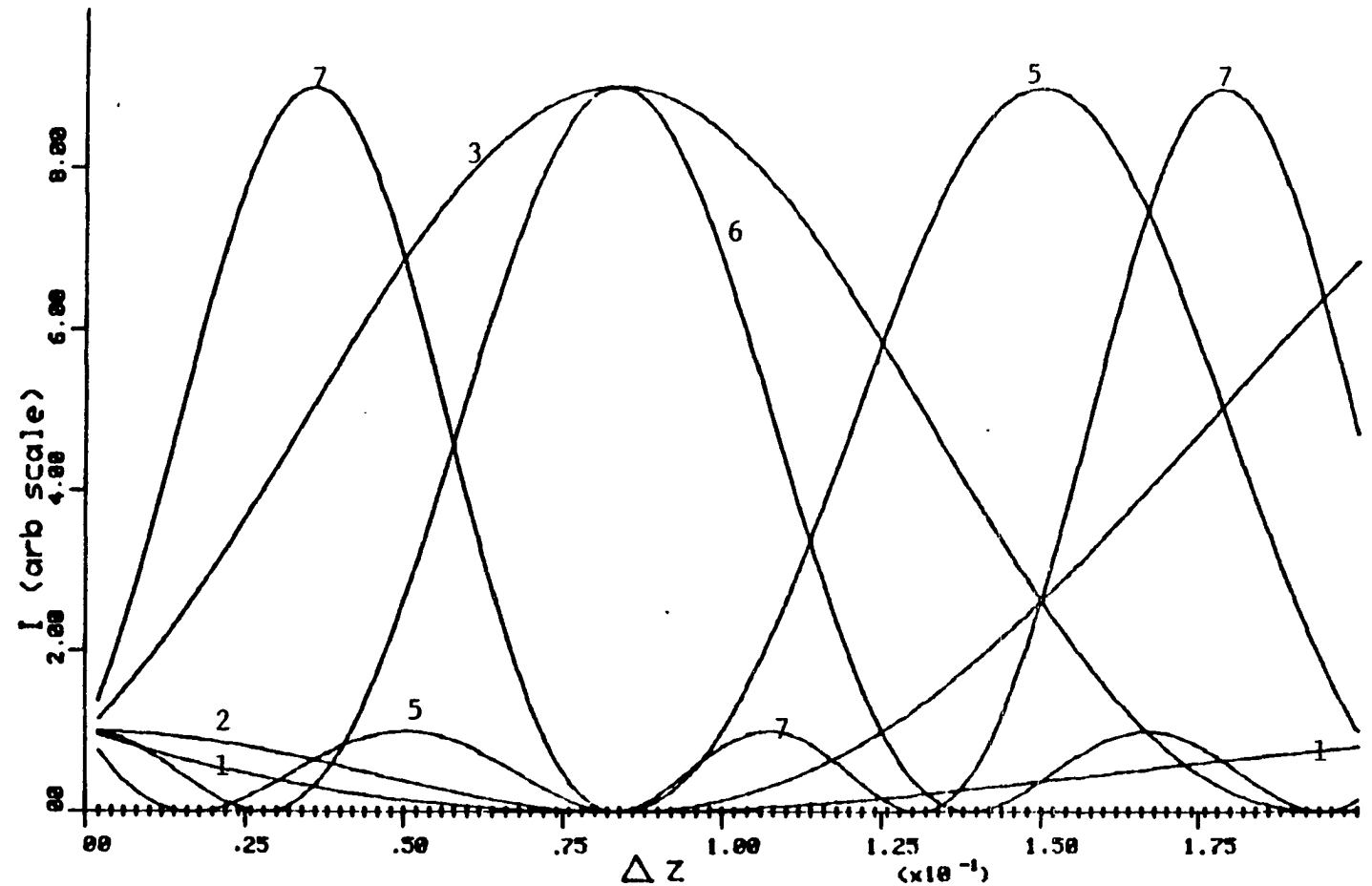

Fig. 2.10. Relative intensities of the superlattice reflections are plotted vs Δz for each ℓ value according to $[1 + 2 \cos 2\pi\ell(1/4 + \Delta z)]^2$

DESCRIPTION OF THE STRUCTURES

Before studying the crystal structures of $InMo_4O_6$ and $Pb_{0.77}Mo_4O_6$, an understanding of M_6X_{12} type cluster may be helpful. Fig. 2.11 shows a view down one of the two-fold axes of a M_6X_{12} cluster. The bigger atoms represent X atoms and the smaller atoms represent M atoms. Different types of circles represent different heights along the two-fold axis. The metal atoms are bonded together to form an octahedral metal cluster. The twelve X atoms lie above the edges of the octahedron. Each metal atom is coordinated by four X atoms. In fact, in real examples, each metal atom is slightly off the plane formed by four X atoms so that the octahedron is inside the cube on which the twelve X atoms lie. As the X/M ratio gets lower, the metal clusters condense by sharing both the M and X atoms. One possible way of M_6X_{12} cluster condensation is shown in Fig. 2.12. If two of the X atoms bridging the trans M(waist)-M(waist) edges in a M_6X_{12} cluster are eliminated and the resulting clusters are fused together by sharing both the trans edges of the M_6 octahedra and all X atoms bridging the M(waist)-M(apex) bonds, then an infinite metal cluster chain with M/X ratio equal to 2:3 is created. The connectivity formula for the resulting infinite metal cluster chain is $Mo_2Mo_{4/2}O_{8/2}O_{4/2}$.

Figure 2.13 shows a three-dimensional view down the tetragonal c axis of $InMo_4O_6$ or $Pb_{0.77}Mo_4O_6$. Indium or lead

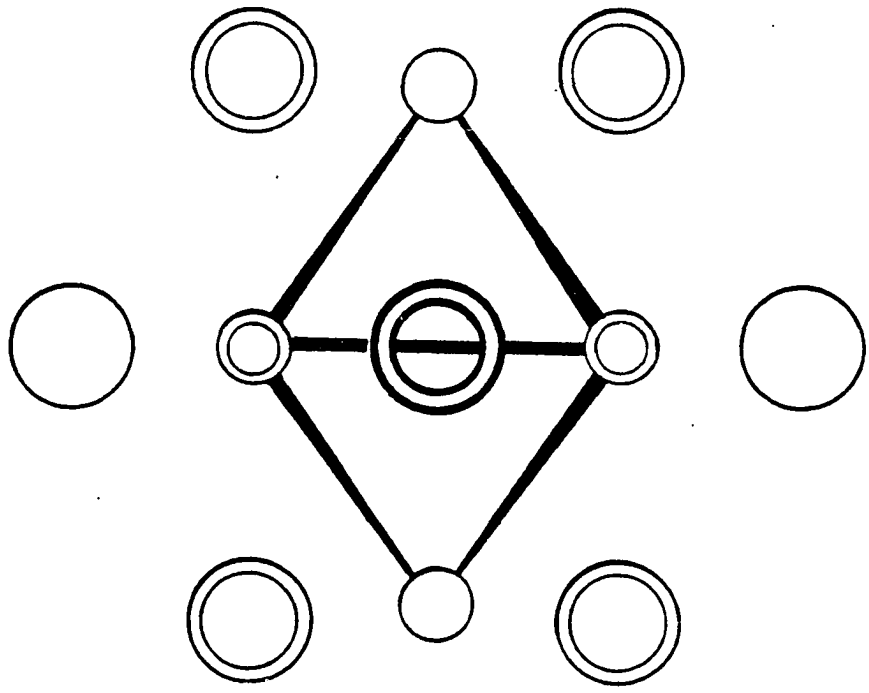

Fig. 2.11. A M_6X_{12} cluster shown as projection along one of the two-fold axes. The larger and the smaller circles represent X and M atoms, respectively. The heights of the atoms along the two-fold axis are indicated by three types of circles. The M-M bonds are shown in the figure

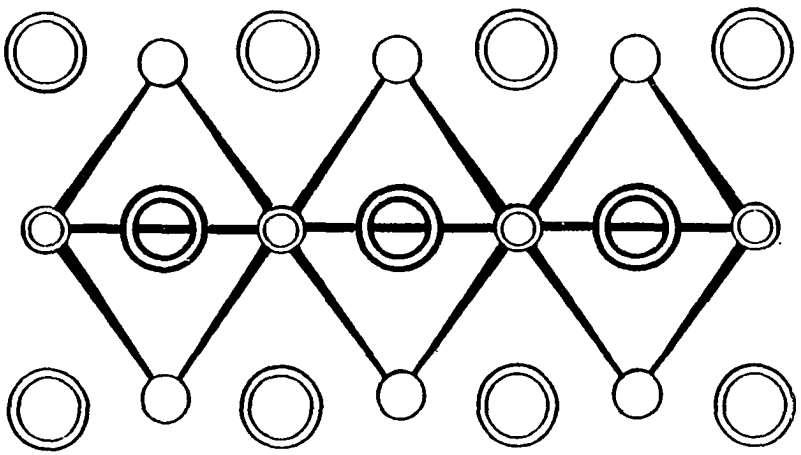

Fig. 2.12. A section of a metal cluster chain containing M_6X_{12} cluster units

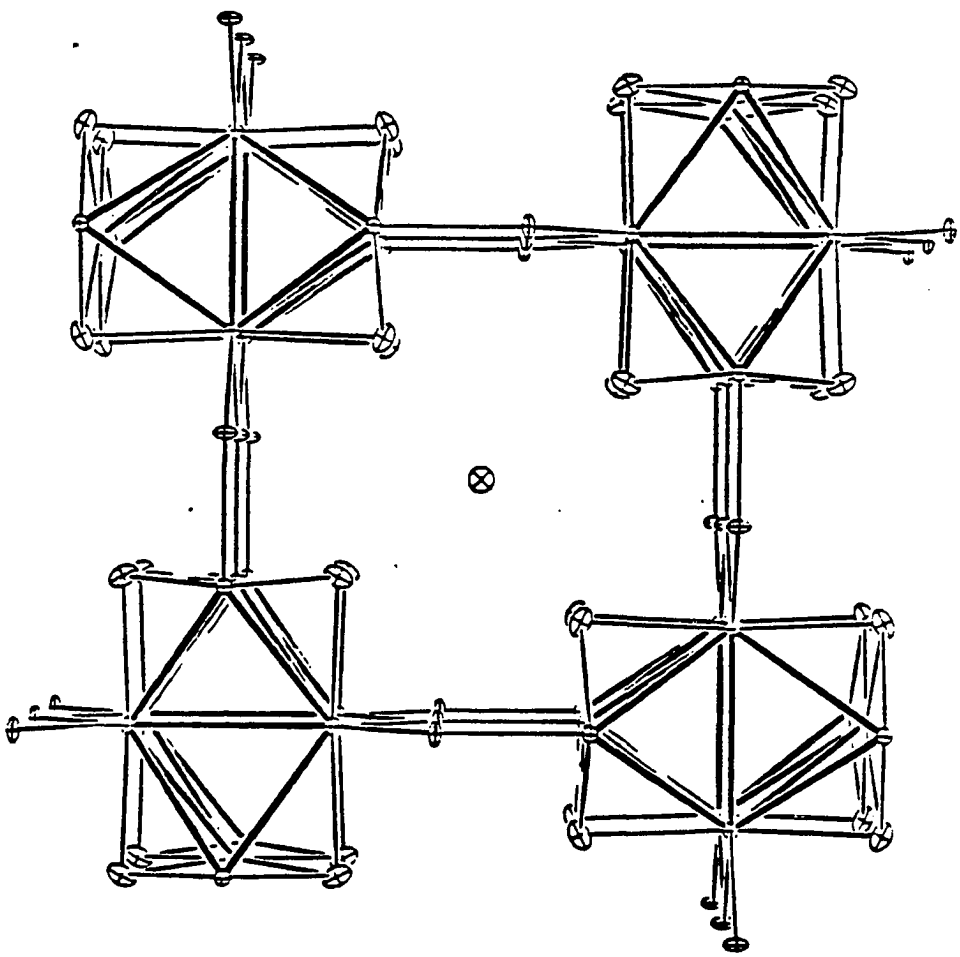

Fig. 2.13. A three-dimensional view of the $InMo_4O_6$ structure as seen along the tetragonal c axis. The Mo-Mo bonds are represented by the thicker lines. The fifty percent probability anisotropic thermal ellipsoids are shown

ions reside in the tunnels formed by four molybdenum-oxide infinite chains. Infinite chains are cross linked by the trigonal-planar oxygen atoms. Each infinite chain is comprised of M_6X_{12} clusters fused on opposite edges (Fig. 2.14). The Mo-Mo bond distance parallel to the chain axis for $Pb_{0.77}Mo_4O_6$ (2.842 A) is slightly shorter than that of $InMo_4O_6$ or $NaMo_4O_6$ (2.862 A). The Mo-Mo bond distances perpendicular to the chain direction for both the indium and lead compounds (2.772 A) are slightly longer than that of the sodium compound (2.753 A). All other Mo-Mo bond distances are essentially the same. The a and b cell parameters for $InMo_4O_6$ and $Pb_{0.77}Mo_4O_6$ are a little longer than that for $NaMo_4O_6$ mainly because of the longer Mo-Mo (perpendicular to c) and Mo(apex)-O1(interchain) bond distances in the former compounds.

The In ions are located at sites slightly displaced (0.28 A) from the plane of four equidistant oxygen atoms, d(In-O) = 2.390(6) A (Fig. 2.16). The oxidation state of the indium ion is estimated from the In-O bond-length bond-strength relation of Brown and Wu (22), $\Sigma s(In\text{-}O) = \Sigma[d(In\text{-}O)/1.959]^{-7.0} = 1.00$. This result is also consistent with the anion charge (-1.15) on the Mo_4O_6 unit, estimated from the Mo-O bond-length bond-strength relation $s(Mo\text{-}O) = [d(Mo\text{-}O)/1.882]^{-6.0}$ (22). The thermal ellipsoid of the indium atom is a little elongated in the c direction. The In-In distance (2.86 A) is a lot shorter than the distances (3.24 and 3.37 A) in indium metal, but longer than the distances in compounds where In-In bonding is

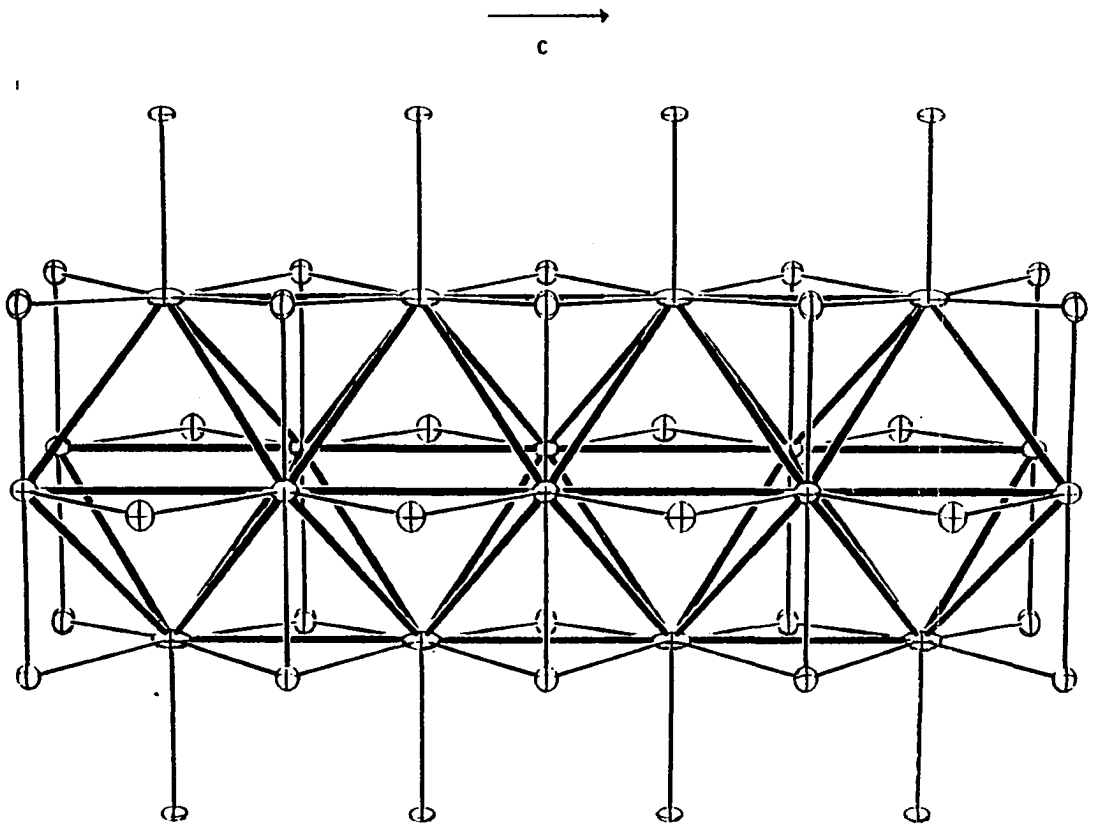

Fig. 2.14. A view of one molybdenum-oxide cluster chain along the c axis. The fifty percent probability anisotropic thermal ellipsoids are shown

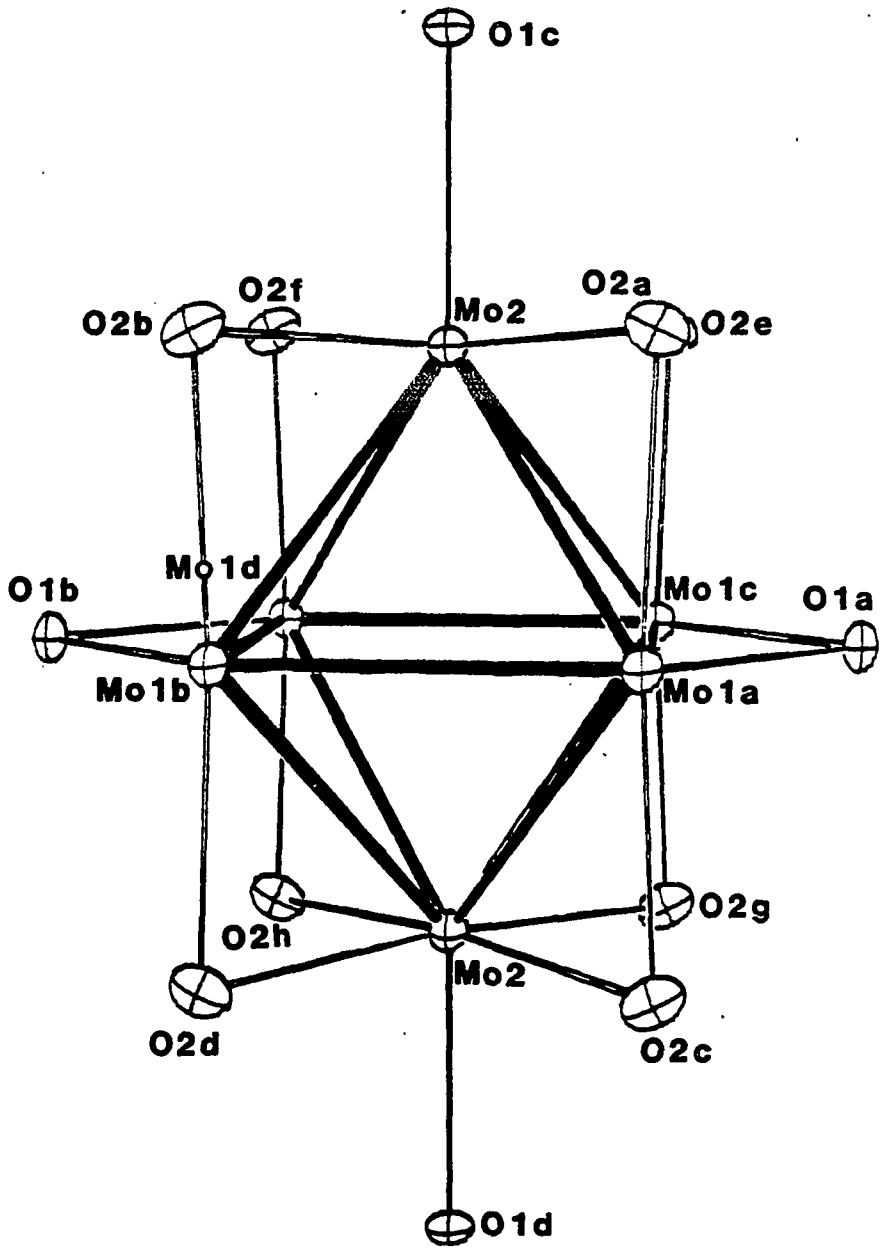

Fig. 2.15. A repeat unit of a molybdenum-oxide cluster chain in $InMo_4O_6$. The fifty percent probability anisotropic thermal ellipsoids are shown

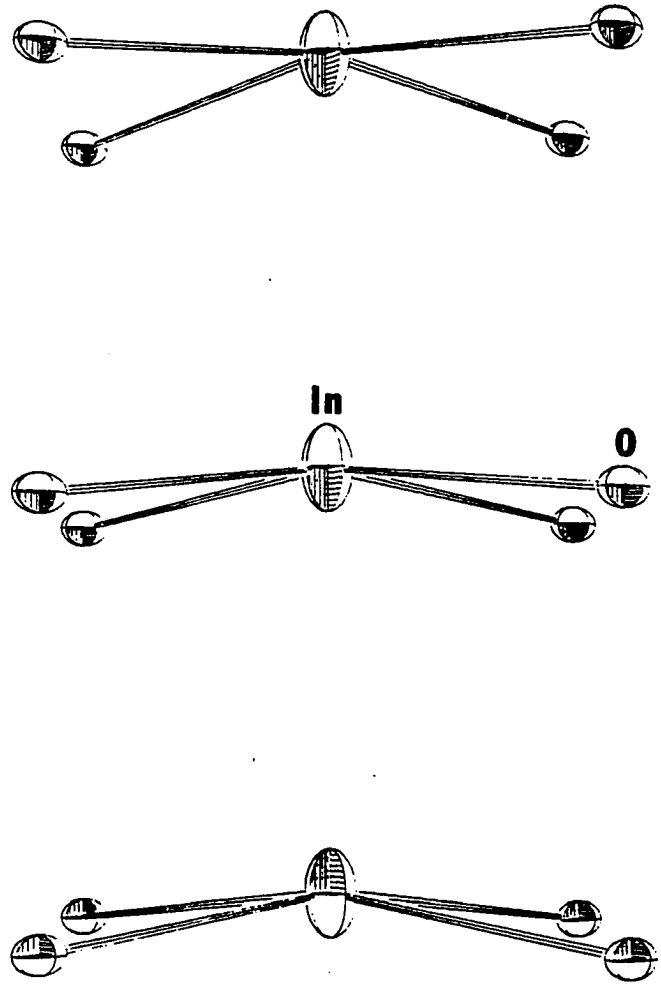

Fig. 2.16. A view perpendicular to the c axis of $InMo_4O_6$ showing the oxygen coordinations around the indium ion sites. The fifty percent probability anisotropic thermal ellipsoids are shown

more certain. For example, the In-In bond distances in In_6S_7 (23), γ-InSe (24), and In_4Se_3 (25) are about 2.76 A. The indium atoms may contribute in an important way to the observed physical properties (vide infra).

According to the subcell refinement, the lead atoms in $Pb_{0.77}Mo_4O_6$ are displaced to (0,0,0.341), resulting in Pb-O distances of 2.511(9) (4x) and 2.978(8) (4x). The refined temperature factor for the lead ion is large in the tunnel direction, indicating additional positional disorder along the tunnel. The oxidation state is assessed from the Pb-O bond-length bond-strength relation (20), $\Sigma s(Pb\text{-}O) = \Sigma[d(Pb\text{-}O)/2.044]^{-5.5} = 1.79$. This result is also in a reasonably good agreement with the anion charge (-1.28) on the Mo_4O_6 unit, estimated from the bond-length bond-strength for Mo-O bonds. (Remember that there is only 0.77(1) lead atom per Mo_4O_6 unit.)

The superstructure of $Pb_{0.77}Mo_4O_6$ has been determined by analyzing the relative intensities of the superlattice reflections. We may apply the Pb-O bond-length bond-strength relation to the supercell structure. The estimated oxidation states for Pb1 (at cell center) and Pb2 are equal to 1.68 and 1.89, respectively. Interestingly enough, the average oxidation state (1.78) is essentially the same as the value (1.79) estimated from subcell data. Another physical method such as ^{207}Pb (I = 1/2, 22% abundance) NMR might reveal more evidences of two different types of lead atoms.

DISCUSSION

One of the most interesting features of the $M_xMo_4O_6$ structures pertains to the positions and occupancies of the tunnel cations. The sodium ion in $NaMo_4O_6$ fully occupies the site at (0,0,1/2). But the sodium ion showed large temperature factors along the a and b directions, suggesting some positional disorder in the ab plane. The indium ion in $InMo_4O_6$ displaces to (0,0,0.0987). Two-thirds of the lead ions in $Pb_{0.77}Mo_4O_6$ displace from the cell center to (0,0,0.28). There is a vacancy every fourth subcell.

It is often found that smaller cations are stabilized by displacing to the off-center sites. The predicted Na-O distance (2.56 A) for Na^+ in eight coordination is a lot shorter than the distance (2.742 A) from the site at (0,0,1/2) to the oxygen atoms. Therefore, Na^+ in $NaMo_4O_6$ may be displaced to the off-center sites, resulting in large temperature factors in a subcell refinement. The reason why Na^+ displaces in the ab plane rather than in the tunnel direction is to reduce the charge repulsion between sodium ions. Similarly, the indium should displace to the off-center site in order to be stabilized. In $InMo_4O_6$, the indium ion displaces in the tunnel direction rather than in the ab plane. Both the Mo-O and Pb-O bond-length bond-strength relations suggest that the lead ions in $Pb_{0.77}Mo_4O_6$ have oxidation states lower than 2. The observed Pb2-O distance (2.45 A) and

Pb1-O distance (2.715 A) seem reasonable because the theoretical contact distances for O-Pb^{2+}(CN = 4, pyramid) and O-Pb^{2+}(CN = 8) are equal to 2.36 and 2.67 A, respectively. The charge repulsion between lead ions gets greater compared to In^{+} so that the tunnels are 3/4 filled by lead ions in $Pb_{0.77}Mo_4O_6$. Because the electrostatic repulsion between Ba^{2+} is greater than that for Pb^{2+} at the same distance, the tunnels can only be about 60% filled by Ba^{2+} in $Ba_{0.62}Mo_4O_6$. According to what we have learned from the hollandite structures, we don't expect to insert M^{3+} cations into the tunnel sites without modifying the structure dramatically. It also appears that the state of order in the tunnels in $M_xMo_4O_6$ is critically dependent upon the charge and size of the ternary metal cation.

According to the film work on a $Pb_{0.77}Mo_4O_6$ crystal, the lead ions are 3-dimensionally ordered in the lattice. This implies that the lead ions in the tunnels formed by condensed molybdenum metal cluster chains are intercommunicating. This observation might be related to the observed differences in resistivities of $NaMo_4O_6$ and $InMo_4O_6$ at low temperature. The resistivity and magnetic susceptibility measurements on $InMo_4O_6$ do not reveal any phase transition down to $2^{o}K$. However, the resistivity data for $NaMo_4O_6$ shows a continuous metal-semiconductor transition at low temperature (26). According to the extended Huckel band calculation performed by Hughbanks and Hoffmann (27), the energy band dispersion curves

for $NaMo_4O_6$ are very anisotropic and the interchain coupling provided by the linking trigonal planar oxygen atoms is very weak. In other words, $NaMo_4O_6$ has one-dimensional character resulting from weak electronic coupling between metal cluster chains. Peierls (28) showed that a one-dimensional metal is inherently unstable to periodic lattice distortions. Therefore, it is asserted that a continuous metal-semiconductor transition has been observed for $NaMo_4O_6$. On the other hand, if the interchain coupling is large enough, then the lattice instability will be quenched.

X-ray and UV valence band photoelectron spectra of $NaMo_4O_6$, $InMo_4O_6$, and $Sn_{0.9}Mo_4O_6$ (29) all show the expected Fermi edge at the ionization threshold, indicating that they are metallic at room temperature. HeI valence band spectra of the tin and the indium compounds show a broadened oxygen 2p band and a relatively more diffuse conduction band compared to those of $NaMo_4O_6$. The differences might be due to the mixing of In or Sn 5s or 5p orbitals with oxygen 2p and Mo 4d orbitals. X-ray valence band spectra show that the conduction bands increase dramatically in intensity relative to oxygen 2p bands on changing from HeI to x-ray excitation. The reason why the conduction band for $Sn_{0.9}Mo_4O_6$ is more intense than that for $InMo_4O_6$ is because of more conduction electrons in the tin compound. Resistivity measurements show that both $Sn_{0.9}Mo_4O_6$ (27) and $InMo_4O_6$ are metallic down to $2^{o}K$. The three-dimensional ordering of the lead ions in $Pb_{0.77}Mo_4O_6$

also imply some interaction between tunnel cations and the molybdenum metal cluster chains. $NaMo_4O_6$ is closer to one-dimensional character than $M_xMo_4O_6$ compounds (M = In, Pb, Sn) because Na^+ is much more electropositive. Analogous physical properties have been observed in $M_2Mo_6X_6$ compounds (M = group IA metals, In, or Tl; X = Se, or Te) (5). The diffuse x-ray scattering, magnetic susceptibility, and resistivity meausrements on MMo_4O_6 compounds (M = group IA metal) would be very interesting and informative.

An interesting feature of the magnetic susceptibility data for $InMo_4O_6$ is the positive value of $d\chi/dT$. If T is small compared with the Fermi temperature, the temperature-dependent correction to the Pauli susceptibility is given by (30):

$$\chi(T) = \chi(0)[1 - (\pi^2/6)(k_BT)^2((g'/g)^2 - g''/g)] \quad \text{Eq. (1)}$$

where g, g', and g" are the density of states and its derivatives at the Fermi energy. Assuming free electrons and three-dimensional band features at E_f,

$$g(E) = (m/h^2\pi^2)(2mE/h^2)^{1/2}.$$

Then, Eq. (1) gives:

$$\chi(T) = \chi(0)[1 - (\pi^2/12)(k_BT/E_f)^2]$$

Therefore, for 3-dimensional structures χ will in general decrease with increasing T. However, for free electrons and one-dimensional band features at E_f,

$$g(E) = (1/\pi h)(m/2E)^{1/2}$$

Equation (1) becomes:

$$\chi(T) = \chi(0)[1 + (\pi^2/12)(k_BT/E_f)^2]$$

Thus, the observed $d\chi/dT > 0$ for $InMo_4O_6$ is reasonable, considering the unidirectional condensed molybdenum metal cluster chains in the structure.

As discussed earlier, $NaMo_4O_6$ is closer to one-dimensional character than $InMo_4O_6$. Resistivity measurements perpendicular to the cluster chain direction would provide more evidences to support the above reasoning. However, the measurement is experimentally infeasible because these compounds grow in needle-like crystals. Nevertheless, a comparison of magnetic susceptibility as a function of temperature for these isomorphous compounds may give us some informative results.

Crystal growth from vapor by the chemical transport technique has been applied to both In-Mo-O and Pb-Mo-O systems. It is believed that larger crystals will be obtained if a better experimental condition and transporting agent are used. Resistivity measurements on a $Pb_{0.77}Mo_4O_6$ single crystal are desirable. Further, one may be able to secure a clean sample surface for photoelectron spectroscopy measurement by cleavage of large crystals obtained from the chemical transport technique.

REFERENCES

1. Potel, M.; Chevrel, R.; Sergent, M. Acta Crystallogr. 1980, B36, 1545.

2. Potel, M.; Chevrel, R.; Sergent, M.; Armici, J. C.; Decroux, M.; Fisher, O. J. Solid State Chem. 1980, 35, 286.

3. Honle, W.; Von Schnering, H.-G.; Lipka, A.; Yvon, K. J. Less-Common Metals 1980, 71, 135.

4. Huster, J.; Schippers, G.; Bronger, W. J. Less-Common Metals 1983, 91, 333.

5. Tarascon, J. M.; DiSalvo, F. J.; Waszczak, J. V. Solid State Commun. 1984, 52, 227.

6. Lokken, D. A.; Corbett, J. D. Inorg. Chem. 1973, 12, 556.

7. Poeppelmeier, K. R.; Corbett, J. D. Inorg. Chem. 1977, 16, 1107.

8. Torardi, C. C.; McCarley, R. E. J. Am. Chem. Soc. 1979, 101, 3963.

9. Torardi, C. C.; McCarley, R. E. J. Solid State Chem. 1981, 37, 393.

10. Torardi, C. C. Ph.D. Dissertation, Iowa State University, Ames, Iowa, 1981.

11. Potel, M.; Gougeon, P.; Chevrel, R.; Sergent, M. Revue de Chimie Minerale 1984, 21, 509.

12. Clark, C. M.; Smith, D. K.; Johnson, G. J. "A Fortran IV Program for Calculating X-Ray Powder Diffractions Patterns-Version 5", Department of Geosciences, Pennsylvania State University, University Park, PA, 1973.

13. Rohrbaugh, W. J.; Jacobson, R. A. Inorg. Chem. 1974, 13, 2535.

14. Coppens, P.; Hamilton, W. C. Acta Crystallogr. 1970, A26, 71.

15. Hanson, H. P.; Herman, F.; Lea, J. D.; Skillman, S. Acta Crystallogr. 1964, 17, 1040.

16. Seiler, P.; Dunitz, J. D. Acta Crystallogr. 1978, A34, 329.

17. Luly, M. H. "APES, A Fortran Program to Analyze Photoelectron Spectra", US DOE Report IS-4694; Iowa State University: Ames, IA, 1979.

18. Michel, J. B.; McCarley, R. E. Inorg. Chem. 1982, 21, 1864.

19. Corbett, J. D.; Meyer, G.; Anderegg, J. W. Inorg. Chem. 1984, 23, 2625.

20. Lin, A. W. C.; Armstrong, N. R.; Kuwana, T. Anal. Chem. 1977, 49, 1228.

21. Carlson, C. D.; McCarley R. E., unpublished research, Department of Chemistry, Iowa State University, Ames, Iowa, 1985.

22. Brown, I. D.; Wu, K. K. Acta Crystallogr. 1976, B32, 1957.

23. Hogg, J. H. C.; Duffin, W. J. Acta Crystallogr. 1967, 23, 111.

24. Rigoult, J.; Rimsky, A. Acta Crystallogr. 1980, B36, 916.

25. Hogg, J. H. C.; Sutherland, H. H. Acta Crystallogr. 1973, B29, 1590.

26. Simon, A. private communication to R. E. McCarley, 1983.

27. Hughbanks, T.; Hoffmann, R. J. Am. Chem. Soc. 1983, 105, 3528.

28. Peierls, R. E. "Quantum Theory of Solids"; Clarendon: Oxford, England, 1955; page 108.

29. Aufdembrink, B.; McCarley, R. E., unpublished research, Department of Chemistry, Iowa State University, Ames, Iowa, 1985.

30. Ashcroft, N. W.; Mermin, N. D. "Solid State Physics", Saunders College: Philadelphia, 1976; page 669.

SECTION 3. SYNTHESES, CRYSTAL STRUCTURE, AND PROPERTIES OF A TERNARY MOLYBDENUM OXIDE CONTAINING THREE DIFFERENT TYPES OF MOLYBDENUM METAL CLUSTER CHAINS: $Ca_{5.45}Mo_{18}O_{32}$

INTRODUCTION

Recently, the preparations and structures of $M_xMo_2O_4$ (M = Li, Na) (1, 2) have been reported. They contain extended cluster chains which are comprised of rhomboidal clusters fused on opposite edges. Their structures are in contrast to that of $Ba_{1.14}Mo_8O_{16}$ (3), $Na_{0.35}BaMo_8O_{16}$ (4), or $K_2Mo_8O_{16}$ (5) where similar chains of molybdenum are broken into discrete rhomboidal clusters. However, as discussed in SECTION 1 of this thesis both the structures can be derived from the rutile structure. The e/Mo ratios for the two structure types are so close that the structure difference appears to be determined by the charges and sizes of the ternary metal cations. The average oxidation states for Mo in these two structure types are about 3.75 - 3.5 which are considerably higher than those in MMo_4O_6 (M = Na, Ba, In, Pb, Sn ... , etc.) (6,3,1,7). The $NaMo_4O_6$ structure contains extended molybdenum metal cluster based on 6-12 type building blocks. For a few ternary cations, such as Na and Ba, different structure types can be adopted depending upon the average oxidation state of Mo. The compounds mentioned above are representative of a large family of oxides containing molybdenum in low oxidation states. Their crystal structures are sensitive to the interplay among several factors, such as metal cluster electron count and the nature of the ternary metal cations. Further research to explore new structure types that might exist in this new realm

led to the discovery of the remarkable compound $Ca_{5.45}Mo_{18}O_{32}$ which contains three different kinds of cluster chains with Mo_1, Mo_2, and Mo_4 repeat units.

EXPERIMENTAL AND RESULTS

Materials

All chemicals used in the syntheses were of reagent grade or better. Calcium molybdate was prepared by mixing an aqueous solution of calcium chloride (Baker Analyzed Reagent) with an aqueous solution containing stoichiometric quantity of sodium molybdate (Fisher Certified A.C.S.). The white precipitate was filtered, washed with water, dried at 120°C under vacuum, and then annealed at 800°C. Yttrium molybdate was obtained by heating an intimate mixture of Y_2O_3 (Alfa, 99.99%) and MoO_3 (Baker, 99.9%) in 1: 3 mole ratio at 800°C for one day. The purity of the product was checked with the x-ray powder diffraction technique. Gd_2O_3 was obtained from Ames Laboratory. Other starting materials used were Aldrich Mo powder (99.99%), Thermo-Electron Mo tubing (99.97%), Alfa Mo foil (99.97%), Baker MoO_3 (99.9%).

Syntheses and Analyses

$\underline{Ca}_{5.45}\underline{Mo}_{18}\underline{O}_{32}$

A compound which was formulated as "$CaMo_5O_8$" (8) was obtained from a reaction mixture of calcium molybdate, molybdenum dioxide, and molybdenum metal at 1100C. A reaction

aiming at "$CaMo_5O_8$" at 1400C gave not only the black chunky crystals but also some black needles. The x-ray powder pattern of the chunky crystals indicated that they were the same as "$CaMo_5O_8$". Unfortunately, most of them were either too small or multiple crystals. The long needles were apparently different from "$CaMo_5O_8$". Some of these crystals were so thin that they could be easily bent without being broken. The microprobe analyses on six different spots of a thicker crystal (50 μm) gave quite consistent results, and the Mo to Ca mole ratio was 3.30(4). The analytical results for the Mo/Ca ratio were in a good agreement with that from single-crystal x-ray diffraction data (vide infra). The exact stoichiometry of the title compound was not known until its x-ray structure was solved. An essentially pure product was obtained by heating a pressed pellet containing a stoichiometric amount of $CaMoO_4$, MoO_3, and Mo in a sealed molybdenum crucible at about 1400C for two days. The reaction product contained numerous black, long, thin slabs growing off the pressed pellet. A reaction to prepare the title compound at much lower temperature (1000C) for four weeks was also conducted. After opening the molybdenum container, it was found that the pelletized sample was covered by extremely thin, long plates. The long plates were collected by scraping them off the pellet with a razor. An x-ray powder pattern of the long plates showed that it was different from $Ca_{5.45}Mo_{18}O_{32}$. The Ca/Mo mole ratio (0.30) from microprobe

analysis was a little lower than that for the title compound. The powder pattern of the plates has not been fully indexed yet. The powder pattern of the cleaned pellet displayed diffraction lines only due to $Ca_{5.45}Mo_{18}O_{32}$.

$\underline{Y_xMo_{18}O_{32}}$

The title compound was discovered in the preparation of "$Y_{0.75}Zn_{1.25}Mo_4O_7$". Subsequently, a reaction to prepare "$Y_4Mo_{18}O_{32}$" was carried out. A pelletized sample containing appropriate quantities of $Y_2(MoO_4)_3$, MoO_3, and Mo was wrapped with a sheet of molybdenum foil which, in turn, was sealed in an evacuated quartz tube. The sample was then heated at 1250C for 48 hours and at 1300C for 4 hours. Although the molybdenum foil was coated with MoO_2, a Guinier powder pattern of the bulk product did not reveal any reflection lines of MoO_2. All the observed lines could be indexed on the basis of the $Ca_{5.45}Mo_{18}O_{32}$ structure. Higher reaction temperatures should give bigger crystals which are suitable for microprobe analysis and single-crystal x-ray diffraction study. More effort on this system is worthwhile.

$\underline{Gd_xMo_{18}O_{32}}$

In an attempt to prepare "$Gd_2Mo_8O_{16}$", the following reaction was conducted:

$$3\ Gd_2O_3 + 13\ MoO_3 + 11\ Mo \xrightarrow[1450^oC,\ 1.5\ d]{Mo\ tube} \text{products}$$

The bulk product gave an x-ray powder pattern which was similar to that for $Ca_{5.45}Mo_{18}O_{32}$. However, the pattern could not be fully indexed on the basis of the $Ca_{5.45}Mo_{18}O_{32}$ structure, suggesting the presence of other phases in the system. Some very small needle-like and columnar crystals were selected for film work. The needle-like crystal was isomorphous with $Ca_{5.45}Mo_{18}O_{32}$. However, the film work on a columnar crystal indicated that the Laue symmetry was mmm with the unit cell constants a = 10.7, b = 16.0, c = 5.67 A. Systematic absences were observed for h0ℓ with h = 2n and 0kℓ with k = 2n. The possible space groups thus were Pbam and Pba2. The structure of the columnar crystal will be further discussed in SECTION 6 of this thesis. X-ray pure $Gd_xMo_{18}O_{32}$ has not been obtained yet. Further work on this promising system at higher reaction temperature should be fruitful.

Preliminary Film Work and X-ray Powder Diffraction

$\underline{Ca}_{5.45}\underline{Mo}_{18}\underline{O}_{32}$

Film work on the long, thin slabs indicated that most of them were not single crystals. Many had to be selected before a satisfactory crystal was obtained. A crystal of dimensions 0.40 x 0.03 x 0.005 mm was mounted on a Weissenberg camera with the b axis parallel to the rotation axis. Oscillation and h0ℓ-h1ℓ layer photographs were registered. The film work suggested that the Laue group was 2/m with the unit cell

parameters a = 24.20, b = 2.86, c = 9.90 A, $\beta = 109.6^{o}$. Systematic absences were observed for hk& reflections with h + k = 2n. The possible space groups thus were C2, Cm, and C2/m. No superlattice reflections were observed between the layer lines on the axial oscillation picture (9). Many diffraction spots displayed streaks along the $\underline{b}^{*}$ direction, suggesting that there was a certain type of disorder in the $\underline{b}$ direction.

About one-half of the reaction product obtained at 1400C was ground into powder and its x-ray powder pattern was taken. The powder was very sticky and the long, thin slabs tended to align themselves in a preferred orientation so that h00 reflections were much stronger than they should be. The product was then mixed with much silicon powder and reground into fine powder. Its Guinier powder pattern could be fully indexed with a C-centered monoclinic cell. The powder pattern is given in Table 3.1 along with the calculated interplanar distances of reflection planes and with intensities calculated from a computer program (10). A least-squares fit of the peak positions of 16 reflections gave a = 24.205(8), b = 2.8501(3), c = 9.868(3) A, $\beta = 109.82(4)^{o}$, V = 640.5(3) A^{3}.

$\underline{Y_xMo_{18}O_{32}}$ and $\underline{Gd_xMo_{18}O_{32}}$

The Guinier powder pattern for $Y_xMo_{18}O_{32}$ is listed in Table 3.2 with the calculated interplanar distances. Some reflections in the powder pattern are weak and broad presumably because of the problem of preferred orientation. A

Table 3.1. X-ray powder diffraction data for $Ca_{5.45}Mo_{18}O_{32}$

d-spacings (A)		intensities		
obsd.	calcd.[a]	obsd.	calcd.[b]	hkℓ
9.19(3)	9.281, 8.803	m, vbr	33, 27	001, -201
5.70(1)	5.694	s	100	400
4.930(7)	4.920	m	22	-202
3.794(4)	3.796	m	16	600
2.847(2)	2.847	m	26	800
2.671(2)	2.672	vw	3	111
2.446(2)	2.446, 2.441	m, br	11, 34	-511, -312
2.417(2)	2.415	w	8	510
2.370(2)	2.369	w	14	112
2.323(2)	2.319, 2.320	w	10, 12	004, -512
2.152(1)	2.150	w, br	14	-313
1.898(1)	1.898	w-m	15	1200
1.865(1)	1.864	vw	4	-314
1.847(1)	1.847	w, br	16	-514
1.4250(5)	1.424	m	14	020
1.4108(5)	1.411	vw, br	2	1311
1.3826(5)	1.381	w	7	420
1.3340(4)	1.333	w	4	116
1.2744(4)	1.273	w	5	820

[a]Some weak or very weak lines on the calculated powder pattern were barely seen on the Guinier powder pattern. These lines are not listed in this table.

[b]Intensities were calculated with a computer program (10). a = 24.211(7), b = 2.8475(7), c = 9.865(7) A, β = 109.82(4)°.

Table 3.2. X-ray powder diffraction data for $Y_xMo_{18}O_{32}$

d-spacings (A) observed	d-spacings (A) calculated[a]	intensities	hkℓ
9.25(2)[b]	9.233	w, br	001
5.643(8)	5.632	s	400
4.907(6)	4.896	w	-202
3.757(4)	3.754	w	600
2.816(2)	2.816	w-m	800
2.741(2)	2.741	vw	203
2.714(2)	2.715	vw	-111
2.646(2)	2.645	vw	310
2.449(2)	2.448	vw	-404
2.426(1)	2.423	w-m	-511, -312
2.394(1)	2.394	w	510
2.136(1)	2.136	m	-313
1.8771(8)	1.877	w	1200
1.6318(6)	1.632	w	-406
1.4129(4)	1.413	m, br	020

[a]Some weak or very weak lines on the calculated powder pattern were barely observed on the Guinier powder pattern. These lines are not listed in the table.

[b]Because this reflection is so broad that the neighboring reflection (-201, at d = 8.746 A) could not be accurately measured.

least-squares fit of the peak positions of 15 reflections gave a = 23.958(9), b = 2.8258(3), c = 9.817(4) A, β = 109.90(5)°, V = 624.9(3) A^3.

An axial oscillation photograph along the needle axis of a $Gd_xMo_{18}O_{32}$ crystal showed weak reflections at 1/2 r.l.u. (reciprocal lattice unit) between the h0ℓ and h1ℓ layer lines. They were most likely due to the three-dimensional ordering of the gadolinium ions.

X-ray Single-Crystal Data Collection for $Ca_{5.45}Mo_{18}O_{32}$

The crystal was centered on a four-circle diffractometer with the needle axis nearly collinear with the φ axis. Determination of the preliminary orientation matrix was accomplished by using an indexing program (11) that uses reflections taken from several ω-oscillation pictures as input. Four strong reflections in the angular range $25^\circ < 2\theta < 36^\circ$ were selected as standards. Their 2θ, ω, and χ settings were accurately determined via an automatic centering routine. These values were used in the determination of the accurate orientation matrix. Unit cell constants which were obtained from a least-squares refinement of peak positions of 19 accurately centered high-angle ($2\theta = 23 - 43^\circ$) reflections were a = 24.211(7), b = 2.8475(7), c = 9.865(7) A, β = 109.82(4)°. They will be used in the later calculations. Important crystallographic parameters are given in Table 3.3.

Table 3.3. Crystallographic data for $Ca_{5.45}Mo_{18}O_{32}$

---

crystal system: monoclinic

space group: C2/m

a = 24.211(7), b = 2.8475(7), c = 9.865(7)A, β = 109.82(4)°

V = 639.8(6) A^3

Z = 1

d(calcd) = 6.380 g/cm^3

crystal size: 0.40 x 0.03 x 0.005 mm

absn coeff: 94.8 cm^{-1}

refln used for empirical absorption correction (hkℓ, 2θ, T_{max}/T_{min}): 020, 28.82°, 1.92

diffractometer: AL[a]

radiation: Mo Kα (λ = 0.70964 A)

monochromator: oriented graphite

scan type: ω-scan

automatic background detn, max scan half width: 0.75 degree

std reflns: 4 measured every 150 reflns; no significant variation in intensity.

reflns measd: hkℓ, $\bar{h}\bar{k}\ell$, $\bar{h}k\bar{\ell}$, $h\bar{k}\bar{\ell}$

max 2θ: 50°

reflns collected: 1508 collected (symmetry extinct reflns not included), 1202 observed ($I > 3\sigma(I)$)

no. of unique reflns with $I > 3\sigma(I)$: 569

no. of parameters refined: 88

R = 0.041[b], R_w = 0.055[c]

quality-of-fit indicator[d]: 1.790

---

[a]For details of the AL diffractometer, see reference 15.

[b]$R = \Sigma||F_o| - |F_c||/\Sigma|F_o|$.

[c]$R_w = [\Sigma w(|F_o|-|F_c|)^2/\Sigma w|F_o|^2]$; $w = 1/\sigma^2(|F_o|)$.

[d]Quality of fit = $[\Sigma w(|F_o|-|F_c|)^2/(N(observns)-N(parameters))]^{1/2}$.

An empirical absorption correction (12) was based on ϕ scans of a suitable reflection with χ near 90^{o}. Lorentz and polarization corrections were also applied. Scattering factors (13) for neutral atoms were used throughout the calculations. Both the real ($\Delta f'$) and imaginary ($\Delta f''$) components of anomalous dispersion (14) were included for Mo and Ca atoms. An examination of the intensity data set revealed that only reflections obeying the condition h + k = 2n for hkℓ were observed. The possible space groups thus were C2, Cm, and C2/m. Since statistical tests indicated a centrosymmetric space group, C2/m was selected.

Solution and Refinement of $Ca_{5.45}Mo_{18}O_{32}$

The five molybdenum atom positions were located by using the computer program ALCAMPS (Ames Laboratory Computer-aided Analysis of Multi-solution Patterson Superposition) (16) with the help of Sue-Lein Wang in Dr. Jacobson's group. A few cycles of full-matrix least-squares refinement of positional parameters of the molybdenum atoms led to R = 24.8% and R_w = 30.4%. A Fourier synthesis then led to the unambiguous locations of the two calcium and eight oxygen atoms. Refinement of positional parameters, calcium multipliers, and anisotropic temperature factors converged at R = 4.1% and R_w = 5.5%. At this point, the B22 thermal parameter of Mo5 (unique molybdenum atom) was relatively large (3.4 x B33 and 6 x B11)

in C2/m refinements in which the molybdenum atom was placed on the mirror plane. Therefore, a displacement of this atom from the mirror plane was allowed with its temperature parameters fixed. After many cycles of least-squares refinement with alternately fixed temperature parameters and y coordinate, the molybdenum atom shifted to (0.5, 0.550, 0.0) with much smaller temperature parameter. Although the agreement factors remained the same, the maximum residual electron density on the ΔF maps decreased from 1.1 e/A^3 to 0.4 e/A^3. The multiplier of Mo5 was 0.25 corresponding to 50% occupancy at each 4g special position. This model could be explained in terms of alternately long and short Mo-Mo distances along the b direction. The calcium content of this compound was determined from the electronmicroprobe analysis results. Assuming the two different calcium sites are equally occupied, then the multiplier for each calcium would be 0.34, which is in good agreement with the results from least-squares refinement. The calcium atoms showed large B22 temperature factors, suggesting some positional disorder in the b direction. Positional parameters are collected in Table 3.4; thermal parameters are listed in Table 3.5. Selected bond distances and bond angles are given in Tables 3.6 and 3.7, respectively.

Table 3.4. Positional parameters for $Ca_{5.45}Mo_{18}O_{32}$

atom	position	multiplier	x	y	z	B(A^2)[a]
Mo1	4i	.5	.00022(6)	.5	.3614(2)	0.63
Mo2	4i	.5	.75870(6)	.5	.3641(2)	0.69
Mo3	4i	.5	.24616(6)	.0	.8537(2)	0.73
Mo4	4i	.5	.08463(7)	.0	.5707(2)	0.91
Mo5	4g	.25	.5	.550(2)	.0	0.80
Ca1	4i	.36(1)	.1188(2)	.0	.9317(7)	3.64
Ca2	4i	.37(1)	.1199(3)	.0	.2684(8)	4.94
O1	4i	.5	.4104(5)	.0	.581(2)	1.25
O2	4i	.5	.1818(6)	.0	.648(2)	1.39
O3	4i	.5	.2950(5)	.0	.5876(14)	0.81
O4	4i	.5	.5894(5)	.0	.7301(14)	0.82
O5	4i	.5	.0000(5)	.0	.2026(14)	1.08
O6	4i	.5	.1958(5)	.0	.1656(13)	0.63
O7	4i	.5	.2986(5)	.0	.0712(13)	0.46
O8	4i	.5	.4342(6)	.0	.947(2)	1.43

[a]The isotropic equivalent thermal parameter is defined as $B = 4/3\,[a^2\beta_{11} + b^2\beta_{22} + c^2\beta_{33} + 2ab(\cos\gamma)\beta_{12} + 2ac(\cos\beta)\beta_{13} + 2bc(\cos\alpha)\beta_{23}]$.

Table 3.5. Thermal parameters for $Ca_{5.45}Mo_{18}O_{32}$

atom	B11	B22	B33	B12	B13	B23
Mo1	0.45(6)	0.42(6)	0.96(7)	0.0	0.16(5)	0.0
Mo2	0.51(6)	0.82(6)	0.77(7)	0.0	0.25(5)	0.0
Mo3	0.52(6)	0.83(7)	0.79(7)	0.0	0.18(5)	0.0
Mo4	0.47(6)	1.50(7)	0.76(7)	0.0	0.21(5)	0.0
Mo5	0.50(8)	1.1(1)	0.9(1)	0.0	0.36(7)	0.0
Ca1	0.5(2)	9.2(7)	1.1(3)	0.0	0.3(2)	0.0
Ca2	0.8(3)	12.2(9)	1.8(3)	0.0	0.4(2)	0.0
O1	1.1(5)	0.7(5)	1.8(6)	0.0	0.2(5)	0.0
O2	2.0(6)	0.7(5)	1.7(6)	0.0	0.8(5)	0.0
O3	1.1(5)	0.5(5)	1.3(6)	0.0	1.1(5)	0.0
O4	0.2(4)	0.7(5)	1.4(6)	0.0	-0.1(4)	0.0
O5	1.2(5)	1.1(5)	0.6(5)	0.0	-0.1(4)	0.0
O6	0.5(4)	0.6(5)	0.6(5)	0.0	0.1(4)	0.0
O7	0.4(4)	0.7(5)	0.6(5)	0.0	0.5(4)	0.0
O8	1.3(5)	1.3(6)	1.8(6)	0.0	0.7(5)	0.0

[a]Anisotropic temperature factors are given in the form $\exp[-1/4(B_{11}h^2a^{*2} + B_{22}k^2b^{*2} + \ldots + 2B_{23}k\&b^*c^*)]$.

Table 3.6. Selected bond distances (A) for $Ca_{5.45}Mo_{18}O_{32}$

Octahedral Cluster			
Mo4-Mo4	2.8475(7)[a]	Mo5-Mo5	2.560(9)
Mo1-Mo1	2.8475(7)[a]		3.135(9)
Mo1-Mo1	2.738(4)[b]	Mo5-O8	1.971(10) (2x)
Mo4-Mo1	2.758(2)		2.169(10) (2x)
	2.762(2)	Mo5-O5	2.004(13) (2x)
Mo4-O4	2.095(10)		
Mo4-O1	2.097(11)	Ca1-O4	2.351(12) (2x)
Mo4-O2	2.213(14)	Ca1-O8	2.480(12) (2x)
Mo1-O5	2.116(10)	Ca1-O7	2.462(10) (2x)
Mo1-O4	2.049(11)	Ca1-O5	2.728(14) (1x)
Mo1-O1	2.043(11)	Ca1-O6	2.424(14) (1x)
		Ca2-O8	2.524(13) (2x)
Rhomboidal Cluster		Ca2-O1	2.348(12) (2x)
Mo3-Mo3	2.8475(7)[a]	Ca2-O3	2.510(11) (2x)
Mo2-Mo2	2.8475(7)[a]	Ca2-O5	2.753(14) (1x)
Mo2-Mo3	2.546(2)	Ca2-O6	2.380(13) (1x)
Mo3-O7a	2.073(8)		
Mo3-O7b	2.090(12)		
Mo3-O6	2.054(8)		
Mo3-O2	2.095(15)		
Mo2-O2	2.058(10)		
Mo2-O6	2.033(12)		
Mo2-O3a	2.089(9)		
Mo2-O3b	2.079(13)		

[a]Parallel to the b axis.

[b]Perpendicular to the b axis.

[c]The atom labels refer to Figs. 3.3, 3.5, and 3.6.

Table 3.7. Selected bond angles (degree) for $Ca_{5.45}Mo_{18}O_{32}$[a]

Mola-Mo4-Molb	59.48(8)
Mola-Mo4-Molc	62.16(6)
Molb-Mo4-Mold	62.05(5)
Mo4-Molb-Mola	60.34(7)
Mo4-Mola-Molb	60.18(6)
Molb-Mola-Molc	90.0
04-Mola-01	170.7(6)
04-Mola-05	86.4(4)
Mo4-04-Mola	83.6(4)
Mo4-01-Mola	83.5(4)
Mola-05-Molb	84.6(5)
04-Mo4-04	85.6(5)
04-Mo4-01	94.1(4)
04-Mo4-02	87.6(4)
01-Mo4-04	173.9(5)
01-Mo4-01	85.5(5)
01-Mo4-02	86.3(4)
Mo3-Mo3-Mo2	56.01(4)
Mo3-Mo2-Mo3	67.99(7)
08-Mo5-08	99.0(5)
	87.4(5)
	86.8(5)
08-Mo5-05	92.1(5)
	93.2(5)
	87.5(5)
	86.5(5)

[a]The atom labels refer to Figs. 3.3, 3.5, and 3.6.

Resistivity Study on $Ca_{5.45}Mo_{18}O_{32}$

A few needles were selected for resistivity measurements. They showed semiconducting behavior and had a large resistance at low temperature. The equipment which was designed for measuring samples with low resistivity was modified by Dr. Cronin Vining in order to work on samples with high resistance. Finally, a very long needle (3.5 x 0.06 x 0.02 mm^3) was used and the cooling rate was maintained at about 1 K/min. At first, the resistance increased gradually and then very rapidly below about 100 K. The resistance could not be measured below 30 K due to resistance > 20 MΩ. Plots of R/R(r.t.) vs. T and log R vs. 1/T are shown in Figs. 3.1 and 3.2, respectively. The linear behavior in Fig. 3.2 is characteristic of a semiconducting material. The room temperature resistivity was about 9 x 10^3 μΩ.cm.

Consider a semiconductor in the intrinsic region. Its conductivity is expressed by the following equation:

$$\sigma = f(T) \exp(-E_g/2kT)$$

where f(T) is a function which depends only weakly on the temperature. If one takes logarithms of both sides of the equation, one obtains

$$\ln \sigma = \ln f(T) - E_g/2kT$$

Because $R = \rho L/A$ and $\rho = 1/\sigma$, the above equation can be rearranged to give:

$$2.303 \log (R_1/R_2) = (E_g/2k)[(1/T_1)-(1/T_2)]$$

Therefore, the plot of log R vs. 1/T should yield a straight line whose slope, $E_g/2k$, determines the energy gap. The slope was obtained from a least-squares fit of the data below 200K and the gap was found to be 0.08 eV. The energy gap is quite small and is about the same as that of grey tin. By careful study of Fig. 3.2, one may notice that the deviation from linearity is more pronounced in the higher temperature range. This observation might be explained by a relatively smaller energy gap at higher temperature. This aspect will be further discussed later.

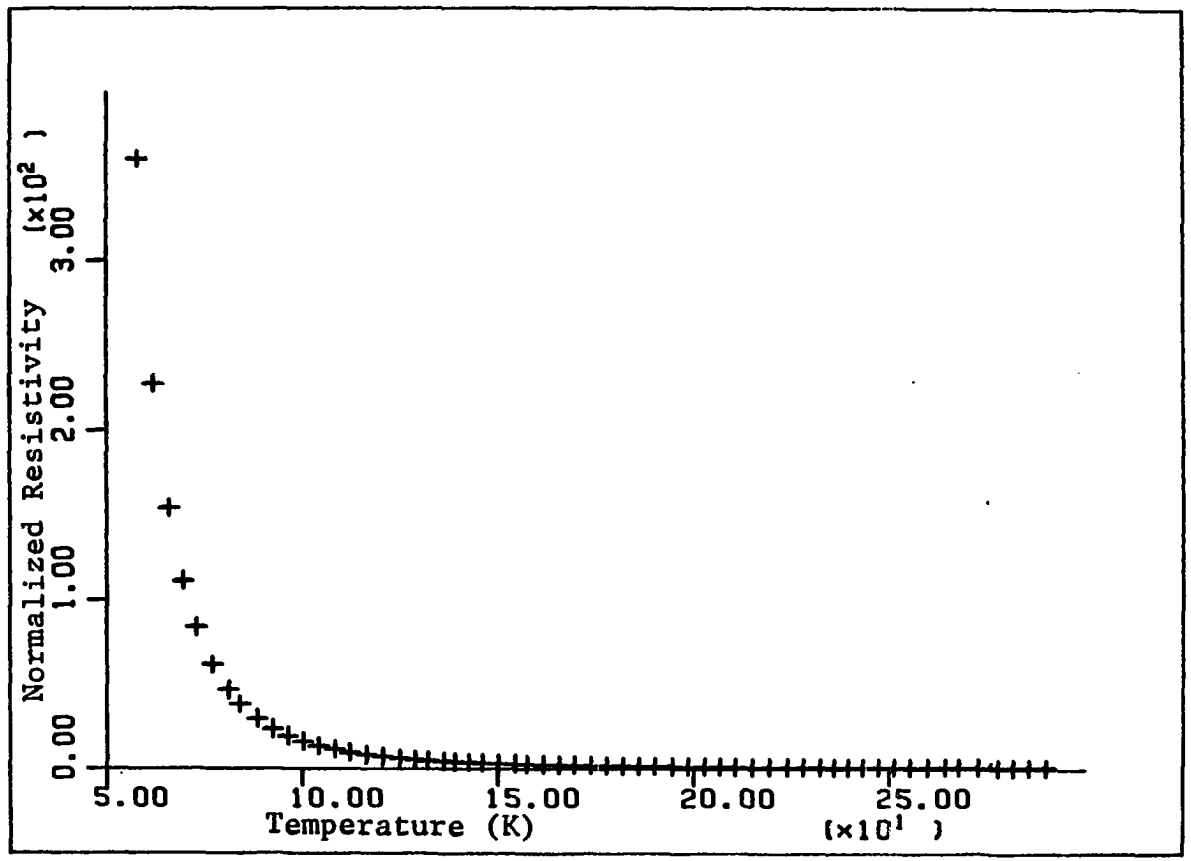

Fig. 3.1. Normalized resistivity ($\rho(T)/\rho(R.T.)$) vs temperature for $Ca_{5.45}Mo_{18}O_{32}$. Electrical resistivities were measured along the needle axis

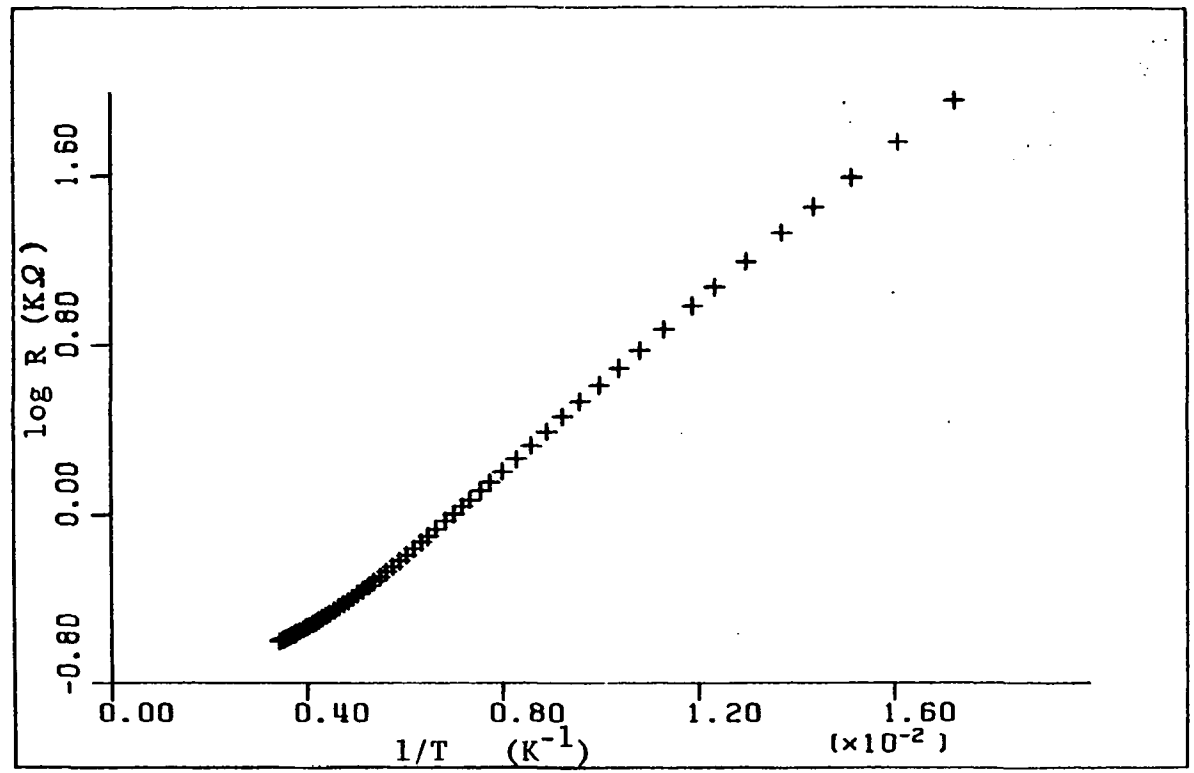

Fig. 3.2. Log R vs 1/T for $Ca_{5.45}Mo_{18}O_{32}$

DESCRIPTION OF THE CRYSTAL STRUCTURE AND DISCUSSION

The compound $Ca_{5.45}Mo_{18}O_{32}$ is the most complicated discovered so far. It contains three different kinds of extended chains (Fig. 3.3). The three types of chains are indicated by the formula $Ca_{5.45}(MoO_3)_2(Mo_2O_{3.5})_4(Mo_4O_6)_2$ where the repeat units (Mo_4O_6) (Figs. 3.4, 3.5) are similar to those found in $NaMo_4O_6$ (6), the repeat units $(Mo_2O_{3.5})$ (Fig. 3.6) consist of fused rhomboidal clusters like those in $NaMo_2O_4$ (1,2), and the repeat units (MoO_3) (Fig. 3.7) are comprised of single Mo atom chains like those found in MoO_2. In the c direction the octahedral cluster chains are connected with single Mo atom chains to form layers in the bc plane. The layer is linked with the neighboring layers consisting of rhomboidal cluster chains mainly through O-Ca-O bondings. (Note that the Mo4-O2 bond distance (2.22 A) is rather long.) Accordingly, the compound can be regarded as a layer structure in which the calcium atoms are located at bicapped trigonal prismatic sites between two neighboring layers. The structure of $Ca_{5.45}Mo_{18}O_{32}$ is reflected in the morphology of the crystals (Fig. 3.8).

The octahedral molybdenum metal cluster units have a local symmetry of C_{2h} where the 2-fold axis is along the b direction. The Mo-Mo bond distances are significantly shorter than those in $NaMo_4O_6$, suggesting that the octahedral cluster unit in the compound $Ca_{5.45}Mo_{18}O_{32}$ has more bonding electrons.

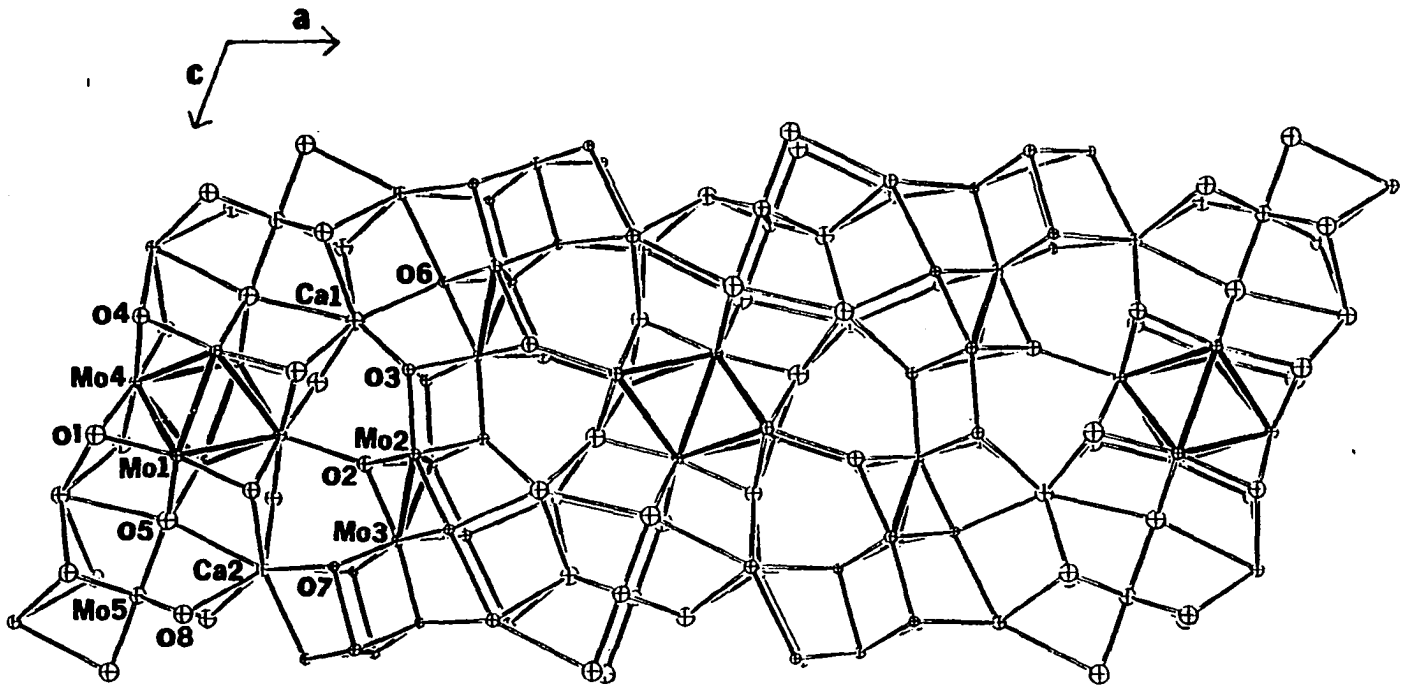

Fig. 3.3. A view of the $Ca_{5.45}Mo_{18}O_{32}$ structure as seen along the monoclinic b axis. The Mo-Mo bonds are represented by the thicker lines

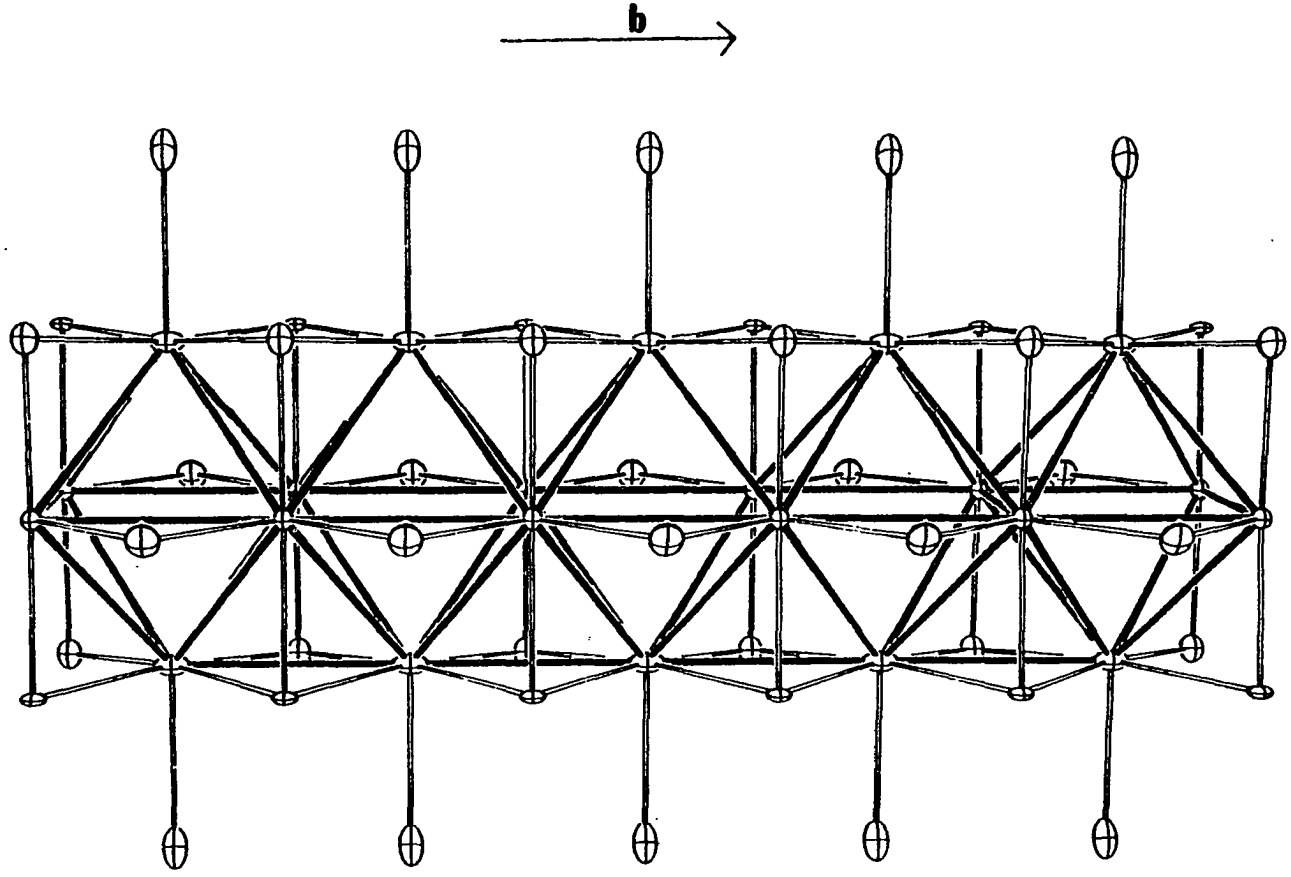

Fig. 3.4. The Mo_4O_6 cluster chain of $Ca_{5.45}Mo_{18}O_{32}$. Heavy lines are Mo-Mo bonds and thin lines are Mo-O bonds

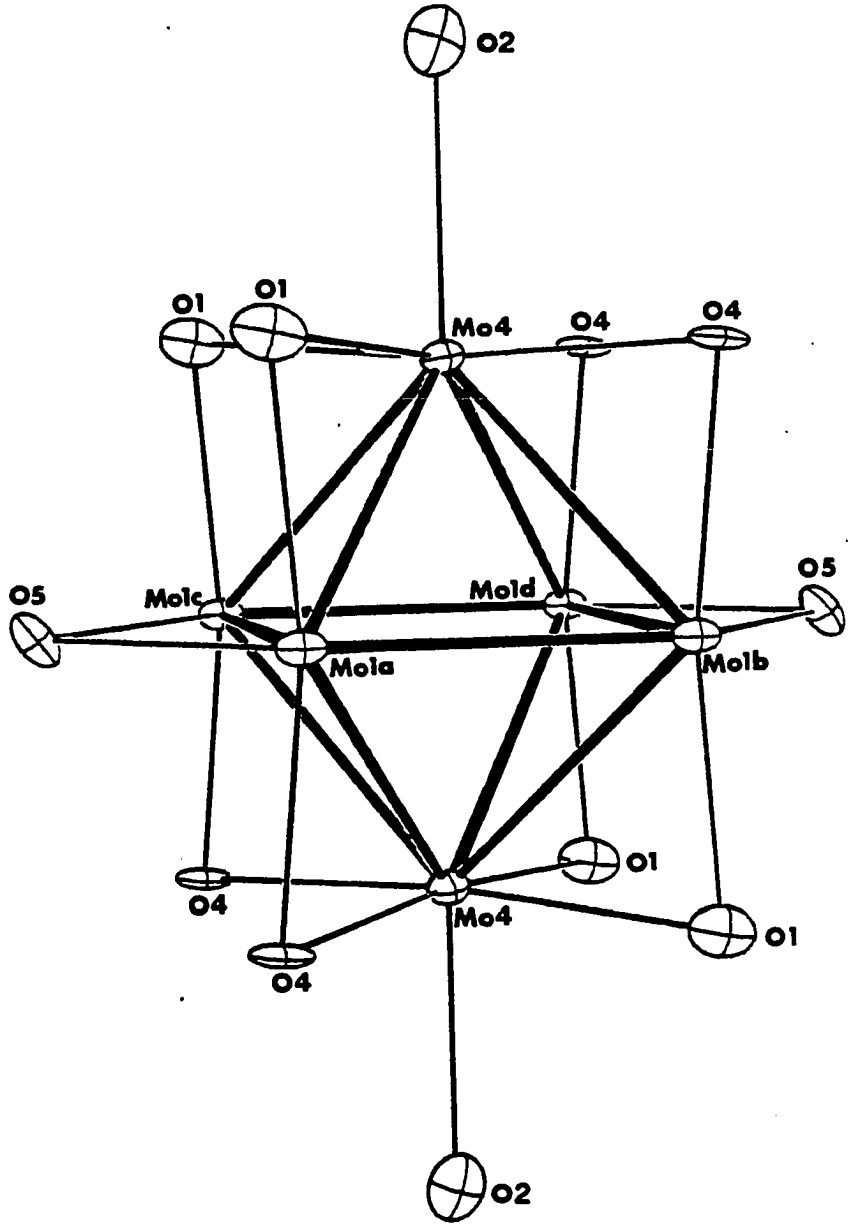

Fig. 3.5. A repeat unit of the Mo_4O_6 cluster chain in $Ca_{5.45}Mo_{18}O_{32}$

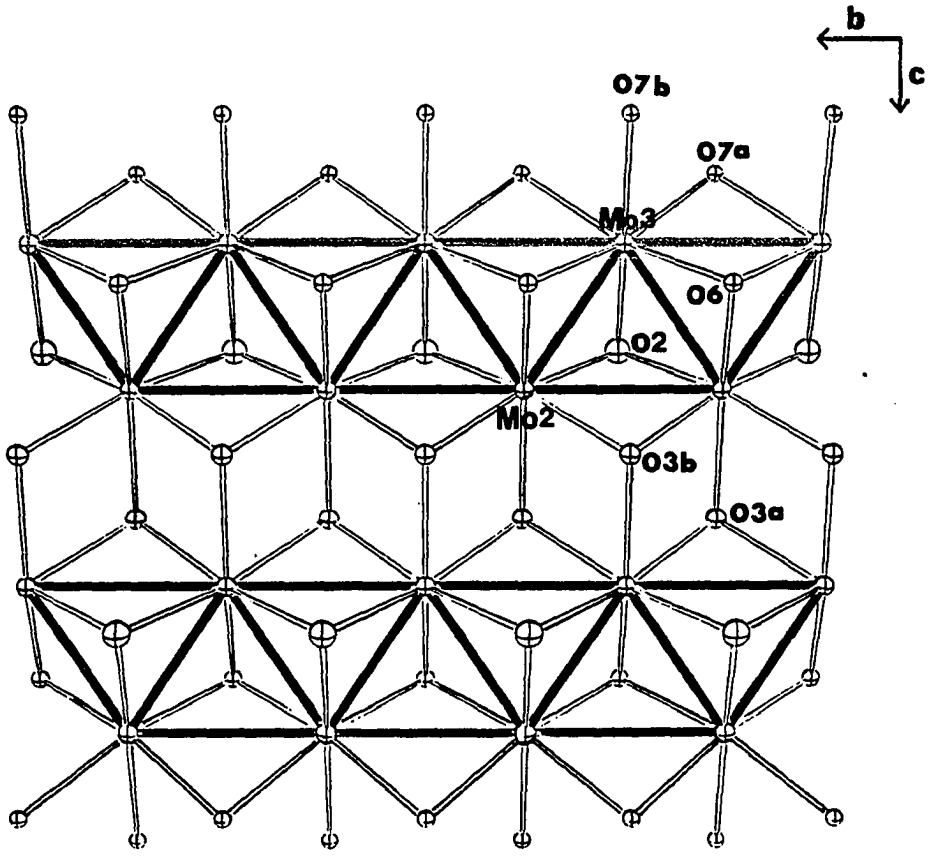

Fig. 3.6. The $Mo_2O_{7/2}$ cluster chains of $Ca_{5.45}Mo_{18}O_{32}$ as viewed perpendicular to the bc plane. Heavy lines are Mo-Mo bonds and thin lines are Mo-O bonds

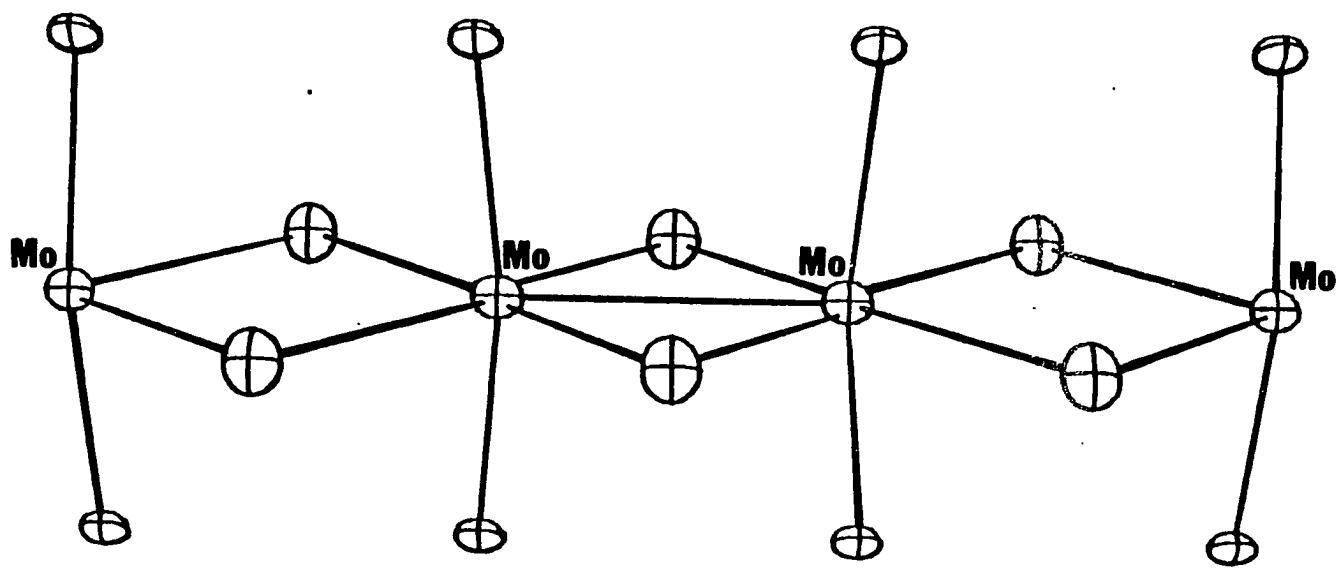

Fig. 3.7. The single-atom chain of $Ca_{5.45}Mo_{18}O_{32}$

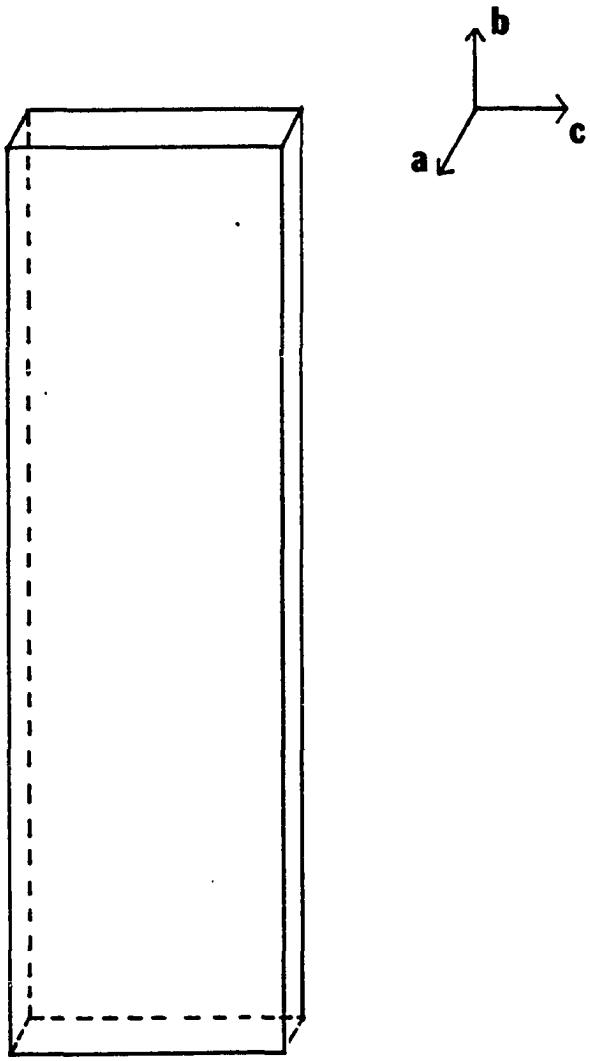

Fig. 3.8. A crystal of $Ca_{5.45}Mo_{18}O_{32}$

The Mo-O bond distances are longer than those in $NaMo_4O_6$, indicating that the molybdenum atoms in the calcium-containing compound have lower oxidation states. The structure was refined with both the apical and waist molybdenum atoms located on the mirror planes.

The unique molybdenum atom (Mo5) was displaced from the mirror plane in the least-squares refinement because it showed a large temperature factor along the b direction. The resulting Mo5-Mo5 bond distances are alternately short and long. The short distance (2.56 A) is a little longer than the corresponding distance (2.51 A) in MoO_2. The longer distance (3.14 A) is essentially nonbonding. If this model is correct, then the repeat distance along b should be doubled in an ordered structure. However, the axial oscillation picture along the needle axis did not reveal any superlattice reflection, except that some of the observed reflections showed streaks along b^*. The absence of superlattice reflections between two layer lines indicates that both Mo5 and Ca atoms are disordered in the b direction. The observed streaks suggest that these atoms might be ordered to some extent in the ac plane.

The intrachain Mo-Mo bond distances (2.848(1), 2.546(2) A) for the rhomboidal clusters compare closely with the related bond distances (2.893(2), 2.535(2) A) in $NaMo_2O_4$ and indicate that the anion chains have comparable e/Mo values in the two compounds.

In SECTION 1 of this thesis, impressive results were obtained in using the bond-length bond-strength relation to estimate the oxidation states of Mo and the charge distribution within the cluster units of $Na_{0.35}BaMo_8O_{16}$. Application of the same procedure to the compound $Ca_{5.45}Mo_{18}O_{32}$ should then provide estimates of the anion charges for the three types of anion chains. If the estimation results are valid, the sum of the anion charges per formula unit should be equal to the total cation charge from Ca^{2+}, i.e. 2 x 5.45 = 10.9. The calculation procedures are shown in Table 3.8 in detail.

The agreement between Σq^- and Σq^+ is extremely good. From the $MoO_3^{2.24-}$ cluster one obtains 2.24 e/Mo for Mo-Mo bonding in the single atom chains, which is a little higher than the 2.0 e/Mo unit in MoO_2. The Mo-Mo bond distance (2.560(9) A) is nearly the same as the related distance (2.55(1) A) in $La_3Mo_4SiO_{14}$ (18). Applying the same approach to the lanthanum-containing compound led to 2.12 e/Mo for the unique molybdenum atom. The charge of -0.24 on the $Mo_2O_{3.5}$ cluster unit gives 5.24 e/Mo_2 which is close to the 5.0 e/Mo_2 unit in $NaMo_2O_4$. The comparable Mo-Mo bond distances within these clusters in the two compounds reflect this agreement in the bonding electron count. The metal cluster electron count (MCE) for the Mo_4O_6 unit in $Ca_{5.45}Mo_{18}O_{32}$ is considerably higher than that in $NaMo_4O_6$. It seems that the MCE value is relatively more variable for extended chains containing Mo_4O_6

Table 3.8. Assessment of oxidation state of Mo and charge distribution in $Ca_{5.45}Mo_{18}O_{32}$

	d(Mo-O)	s(Mo-O)[a]	f[b]	f x s
		MoO_3^{m-} units		
Mo5	2.004(13)	0.69(3)[c]	2	1.38(4)
	1.971(10)	0.76(2)	2	1.52(3)
	2.169(10)	0.43(1)	2	0.86(1)
			v = Σs =	3.76(5)
	$m^- = 3.76(5) - 2 \times 3 = -2.24(5)$			
		$Mo_2O_{3.5}^{n-}$ units		
Mo2	2.058(10)	0.58(1)	2	1.16(1)
	2.033(12)	0.63(2)	1	0.63(2)
	2.089(9)	0.53(1)	2	1.06(1)
	2.079(13)	0.55(2)	1	0.55(2)
			v = Σs =	3.40(3)
Mo3	2.073(8)	0.56(1)	2	1.12(1)
	2.090(12)	0.53(1)	1	0.53(1)
	2.054(8)	0.59(1)	2	1.18(1)
	2.095(15)	0.53(3)	1	0.53(3)
			v = Σs =	3.36(3)
	$n^- = (3.40(3) + 3.36(3)) - 2 \times 3.5 = -0.24(4)$			
		$Mo_4O_6^{p-}$ units		
Mo4 (apex)	2.095(10)	0.53(2)	2	1.06(3)
	2.097(11)	0.52(2)	2	1.04(3)
	2.213(14)	0.38(2)	1	0.38(2)
			v = Σs =	2.48(4)
Mo1 (waist)	2.116(10)	0.50(2)	2	1.00(3)
	2.049(11)	0.60(2)	1	0.60(2)
	2.043(11)	0.61(2)	1	0.61(2)
			v = Σs =	2.21(4)
	$p^- = [2.48(4) + 2.21(4)] \times 2 - 2 \times 6 = -2.62(8)$			
	$\Sigma q^- = 2 \times (m + p) + 4 \times n = 10.7(2)$			

[a] $s(Mo-O) = [d(Mo-O)/1.882]^{-6}$, valence of Mo = Σs (ref.17).

[b] Number of times each bond type occurs.

[c] Number in parentheses indicates maximum error produced by change in bond distance of one standard deviation.

repeat units.

The calcium positions in $Ca_{5.45}Mo_{18}O_{32}$ are only approximately 2/3 occupied. Therefore, the MCE might be varied by changing the calcium content. $Ca_{5.45}Mo_{18}O_{32}$ was first discovered in a reaction aiming at "$CaMo_5O_8$". The Ca/Mo mole ratio for $Ca_{5.45}Mo_{18}O_{32}$ is considerably greater than that for "$CaMo_5O_8$". A few reactions with the Ca/Mo ratios greater than 5.45/18 have been carried out. The x-ray powder patterns of the reaction products revealed the presence of unreacted $CaMoO_4$, suggesting that 5.45 Ca atoms per formula unit is about the maximum amount obtainable in the structure. Why does the compound choose the particular composition? The amount of the ternary metal cation could be mainly determined by its charge and size. One may change the MCE count for the structure by synthesizing compounds containing different ternary metal cations. Other examples of structures of this type have already been uncovered (vide supra). Further synthetic work on this interesting system will be fruitful.

According to the stoichiometry of this compound, the energy band is likely partially filled with electrons. The band theory of solids resulting from a one-electron Hamiltonian predicts that crystalline materials with an odd number of electrons per unit cell should be metallic. However, this model breaks down for many transition metal oxides, primarily because it neglects Coulomb interaction between the d electrons, and these are important when the

energy bands are narrow. In compounds with very narrow energy bands, the electrons will stay apart to reduce the Coulomb repulsion. In other words, electron localization occurs even though the band is only partially filled. In $Ca_{5.45}Mo_{18}O_{32}$, molybdenum atoms are strongly bonded and the energy bands are not expected to be narrow. On the other hand, the compound is a semiconductor with a narrow energy gap. It is now common knowledge that, by opening up a new band gap, a doubling of a unit cell can convert a metal into an insulator. This possible mechanism could be the reason why the unique molybdenum atoms (Mo5) are off the crystallographic mirror plane. By opening up a new energy gap, the electron energy of the system is reduced and this provides a driving force for doubling the unit cell. As the material is heated, some of the electrons will be thermally excited across the energy gap, and this will reduce the driving force which sustains the perturbation. Consequently, the distortion is reduced, and thus the energy gap becomes smaller. It follows that the energy gap will vanish at some temperature, at which point the material reverts back to the metallic configuration, i.e., equally spaced Mo5 atoms. Further work will be necessary to test this interpretation.

REFERENCES

1. McCarley, R. E.; Lii, K.-H.; Edwards, P. A.; Brough, L. F. J. Solid State Chem. 1985, 57, 17.

2. Aleandri, L. E.; McCarley, R. E. presented at the 11th Midwest High Temperature Chemistry Conference, Ames, Iowa, June 1985.

3. Torardi, C. C.; McCarley, R. E. J. Solid State Chem. 1981, 37, 393.

4. Lii, K.-H. Ph.D. Dissertation, Iowa State University, Ames, Iowa, 1985, Section 1.

5. Torardi, C. C.; Calabrese, J. C. Inorg. Chem. 1984, 23, 3281.

6. Torardi, C. C.; McCarley, R. E. J. Am. Chem. Soc. 1979, 101, 3963.

7. Lii, K.-H. Ph.D. Dissertation, Iowa State University, Ames, Iowa, 1985, Section 2.

8. Torardi, C. C. Ph.D. Dissertaion, Iowa State University Ames, Iowa, 1981.

9. On one of the axial oscillation pictures there was one very weak spot at 1/2 r.l.u. (reciprocal lattice unit) between h0ℓ and h1ℓ layer lines. Another photograph was taken on the same crystal but at a different spindle angle. The weak spot was not observed but there seemed a very faint streak at the position of h,1/2,ℓ.

10. Clark, C. M.; Smith, D. K.; Johnson, G. J. "A Fortran IV Program for Calculating X-Ray Powder Diffractions Patterns-Version 5", Department of Geosciences, Pennsylvania State University, University Park, PA, 1973.

11. Jacobson, R. A. J. Appl. Crystallogr. 1976, 9, 115.

12. Karcher, B. A. Ph.D. Dissertation, Iowa State University, Ames, Iowa, 1981.

13. Hanson, H. P.; Herman, F.; Lea, J. D.; Skillman, S. Acta Crystallogr. 1964, 17, 1040.

14. Templeton, D. H. In "International Tables for X-Ray Crystallography", 1st ed.; Macgillavry, C. H. and Rieck, G. D., Eds.; Kynoch Press: Birmingham, England, 1962; Vol. III, page 215.

15. Rohrbaugh, W. J.; Jacobson, R. A. Inorg. Chem. 1974, 13, 2535.

16. Richardson, J. W. Jr. Ph.D. Dissertation, Iowa State University, Ames, Iowa, 1984.

17. Brown, I. D.; Wu, K. K. Acta Crystallogr. 1976, B32, 1957.

18. Betteridge, P. W.; Cheetham, A. K.; Howard, J. A. K.; Jakubicki, G.; McCarroll, W. H. Inorg. Chem. 1984, 23, 737.

SECTION 4. SYNTHESES, CRYSTAL STRUCTURES, AND PROPERTIES OF $^{o}M_{x}{}^{o}M'_{1-x-y}{}^{o}Mo_{y}{}^{t}M_{1}Mo_{4}O_{7}$ COMPOUNDS (^{o}M = Fe, Zn; $^{o}M'$ = Al, Sc, Ti, Cr; ^{t}M = Fe, Zn). COMPOUNDS CONTAINING CLOSEST-PACKING OF MOLYBDENUM METAL CLUSTER CHAINS WITH THE TERNARY OR QUATERNARY METAL CATIONS AT THE OCTAHEDRAL (^{o}M) OR TETRAHEDRAL (^{t}M) SITES IN THE NARROW CHANNELS CREATED BY THE INFINITE CHAINS

INTRODUCTION

Parallel chains consisting of trans edge-linked M_6X_{12} octahedra have been the dominant structure feature of the highly reduced ternary molybdenum oxide phases discovered so far. The structure types of these oxides are determined by how the cluster chains are arranged in the lattice. One may visualize the infinite chain as a rectangular column of which the shortest dimension corresponds to the Mo(waist)-Mo(waist) distance perpendicular to the chain direction. Accordingly, the $NaMo_4O_6$ structure is shown in Fig. 4.1a. The interchain oxygen atoms are located in the narrow channels between two neighboring columns. Square tunnels surrounded by four columns are created in the structure. The driving force directing the mode of stacking of the columns in the crystal might be largely determined by the nature of the ternary metal cations. However, for a binary phase the structure type is governed by how they share the nonmetal atoms. Er_4I_5 (1) presents a good illustrative example for our purpose. The mode of column stacking in Er_4I_5 is depicted in Fig. 4.1b. Columns are aligned in parallel and they are linked by square-planar nonmetal atoms to form layers. Layers are connected by sharing the nonmetal atoms which belong to neighboring columns. The columns in one layer can not be right on top of those in the neighboring layers. However, other possible arrangements have been observed if ternary metal cations are

introduced into the lattice. For example, in Sc_5Cl_8 (= $ScCl_2^+Sc_4Cl_6^-$) (2) a scandium atom behaves as a ternary metal cation in the lattice and a rather different structure type is created. In this section, a new structure type in reduced ternary molybdenum oxide systems, as shown in Fig. 4.1c., will be presented.

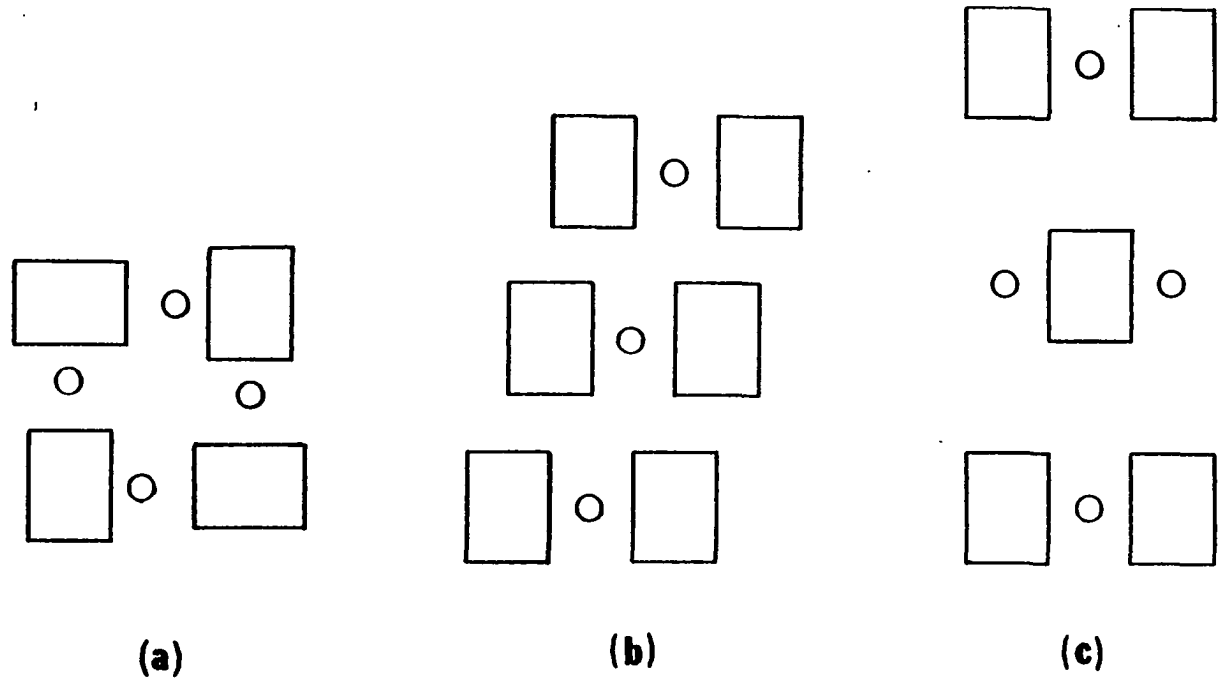

Fig. 4.1. Three different structure types: (a) $NaMo_4O_6$, (b) Er_4I_5, and (c) $Sc_{0.75}Zn_{1.25}Mo_4O_7$. The rectangles represent the molybdenum-oxide chains running perpendicular to this plane. The circles represent the oxygen atoms shared by neighboring chains

EXPERIMENTAL AND RESULTS

Materials

The starting materials used were Fisher Certified A.C.S. ZnO, TiO_2, and Al_2O_3, Aldrich Mo powder (99.99%), Thermo-Electron Mo tubing (99.97%), Alfa Sc_2O_3 (99.99%), and Y_2O_3 (99.99%), Baker Fe_2O_3 (99.2%), and MoO_3 (99.9%). Cr_2O_3 was prepared by heating CrO_3 (Fisher Certified A.C.S.).

Syntheses and Analyses

$\underline{Fe}_{1.89}\underline{Mo}_{4.11}\underline{O}_7$

In an attempt to prepare $FeMo_2O_4$, the following reaction was conducted:

$$Fe_2O_3 + 7/3\ Mo + 5/3\ MoO_3 \xrightarrow[1500C,\ 48\ hrs]{Mo\ tube} \text{products}$$

The reaction products contained black octahedral crystals, black truncated dipyramidal crystals, and gray ellipsoidal solid. The ellipsoidal solid was so hard that it was not ground into powder for x-ray powder diffraction measurements. An octahedral crystal which was indexed on a four-circle diffractometer had cubic symmetry and the cell constants expected for a spinel structure. This interesting compound will be further discussed in SECTION VI of this thesis. The film work on the truncated dipyramidal crystals indicated that

they had the $Sc_{0.75}Zn_{1.25}Mo_4O_7$ structure type (3). Therefore, another reaction was performed at a lower temperature (1400°C) for 3.5 days. A pressed pellet, was used in this reaction. There were numerous small black truncated dipyramidal crystals in the product. Some purple-black solid (MoO_2) was found on the Mo cap. On the edge of the pressed pellet there was a little seemingly grey solid which was scraped off the pellet before an x-ray powder was taken. An x-ray powder pattern of the black product showed that MoO_2, $Fe_2Mo_3O_8$, and Fe_2MoO_4 were absent and that there was probably very little Mo metal. The observed powder pattern was compared with a calculated powder pattern which was based upon the $Sc_{0.75}Zn_{1.25}Mo_4O_7$ structure type. They were in good agreement both in the peak positions and the relative intensities. Electronmicroscope pictures of this product showed that there was only one kind of crystal, which exhibited much more rounded edges compared with those obtained at 1500°C. The microprobe analyses on 15 different crystals gave quite consistent results, but the Mo to Fe mole ratio was 2.18(4). The black product was also qualitatively analyzed by the method of emission spectroscopy. The analyses were obtained for 39 elements, most of which were heavier than Fe. Two of these elements (Mg and Mn) were found to be about 0.01 wt. % and ca. 0.1 wt. %, respectively, five of them were found to be present in trace (< 0.02%) or faint trace (<0.005%) amount, and 32 of them were not detected. This sample was sent to Dr. William Reiff at Northeastern

University for magnetic susceptibility and Mossbauer spectroscopy measurements (vide infra). An x-ray pure product could also be obtained from a reaction mixture of Fe_2O_3, MoO_3, and Mo in 3: 4: 8 mole ratio (i.e., aiming at $Fe_2Mo_4O_7$) in a Mo container at 1300°C for 3 days. The wall of the molybdenum tube seemed to be coated with some material. Even though the stoichiometry of the reactants was a little off, no impurities were detected in the x-ray powder patterns.

$\underline{Sc}_{0.5}\underline{Fe}_{1.5}\underline{Mo}_4\underline{O}_7$

The synthesis of "$ScFeMo_4O_7$" was attempted by heating in an evacuated, sealed Mo tube an intimate mixture of reactants according to the following equation:

$$Sc_2O_3 + Fe_2O_3 + 8/3\ MoO_3 + 16/3\ Mo \text{ -------> } 2\ \text{"}ScFeMo_4O_7\text{"}$$

The sample was heated at 1495°C for 2 days. The products contained black, truncated dipyramidal crystals which gave an x-ray powder pattern of the $Sc_{0.75}Zn_{1.25}Mo_4O_7$ structure type. The microprobe analyses on eleven crystals resulted in the atom ratio Sc/Fe = 0.52(1)/1.50(5). Subsequently, a reaction to prepare pure $Sc_{0.5}Fe_{1.5}Mo_4O_7$ was conducted. The appropriate quantities of reactants were mixed, pressed into a pellet and heated in a Mo tube at 1450°C for 2 days. An x-ray powder pattern of the product indicated that there was a small amount of molybdenum metal and that all other diffraction lines could be indexed on the basis of an orthorhombic unit

cell similar to that found for $Sc_{0.75}Zn_{1.25}Mo_4O_7$. This sample was also sent to Dr. William Reiff for Mossbauer spectroscopy measurements.

$Al_{0.41}Fe_{1.51}Mo_{4.08}O_7$

Owing to the discovery of $Sc_{0.5}Fe_{1.5}Mo_4O_7$, the following reaction was carried out to prepare $Al_{0.5}Fe_{1.5}Mo_4O_7$.

$$Al_2O_3 + 3\ Fe_2O_3 + 16/3\ MoO_3 + 32/3\ Mo \text{ -----} > 4\ Al_{0.5}Fe_{1.5}Mo_4O_7$$

The reactants were pelletized and heated in a Mo tube at 1450°C for 2 days. The products also contained many truncated dipyramidal crystals. A Guinier powder pattern of the bulk product did not reveal any diffraction lines of MoO_2, α-Al_2O_3, or Fe_2O_3, but lines of Mo indicated the presence of some Mo-metal. After subtraction of the lines of Mo, all other lines could be indexed based on the $Sc_{0.75}Zn_{1.25}Mo_4O_7$ structure. The sample was sent to Dr. Reiff for Mossbauer spectrum measurement. Some crystals were analyzed by electronmicroprobe method. At first, the crystals were mounted on Cu tape with adhesive. While collecting data, instabilities in operating conditions were observed and the image exhibited charging phenomona with accompanying movement of the crystals. The results were much too variable. Also, a Cu fluorescent peak was observed. Therefore, two crystals were transferred onto a carbon substrate and analyzed under the same operating conditions. The above problems no longer

existed and the results should be much more reliable. The analytical results, listed in Table 4.1, gave the following formula: $Al_{0.41}Fe_{1.51}Mo_{4.08}O_7$.

$\underline{Al}_{0.5}\underline{Zn}_{1.4}\underline{Mo}_{4.1}\underline{O}_7$

The chemistry of scandium is more like aluminum than its homologues yttrium and lanthanum. Therefore, Al_2O_3 was used instead of Sc_2O_3 according to the following equation to prepare "$Al_{0.75}Zn_{1.25}Mo_4O_7$".

$$3/2\ Al_2O_3 + 5\ ZnO + 37/6\ MoO_3 + 59/6\ Mo \xrightarrow[1450C,\ 2\ days]{Mo\ tube} products$$

In the reaction product, there were numerous small, black needles and some colorless solid. Most of the diffraction peaks on the x-ray powder pattern could be indexed based on the $Sc_{0.75}Zn_{1.25}Mo_4O_7$ structure. So, this aluminum-containing compound had a different habit from other isostructural compounds. Some of the black needles grew on the wall of the molybdenum tube. The film work on crystals selected from either the wall or the bulk product showed that they were isomorphous and their unit cell parameters were indistinguishable. The film work also indicated that the needle direction corresponded to the a axis and was perpendicular to the cluster chain direction. This surprising result was later confirmed by indexing on a four-circle diffractometer. A single crystal from the wall was selected for x-ray intensity data collection because of its bigger

Table 4.1. Microprobe analytical results for AlFeMoO crystals

specimen	exptl. (wt. %)		
	Al	Fe	Mo
crystal 1 - pt. 1	1.8	14.0	65.3
pt. 2	1.8	13.6	65.4
pt. 3	1.7	14.1	64.5
crystal 2 - pt. 1	1.8	13.8	63.9
pt. 2	1.8	13.7	63.8
pt. 3	1.9	14.2	64.2
average	1.8	13.9	64.4

crystal size. A few truncated dipyramidal crystals were also found on the wall of the Mo tube. However, they have a different crystal structure which will be discussed in SECTION V of this thesis. Some needle-like crystals were selected from the wall and the bulk product for electronmicroprobe analyses. Accuracy of data from crystals taken from the wall was suspect since beam charging of crystals existed. The electrical properties of the wall crystals seemed different from the bulk crystals. The analytical results for the bulk crystals are tabulated in Table 4.2.

The analytical results for most crystals were not satisfactory because of the small size, orientation, and charging effect. Therefore, only data for the larger crystals 1 and 2 from the bulk product were taken into consideration and the averaged results gave the following formula: $Al_{0.5}Zn_{1.4}Mo_{4.1}O_7$.

The following reaction was then carried out to prepare pure $Al_{0.5}Zn_{1.4}Mo_{4.1}O_7$.

$$1/2\ Al_2O_3 + 2.8\ ZnO + 3.233\ MoO_3 + 4.97\ Mo \longrightarrow Al_{0.5}Zn_{1.4}Mo_{4.1}O_7$$

The reactants were mixed, pelletized, sealed in a molybdenum tube, and then fired at 1450°C for 47 hrs. The black, crystalline product was ground into powder and it's x-ray powder pattern indicated that MoO_2, and ZnO were absent, but a little Mo metal, α-Al_2O_3, and $ZnMo_8O_{10}$ (see SECTION V of this thesis) were present. All other lines ranging from $2\theta = 10^o$

Table 4.2. Microprobe analytical results for AlZnMoO crystals from bulk product[a]

no.	exptl. (wt. %)			mole ratio		
	Al	Zn	Mo	Al/Zn/Mo	Mo/(Al+Zn)	X[b]
1	2.2	15.2	64.7	.082/.233/.674	2.14	0.089
2	2.2	14.8	64.2	.082/.226/.669	2.17	0.107
3	1.9	14.7	65.5	.070/.225/.683	2.32	
4	2.1	12.8	63.6	.078/.196/.663	2.42	
5	2.0	14.4	61.4	.074/.220/.640	2.18	

[a]Crystals 1 and 2 were the largest and the electron beam was normal to them. These two crystals gave best results. Other results might show effects of orientation and/or crystal size.

[b]Mo/(Al+Zn) = (4 + X)/(2 - X).

to 85° could be indexed based on the $Sc_{0.75}Zn_{1.25}Mo_4O_7$ structure. The product prepared at lower temperature (1400°C) also contained the impurities.

$\underline{Ti_xFe_yMo_4O_7}$

The title compound was discovered by reacting a mixture of TiO_2, Fe_2O_3, MoO_3, and Mo in mole ratio of 2: 3: 5: 11 (i.e. aiming at $Ti_{0.5}Fe_{1.5}Mo_4O_7$) in a Mo tube at 1450°C for 42 hours. An x-ray powder pattern of the bulk product revealed the presence of Mo metal and the Fe-Mo-O spinel phase. A weak diffraction line at d = 3.379 A was not identified. All other peaks could be indexed on the basis of the $Sc_{0.75}Zn_{1.25}Mo_4O_7$ structure type. This phase must contain titanium because its unit cell parameters are significantly different from those of $Fe_{1.89}Mo_{4.11}O_7$. Its exact stoichiometry and x-ray single-crystal diffraction data have not been obtained yet. Further work on this system is worthwhile.

Others

The starting materials were intimately mixed and electron beam sealed in molybdenum crucibles. All of the reaction products were carefully evaluated using the Guinier camera. The reaction results are summarized in the following way: compound attempted to synthesize (reactants and reaction conditions), identified products.

$CrZnMo_4O_7$ (Cr_2O_3, ZnO, MoO_3, Mo, 1430°C, 70 hrs), Mo

metal, MoO_2, Cr(III) oxide (JCPDS 6-532), and $Cr_xZn_yMo_4O_7$. $FeZnMo_4O_7$ (Fe_2O_3, ZnO, MoO_3, Mo, 1450°C, 42 hrs), Mo metal, M-Mo-O spinel phases, and $M_2Mo_3O_8$ (M = Fe, Zn). $Al_{0.5}Co_{1.5}Mo_4O_7$ (α-Al_2O_3, CoO, MoO_3, Mo, 1400°C, 66 hrs), MoO_2, α-Al_2O_3, and Co_2Mo_3 alloy. $Y_{0.75}Zn_{1.25}Mo_4O_7$ (Y_2O_3, ZnO, MoO_3, Mo, 1430°C, 2d), Mo metal, Zn-Mo-O spinel phase, and a phase having the $Ca_{5.45}Mo_{18}O_{32}$ *structure type*.

The $Cr_xZn_yMo_4O_7$ phase is the first highly reduced quaternary molybdenum oxide containing the element chromium. More effort on this system is worthwhile.

Preliminary Film Work and X-ray Powder Diffraction

Before taking data on four-circle diffractometers, all crystals were checked by film work such as axial oscillation and Weissenberg photographs in order to confirm their good crystal quality and crystal symmetry. The FeMoO, ScFeMoO, AlFeMoO, and TiFeMoO crystals have the truncated dipyramidal habit, but the AlZnMoO crystal is needle-like. Unit cell constants obtained from the film work agree well with those from least-squares refinements of the peak positions in Guinier powder patterns. Cell constants from Guinier powder diffraction will be used in later calculations because of their high accuracy. Their x-ray powder patterns are tabulated in Tables 4.3, 4.4, 4.5, 4.6, and 4.7, respectively.

Table 4.3. X-ray powder diffraction data for $Fe_{1.89}Mo_{4.11}O_7$

d-spacings (Å) observed	d-spacings (Å) calculated	intensities	hkℓ
8.56(4)	8.518	s	002
5.65(2)	5.642	s	101
4.259(9)	4.259	vw	004
4.120(8)	4.118	vw	103
4.048(8)	4.047	vw	013
3.733(7)	3.732	vw	112
2.960(4)	2.960	m-s	105
2.937(4)	2.934	w	015
2.886(4)	2.885	m	020
2.823(4)	2.821	m	202
2.734(4)	2.734	w	022
2.624(3)	2.623	m	211
2.570(3)	2.569	m-s	121
2.448(3)	2.447	m-s	204
2.390(3)	2.389	s	024
2.364(3)	2.363	m-s	123
2.130(2)	2.130	m	008
2.076(2)	2.076	s	220
2.067(2)	2.066	w-m	125
2.058(2)	2.059	w-m	206
2.024(2)	2.024	m	026
2.017(2)	2.017	m	222
1.881(2)	1.881	vw	303
1.804(1)	1.805	w	109
1.798(1)	1.799	vw	019
1.791(1)	1.790	vw	132
1.735(1)	1.734	vw	208
1.721(1)	1.720	w	305
1.704(1)	1.704	w	0010
1.632(1)	1.632	w	321
1.611(1)	1.610	vw	231
1.556(1)	1.556	vw	233
1.530(1)	1.530	w	129
1.495(1)	1.495	w	400
1.487(1)	1.487	s	228
1.4422(9)	1.443	m-s	040
1.4224(9)	1.422	vw	042
1.3978(8)	1.398	vw	141
1.3169(7)	1.317	w	2210
1.2967(7)	1.297	w	145
1.2826(7)	1.282	vw	2012
1.2740(7)	1.274	vw	0212
1.2669(7)	1.267	w	424
1.2428(6)	1.243	w-m	244
1.2395(6)	1.239	w	329

Table 4.4. X-ray powder diffraction data for $Sc_{0.5}Fe_{1.5}Mo_4O_7$

d-spacings (A) observed	d-spacings (A) calculated	intensities	hkℓ
8.60(2)	8.5595	s	002
5.696(9)	5.6829	s	101
4.279(5)	4.2798	vw	004
4.144(5)	4.1429	vw	103
4.060(5)	4.0568	vw	013
3.745(4)	3.7463	vw	112
2.976(2)	2.9767	m-s	105
2.941(2)	2.9443	w	015
2.881(2)	2.8843	m	020
2.841(2)	2.8414	m	202
2.733(2)	2.7333	w	022
2.638(2)	2.6382	m	211
2.572(2)	2.5720	m-s	121
2.464(2)	2.4633	m-s	204
2.392(2)	2.3918	s	024
2.366(2)	2.3671	m-s	123
2.139(1)	2.1399	m-s	008
2.083(1)	2.0833	s	220
2.071(1)	2.0714	m	125
2.029(1)	2.0284	m	026
2.023(1)	2.0242	m	222
1.894(1)	1.8943	vw	303
1:8136(9)	1.8138	w	109
1.8059(9)	1.8064	vw	019
1.7906(8)	1.7913	vw	132
1.7818(8)	1.7819	vw	127
1.7442(8)	1.7445	vw	208
1.7319(8)	1.7322	w-m	305
1.7118(8)	1.7119	w	0010
1.6399(7)	1.6405	w	321
1.6130(7)	1.6136	vw	231
1.5828(6)	1.5834	vw	323
1.5590(6)	1.5591	vw	233
1.5355(6)	1.5355	w	129
1.5062(6)	1.5061	w	400
1.4928(6)	1.4927	m-s	228
1.4421(5)	1.4422	m-s	040
1.4221(5)	1.4221	vw	042
1.3980(5)	1.3978	vw	141
1.3230(4)	1.3226	w	2210
1.2981(4)	1.2978	w	145

Table 4.5. X-ray powder diffraction data for $Al_{0.41}Fe_{1.51}Mo_{4.08}O_7$

d-spacings (A) observed	d-spacings (A) calculated	intensities	hkℓ
8.45(2)	8.439	s	002
5.648(7)	5.646	s	101
4.221(4)	4.220	vw	004
4.101(4)	4.101	w	103
4.028(4)	4.023	vw	013
3.723(3)	3.724	vw	112
2.958(2)	2.959	vw	114
2.939(2)	2.941	s	105
2.910(2)	2.912	w	015
2.878(2)	2.877	w-m	020
2.823(2)	2.823	m-s	202
2.722(2)	2.723	w-m	022
2.624(2)	2.624	m	211
2.565(1)	2.564	s	121
2.444(1)	2.443	s	204
2.403(1)	2.403	vw	213
2.378(1)	2.377	s	024
2.355(1)	2.355	s	123
2.327(1)	2.329	vw	116
2.110(1)	2.110	m-s	008
2.0760(9)	2.075	s	220
2.0563(9)	2.057	w-m	125
2.0510(9)	2.051	w-m	206
2.0154(9)	2.015	m	026
2.0108(9)	2.011	w-m	222
1.8820(8)	1.882	w	303
1.7892(7)	1.790	w	109
1.7242(6)	1.725	vw	208
1.7187(6)	1.719	w-m	305
1.6874(6)	1.688	w	0010
1.6331(6)	1.633	w	321
1.5522(5)	1.553	vw	233
1.5198(5)	1.520	w	129
1.4981(4)	1.498	m	400
1.4800(4)	1.479	s	228
1.4388(4)	1.439	m	040
1.4182(4)	1.418	vw	042
1.3936(4)	1.394	w	141
1.3092(3)	1.309	w	2210
1.2925(3)	1.292	w	145

Table 4.6. X-ray powder diffraction data for $Al_{0.5}Zn_{1.4}Mo_{4.1}O_7$

d-spacings (A) observed	d-spacings (A) calculated	intensities	hkℓ
8.42(2)A	8.382	s	002
5.629(8)	5.620	s	101
4.193(4)	4.191	vw	004
4.084(4)	4.078	vw	103
3.717(3)	3.715	vw	112
2.948(2)	2.947	w	114
2.922(2)	2.923	s	105
2.897(2)	2.898	vw	015
2.883(2)	2.881	w	020
2.811(2)	2.810	m-s	202
2.725(2)	2.725	vw	022
2.616(2)	2.616	m	211
2.565(2)	2.564	m	121
2.430(1)	2.430	s	204
2.393(1)	2.394	vw	213
2.375(1)	2.374	s	024
2.353(1)	2.353	m-s	123
2.316(1)	2.317	vw	116
2.095(1)	2.096	m-s	008
2.073(1)	2.072	s	220
2.052(1)	2.052	w-m	125
2.038(1)	2.039	w-m	206
2.0120(9)	2.012	m	222
2.0052(9)	2.006	w-m	026
1.8729(8)	1.873	vw	303
1.7774(7)	1.778	w	109
1.7719(7)	1.772	vw	019
1.7145(7)	1.715	vw	208
1.7098(7)	1.710	w-m	305
1.6764(6)	1.676	w	0010
1.6288(6)	1.629	w-m	321
1.6073(6)	1.607	vw	231
1.5523(5)	1.551	vw	233
1.5128(5)	1.513	w	129
1.4914(5)	1.491	m-s	400
1.4735(5)	1.473	s	228
1.4409(4)	1.441	m	040
1.3960(4)	1.395	vw	141
1.3030(3)	1.303	vw	2210

Table 4.7. X-ray powder diffraction data for $Ti_xFe_yMo_4O_7$

d-spacings (Å) observed	d-spacings (Å) calculated	intensities	hkℓ
8.53(2)	8.480	s	002
5.679(8)	5.667	s	101
4.244(4)	4.240	vw	004
4.124(4)	4.119	w	103
4.040(4)	4.039	vw	013
3.740(3)	3.737	vw	112
2.969(2)	2.971	vw	114
2.955(2)	2.954	s	105
2.926(2)	2.925	w	015
2.885(2)	2.886	w	020
2.833(2)	2.833	m	202
2.731(2)	2.732	w	022
2.633(2)	2.634	w-m	211
2.573(2)	2.572	s	121
2.453(1)	2.452	s	204
2.387(1)	2.386	s	024
2.363(1)	2.363	s	123
2.120(1)	2.120	m-s	008
2.081(1)	2.082	s	220
2.064(1)	2.064	w	125
2.0588(9)	2.059	w	206
2.0198(9)	2.022	s	222, 026
1.7981(7)	1.798	w	109
1.7918(7)	1.791	vw	019
1.7255(6)	1.725	w-m	305
1.6958(6)	1.696	w	0010
1.5261(5)	1.526	vw	129
1.5032(5)	1.503	w	400
1.4858(4)	1.485	s	228
1.4432(4)	1.443	m-s	040

Diffraction data for all of these crystals could be well indexed on the basis of Imma space group. Cu Kα1 (λ = 1.54056 A) was used to calculate observed d-spacings. Unit cell parameters which were obtained from Guinier powder patterns are listed in Table 4.8 in the order of decreasing c constants.

X-ray Single Crystal Diffraction Studies of $Fe_{1.89}Mo_{4.11}O_7$, $Sc_{0.5}Fe_{1.5}Mo_4O_7$, $Al_{0.51}Fe_{1.41}Mo_{4.08}O_7$, and $Al_{0.5}Zn_{1.4}Mo_{4.1}O_7$.

Each crystal was mounted on the tip of a glass fiber with a small amount of epoxy resin. Determination of preliminary unit cell parameters and orientation matrix were carried out as described in SECTION 1 of this thesis. Crystal data and details of the parameters associated with data collection for all compounds except $Al_{0.5}Zn_{1.4}Mo_{4.1}O_7$ are given in Tables 4.9, 4.10, and 4.11, respectively. Intensity data were corrected for absorption via an empirical absorption correction technique based on ϕ scans (ϕ 0-360^o every 10^o) of suitable reflections with χ values close to 90^o (5), and for Lorentz and polarization effects. Each intensity data set showed mmm Laue symmetry and the extinction conditions h + k + ℓ = 2n for hkℓ reflections, and h = 2n for hk0 reflections. The possible space group thus was Imma or its noncentrosymmetric subgroup I2mb. Since the N(z) distribution of the entire data set (excluding systematic absences) favors

a centrosymmetric space group, Imma was selected. Neutral-atom scattering factors (6) were used, and the real and imaginary corrections for anomalous dispersion (7) were applied to all atoms heavier than oxygen atom. In the initial stage of least-squares refinement (8) isotropic temperature factors were assumed, and all the positional parameters for Mo atoms were assigned initial values equal to those for $Sc_{0.75}Zn_{1.25}Mo_4O_7$. The remaining atoms were located from successive ΔF maps (9). All of the crystals except the AlZnMoO crystal showed strong secondary extinction effects. The isotropic secondary extinction coefficient was included as a variable in the least-squares refinements (10) for each of the other three compounds. The refinement results for each crystal will be discussed separately in the following paragraphs.

$\underline{Fe}_{1.89}\underline{Mo}_{4.11}\underline{O}_7$

The data set was averaged in mmm symmetry without any reflections being eliminated. The good agreement between symmetry-equivalent reflections is reflected in the low agreement factor (R_{int} = 3.3% based on F_o). The structure was initially refined on the basis of $Fe_2Mo_4O_7$. However, the microprobe analyses suggested that either some of the iron sites were vacant or some iron atoms (Fe2) in octahedrally coordinated sites were replaced by molybdenum atoms. Thus, a few cycles of least-squares refinements were made while

varying the temperature factors and multipliers of both kinds of Fe atoms. The results showed that the multiplier for the tetrahedrally coordinated iron (Fe1) remained the same while that for octahedral iron increased from 0.250 to 0.270(3), and the R factor lowered 0.2%. These refinement results could be explained by the partial replacement of octahedral Fe by Mo atoms. The number of unique molybdenum atoms (y) per formula unit may be estimated in the following way: $y = [4 \times 26 \times (0.270 - 0.250)/(42 - 26)] = 0.13$, where 26 and 42 are the atomic numbers for Fe and Mo, respectively. This estimation is in good agreement with the result from microprobe analysis ($(4 + y)/(2 - y) = 2.18$, $y = 0.11$). In the subsequent refinements, an unique Mo atom was included and its multiplier was equal to 0.25 - X, where X was the multiplier for the octahedral Fe atom. A final full-matrix least-squares refinement using anisotropic thermal parameters for all atoms led to R = 3.0%, R_w = 4.5%, and the following stoichiometry $Fe_{1.84(2)}Mo_{4.16(2)}O_7$, which agrees well with the microprobe analysis. The value for the secondary extinction parameter (k) was 2.12×10^{-4}. A final difference map showed residual electron density of approximately $\leq |\pm 0.4e/A^3|$ near heavy atoms. The largest residual density ($0.8e/A^3$) was located at (0.5, 0.37, 0.59). Final atomic parameters are listed in Tables 4.12, and 4.13. Selected bond distances and angles are given in Table 4.14.

$Sc_{0.5}Fe_{1.5}Mo_4O_7$

Six reflections having $|I_o - I_{av}| > 6.0\sigma(I)$ were eliminated in the data averaging. The agreement factor (R_{int}) which was based on F_o was 4.6%. The structure was refined on the basis of $^{o}Sc_{0.5}{}^{o}Fe_{0.5}{}^{t}Fe_{1.0}Mo_4O_7$. The temperature factors of Sc were set equal to those of octahedral Fe. The structure was refined anisotropically for all atoms. Inspection of a final difference Fourier map showed no peaks greater than 0.6 e/A^3. The residual electron density at the Sc/Fe position is $\leq$ 0.4 e/A^3. Full-matrix least-squares refinement resulted in R = 3.2%, R_w = 4.6%. The secondary extinction parameter was 1.09×10^{-4}. The final positional and thermal parameters appear in Tables 4.15 and 4.16. Selected bond distances and angles are listed in Table 4.17.

$Al_{0.41}Fe_{1.51}Mo_{4.08}O_7$

The agreement between the symmetry-equivalent reflections for this data set R_{int} ($= \Sigma|F_o - \langle F_o \rangle|/\Sigma F_o$) was 0.0193. The structure was initially refined by assuming that the aluminum ions were at octahedral sites. Thus, the multiplier for the octahedral iron (Fe2) was varied in the least-squares refinement. Refinement using this model resulted in R = 3.1%, R_w = 4.2% using anisotropical temperature factors for all atoms except O1. (O1 gave negative temperature factors when it was anisotropically varied.) The multiplier for Fe2 reduced to 0.235(3) suggesting that some aluminum atoms were at

octahedral sites. However, the number of electrons at the octahedral sites (26 x 0.235 ÷ 0.25 = 24.44) was significantly higher than that based on the microprobe analysis (13 x 0.041 + 26 x 0.51 + 42 x 0.08 = 21.95). Consequently, the multipliers for both of the iron atoms were varied independently. This refinement reduced the value of R to 2.9% with the multipliers 0.229(3) and 0.231(3) for Fe1 and Fe2, respectively. The total number of electrons at both tetrahedral and octahedral sites were equal to 47.84 which was in excellent agreement with the microprobe analysis results (13 x 0.41 + 26 x 1.51 + 42 x 0.08 = 47.95). This surprising result indicated that aluminum atoms were at both octahedral and tetrahedral sites. The value for the secondary extinction coefficient was 3.14×10^{-4}. A difference Fourier map calculated at this stage revealed no peaks greater than 0.4 e/A^3. The residual electron densities near Fe1 and Fe2 sites were from -0.3 to 0.2 e/A^3 and from -0.2 to 0 e/A^3, respectively. The final positional and thermal parameters are given in Tables 4.18 and 4.19. Selected bond distances and angles are tabulated in Table 4.20.

$\underline{Al}_{0.5}\underline{Zn}_{1.4}\underline{Mo}_{4.1}\underline{O}_7$

The crystal has presented some problems in the structure refinement. The needle-like crystal (0.36 x 0.02 x 0.02 mm) for intensity data collection was scraped off the wall of the reaction container. The intensity data were collected on

SYNTEX $P2_1$ diffractometer with Zr-filtered Mo radiation. The other crystallographic data are: θ-2θ scan; scan range: symmetrical, $[1.0 + \Delta(\alpha_2-\alpha_1)]^\circ$; reflections measured: hkl, $\bar{h}k\bar{l}$; max 2θ: 55°; T_{max}/T_{min} = 1.74; no significant variation in intensity for the standard reflection, R_{int}= 4.0%. However, only about 53% of the collected reflections had intensity greater than $2\sigma(I)$. The anisotropic least-square refinement always resulted in negative temperature factors for most of the atoms and relatively high R factor (6.3%) although the data set was corrected properly and weighted in different ways. In contrast to other $M_2Mo_4O_7$ crystals, the data set did not reveal secondary extinction effect. Nevertheless, the following refinement results are believed to be valid. An electron density map based on F_o using phases from molybdenum atoms indicated that the total number of electrons at the tetrahedral site is significantly higher compared to the octahedral site. An isotropic least-squares refinement varying the multipliers for two different zinc atoms showed that m(tetr) remained about the same but m(oct) fell to 0.19(1). Therefore, the aluminum atoms in $Al_{0.5}Zn_{1.4}Mo_{4.1}O_7$ occupy octahedral sites. The molybdenum metal cluster chain in this compound is much less distorted in comparison with its analogues. The alternate Mo(apex)-Mo(apex) bond distances are 2.95(1) and 2.82(1) A. Other bond distances and bond angles will not be listed for comparison because of the poor refinement results.

Table 4.8. Unit cell parameters of seven $M_xM_y'Mo_4O_7$ compounds

compounds	a (A)	b (A)	c (A)	volume (A^3)
$Sc_{0.5}Fe_{1.5}Mo_4O_7$	6.0245(8)	5.7686(4)	17.119(2)	595.0(1)
$Fe_{1.89}Mo_{4.11}O_7$	5.9793(5)	5.7704(4)	17.036(1)	587.80(8)
$Sc_{0.75}Zn_{1.25}Mo_4O_7$[a]	6.085(1)	5.764(1)	17.002(4)	596.3(2)
$Ti_xFe_yMo_4O_7$	6.0120(8)	5.7719(7)	16.961(2)	588.6(1)
$Al_{0.41}Fe_{1.51}Mo_{4.08}O_7$	5.991(1)	5.7545(8)	16.878(3)	581.3(2)
$Al_{0.5}Zn_{1.4}Mo_{4.1}O_7$	5.9652(6)	5.7623(6)	16.764(2)	576.2(1)
$Ti_{0.5}Zn_{1.5}Mo_4O_7$[a]	6.030(1)	5.782(1)	16.759(4)	584.4(2)

[a]The cell parameters are from reference 4.

Table 4.9. Crystallographic data for $Fe_{1.89}Mo_{4.11}O_7$

---

crystal system: orthorhombic
space group: Imma
a = 5.9793(5), b = 5.7704(4), c = 17.036(1) A
V = 587.80(8) A^3
z = 4
d(calcd) = 6.917 g/cm^3
crystal dimens: 0.20 x 0.07 x 0.04 mm^3
abs coeff: 129.9 cm^{-1}
reflns used for empirical absorption correction (hkℓ, 2Θ, T_{max}/T_{min}): 040, 28.49°, 1.32
diffractometer: AL[a]
radiation: Mo Kα (λ = 0.71034 A)
monochromator: graphite
scan type: ω-scan
automatic background detn, max scan half width: 0.5 degree
std reflns: 3 measured every 75 reflns; no significant variation in intensity.
reflns measd: hkℓ, $\bar{h}\bar{k}\ell$, $\bar{h}k\bar{\ell}$, $h\bar{k}\bar{\ell}$
max 2Θ: 55°
reflns collected: 1551 collected (symmetry extinct reflns not included), 1416 observed
no. of unique reflns with I > 3σ(I): 389
no. of parameters refined: 45
R = 3.0%[b]
R_w = 4.5%[c]
quality-of-fit indicator[d]: 1.625

---

[a]For details of the AL diffractometer, see reference 11.
[b]$R = \Sigma||F_o| - |F_c||/\Sigma|F_o|$.
[c]$R_w = [\Sigma w(|F_o|-|F_c|)^2/\Sigma w|F_o|^2]$; $w = 1/\sigma^2(|F_o|)$.
[d]Quality of fit = $[\Sigma w(|F_o|-|F_c|)^2/(N(observns)-N(parameters))]^{1/2}$.

Table 4.10. Crystallographic data for $Sc_{0.5}Fe_{1.5}Mo_4O_7$

---

crystal system: orthorhombic

space group: Imma

a = 6.0245(8), b = 5.7686(4), c = 17.119(2) A

V = 595.0(1) A^3

z = 4

d(calcd) = 6.723 g/cm^3

crystal dimens: 0.09 x 0.06 x 0.05 mm^3

abs coeff: 121.6 cm^{-1}

refln used for empirical absorption correction (hkℓ, 2Θ, T_{max}/T_{min}): 040, 28.48°, 1.47

diffractometer: DATEX[a]

radiation: Mo Kα (λ = 0.70966 A)

monochromator: graphite

scan type: ω-scan

scan half width: 0.6 degree

std reflns: 3 measured every 50 reflns; no significant variation in intensity.

reflns measd: hkℓ, $\bar{h}\bar{k}\ell$

max 2Θ: 50°

reflns collected: 716 collected (symmetry extinct reflns not included), 601 observed ($I > 3\sigma(I)$)

no. of unique reflns with $I > 3\sigma(I)$: 274

no. of parameters refined: 44

R = 3.2%[b]

R_w = 4.6%[c]

quality-of-fit indicator[d]: 1.86

---

[a] See reference 12.

[b] $R = \Sigma||F_o| - |F_c||/\Sigma|F_o|$.

[c] $R_w = [\Sigma w(|F_o|-|F_c|)^2/\Sigma w|F_o|^2]^{1/2}$; $w = 1/\sigma^2(|F_o|)$.

[d] Quality of fit = $[\Sigma w(|F_o|-|F_c|)^2/(N(observns)-N(parameters))]^{1/2}$.

Table 4.11. Crystallographic data for $Al_{0.41}Fe_{1.51}Mo_{4.08}O_7$

---

crystal system: orthorhombic
space group: Imma
a = 5.991(1), b = 5.7545(8), c = 16.878(3) A
V = 581.9(2) A^3
z = 4
d(calcd) = 6.838 g/cm^3
crystal dimens: 0.10 x 0.04 x 0.04 mm^3
abs coeff: 121.5
refln used for empirical absorption correction (hkℓ, 2Θ, T_{max}/T_{min}): 501, 34.54, 1.74
diffractometer: DATEX[a]
radiation: Mo Kα (λ = 0.70966 A)
monochromator: graphite
scan type: ω-scan
scan half width: 0.6 degree
std reflns: 3 measured every 50 reflns; no significant variation in intensity.
reflns measd: hkℓ, $\bar{h}\bar{k}\ell$
max 2Θ: 50°
reflns collected: 675 collected (symmetry extinct reflns not included), 597 observed ($I > 1.5\sigma(I)$)
no. of unique reflns with $I > 1.5\sigma(I)$: 285
no. of parameters refined: 43
R = 2.9%[b]
R_w = 3.8%[c]
quality-of-fit indicator[d]: 2.230

---

[a] See reference 12.

[b] $R = \Sigma||F_o| - |F_c||/\Sigma|F_o|$.

[c] $R_w = [\Sigma w(|F_o|-|F_c|)^2/\Sigma w|F_o|^2]$; $w = 1/\sigma^2(|F_o|)$.

[d] Quality of fit = $[\Sigma w(|F_o|-|F_c|)^2/(N(observns)-N(parameters))]^{1/2}$.

Table 4.12. Positional parameters for $Fe_{1.89}Mo_{4.11}O_7$

atom	position	multiplier	x	y	z	B(A^2)[a]
Mo1	8h	.5	.0	.0102(1)	.11084(5)	0.95
Mo2	8i	.5	.2320(1)	.25	-.00294(4)	0.66
Fe1	4e	.25	.5	.25	.1948(1)	1.33
Fe2	4d	.210(4)	.75	.25	.75	1.19
Mo	4d	.040(4)	.75	.25	.75	1.19
O1	4b	.25	.5	.5	.0	0.88
O2	8i	.5	.253(1)	.25	.1174(4)	1.1
O3	8i	.5	.239(1)	.25	.8776(4)	0.90
O4	8h	.5	.0	.512(1)	.2350(5)	1.2

[a]The isotropic equivalent thermal parameter is defined as $B = 4/3\,[a^2\beta_{11} + b^2\beta_{22} + c^2\beta_{33} + 2ab(\cos\gamma)\beta_{12} + 2ac(\cos\beta)\beta_{13} + 2bc(\cos\alpha)\beta_{23}]$.

Table 4.13. Thermal parameters for $Fe_{1.89}Mo_{4.11}O_7$

atoms	B11	B22	B33	B12	B13	B23
Mo1	0.56(4)	1.63(4)	0.66(4)	0.0	0.0	0.03(2)
Mo2	0.73(4)	0.57(4)	0.70(4)	0.0	0.02(2)	0.0
Fe1	1.30(7)	1.43(7)	1.28(7)	0.0	0.0	0.0
Fe2/Mo	1.56(8)	0.95(7)	1.07(7)	0.0	-0.33(5)	0.0
O1	1.0(4)	0.6(4)	0.9(4)	0.0	0.0	0.0(3)
O2	2.2(3)	0.5(2)	0.6(2)	0.0	-0.1(2)	0.0
O3	1.1(3)	0.7(2)	0.8(3)	0.0	0.3(2)	0.0
O4	1.3(3)	1.4(3)	0.8(2)	0.0	0.0	0.1(2)

Table 4.14. Bond distances and angles for $Fe_{1.89}Mo_{4.11}O_7$

distances (A)		angles (degree)[a]	
Mo1-Mo1	2.771(1)	Mo2a-Mo1-Mo2b	60.46(4)
	3.006(2)	Mo2a-Mo1-Mo2c	63.24(2)
Mo1-Mo2	2.7524(9)	Mo2c-Mo1-Mo2d	60.63(4)
	2.7597(9)	Mo1-Mo2a-Mo2b	59.77(2)
Mo2-Mo2	2.8900(4)[b]	Mo1-Mo2c-Mo2d	59.68(2)
	2.778(2)[c]	Mo1-Mo2a-Mo2c	58.26(2)
Fe1-Fe1	3.536(2)	Mo1-Mo2c-Mo2a	58.50(2)
Fe1-Fe2	3.3864(6)	Mo1-Mo1-Mo2a	59.89(2)
Fe2-Fe2	2.9935(5)	Mo1-Mo1-Mo2c	56.88(2)
Mo1-O2	2.058(5)	O3-Mo1-O3	86.56(30)
Mo1-O3	2.084(5)	O2-Mo1-O2	94.98(30)
Mo1-O4	2.122(8)	O4-Mo1-O2	89.37(24)
Mo2-O1	2.1593(6)	O4-Mo1-O3	81.99(23)
MO2-O2	2.058(7)	O4-Mo1-Mo1	93.57(18)
Mo2-O3	2.039(6)		86.43(18)
Fe1-O2	1.980(7) (2X)	Mo2a-O1-Mo2c	84.03(3)
Fe1-O4	1.931(7) (2X)	Mo1-O2-Mo2a	84.37(25)
Fe2-O3	2.177(6) (2X)	Mo1-O3-Mo2c	83.82(23)
Fe2-O4	2.047(4) (4X)	O3-Fe2-O3	180.0
		O3-Fe2-O4	98.58(28)
			81.42(28)
		O4-Fe2-O4	84.18(27)
			95.82(27)
		O4-Fe1-O4	103.30(48)
		O2-Fe1-O2	96.30(45)
		O2-Fe1-O4	114.45(18)

[a]The atom labels refer to Fig. 4.2.

[b]It is parallel to the c axis.

[c]It is perpendicular to the c axis.

Table 4.15. Positional parameters for $Sc_{0.5}Fe_{1.5}Mo_4O_7$

atom	position	multiplier	x	y	z	B(A^2)[a]
Mo1	8h	.5	.0	.0125(1)	.11026(6)	0.68
Mo2	8i	.5	.2317(1)	.25	-.00339(6)	0.44
Fe1	4e	.25	.5	.25	.1931(2)	0.88
Fe2	4d	.125	.75	.25	.75	0.73
Sc	4d	.125	.75	.25	.75	0.73
O1	4b	.25	.5	.5	.0	0.99
O2	8i	.5	.252(2)	.25	.1162(5)	0.64
O3	8i	.5	.236(1)	.25	.8766(5)	0.69
O4	8h	.5	.0	.508(1)	.2336(6)	0.74

[a]The isotropic equivalent thermal parameter is defined as $B = 4/3\ [a^2\beta_{11} + b^2\beta_{22} + c^2\beta_{33} + 2ab(\cos\gamma)\beta_{12} + 2ac(\cos\beta)\beta_{13} + 2bc(\cos\alpha)\beta_{23}]$.

Table 4.16. Thermal parameters for $Sc_{0.5}Fe_{1.5}Mo_4O_7$

atoms	B11	B22	B33	B12	B13	B23
Mo1	0.19(6)	1.31(6)	0.55(5)	0.0	0.0	0.03(3)
Mo2	0.33(6)	0.40(5)	0.58(5)	0.0	-0.07(3)	0.0
Fe1	0.9(1)	0.7(1)	1.0(1)	0.0	0.0	0.0
Fe2/Sc	0.9(1)	0.4(1)	0.8(1)	0.0	-0.1(1)	0.0
O1	0.1(5)	2.1(7)	0.7(4)	0.0	0.0	-0.7(4)
O2	0.6(4)	0.3(3)	1.0(4)	0.0	0.2(3)	0.0
O3	0.6(4)	0.4(3)	1.1(4)	0.0	-0.3(3)	0.0
O4	1.0(4)	0.9(4)	0.3(3)	0.0	0.0	0.2(3)

Table 4.17. Bond distances and angles for $Sc_{0.5}Fe_{1.5}Mo_4O_7$

distances (A)		angles (degree)[a]	
Mo1-Mo1	2.740(2)	Mo2a-Mo1-Mo2b	60.80(5)
	3.028(2)	Mo2a-Mo1-Mo2c	63.14(2)
Mo1-Mo2	2.755(1)	Mo2c-Mo1-Mo2d	60.90(4)
	2.759(1)	Mo1-Mo2a-Mo2b	59.60(2)
Mo2-Mo2	2.8866(2)[b]	Mo1-Mo2c-Mo2d	59.55(2)
	2.792(2)[c]	Mo1-Mo2a-Mo2c	58.36(3)
Fe1-Fe1	3.588(3)	Mo1-Mo2c-Mo2a	58.50(3)
Fe1-Fe2	3.3967(8)	Mo1-Mo1-Mo2a	60.22(2)
Fe2-Fe2	3.0122(4)	Mo1-Mo1-Mo2c	56.66(2)
Mo1-O2	2.047(6)	O3-Mo1-O3	85.75(35)
Mo1-O3	2.088(6)	O2-Mo1-O2	95.66(33)
Mo1-O4	2.11(1)	O4-Mo1-O2	89.32(30)
Mo2-O1	2.1668(7)	O4-Mo1-O3	81.51(29)
Mo2-O2	2.051(9)	O4-Mo1-Mo1	93.25(21)
Mo2-O3	2.053(9)		86.75(21)
Fe1-O2	1.992(9) (2X)	Mo2a-O1-Mo2c	83.54(3)
Fe1-O4	1.949(9) (2X)	Mo1-O2-Mo2a	84.64(31)
Fe2-O3	2.171(9) (2X)	Mo1-O3-Mo2c	83.40(28)
Fe2-O4	2.072(6) (4X)	O3-Fe2-O3	180.0
		O3-Fe2-O4	99.46(34)
			80.54(34)
		O4-Fe2-O4	84.61(33)
			95.39(33)
		O4-Fe1-O4	99.72(58)
		O2-Fe1-O2	97.33(53)
		O2-Fe1-O4	115.20(21)

[a]The atom labels refer to Fig. 4.2.

[b]It is parallel to the c axis.

[c]It is perpendicular to the c axis.

Table 4.18. Positional parameters for $Al_{0.41}Fe_{1.51}Mo_{4.08}O_7$

atom	position	multiplier	x	y	z	B(A^2)[a]
Mo1	8h	.5	.0	.0130(2)	.11195(5)	0.46
Mo2	8i	.5	.2318(1)	.25	-.00312(5)	0.27
Fe1 site	4e	.229(3)	.5	.25	.1958(1)	0.68
Fe2 site	4d	.231(3)	.75	.25	.75	0.62
O1	4b	.25	.5	.5	.0	0.45
O2	8i	.5	.255(1)	.25	.1180(5)	0.68
O3	8i	.5	.235(1)	.25	.8768(5)	0.61
O4	8h	.5	.0	.517(1)	.2364(6)	1.12

[a]The isotropic equivalent thermal parameter is defined as $B = 4/3\,[a^2\beta_{11} + b^2\beta_{22} + c^2\beta_{33} + 2ab(\cos\gamma)\beta_{12} + 2ac(\cos\beta)\beta_{13} + 2bc(\cos\alpha)\beta_{23}]$.

Table 4.19. Thermal parameters for $Al_{0.41}Fe_{1.51}Mo_{4.08}O_7$

atoms	B11	B22	B33	B12	B13	B23
Mo1	0.12(5)	1.14(5)	0.14(4)	0.0	0.0	0.02(2)
Mo2	0.23(5)	0.36(5)	0.20(5)	0.0	-0.03(3)	0.0
Fe1 site	0.7(1)	0.8(1)	0.5(1)	0.0	0.0	0.0
Fe2 site	0.7(1)	0.7(1)	0.4(1)	0.0	-0.11(7)	0.0
O2	1.2(3)	0.3(3)	0.5(3)	0.0	-0.1(2)	0.0
O3	0.6(3)	0.5(3)	0.8(3)	0.0	0.0(2)	0.0
O4	2.1(4)	1.1(3)	0.2(3)	0.0	0.0	0.2(2)
O1	0.5(2)[a]					

[a] O1 was isotropically refined.

Table 4.20. Bond distances and angles for $Al_{0.41}Fe_{1.51}Mo_{4.08}O_7$

distances (A)		angles (degree)[a]	
Mo1-Mo1	2.727(2)	Mo2a-Mo1-Mo2b	60.68(4)
	3.027(2)	Mo2a-Mo1-Mo2c	63.07(2)
Mo1-Mo2	2.756(1)	Mo2c-Mo1-Mo2d	60.52(4)
	2.750(1)	Mo1-Mo2a-Mo2b	59.66(2)
Mo2-Mo2	2.8792(4)[b]	Mo1-Mo2c-Mo2d	59.74(2)
	2.778(2)[c]	Mo1-Mo2a-Mo2c	58.57(2)
Fe1-Fe1	3.511(2)	Mo1-Mo2c-Mo2a	58.36(2)
Fe1-Fe2	3.3704(7)	Mo1-Mo1-Mo2a	60.27(2)
Fe2-Fe2	2.9955(5)	Mo1-Mo1-Mo2c	56.68(2)
Mo1-O2	2.052(6)	O3-Mo1-O3	85.34(32)
Mo1-O3	2.075(5)	O2-Mo1-O2	96.42(30)
Mo1-O4	2.11(1)	O4-Mo1-O2	90.30(27)
Mo2-O1	2.1573(7)	O4-Mo1-O3	81.26(26)
MO2-O2	2.050(8)	O4-Mo1-Mo1	94.76(19)
Mo2-O3	2.027(8)		85.24(19)
Fe1-O2	1.967(8) (2X)	Mo2a-O1-Mo2c	83.72(3)
Fe1-O4	1.918(8) (2X)	Mo1-O2-Mo2a	84.19(28)
Fe2-O3	2.142(8) (2X)	Mo1-O3-Mo2c	84.40(26)
Fe2-O4	2.022(5) (4X)	O3-Fe2-O3	180.0
		O3-Fe2-O4	98.34(32)
			81.66(32)
		O4-Fe2-O4	82.93(30)
			97.07(30)
		O4-Fe1-O4	106.69(55)
		O2-Fe1-O2	96.33(49)
		O2-Fe1-O4	113.47(19)

[a]The atom labels refer to Fig. 4.2.

[b]It is parallel to the c axis.

[c]It is perpendicular to the c axis.

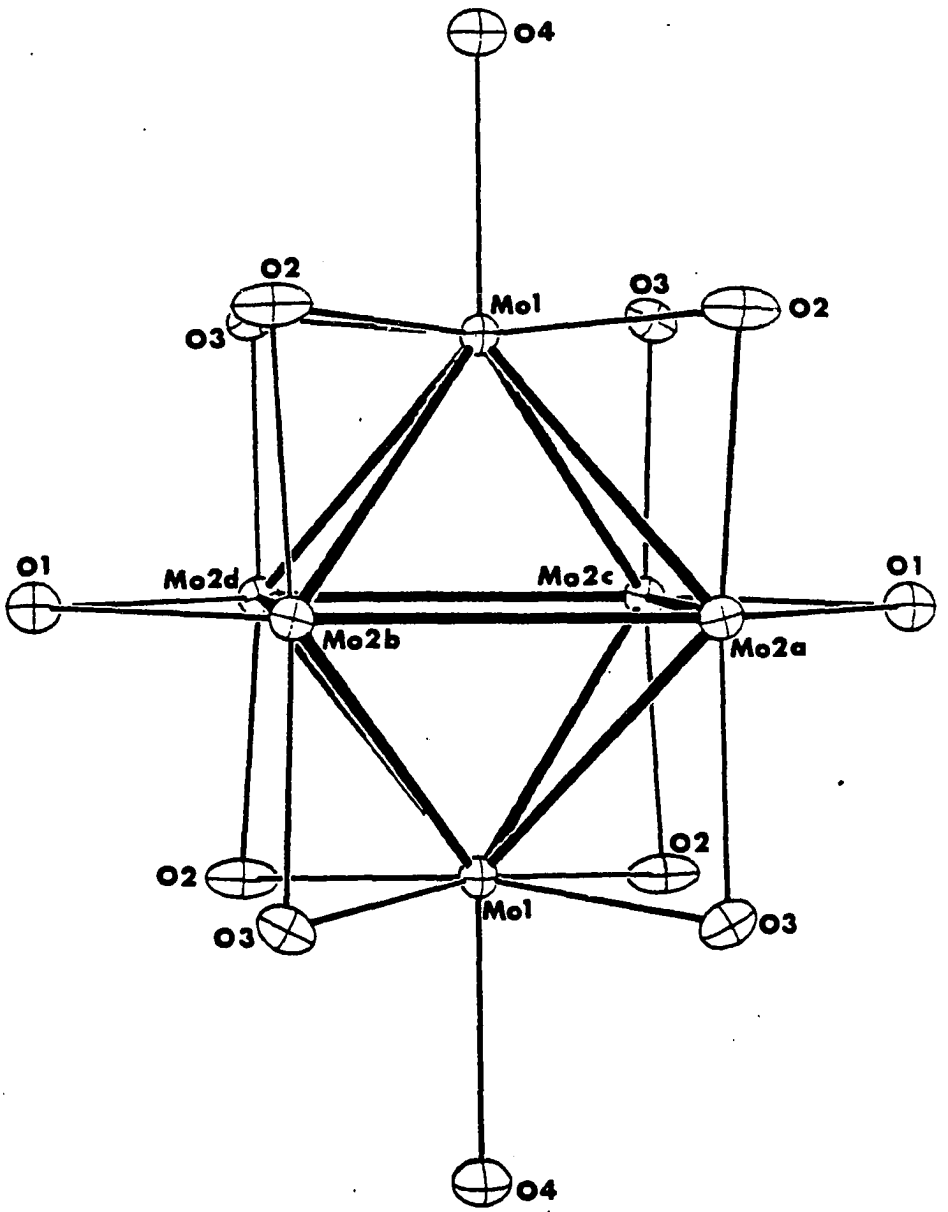

Fig. 4.2. A repeat unit of a molybdenum-oxide cluster chain in the $M_2Mo_4O_7$ structure

Magnetic Susceptibility and Mossbauer Spectroscopy Studies

$\underline{Fe}_{1.89}\underline{Mo}_{4.11}\underline{O}_7$

The sample was checked for purity by means of an x-ray powder pattern before being sent to Dr. William Reiff at Northeastern University for magnetic susceptibility and Mossbauer spectroscopy measurements. Magnetic susceptibilities were measured by the Faraday technique on 0.346 g powdered sample of $Fe_{1.89}Mo_{4.11}O_7$ in the temperature range from 300 to 51 K. Figure 4.3 shows a plot of inverse molar susceptibility (χ_M^{-1}) vs. temperature at H_o = 5.1 KG. The temperature variations of the molar susceptibilities at various applied magnetic fields are shown in Fig. 4.4. The material undergoes a very sharp magnetic transition at about 190 K. As expected for a magnetically condensed system, the susceptibility becomes field dependent below the Neel point.

The Mossbauer spectrum (Fig. 4.5) obtained at 300 K showed two broad peaks with shoulders. The solid line through the data points represent a best fit for three quadrupole doublets, corresponding to iron in three different sites. The relative areas of the three quadrupole doublets are 1.00: 0.78: 0.27. The Mossbauer parameters are listed in Table 4.21.

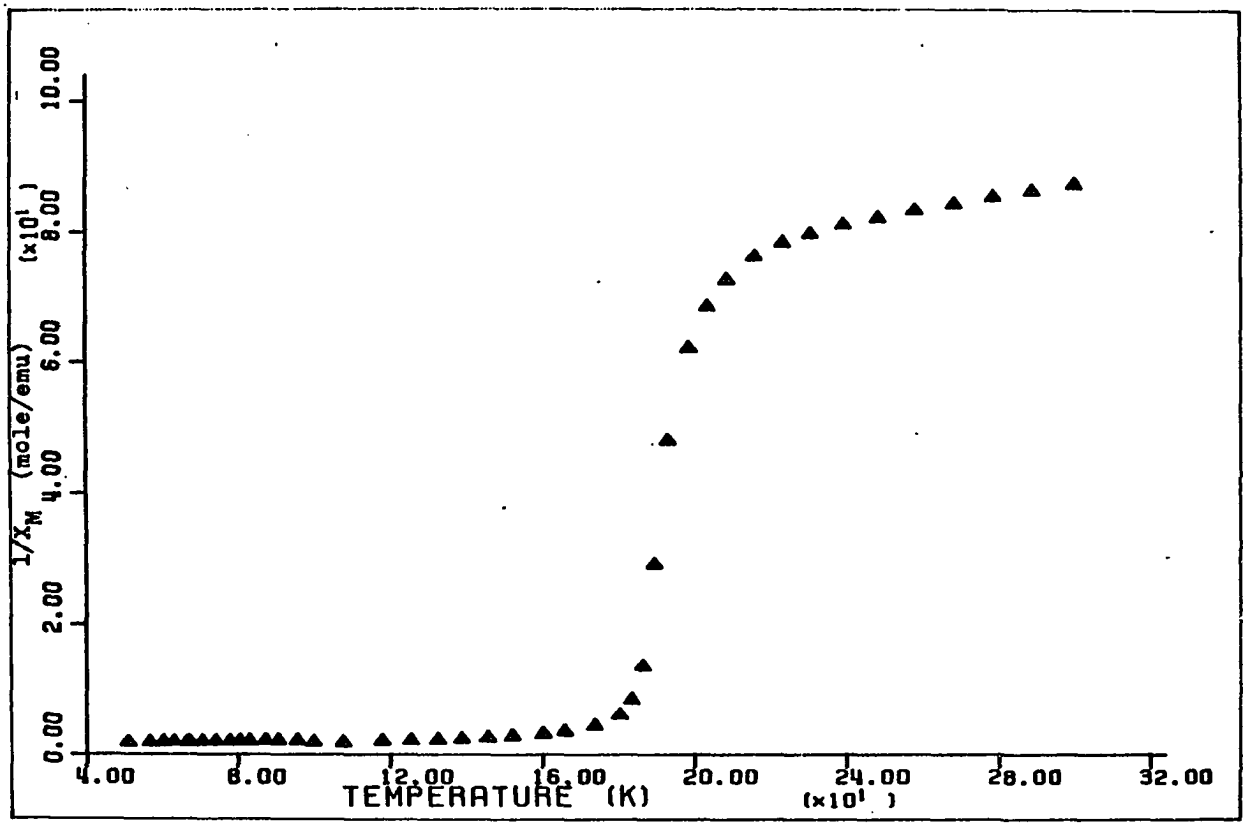

Fig. 4.3. A plot of the inverse molar magnetic susceptibility of $Fe_{1.89}Mo_{4.11}O_7$ powder as a function of temperature

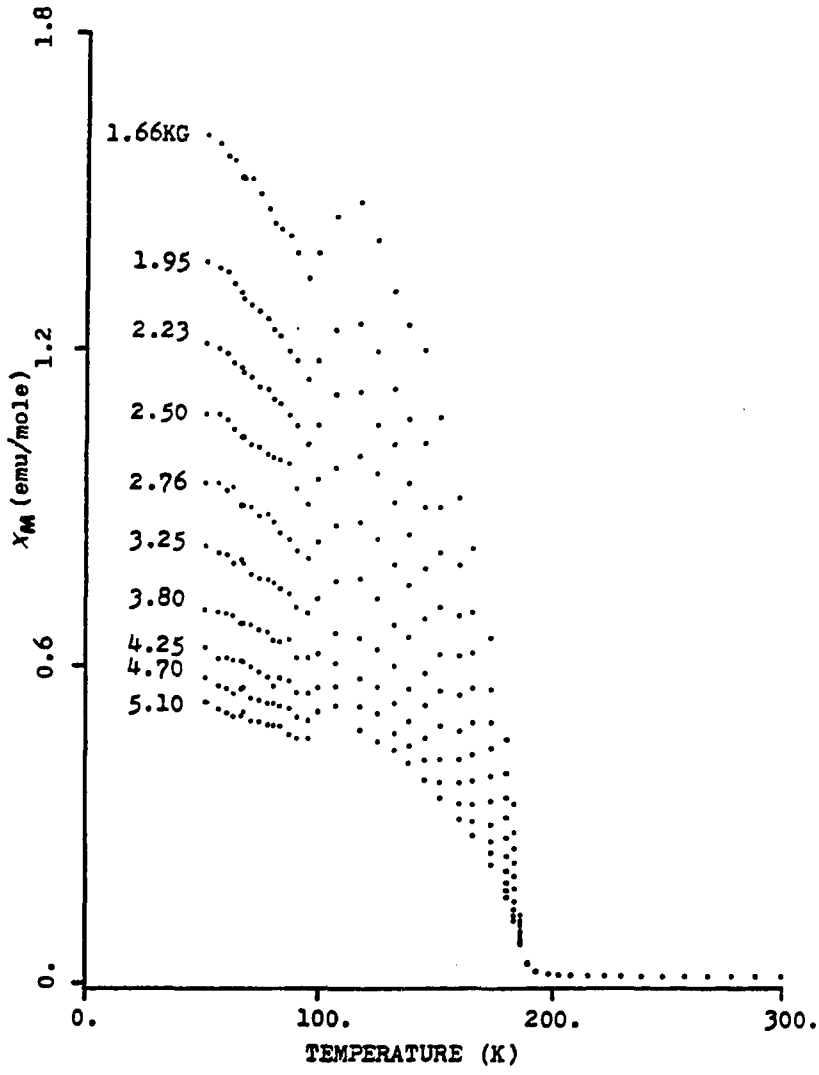

Fig. 4.4. Plots of the molar magnetic susceptibility of $Fe_{1.89}Mo_{4.11}O_7$ powder as a function of temperature at different applied magnetic fields

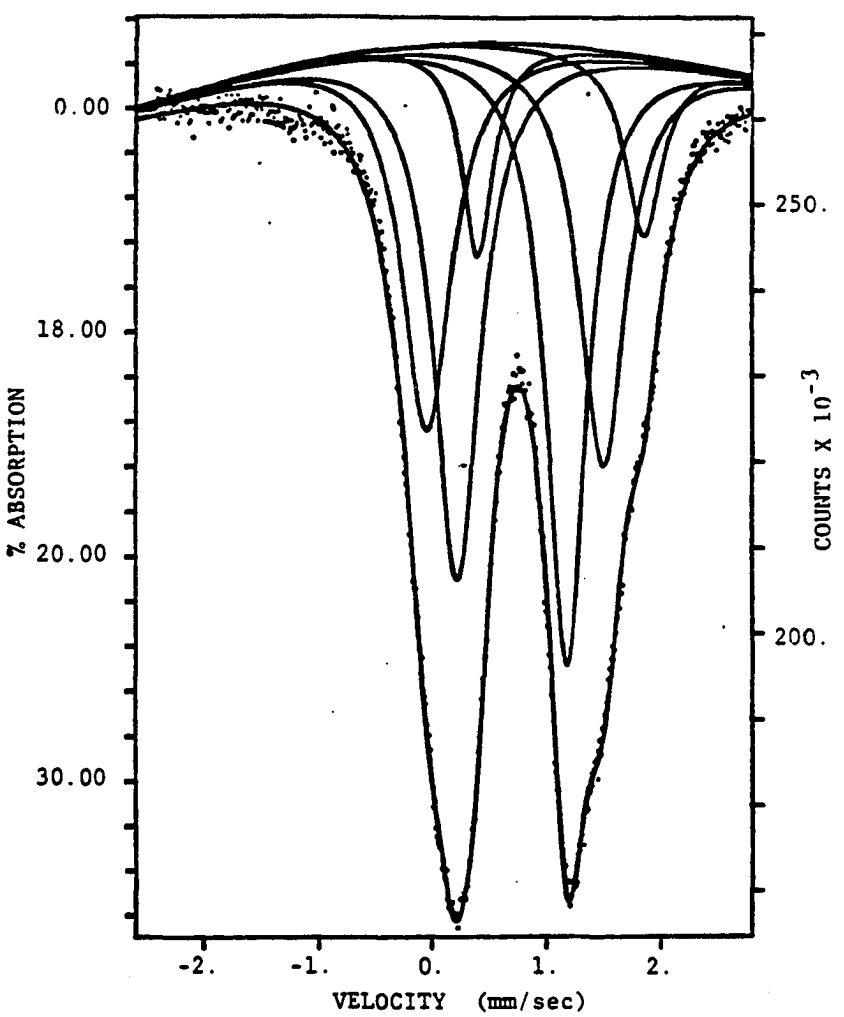

Fig. 4.5. Room-temperature Mossbauer spectrum for $Fe_{1.89}Mo_{4.11}O_7$. The spectrum can be best fit by three different iron sites as shown in the figure

Table 4.21. Mossbauer parameters for $Fe_{1.89}Mo_{4.11}O_7$ at 300 K

iron site	δ	Δ	relative area
1	0.701[a]	0.956[a]	1.00
2	0.728	1.538	0.78
3	1.129	1.452	0.27

[a]All values for isomer shifts (δ) and quadrupole splittings (Δ) are in mm/s, and isomer shifts are relative to natural iron foil.

$\underline{Sc}_{0.5}\underline{Fe}_{1.5}\underline{Mo}_4\underline{O}_7$ and $\underline{Al}_{0.41}\underline{Fe}_{1.51}\underline{Mo}_{4.08}\underline{O}_7$

Magnetic susceptibility data were obtained using a SQUID instrument from 380 K to 4 K on 90.6 mg of $Sc_{0.5}Fe_{1.5}Mo_4O_7$ powder and 71.9 mg of $Al_{0.41}Fe_{1.51}Mo_{4.08}O_7$ powder by Dr. R. N. Shelton. The signal in the low temperature range was so strong that relatively low magnetic fields had to be used in the measurement.

Figures 4.6 and 4.7 show the plots of χ_g vs. T and χ_g^{-1} vs. T at H_o = 2.0 KG for $Sc_{0.5}Fe_{1.5}Mo_4O_7$. There is a rapid increase in magnetic susceptibility such that χ_g^{-1} falls effectively to zero at about 110 K. Because the Neel point was a lot lower than that for $Fe_{1.89}Mo_{4.11}O_7$ and more data points were taken in the paramagnetic state, a least-squares fit to Curie-Weiss law in the temperature interval 270 - 380 K was performed. The calculation led to $\chi_M = 4.67/(T + 140)$. The effective magnetic moment, calculated from $\mu_{eff} = 2.828(C^{1/2})$ is 6.11 μ_B which is in very good agreement with the spin only value (6.00 μ_B) for noninteracting high-spin Fe^{2+}, that is $\mu_{eff} = [1.5 \times (\mu_{Fe^{2+}})^2]^{1/2}$.

The magnetic susceptibilities for $Al_{0.41}Fe_{1.51}Mo_{4.08}O_7$ were collected at H_o = 1.0 KG. It displayed a similar behavior as a function of temperature except that both the Neel temperature (80 K) and the overall moment in the ordered state were lower compared to $Sc_{0.5}Fe_{1.5}Mo_4O_7$. The data in the paramagnetic state gave the following results: $\chi_M = 5.99/(T + 344)$, and $\mu_{eff} = 6.92\ \mu_B$.

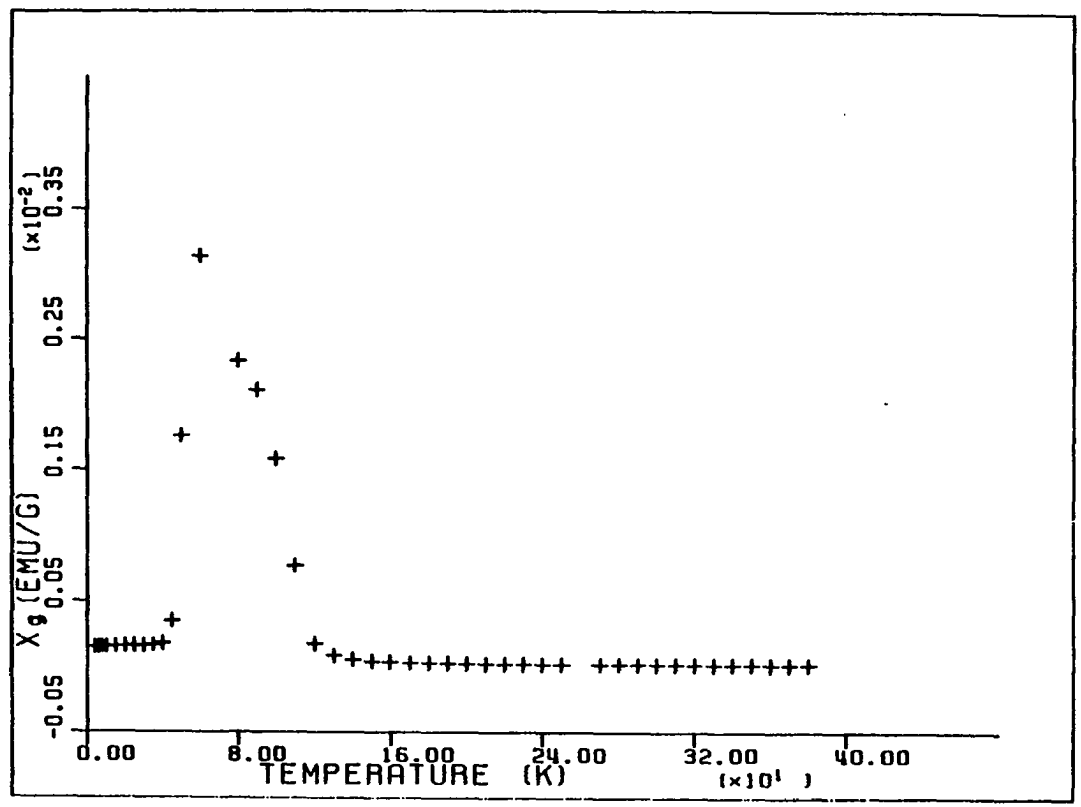

Fig. 4.6. A plot of the gram magnetic susceptibility of $Sc_{0.5}Fe_{1.5}Mo_4O_7$ powder as a function of temperature

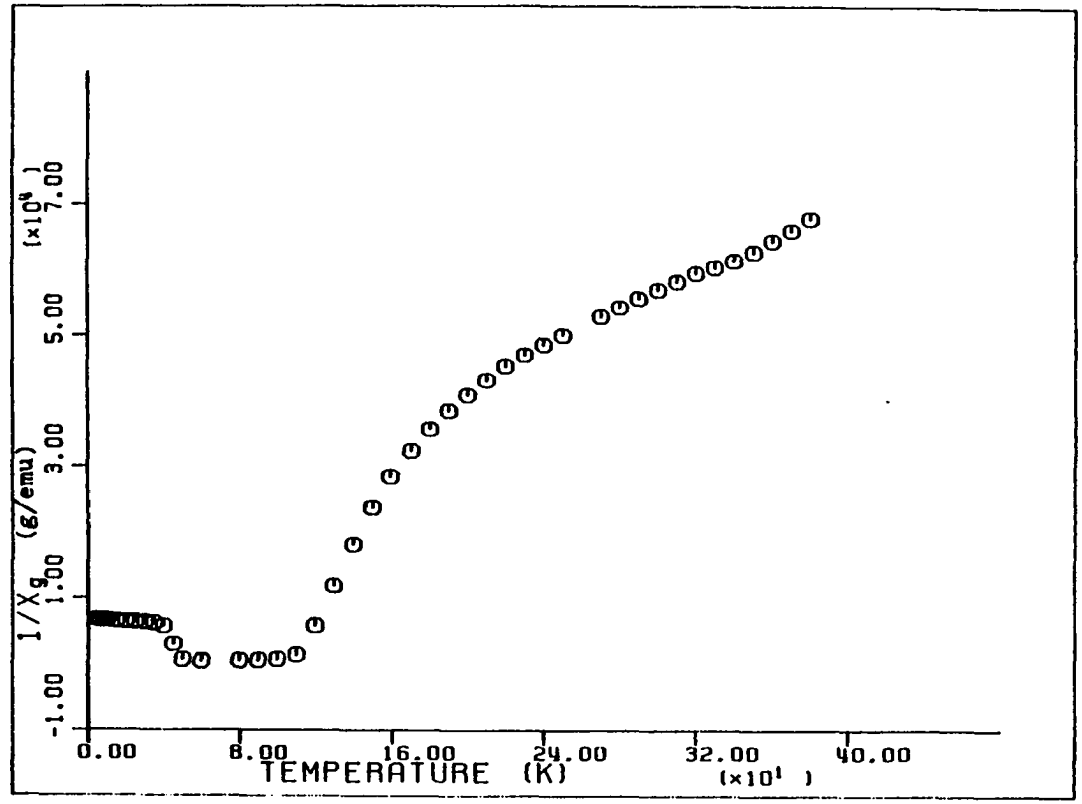

Fig. 4.7. A plot of the inverse gram magnetic susceptibility of $Sc_{0.5}Fe_{1.5}Mo_4O_7$ powder as a function of temperature

DESCRIPTION OF THE CRYSTAL STRUCTURES

Morphology of the Crystals

So far all of the $M_2Mo_4O_7$ phases except $Al_{0.5}Zn_{1.4}Mo_{4.1}O_7$ have similar habits. Some of the crystals in the reaction products were found to be well-formed. A drawing of a well-formed crystal is shown in Fig. 4.8. It is evident there are three mutually perpendicular mirror planes with three mutually orthogonal two-fold rotation axes along their lines of intersection. Three axes are also designated in the Figure. It is customary to orient an orthorhombic crystal so that its shortest axis is vertical (c axis) and the shorter of the two remaining axes runs from back to front and is the a axis. This simple convention is consistent with the results from single crystal x-ray diffraction experiments if the standard space group Imma is used. The appearance of the truncated dipyramidal crystal is a combination of the {101}, {011}, and {001} forms. The interfacial angles can be measured with an optical goniometer and hence the a:b:c ratio can be obtained. In these compounds, molybdenum octahedral clusters are fused on opposite edges to form infinite chains along the b direction. Some of the $Sc_{0.75}Zn_{1.25}Mo_4O_7$ crystals have a lot longer dimension along b so that resistivity measurement along the infinite chain direction becomes more likely.

As mentioned earlier, crystals of $Al_{0.5}Zn_{1.4}Mo_{4.1}O_7$ are

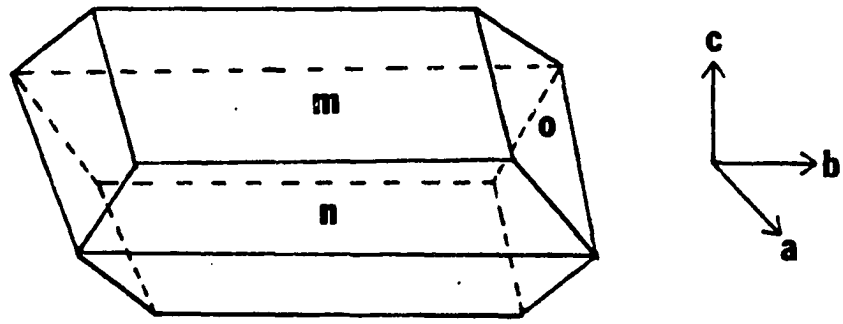

Fig. 4.8. A crystal of $Sc_{0.75}Zn_{1.25}Mo_4O_7$ of dipyramidal habit. It is a combination of the m{001}, n{101}, and o{011} orthorhombic forms

needle-like and their needle direction corresponds to the a axis. This is rather unusual among all the reduced ternary molybdenum oxides discovered so far. It is not obvious why the metal cluster chain grows perpendicular to the needle direction.

Crystal Structures

Figure 4.9 shows a view of the $M_2Mo_4O_7$ structure along the infinite chain direction. Within each infinite chain the sharing of M_6X_{12} cluster units is much like that found in $NaMo_4O_6$ except that the molybdenum metal cluster chain in $M_2Mo_4O_7$ is distorted (vide infra). Infinite chains are interlinked in the ab plane by Mo(waist)-O1-Mo(waist) bonding to form layers (Fig. 4.10). In the c direction, the layers are linked by Mo-O-M and Mo-O-M′ bonding. The structure can also be regarded as a closest-packing of the cluster chains with the ternary metal cations at the octahedral and tetrahedral sites created by the close packing.

These compounds have an ordered defect rock salt structure. The unit cell can be divided into eight layers which are perpendicular to the c axis of the $M_2Mo_4O_7$ structure and correspond to the {h00} planes of the sodium chloride structure. Four of the eight layers are shown in Fig. 4.11 and the other four layers can be easily generated by the I-centering operation. The unit cell and the z value for each

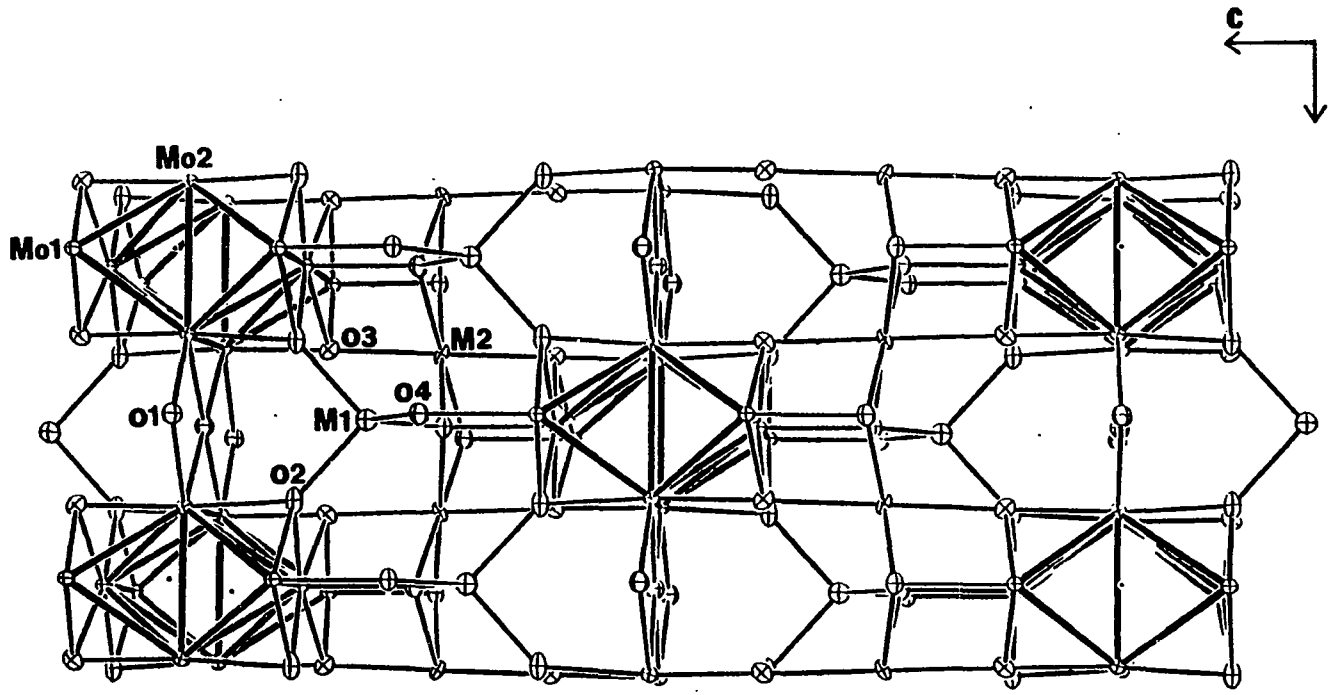

Fig. 4.9. A three-dimensional representation of the structure of $M_2Mo_4O_7$ as viewed down the b axis. The positions of tetrahedral and octahedral ternary metal cations are labelled with M1 and M2, respectively. The Mo-Mo bonds are represented by the thicker lines

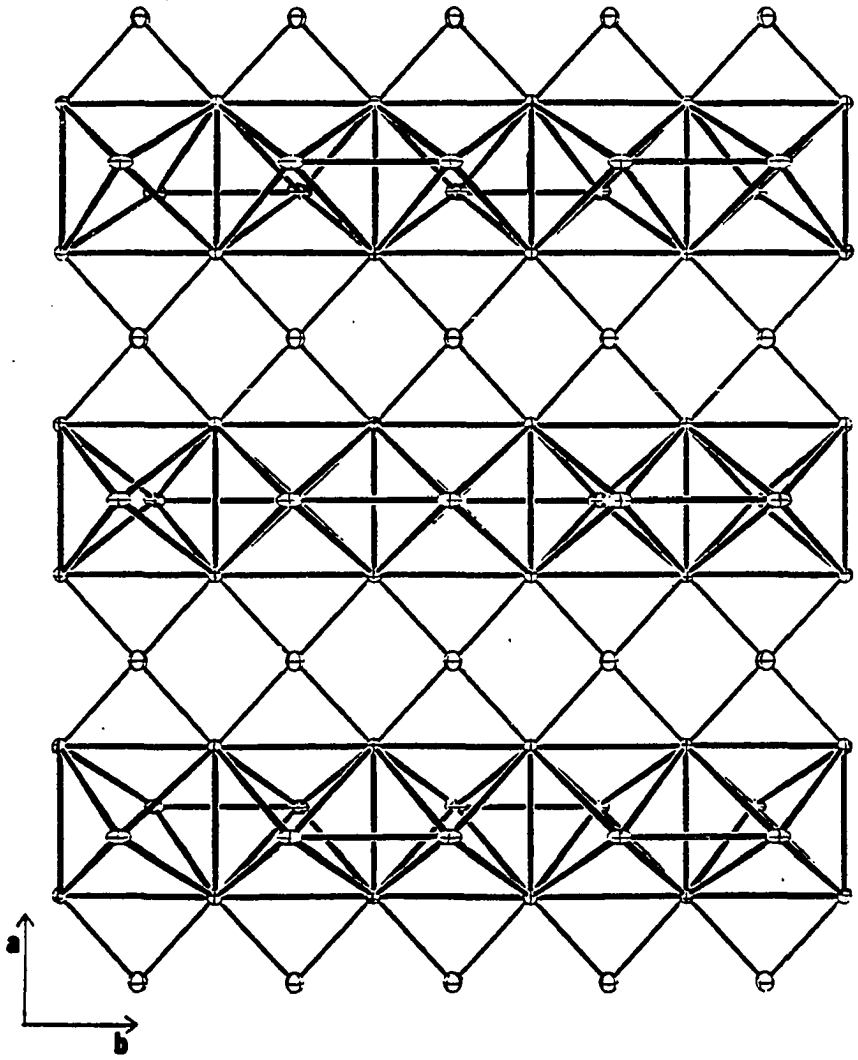

Fig. 4.10. A view of the infinite chains containing octahedral cluster units fused on opposite edges in the $M_2Mo_4O_7$ structure. Only the molybdenum atoms and the square-planar oxygen atoms are shown in the figure

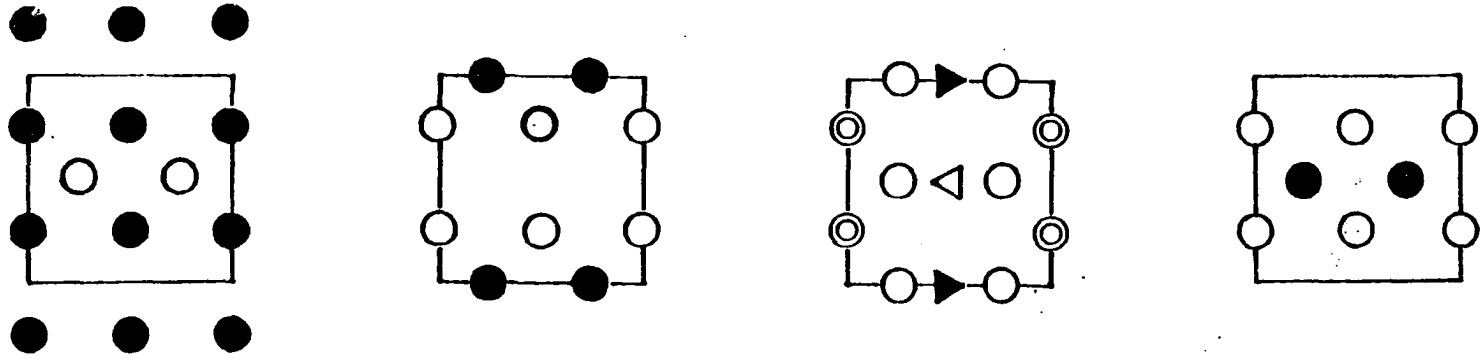

Fig. 4.11. The $M_2Mo_4O_7$ structure, projected on (001). The four diagrams show successive layers of the structure. The solid, double, and single circles represent molybdenum metal, octahedral ternary metal, and oxygen atoms, respectively. The solid and open triangles designate the tetrahedral ternary metal atom sites at c/16 above or below the third layer

layer are designated in the Figure. The solid, double, and single circles represent molybdenum metal, octahedral ternary metal, and oxygen atoms, respectively. The Mo-Mo bonds are not shown for clarity. The solid and open triangles designate the tetrahedral ternary metal atom sites at c/16 above or below the third layer. Only 1/8 of the tetrahedral sites are occupied by the ternary metal atoms. Each layer contains four oxygen and four molybdenum atoms if it is fully loaded. Two oxygen or two molybdenum sites are vacant in each layer in an ordered way such that the overall stoichiometry is $M_2Mo_4O_7$. Note that the octahedral ternary metal atoms form infinite chains which are perpendicular to the molybdenum metal cluster chains. The compounds crystallize in orthorhombic crystal system because of the basic difference between these two orthogonal chains. The structure may become tetragonal if the orthogonal chains are identical and distorted such that the repeat distances along a and b directions are equal. The structure may also be related to the spinel structure. In fact, the third layer in Fig. 4.11 is essentially identical to that in Fe_3O_4. The very interesting structural relationship will be further discussed in SECTION V of this thesis.

As shown in Fig. 4.12, both the apex and the waist molybdenum atoms reside on mirror planes. Each octahedral molybdenum metal cluster sits on an inversion center. The apical molybdenum atoms are not required to be evenly spaced. A b-glide plane rather than a mirror plane intersects the c

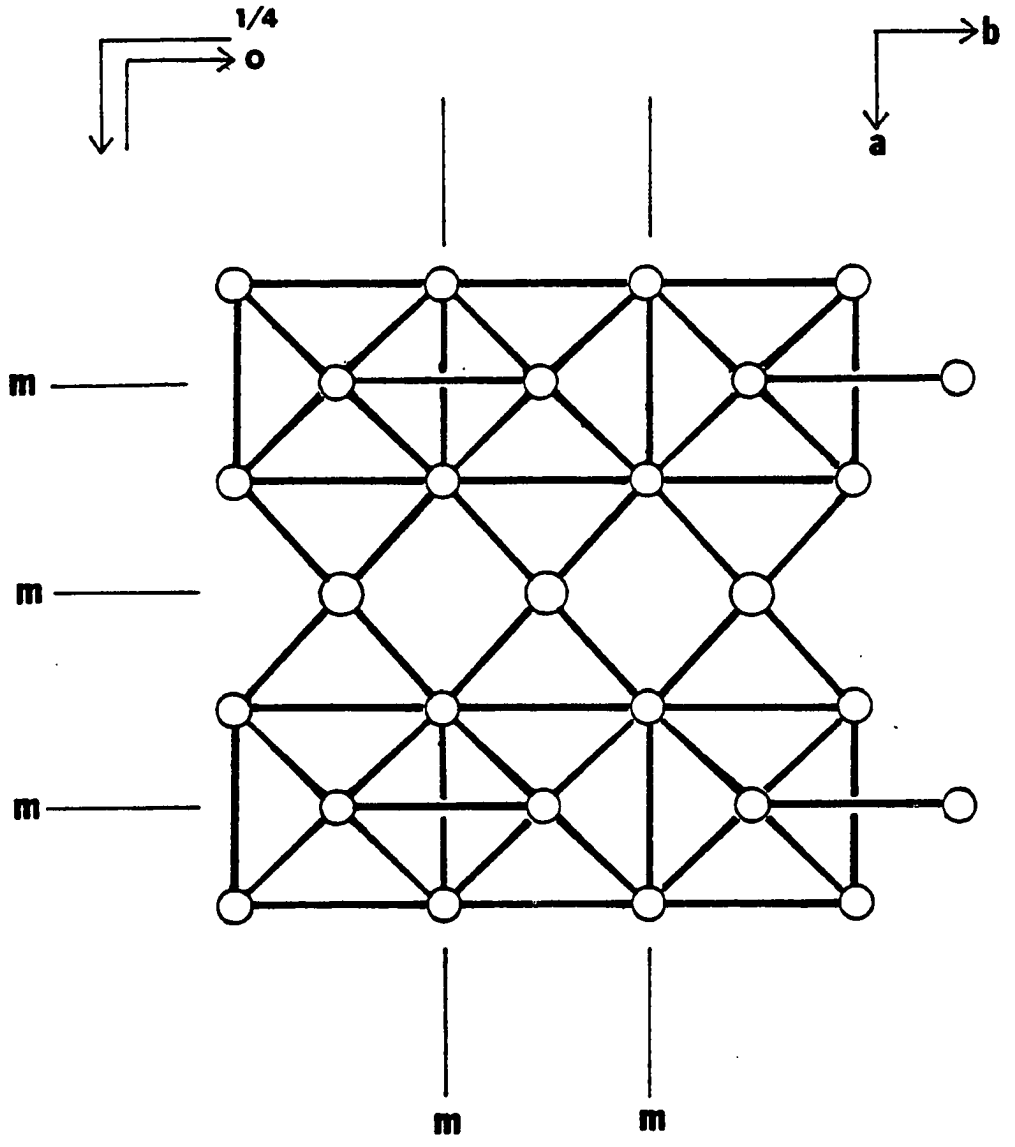

Fig. 4.12. The $M_2Mo_4O_7$ structure: projection of parts of structure on (001). Positions and directions of a few symmetry elements are designated

axis at z = 0 so that the basal planes of adjacent octahedra are slightly puckered and the short Mo(apex)-Mo(apex) bond distance is displaced to the opposite side of the next pair of octahedra. The octahdral iron atom is located on an inversion center, and the tetrahedral iron has a local symmetry of C_{2v}.

The Mo(apex)-Mo(waist) bond distances in the $M_2Mo_4O_7$ structures are generally shorter than the corresponding distances in $NaMo_4O_6$ (see Table 4.22). However, the Mo(waist)-Mo(waist) distances for bonds both along and perpendicular to the chain direction are longer compared to the sodium compound. The Mo(waist)-Mo(waist) distance perpendicular to the cluster chain for $Sc_{0.75}Zn_{1.25}Mo_4O_7$ is particularly long. Perhaps one of the most interesting features about the $M_2Mo_4O_7$ structures is the alternate short and long Mo(apex)-Mo(apex) distances. In Table 4.22, the Mo(apex)-Mo(apex) distances, Δ's, and ϕ's are also listed for comparison. Δ and ϕ represent differences between short and long distances and the dihedral angle between the basal planes of adjacent octahedra, respectively. $Sc_{0.75}Zn_{1.25}Mo_4O_7$ exhibited much larger distortions in comparison with the other five isomorphous compounds.

The four crystallographically different oxygen atoms may be classified into three distinct types according to their coordination geometries. Both O2 and O4 are pseudo-tetrahedral. Oxygen 2 is coordinated by three molybdenum atoms and one Fe1 atom, but O4 is surrounded by two Fe2, one

Table 4.22. Mo-Mo bond distances for six $M_2Mo_4O_7$ compounds[a]

compounds	Mo1-Mo2[b]	Mo2-Mo2[c]	Mo1-Mo1[d]	Δ[e]	ϕ[f]
$Al_{.5}Zn_{1.4}Mo_{4.1}O_7$	2.742 A	2.772 A	2.82 A	.13 A	176.9°
	2.762	2.882	2.95		
$Ti_{.5}Zn_{1.5}Mo_4O_7$	2.742	2.784	2.791	.200	176.1
	2.756	2.893	2.991		
$Fe_{1.89}Mo_{4.11}O_7$	2.752	2.778	2.771	.235	176.0
	2.760	2.890	3.006		
$Sc_{.5}Fe_{1.5}Mo_4O_7$	2.755	2.792	2.740	.288	175.4
	2.759	2.887	3.028		
$Al_{.41}Fe_{1.51}Mo_{4.08}O_7$	2.750	2.778	2.728	.300	175.8
	2.756	2.879	3.027		
$Sc_{.75}Zn_{1.25}Mo_4O_7$	2.748	2.817	2.629	.507	174.0
	2.782	2.886	3.136		

[a]The corresponding distances for $NaMo_4O_6$ are: Mo1-Mo2, 2.780 A; Mo2-Mo2, 2.753, 2.862 A; Mo1-Mo1, 2.862 A.

[b]Mo(apex)-Mo(waist) bond distances.

[c]Mo(waist)-Mo(waist) bond distances. The first value for each compound is the distance perpendicular to the chain direction. The second value is for bonds parallel to the chain axis.

[d]Distances are alternate short and long d(Mo(apex)-Mo(apex)).

[e]Δ is the difference between short and long d(Mo1-Mo1).

[f]ϕ is the dihedral angle between the basal planes of adjacent octahedra.

Fe1, and one apical Mo. Oxygen 1 is rather unusual. It is coordinated by four waist Mo atoms in an approximately square-planar symmetry. In fact, O1 has a local symmetry of D_{2h}. The Mo-O1 bond distances are about 2.16 Å which are longer than other Mo-O bonds in the $M_2Mo_4O_7$ structures. Oxygen atoms having square-planar coordination geometry have also been found in other oxide phases, such as NbO, $Mg_3Nb_6O_{11}$ (13), MMo_8O_{10} (M = Li, Zn) (14), and $Mn_{1.5}Mo_8O_{11}$ (15). The third type of oxygen (O3) is unique. It has only been found in $M_2Mo_4O_7$ and the related MMo_8O_{10} structures. It is bonded to two apex Mo, one waist Mo, and one Fe2 in a sawhorse geometry. The Mo(waist)-O3-Fe2 and the Mo(apex)-O3-Fe2 bond angles are 178^o and 97^o, respectively.

The preferential locations of the ternary metal cations in the $M_2Mo_4O_7$ structures may be rationalized by the closely related spinel structures. Ti and Sc are expected to be at octahedral sites because $ZnSc_2O_4$ and $FeSc_2O_4$ are normal spinels and $TiZn_2O_4$ is an inverse spinel. Aluminum atoms are located at the octahedral sites in $Al_{0.5}Zn_{1.4}Mo_{4.1}O_7$ which is in agreement with the normal spinel $ZnAl_2O_4$. The normal spinel $FeAl_2O_4$ falls on the borderline in the impressive structural sorting map for AB_2X_4 chalconide spinels based on pseudo-potential radii (16). Some borderline examples are often partially disordered with varying amounts of normal and inverse character. Therefore, it is not surprising that Al atoms were found at both the octahedral and the tetrahedral

sites in $Al_{0.41}Fe_{1.51}Mo_{4.08}O_7$, which was prepared at high temperature (1400°C) and quenched by rapid cooling (ca. 700°C in two minutes). The unique molybdenum atom is at the octahedral site because its oxidation state is expected to be equal or a little lower than 4+ so that the crystal-field stabilization energy for octahedral coordination is greater. The ternary metal cations at the octahedral sites are assumed to be disordered because no superlattice reflections have been observed so far.

DISCUSSION

All of the $M_2Mo_4O_7$ compounds discovered so far exhibit pairing between apical molybdenum atoms in the infinite chains. The extent of distortion is supposed to be related to the MCE (metal cluster electron) in the Mo_4O_7 unit. In order to learn the relationship between MCE and the degree of distortion, it is necessary to know the oxidation states of the ternary metal cations. A few different approaches to estimate their oxidation states have been attempted.

The variations of a and b cell constants among the six compounds are so small that it is difficult to correlate these constants with MCE and/or cation sizes, but note that the a constant of $Sc_{0.75}Zn_{1.25}Mo_4O_7$ and the b constant of $Ti_{0.5}Zn_{1.5}Mo_4O_7$ are significantly longer than others. However, the c cell constants show marked dependence on radii of the cations. In the following paragraphs, $r(M^{n+})$ will be used to designate the effective ionic radius proposed by Shannon (17) based on $r(^{VI}O^{2-}) = 1.40$ A. The formula for each compound will be abbreviated to MM'MoO.

The scandium-containing compounds have relatively larger c constants simply because the effective ionic radius of Sc^{3+} is larger than those of Al^{3+} and Ti^{+4}. Firstly, we may compare ScFeMoO with ScZnMoO. Because the c constant of ScFeMoO is about 0.12 A longer than that of ScZnMoO, the iron ion can not be all Fe^{+3}. This is because $r(Fe^{3+})$ (CN = 4 or 6) is

appreciably smaller than the corresponding $r(Zn^{2+})$. Preliminary Mossbauer spectroscopy measurements on ScFeMoO gave a spectrum essentially composed of two peaks corresponding to the octahedrally and tetrahedrally coordinated iron ions. The magnetic susceptibility data in the paramagnetic state strongly indicate that both the octahedral and tetrahedral iron atoms are in high-spin +2 state. A similar argument can be applied to AlFeMoO and AlZnMoO compounds and the iron ions in AlFeMoO should be mostly high-spin Fe^{2+}.

Now we may compare the c constant of FeMoO with that of ScFeMoO. Because FeMoO has smaller $\underline{c}$ constant and $r(Fe^{2+})$ (CN = 6, HS) is larger than $r(Sc^{3+})$ (CN = 6), some iron atoms in FeMoO must have oxidation state 3+. As mentioned in the EXPERIMENTAL AND RESULTS section the Mossbauer spectra for FeMoO in the paramagnetic region are best fit by three doublets. The relative area of the three different iron sites can be readily explained by the following argument. The octahedrally coordinated iron atoms form a straight chain along the $\underline{a}$ direction. Assuming 10% iron atoms are replaced by molybdenum atoms and each molybdenum atom has two neighboring iron atoms, there are roughly two different kinds of octahedral sites with relative ratio of 0.7: 0.2. Thus, the three different types of iron atoms have relative ratio of 1.0: 0.7: 0.2. The peak appearing at 0.701 mm/s with quadrupole splitting 0.956 mm/s has smaller isomer shift and

suggests that it is due to tetrahedrally coordinated iron sites which is consistent with the above argument. However, comparing these Mossbauer parameters with those of some other known compounds, the isomer shift for site 1 suggests the oxidation state is between 2+ and 3+. Similarly, the oxidation state of iron site 2 is also probably between 2+ and 3+. The isomer shift for iron site 3 can be explained by ferrous ion in distorted octahedral symmetry. The reason why the ferrous ions are located next to the unique molybdenum atoms is probably due to the reduction of electrostatic repulsion between the cations.

It is not obvious why the c constant of TiZnMoO is about the same as that of AlZnMoO. Because either $r(Ti^{4+})$(C.N.=6; 0.605 A) or $r(Ti^{3+})$(C.N.=6; 0.67 A) is larger than $r(Al^{3+})$ (C.N.=6; 0.53 A), the c constant of TiZnMoO is expected to be a little larger. However, the unit cell volume of TiZnMoO is larger than that of AlZnMoO. In Fig. 4.13, the unit cell c constants were plotted vs. the sums of $r(M^{n+})$ at octahedral and tetrahedral sites. $\Sigma\ r(M^{n+})$ for each compound was calculated by assuming that there was no substitution by the unique molybdenum atom and that all of the Al^{3+} ions were at octahedral sites in $Al_{0.41}Fe_{1.51}Mo_{4.08}O_7$. These plots are linear for ScFeMoO, ScZnMoO, AlFeMoO, and AlZnMoO compounds. FeMoO compound is not shown in the figure because of the uncertainty as to oxidation state. Neither Ti^{3+}ZnMoO nor Ti^{4+}ZnMoO falls in line with other compounds. $\Sigma\ r(M^{n+})$ for

FeMoO compound could be estimated from this plot by interpolation method. The estimated value is about 1.36 A indicating that both Fe^{2+} and Fe^{3+} are present, but Fe^{2+} is in larger amount.

With a constant anion charge and a constant volume of the molybdenum cluster unit, the unit cell volume of this isostructural series should be proportional to the volume of the ternary cations. Fig. 4.14 shows the plot of unit cell volume vs. $\Sigma r(M^{n+})^3$. ScFeMoO, AlFeMoO, AlZnMoO, and Ti^{3+}ZnMoO provide a straight line, but Ti^{4+}ZnMoO and ScZnMoO deviate very much from linearity. This result suggests that the titanium ion in TiZnMoO has oxidation state 3+. The result also implies that the volume of molybdenum metal cluster in ScZnMoO is so large that it does not fall in the line with other compounds. It has the largest volume because of the long Mo2-Mo2 bond distance perpendicular to the infinite metal chain, which in turn results in the longest unit cell a constant.

Bond-length bond-strength calculations on Mo-O bonds did not give satisfactory results for estimating oxidation states of the ternary metal cations. The oxidation states derived from the M(oct)-O bonds in TiZnMoO, AlFeMoO, and ScFeMoO compounds would be less reliable because cations with different sizes occupy the same sites. The calculations on $Fe_{1.89}Mo_{4.11}O_7$ should be more informative. The estimated oxidation states for the tetrahedral irons are expected to be

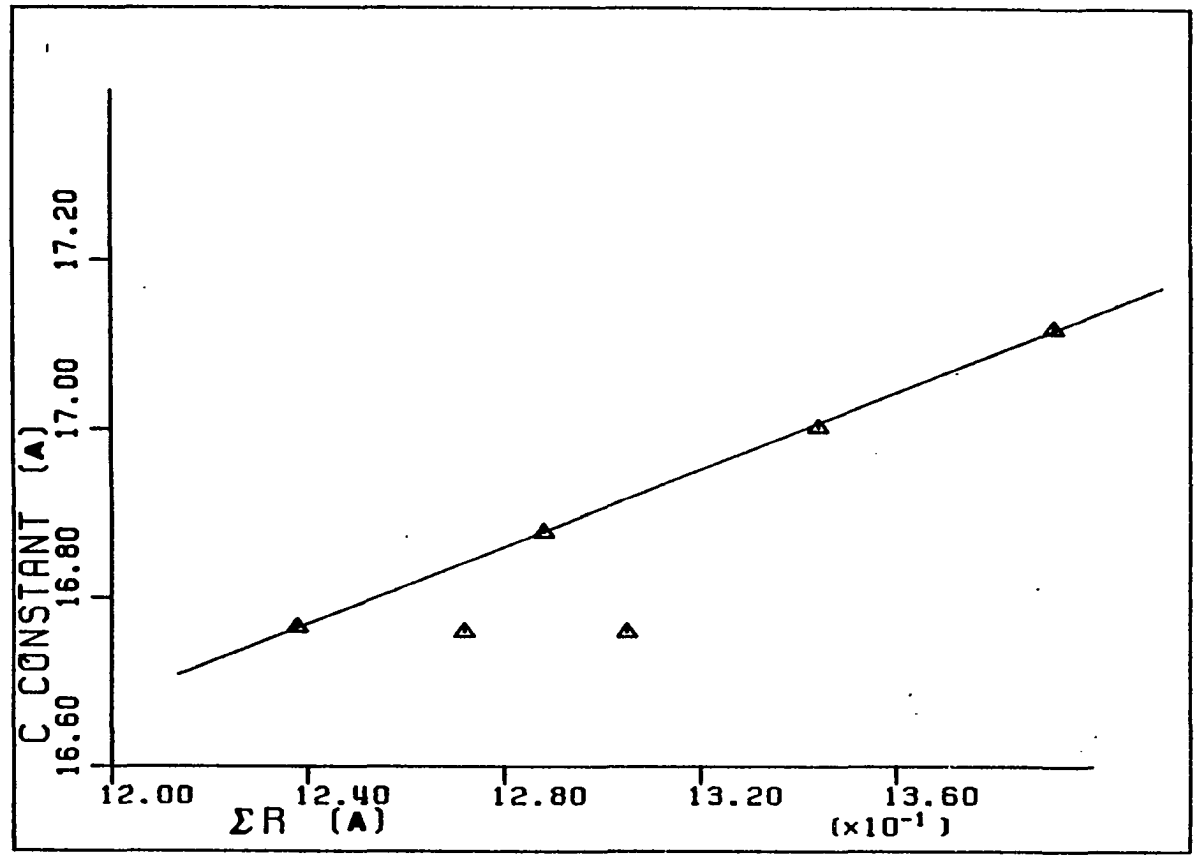

Fig. 4.13. Unit cell c constant vs Σr for some compounds with the $M_2Mo_4O_7$ structure

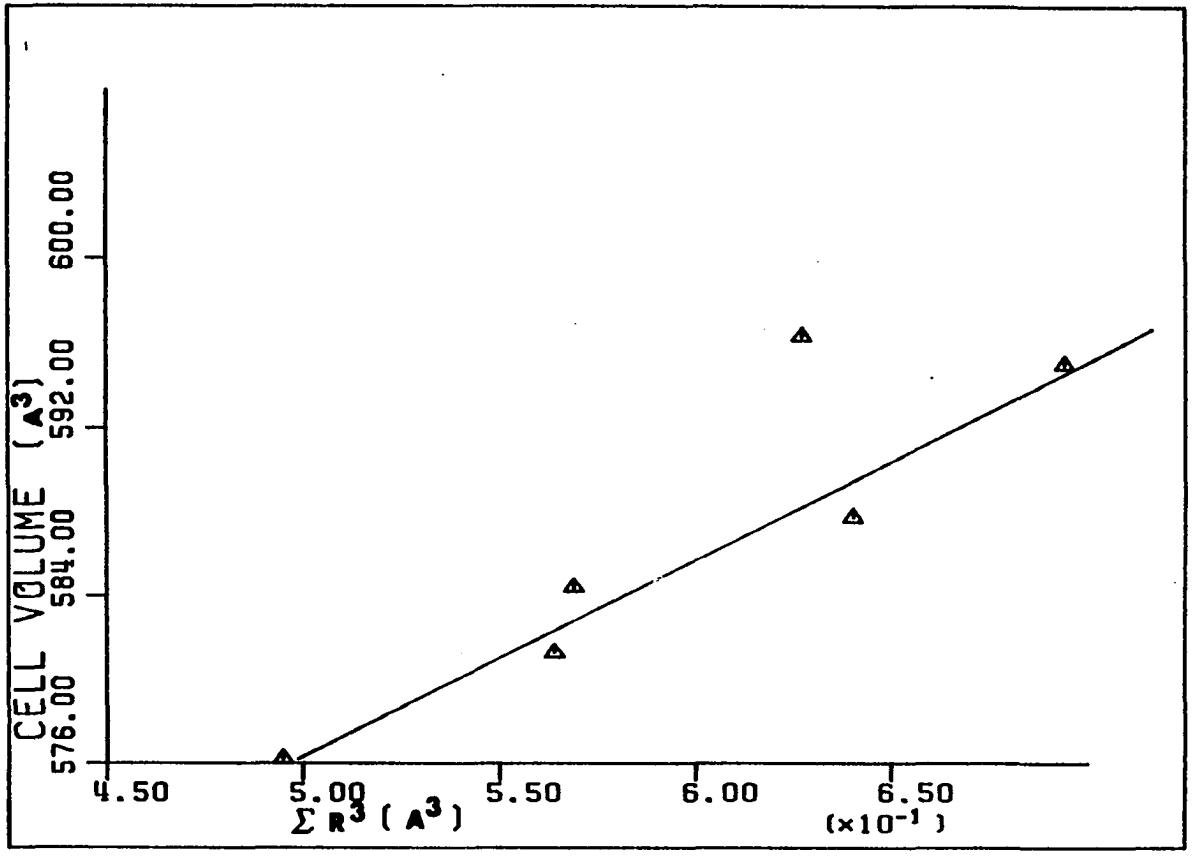

Fig. 4.14. Cell volume vs. $\Sigma r(M)^3$ for some compounds with the $M_2Mo_4O_7$ structure

more reliable. The results of these estimates for iron and titanium ions are given in Tables 4.23 and 4.24, respectively.

The agreement between the estimated values and the formal oxidation states for the tetrahedrally coordinated irons in known compounds is generally good. The equation works equally well for octahedral iron ions except for the compounds with different cations occupying the same sites. Interestingly enough, the estimated oxidation state for the octahedral iron in Fe_3O_4 is 2.52 which is in excellent agreement with its inverse spinel structure. Now we may turn to the $M_2Mo_4O_7$ structures. Both of the octahedral and tetrahedral iron ions in ScFeMoO are in 2+ state. In the case of AlFeMoO compound, some of the tetrahedral iron atoms have oxidation state 3+, but Fe^{2+} ions are in larger fraction. Although it is harder to estimate the oxidation state of octahedral irons in AlFeMoO, it is believed that most of them should be in 2+ state. Some iron ions in FeMoO must have oxidation state 3+, but they are in smaller fraction. The titanium atom in TiZnMoO is likely 3+ because its $\Sigma s(Ti-O)$ is a lot lower than that for Zn_2TiO_4. In general, the conclusions from magnetic susceptibilities, Mossbauer spectra, volume vs. Σr^3 plots, and bond-length bond-strength calculations are quite consistent.

$Al_{0.5}Zn_{1.4}Mo_{4.1}O_7$ offers a good opportunity to study the oxidation state of the unique molybdenum atom. Because Al^{3+}, Zn^{2+}, and infinite metal chains are diamagnetic or temperature-independent weakly paramagnetic, any observed

Table 4.23. Assessment of oxidation states of iron by using bond-length bond-strength relationship[a]

compounds	oxid. state (C.N.)	Σs(tet)	Σs(oct)	ref.
Fe_2SiO_4	+2(VI)		1.91, 1.99	19
FeO	+2(VI)		1.99	20
FeV_2O_4	+2(IV)	2.06		21
Fe_2TiO_4	+2(IV), +2(VI)	1.95	2.67	22
Fe_2MoO_4	+2(IV), +2(VI)	2.25	2.55	23
$GaFeO_3$	+3(VI)		2.99, 2.86	24
Fe_2O_3	+3(VI)		3.22	25
$Y_3Fe_5O_{12}$	+3(VI), +3(IV)	2.82	2.91	26
$Na_3Fe_5O_9$	+3(IV)	2.93		27
$NaFeO_2$	+3(IV)	2.97		28
Fe_3O_4(magnetite)	+3(IV), +2,+3(VI)	2.86	2.52	29
$Fe_2Mo_3O_8$	+2(IV), +2(VI)	2.08	2.29	30
$Sc_{.5}Fe_{1.5}Mo_4O_7$	+2(IV), +2(VI)	2.18	2.29	
$Al_{.4}Fe_{1.5}Mo_{4.1}O_7$	?(IV), ?(VI)	2.36	2.58	
$Fe_{1.89}Mo_{4.11}O_7$	?(IV), ?(VI)	2.28	2.39	

[a] $S(Fe-O) = (1.764/R)^{5.5}$ was used in the calculations (18).

Table 4.24. Assessment of oxidation states of titanium by using bond-length bond-strength relationship[a]

compounds	oxid. state(C.N.)	Σs(Ti-O)	ref.
TiO_2(rutile)	+4(VI)	3.942	31
$BaTiO_3$(tetr.)	+4(VI)	3.580	32
$BaTiO_3$(orth.)	+4(VI)	3.61	32
$PbTiO_3$(tetr.)	+4(VI)	3.80	32
$SrTiO_3$(cubic)	+4(VI)	4.005	32
$CoTiO_3$	+4(VI)	3.69	33
Mg_2TiO_4	+4(VI)	3.72	25
Zn_2TiO_4	+4(VI)	3.72	34
$Zn_2Ti_3O_8$	+4(VI)	4.03	34
Ti_2O_3	+3(VI)	3.172	35
$CaTi_2O_4$	+3(VI)	3.13	36
$LiTiO_2$	+3(VI)	2.95	37
TiO	+2(20% IV)	1.87	38, 39
	+2(80% VI)	2.34	
$Ti_{0.5}Zn_{1.5}Mo_4O_7$	?(VI)	3.10	

[a] $S(Ti-O) = (1.806/R)^{5.2}$ was used in the calculations (18).

temperature-dependent paramagnetism may arise from the unique molybdenum atoms. However, the sample purity should be carefully checked. The observed impurity $ZnMo_8O_{10}$ may not interfere with the measurement results because it is essentially temperature-independent paramagnetic (14). Very pure starting materials must be used in the sample preparation. Nevertheless, one may consider the oxidation state of the unique molybdenum atom on the basis of a few related structures. As discussed in SECTION III, of this thesis the oxidation state of the unique molybdenum atom in $Ca_{5.45}Mo_{18}O_{32}$ is 3.76. Bond-length bond-strength calculations on $La_3Mo_4SiO_{14}$ (40) give very consistent results with its stochiometry. The unique molybdenum atom in the lanthanum-containing compound has the oxidation state +3.88. Accordingly, one may assume that the oxidation state of the unique molybdenum in $M_2Mo_4O_7$ structures is approximately +3.8 in the following discussion.

Perhaps the most interesting result from the structure refinements is the Mo(apex)-Mo(apex) bond distances. The alternate short and long Mo(apex)-Mo(apex) distances arise because the Fermi level lies near a band crossing so that a tilting distortion occurs. Extended Huckel band calculations (41) indicated that systems with 13 or fewer electrons per Mo_4 need not distort and systems with 14 to 15 electrons should distort. But the calculation results were unable to distinguish theoretically between $Sc_{0.75}Zn_{1.25}Mo_4O_7$ and

$Ti_{0.5}Zn_{1.5}Mo_4O_7$. We hope to experimentally decide what electron count should favor the largest distortion in the $M_2Mo_4O_7$ structures. On the basis of the above discussion about the oxidation states of the ternary metal cations and the unique molybdenum atom, one is able to calculate the MCE for a Mo_4O_7 unit from the formula. The following assumptions were made in the calculation: all of the iron atoms in AlFeMoO are Fe^{2+}, all of the titanium atoms in TiZnMoO are Ti^{3+}, 75% of the iron atoms in FeMoO are Fe^{2+} and the rest of them are Fe^{3+}, and the unique molybdenum atoms in each compound are $Mo^{3.8+}$. The estimation results are listed (with their MCE's in the parentheses): AlZnMoO (14.68), TiZnMoO (14.5), FeMoO (14.68), ScFeMoO (14.5), AlFeMoO (14.55), and ScZnMoO (14.75). It appears that the extent of distortion is insensitive to the MCE if it is below a certain limit. Other competitive factors might be equally important. As the MCE is above the limit, the metal cluster chain distorts drastically. However, the range for the MCE is so narrow that one may surmise other possible reasons for the alternate short and long Mo(apex)-Mo(apex) distances. The distance between the octahedral ternary metal sites is one-half of the unit cell a constant. As the content of octahedral M^{3+} cation gets higher, the electrostatic repulsion between these sites becomes greater. The a constant is expected to be lengthened in order to stabilize the structure. This is exactly what we have observed in $Sc_{0.75}Zn_{1.25}Mo_4O_7$. The elongation of the a

constant would affect the coordination sphere of the scandium atom and simultaneously weaken or strengthen the related Mo-O bonds. A change in Mo-O bonding should have some effects on the Mo-Mo bonds. At this point, one may ask why $Sc_{0.75}Zn_{1.25}Mo_4O_7$ is so special. Why cannot other compounds adopt the same stoichiometry? But the answer to the above question has not been obtained yet.

Both the size effect and the number of MCE appear important in stabilizing the $M_2Mo_4O_7$ structures. For example, the attempted preparation of "$Y_{0.75}Zn_{1.25}Mo_4O_7$" led to a ternary phase which is related to $Ca_{5.45}Mo_{18}O_{32}$. Yttrium ion is evidently too big to be at the octahedral sites in the $M_2Mo_4O_7$ structure. Although the size effect is no longer a problem in the preparation of "$Zn_2Mo_4O_7$", the compound has not been obtained probably because of its significantly lower MCE (14 e/Mo_4O_7).

The iron-containing $M_2Mo_4O_7$ phases have interesting magnetic structures and are ferrimagnetic. They show large susceptibilities at low temperature that decreases increasingly rapidly with rising temperature. Above the Neel temperature, the material reverts to the normal paramagnetic state. Extrapolation of the paramagnetic region to $\chi^{-1} = 0$ leads to a large negative intercept. $Fe_{1.89}Mo_{4.11}O_7$ would have zero overall moment and be antiferromagnetic if both of the octahedral and tetrahedral irons had the same oxidation state and there were no unique molybdenum atoms at the

octahedral sites. In fact, a residual overall moment results and it is ferrimagnetic because of the partial cancellation of the opposite magnetic spins at octahedral and tetrahedral sites. A similar result is expected for $Sc_{0.5}Fe_{1.5}Mo_4O_7$. It has, in fact, a larger overall moment which is consistent with its stoichiometry.

REFERENCES

1. Simon, A. Angew. Chem. Int. Ed. Engl. 1981, 20, 1.

2. Poeppelmeier, K. R.; Corbett, J. D. J. Am. Chem. Soc. 1978, 100, 5039.

3. McCarley, R. E. Phil. Trans. R. Soc. Lond. 1982, A308, 141.

4. Brough, L. F.; McCarley, R. E. unpublished research, Department of Chemistry, Iowa State University, Ames, Iowa, 1982.

5. Karcher, B. A. Ph.D. Dissertation, Iowa State University, Ames, Iowa, 1981.

6. Hanson, H. P.; Herman, F.; Lea, J. D.; Skillman, S. Acta Crystallogr. 1964, 17, 1040.

7. Templeton, D. H. In "International Tables for X-Ray Crystallography", 1st ed.; Macgillavry, C. H. and Rieck, G. D., Eds.; Kynoch Press: Birmingham, England, 1962; Vol. III, page 215.

8. Lapp, R. L.; Jacobson, R. A. "ALLS, A Generalized Crystallographic Least Squares Program", US DOE Report IS-4708, 1979.

9. Powell, D. R.; Jocobson, R. A. "Four: A General Crystallographic Fourier Program", US DOE Report, IS-4737, 1980.

10. Coppens, P.; Hamilton, W. C. Acta Crystallogr. 1970, A26, 71.

11. Rohrbaugh, W. J.; Jacobson, R. A. Inorg. Chem. 1974, 13, 2535.

12. This E&A four-circle diffractometer was modified in Dr. R. A. Jacobson's laboratory. Stepping motors and encoders were attached and interfaced to a LSI/11 computer, which in turn was interfaced to a VAX11/730 computer. It is equipped with a scintillation counter and incorporates a graphite monochromator in the detection system.

13. Marinder, B.-O. Chemica Scripta 1977, 11, 97.

14. Lii, K.-H. Ph.D. Dissertation, Iowa State University, Ames, Iowa 1985.

15. Carlson, C. D.; McCarley, R. E. presented at the 11th Midwest High Temperature Chemistry Conference, Ames, Iowa State University, Iowa, June 1985.

16. Burdett, J. K.; Price, G. D.; Price, S. L. J. Am. Chem. Soc. 1982, 104, 92.

17. Shannon, R. D. Acta Crystallogr. 1976, A32, 751.

18. Brown, I. D.; Wu, K. K. Acta Crystallogr. 1976, B32, 1957.

19. Smith, D. K. et al. Acta Crystallogr. 1965, 18, 787.

20. Wyckoff, R. W. G. "Crystal Structures", 2nd ed.; Wiley Interscience: New York, 1963; Vol. I.

21. Von Reuter, B.; Riedal, E. Z. Anorg. Alleg. Chem. 1969, 369, 306.

22. Ishikawa, Y. et al. J. Phys. Soc. Japan 1971, 31, 452.

23. Abe, M. et al. J. Phys. Soc. Japan 1972, 33, 1296.

24. Abrahams, S. C. et al. J. Chem. Phys. 1965, 42, 3957.

25. Wyckoff, R. W. G. "Crystal Structures", 2nd ed.; Wiley Interscience: New York, 1964; Vol. II.

26. Batt, A. et al. Acta Crystallogr. 1962, 15, 1268.

27. Romers, C. et al. Acta Crystallogr. 1967, 22, 766.

28. Bertaut, F. et al. Compt. Rend. 1963, 257, 421.

29. Wycokoff, R. W. G. "Crystal Structures", 2nd ed.; Wiley Interscience: New York, 1965; Vol. III.

30. Le Page, Y.; Strobel, P. Acta Crystallogr. 1982, B38, 1265.

31. Baur, W. H. Acta Crystallogr. 1956, 9, 515.

32. Muller, O.; Roy, R. "The Major Ternary Structural Families"; Springer-Verlag: New York, 1974.

33. Newnham, R. E.; Fang, J. H.; Santoro, R. P. Acta Crystallogr. 1964, 17, 240.

34. Bartram, S. F.; Slepetys, R. A. J. Am. Ceram. Soc. 1961, 44, 493.

35. Abrahams, S. C. Phys. Rev. 1963, 130, 2230.

36. Bertant, E. F.; Blum, P. Acta Crystallogr. 1956, 9, 121.

37. Lecerf, A. Compt. Rend. 1962, 254, 2003.

38. Andersson, S. et al. Acta Chim. Scand. 1957, 11, 1653.

39. Watanabe, D. et al. Acta Crystallogr. 1967, 23, 307.

40. Betteridge, P. W.; Cheetham, A. K.; Howard, J. A. K.; Jakubicki, G.; McCarroll, W. H. Inorg. Chem. 1984, 23, 737.

41. Hughbanks, T.; Hoffmann, R. J. Am. Chem. Soc. 1983, 105, 3528.

SECTION 5. SYNTHESES, CRYSTAL STRUCTURES, AND PROPERTIES OF TWO TERNARY MOLYBDENUM OXIDES CONTAINING ORTHOGONAL, BUT NONINTERSECTING MOLYBDENUM METAL CLUSTER CHAINS: $LiMo_8O_{10}$ AND $ZnMo_8O_{10}$

INTRODUCTION

The structures of the reduced ternary and quaternary molybdenum oxides have been dominated by molybdenum metal cluster chains which are comprised of trans edge-sharing M_6X_{12} units. A common feature of the previously discussed structure types is that the cluster chains are unidirectional. One may regard the molybdenum-oxide chain as a rectangular column. Then, the various structure types can be simulated by arranging rectangles in a two-dimensional space. The arrangement of the rectangles appears to be largely determined by the ternary metal cations. One may even direct one's synthesis by contriving new structure types. For example, Fig. 5.1 shows a structure containing two types of tunnels which are created by different arrangements of the rectangles. Tunnels A and B are adopted by $NaMo_4O_6$ (1) and $Mn_{1.5}Mo_8O_{11}$ (2), respectively. Accordingly, one might be able to synthesize a quaternary compound with sodium and manganese cations in separate tunnels.

In an attempt to extend the imagination to a three-dimensional space, one may notice that the manner in which the oxygen atoms are shared between two infinite chains remain basically unchanged even though the neighboring chains are in orthogonal directions. This is mainly because the M_6X_{12} cluster unit has a C_4 axis running through the apex metal atoms. The ability to predict new structure types in a three-

dimensional space would be greatly facilitated if computer graphics comes to one's assistance. The next logical step of the concept of column packing leads one to ask, "Can reduced ternary molybdenum oxides adopt some interpenetrating structures, as the Cr_3Si structure (A15-type)?"

Compounds containing interpenetrating metal chains have been observed in a number of fascinating systems, such as $NaPt_3O_4$ (3-dimensional Pt-Pt interaction) (3), $CaPt_2O_4$ (2-dimensional Pt-Pt interaction) (4), and $Hg_{2.86}AsF_6$ (2-dimensional Hg-Hg interaction) (5). In the system of reduced ternary molybdenum oxides, a new structure type containing orthogonal molybdenum metal cluster chains has been discovered. The syntheses, structure characterizations, and magnetic properties of MMo_8O_{10} (M = Li, or Zn) will be discussed in this section.

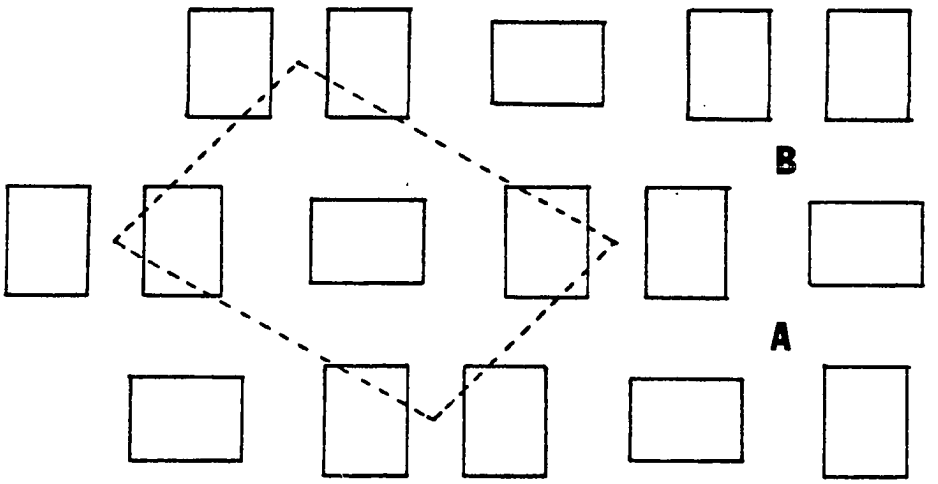

Fig. 5.1. A hypothetical structure. The rectangles represent the molybdenum-oxide chains running perpendicular to this plane. Tunnels A and B are adopted by $NaMo_4O_6$ and $Mn_{1.5}Mo_8O_{11}$, respectively. A unit cell is indicated by the dashed lines

EXPERIMENTAL AND RESULTS

Materials

The starting materials used were Fisher Certified A.C.S. ZnO, Aldrich Mo powder (99.99%), Thermo-Electron Mo tubing (99.97%), Baker MoO_3 (99.9%). Anhydrous lithium molybdate (98.5%) was obtained from Alfa products. It was heated at 120°C under dynamic vacuum overnight and then stored in a dry box.

Syntheses and Analyses

$LiMo_8O_{10}$

The discovery of the title compound was again serendipitous. Small chunky crystals of $LiMo_8O_{10}$ were discovered in a product mixture resulting from the reaction of Li_2MoO_4, MoO_3, and Mo in 3: 8: 13 mole ratio (i.e., aiming at $LiMo_4O_6$) in a sealed molybdenum tube at 1450°C for one and a half days. Although the chunky crystals showed a little purple tint, an x-ray powder pattern of the bulk product revealed Mo metal and an unknown phase which was definitely not MoO_2. Because the x-ray emission by lithium is too soft to be analyzed by the microprobe technique, the stoichiometry of the title compound was not known until its x-ray single-crystal structure was solved. An essentially pure product was

obtained by heating a pressed pellet containing a stoichiometric amount of Li_2MoO_4, MoO_3, and Mo in a sealed molybdenum crucible at 1410°C for 2 days. It was found that many chunky crystals deposited on the Mo cap which was in the colder end of the Mo crucible. An x-ray powder pattern of the bulk product showed that it contained a little Mo and all other diffraction lines were due to $LiMo_8O_{10}$. Some crystals were scrapped off the Mo cap and their powder pattern could be explained by $LiMo_8O_{10}$ and a little MoO_2. Evidently, some interesting chemical transport reaction took place.

The reactivity of $LiMo_8O_{10}$ with water was tested by mixing 0.1 g of fine powder and 15 ml of H_2O. No pH change was detected with a pH meter after constant stirring for 10 minutes.

$\underline{ZnMo_8O_{10}}$

As mentioned in SECTION IV of this thesis, a few chunky crystals grew on the wall of a molybdenum crucible in the preparation of $Al_{0.5}Zn_{1.4}Mo_4O_7$. The film work on a chunky crystal showed that it had a different structure from $Al_{0.5}Zn_{1.4}Mo_4O_7$ and was isomorphous with $LiMo_8O_{10}$. A chunky crystal was selected for electronmicroprobe analysis. Four measurements were made on different spots of the same crystal. The back-scattering electron photographs showed heterogeneity of the sample and some dark regions with low Z inclusions. The crystal surfaces were inclined at varying angles to the

electron beam. This could affect quantitative accuracy. The measurements indicated that the aluminum content in the crystal was essentially zero and the Zn to Mo mole ratio was 0.108(4). The Zn/Mo ratio from microprobe analysis was a little lower than that from single-crystal x-ray diffraction data (vide infra). Because of the problems encountered in the microprobe analysis, the results from x-ray data would be more reliable. Subsequently, a reaction to prepare pure $ZnMo_8O_{10}$ was carried out. The appropriate quantities of reactants (ZnO, MoO_3, Mo) were mixed, pelletized, and heated in a sealed Mo tube at 1370°C for about 2 days. An x-ray powder pattern of the bulk product indicated that there was a little Mo metal and that all other reflections were due to $ZnMo_8O_{10}$. Some black chunky crystals and purple needle-like crystals were also found on the wall of the molybdenum crucible. The Mo crucible seemed to be coated with some material. A reaction at lower temperature (1250°C) for 65 hours was performed. The reaction products contained $ZnMo_8O_{10}$, $Zn_2Mo_3O_8$, MoO_2, and Mo.

Others

Reactions to synthesize MMo_8O_{10} with other cations have been performed but none of them was successful. The reaction results are summarized in the following way: compound attempted to be synthesized (reactants and reaction conditions), identified products.

$MgMo_8O_{10}$ (MgO, MoO_3, Mo, 1410°C, 2 days), MoO_2, Mo, and $Mg_2Mo_3O_8$. $FeMo_8O_{10}$ (Fe_2O_3, MoO_3, Mo, 1400°C, 42 hrs), MoO_2, Mo, and $Fe_{1.89}Mo_{4.11}O_7$. $SiMo_8O_{10}$ (Si, MoO_3, Mo, 1630°C, 2 days), Mo, SiO_2 (JCPDS 11-695). $CoMo_8O_{10}$ (CoO, MoO_3, Mo, 1375°C, 3 days), MoO_2, Mo. $NiMo_8O_{10}$ (NiO, MoO_3, Mo, 1375°C, 3 days), MoO_2, Mo, α-$NiMoO_4$.

Preliminary Film Work and X-ray Powder Diffraction

A single crystal of the lithium compound in the form of a chunk was mounted on a Weissenberg camera with the a axis parallel to the rotation axis. Oscillation ahd 0kℓ-1kℓ layer photographs were registered. The Weissenberg photographs suggested that the Laue group was 4/mmm with the unit cell parameters a = b = 5.88, c = 24.7 A. Systematic absences were observed for hkℓ with h+k+ℓ=2n and hhℓ with 2h+ℓ=4n.

The film work on a single crystal of $ZnMo_8O_{10}$ indicated that it was isomorphous with $LiMo_8O_{10}$. The unit cell parameters which were calculated from the axial oscillation and Weissenberg photographs were a = b = 5.90, c = 24.9 A.

The Guinier powder patterns of both compounds could be completely indexed with body-centered tetragonal cells with a = b = 5.8515(6), c = 24.783(3) A for $LiMo_8O_{10}$, and a = b = 5.8961(4), c = 24.840(3) A for $ZnMo_8O_{10}$. The indexing results are given in Tables 5.1 and 5.2. Cell constants from Guinier powder diffraction will be used in later calculations because

of their high accuracy.

Because $ZnMo_8O_{10}$ showed a phase transition in the magnetic susceptibility data (vide infra), a low-temperature (100 - 110 K) x-ray powder pattern was taken below the transition temperature (ca. 200K) with a Rigaku powder diffractometer. NBS Si powder was mixed with the sample as an internal standard. Both R.T. and L.T. powder patterns were taken under the same conditions for data collection. Cu $K\alpha_1$ (λ = 1.54056 A) was used for calculating the unit cell parameters. The cell constants calculated from R.T. and L.T. powder patterns are a = b = 5.9003(4), c = 24.848(2) A and a = b = 5.896(1), c = 24.836(5) A, respectively. There seems a very slight shrinkage in cell parameters at low temperature. No extra reflections were detected at 100 K. Although the intensities of a few diffraction peaks appear different at low temperature, atomic positions from single-crystal x-ray diffraction data collected at 160 K did not show any significant differences.

X-ray Single Crystal Diffraction Studies of

The crystals were transferred to four-circle diffractometers and were centered. The preliminary unit cell constants and orientation matrices were determined by using an automatic indexing program (6) that uses reflections from ω-oscillation pictures as input. Crystal data and details of

Table 5.1. X-ray powder diffraction data for $LiMo_8O_{10}$

d-spacings (A) observed	d-spacings (A) calculated	intensities	hkℓ
6.195(9)	6.1958	m	004
5.691(7)	5.6949	s	101
4.772(5)	4.7750	vw	103
3.782(3)	3.7821	m	105
3.030(2)	3.0291	m	107
2.848(2)	2.8475	m	202
2.603(1)	2.6024	m	211
2.496(1)	2.4947	vw	213
2.388(1)	2.3875	vs	206
2.314(1)	2.3142	m	215
2.1041(9)	2.1044	m	217
2.0686(9)	2.0688	s	220
2.0646(9)	2.0652	s	0012
1.9618(8)	1.9623	w	224
1.9439(8)	1.9445	vw	301
1.8977(8)	1.8969	vw	219
1.8906(7)	1.8910	m	2010
1.8496(7)	1.8504	vw	310
1.8122(7)	1.8126	w	1013
1.7728(6)	1.7730	vw	314
1.7079(6)	1.7084	w	307
1.6190(5)	1.6194	w	321
1.5912(5)	1.5917	w	309
1.5484(5)	1.5489	w	0016
1.5406(5)	1.5409	w	2113
1.4747(4)	1.4753	vw	327
1.4615(4)	1.4616	s	2212
1.4232(4)	1.4237	w	404
1.4162(4)	1.4169	w	411
1.3634(4)	1.3634	vw	3013
1.3167(3)	1.3173	w	417
1.3007(3)	1.3012	w	422
1.2727(3)	1.2731	vw	1019

Table 5.2. X-ray powder diffraction data for $ZnMo_8O_{10}$

d-spacings (A) observed	d-spacings (A) calculated	intensities	hkℓ
6.23(1)	6.2125	m-s	004
5.755(8)	5.7377	vs	101
4.813(6)	4.8040	m	103
3.957(4)	3.9531	w	112
3.802(4)	3.8003	w	105
3.104(2)	3.1062	vw	008
3.041(2)	3.0414	s	107
2.947(2)	2.9485	vw	200
2.937(2)	2.9385	vw	116
2.868(2)	2.8688	s	202
2.663(2)	2.6637	vw	204
2.621(2)	2.6225	s	211
2.512(2)	2.5129	w	213
2.499(2)	2.5006	vw	109
2.401(1)	2.4020	vs	206
2.329(1)	2.3296	s	215
2.116(1)	2.1170	m	217
2.085(1)	2.0849	vs	220
2.070(1)	2.0708	s	0012
1.9762(9)	1.9766	m	224
1.9583(9)	1.9596	vw	301
1.8993(8)	1.9002	m-s	2010
1.8644(8)	1.8648	w	310
1.8434(8)	1.8441	vw	312
1.8274(8)	1.8279	w	305
1.8171(8)	1.8184	w-m	1013
1.7193(7)	1.7196	m	307
1.7000(7)	1.7004	vw	316
1.6317(6)	1.6320	m-s	321
1.6012(6)	1.6013	vw-w	309
1.5531(5)	1.5531	w	0016
1.5474(5)	1.5477	vw	2113
1.4858(5)	1.4855	vw	327
1.4745(5)	1.4742	s	400
1.4688(5)	1.4692	s	2212
1.4345(4)	1.4344	vw	404
1.4281(4)	1.4279	vw	411
1.3852(4)	1.3857	vw	3112
1.3257(4)	1.3266	vw-w	417

the parameters associated with data collection for both compounds are tabulated in Tables 5.3, and 5.4, respectively. Corrections for absorption effects were based on ϕ scans of suitable reflections with χ values close to 90° (7). Lorentz and polarization corrections were also applied. Both data sets showed 4/mmm Laue symmetry and the extinction conditions $h + k + \ell = 2n$ for $hk\ell$ reflections, and $2h + \ell = 4n$ for $hh\ell$ reflections. The possible space groups thus were $I4_1md$ (No. 109), and $I\bar{4}2d$ (No. 122). The structures can be better described in space group $I4_1md$ (vide infra). The atomic scattering factors (8) for neutral atoms were used throughout the calculations. Both real and imaginary components of anomalous dispersion (9) were included for all atoms heavier than oxygen. The data sets were averaged in 4/mmm symmetry without any reflections being eliminated. The agreement factors (R_{int}) for $LiMo_8O_{10}$ and $ZnMo_8O_{10}$ are 5.9% and 3.0%, respectively.

$\underline{LiMo_8O_{10}}$

The structure solution of $LiMo_8O_{10}$ was in cooperation with Sangsoo Kim in Dr. Jacobson's group. Space group $I4_1md$ was tentatively selected because it could fully explain the vectors on the Patterson-superposition maps. The very complex Patterson-superposition maps were finally solved by Sangsoo. Interestingly, the shift vector for the superposition map was later proved to be an extraneous peak. The positions of all

the oxygen atoms were revealed on a Fourier synthesis using phases from molybdenum atoms. Inspection of observed and calculated structure factors showed that some reflections were strongly affected by secondary extinction effect. A least-squares refinement with anisotropic thermal parameters on all molybdenum atoms and with an isotropic extinction factor yielded an agreement factor R = 4.7%. A subsequent ΔF map clearly showed peaks at the 4a special position which were most likely due to lithium ions. The lithium atom was then included in our model. A refinement including the multiplier for the lithium atom resulted in m(Li) = 0.33(3) suggesting that the lithium site was probably fully occupied. Final refinement of all positional parameters, anisotropic thermal parameters for Mo atoms, isotropic thermal factors for oxygen and lithium atoms, and isotropic extinction factor led to convergence with R = 4.2% and R_w = 5.2%. The oxygen atoms were isotropically refined because some of them gave negative thermal parameters when they were anisotropically varied. The secondary extinction parameter was 4.38×10^{-4}. A final difference-Fourier synthesis based on all data showed a maximum residual electron density of 1.1 e/A^3 which is near the Mo1 site. The final positional and thermal parameters are collected in Tables 5.5 and 5.6. The selected bond distances and bond angles are given in Tables 5.7 and 5.8.

The structure description in $I\bar{4}2d$ was also attempted. The coordinate transformation involves a shift in the origin

by 1/8 in z. A least-squares refinement on all atomic positions gave significantly higher R factors than that obtained when the space group $I4_1md$ was used. Accordingly, the structure should be described in space group $I4_1md$.

$\underline{ZnMo_8O_{10}}$

In the initial stage of refinement, isotropic thermal parameters were assumed, and all the positional parameters for Mo atoms were assigned initial values equal to $LiMo_8O_{10}$. The remaining atoms were located from successive ΔF maps. The structure was then refined with anisotropic thermal parameters for all atoms except O4 and with an isotropic extinction parameter which yielded final R = 2.6% and R_w = 3.2%. The value for the secondary extinction parameter was 2.91×10^{-4}. A refinement including the multiplier for the zinc atom gave m(Zn) = 0.251(2) indicating that the zinc site was fully loaded. O4 gave negative temperature factors when it was anisotropically refined. A difference Fourier map calculated from the final refinement showed the maximum residual electron density 0.8 e/A^3 near Mo2. The final positional and thermal parameters are given in Tables 5.9 and 5.10. The selected bond distances and bond angles are listed in Tables 5.11 and 5.12.

Table 5.3. Crystallographic data for $LiMo_8O_{10}$

---

crystal system: tetragonal

space group: $I4_1md$

a = b = 5.8515(6), c = 24.783(3) A

V = 848.6(2) A^3

Z = 4

d(calcd) = 7.317 g/cm^3

crystal dimens: 0.20 x 0.14 x 0.08 mm^3

abs coeff: 112.1 cm^{-1}

reflns used for empirical absorption correction (hkℓ, 2Θ, T_{max}/T_{min}): 040, 28.08, 2.06

diffractometer: AL[a]

radiation: Mo Kα (λ = 0.71034 A)

monochromator: graphite

scan type: ω-scan

automatic background detn, max scan half width: 0.5 degree

std reflns: 3 measured every 75 reflns; no significant variation in intensity.

reflns measd: hkℓ, $\bar{h}\bar{k}\ell$, $\bar{h}k\bar{\ell}$, $h\bar{k}\bar{\ell}$

max 2Θ: 60°

reflns collected: 2356 collected (symmetry extinct reflns not included), 2156 observed ($I > 3\sigma(I)$)

no. of unique reflns with $I > 3\sigma(I)$: 374

no. of parameters refined: 42

R = 4.2%[b]

R_w = 5.2%[c]

quality-of-fit indicator[d]: 1.94

---

[a]For details of the AL diffractometer, see reference 10.

[b]$R = \Sigma||F_o| - |F_c||/\Sigma|F_o|$.

[c]$R_w = [\Sigma w(|F_o|-|F_c|)^2/\Sigma w|F_o|^2; w = 1/\sigma^2(|F_o|)$.

[d]Quality of fit = $[\Sigma w(|F_o|-|F_c|)^2/(N(observns)-N(parameters))]^{1/2}$.

Table 5.4. Crystallographic data for $ZnMo_8O_{10}$

---

crystal system: tetragonal

space group: $I4_1md$

a = b = 5.8961(4), c = 24.840(3) A

V = 863.5(1) A^3

Z = 4

d(calcd) = 7.640 g/cm^3

crystal dimens: 0.30 x 0.14 x 0.08 mm^3

abs coeff: 137.8 cm^{-1}

reflns used for empirical absorption correction (hkℓ, 2θ, T_{max}/T_{min}): 600, 42.38, 1.61; 200, 13.84, 1.77.

diffractometer: Datex[a]

radiation: Mo Kα (λ = 0.70966 A)

monochromator: graphite

scan type: ω-scan

scan half width: 0.6 degree

std reflns: 3 measured every 50 reflns; no significant variation in intensity.

reflns measd: hkℓ, $\bar{h}\bar{k}\ell$, $\bar{h}k\bar{\ell}$

max 2θ: 62.5°

reflns collected: 2022 collected (symmetry extinct reflns not included), 2001 observed ($I > 3\sigma(I)$).

no. of unique reflns with $I > 3\sigma(I)$: 443

no. of parameters refined: 56

R = 2.6%[b]

R_w = 3.2%[c]

quality-of-fit indicator[d]: 1.315

---

[a] For details of the Datex diffractometer, see ref. 11.

[b] $R = \Sigma||F_o| - |F_c||/\Sigma|F_o|$.

[c] $R_w = [\Sigma w(|F_o|-|F_c|)^2/\Sigma w|F_o|^2]$; $w = 1/\sigma^2(|F_o|)$.

[d] Quality of fit = $[\Sigma w(|F_o|-|F_c|)^2/(N(observns)-N(parameters))]^{1/2}$.

Table 5.5. Positional parameters for $LiMo_8O_{10}$

atom	position	multiplier	x	y	z	$B(A^2)^a$
Mo1	8b	.5	.5	.2262(2)	.0	0.56
Mo2	8b	.5	.0	.2353(3)	.00429(6)	0.64
Mo3	8b	.5	.0	.2480(3)	.32808(7)	0.96
Mo4	8b	.5	.0	.2760(2)	.17549(6)	0.63
O1	8b	.5	.5	.246(2)	.250(1)	0.59
O2	8b	.5	.5	.239(2)	.0811(7)	0.48
O3	8b	.5	.5	.230(2)	.4224(9)	1.06
O4	8b	.5	.0	.242(3)	.085(1)	1.36
O5	8b	.5	.0	.263(2)	.4144(9)	0.24
Li	4a	.25	.5	.5	.131(2)	1.33

[a]The isotropic equivalent thermal parameter is defined as $B = 4/3\ [a^2\beta_{11} + b^2\beta_{22} + c^2\beta_{33} + 2ab(\cos\gamma)\beta_{12} + 2ac(\cos\beta)\beta_{13} + 2bc(\cos\alpha)\beta_{23}]$.

Table 5.6. Thermal parameters for $LiMo_8O_{10}$[a,b]

atoms	B or B11	B22	B33	B12	B13	B23
Mo1	0.73(7)	0.72(5)	0.24(7)	0.0	0.0	0.12(5)
Mo2	0.64(6)	0.80(5)	0.49(9)	0.0	0.0	0.08(6)
Mo3	0.65(7)	1.99(7)	0.24(8)	0.0	0.0	-.03(4)
Mo4	0.75(7)	0.71(5)	0.42(8)	0.0	0.0	-.02(4)
O1	0.6(2)					
O2	0.5(3)					
O3	1.1(3)					
O4	1.4(4)					
O5	0.2(2)					
Li	1.3(5)					

[a]Anisotropic temperature factors are given in the form $\exp[-1/4(B_{11}h^2a^{*2} + B_{22}k^2b^{*2} + \ldots + 2B_{23}kℓb^*c^*)]$.

[b]All oxygen and lithium atoms were refined isotropically.

Table 5.7. Bond distances (A) for $LiMo_8O_{10}$

Mo1-Mo1	2.648(2)	Mo1-O1	2.153(9)
Mo1-Mo2	2.9282(3)	Mo1-O2	2.01(2)
Mo1-Mo3	2.757(2)	Mo1-O5	2.12(2)
Mo1-Mo4	2.788(2)	Mo2-O1	2.149(9)
Mo2-Mo2	2.754(3)	Mo2-O3	2.04(2)
Mo2-Mo3	2.723(2)	Mo2-O4	2.01(3)
Mo2-Mo4	2.725(2)	Mo3-O2	2.015(8)
Mo3-Mo3	2.950(3)	Mo3-O4	2.05(1)
	2.902(3)	Mo3-O5	2.14(2)
Mo4-Mo4	2.621(3)	Mo4-O3	2.05(1)
	3.230(3)	Mo4-O4	2.24(3)
Mo3-Mo4[a]	3.258(2)	Mo4-O5	2.147(9)
Mo1-Mo1[a]	3.204(2)	Li-O2	1.96(3)
Mo2-Mo2[a]	3.098(3)	Li-O3	1.70(3)

[a]Interchain distance.

Table 5.8. Bond angles (degree) for $LiMo_8O_{10}$[a]

Mo1-Mo1-Mo2	91.04(4)	O1-Mo1-O1	88.9(5)
Mo2-Mo1-Mo2	175.35(6)[b]	O1-Mo1-O2	88.4(8)
Mo1-Mo2-Mo2	88.96(4)	O1-Mo1-O5	88.7(8)
Mo4-Mo1-Mo1	61.64(3)	O2-Mo1-O5	176.2(5)
Mo4-Mo2-Mo2	59.65(3)	O1-Mo2-O1	87.5(5)
Mo3-Mo1-Mo1	61.30(3)	O1-Mo2-O3	83.1(8)
Mo3-Mo2-Mo2	59.62(3)	O1-Mo2-O4	92.0(8)
Mo4-Mo1-Mo2	56.89(4)	O3-Mo2-O4	173.2(6)
Mo3-Mo1-Mo2	57.14(4)	O2-Mo3-O2	87.8(5)
Mo1-O1-Mo2	85.77(5)	O2-Mo3-O4	92.0(4)
Mo2-O4-Mo4	176.1(9)	O2-Mo3-O4	172.8(9)
Mo3-O4-Mo4	98.6(9)	O2-Mo3-O5	89.6(5)
Mo1-O5-Mo3	179.4(7)	O4-Mo3-O4	87.3(7)
Mo3-O5-Mo4	98.9(7)	O4-Mo3-O5	83.2(8)
O2-Li-O2	103(2)	O3-Mo4-O3	100.5(5)
O2-Li-O3	112.4(4)	O3-Mo4-O4	91.1(7)
O3-Li-O3	105(2)	O3-Mo4-O5	88.8(4)
		O3-Mo4-O5	166.5(7)
		O4-Mo4-O5	78.8(7)
		O5-Mo4-O5	80.5(5)

[a]The atom labels refer to Fig. 5.2.

[b]This angle corresponds to the dihedral angle between basal planes of adjacent octahedra.

Table 5.9. Positional parameters for $ZnMo_8O_{10}$

atom	position	multiplier	x	y	z	$B(A^2)^a$
Mo1	8b	.5	.5	.2192(1)	.0	.23
Mo2	8b	.5	.0	.2389(1)	.00451(4)	.25
Mo3	8b	.5	.0	.2715(1)	.32858(5)	.22
Mo4	8b	.5	.0	.2752(2)	.17670(5)	.22
O1	8b	.5	.5	.244(2)	.2538(7)	.50
O2	8b	.5	.5	.226(2)	.0814(4)	.39
O3	8b	.5	.5	.238(1)	.4236(5)	.30
O4	8b	.5	.0	.266(2)	.0876(7)	.36
O5	8b	.5	.0	.276(2)	.4168(7)	.45
Zn	4a	.25	.5	.5	.12030(9)	.44

[a]The isotropic equivalent thermal parameter is defined as $B = 4/3\ [a^2\beta_{11} + b^2\beta_{22} + c^2\beta_{33} + 2ab(\cos\gamma)\beta_{12} + 2ac(\cos\beta)\beta_{13} + 2bc(\cos\alpha)\beta_{23}]$.

Table 5.10. Thermal parameters for $ZnMo_8O_{10}$[a]

atoms	B11 or B	B22	B33	B12	B13	B23
Mo1	.29(3)	.25(3)	.15(3)	.0	.0	.01(3)
Mo2	.34(3)	.25(2)	.16(3)	.0	.0	.02(3)
Mo3	.24(3)	.23(3)	.20(3)	.0	.0	-.02(2)
Mo4	.29(3)	.23(3)	.12(3)	.0	.0	-.01(2)
O1	.2(2)	.5(2)	.8(3)	.0	.0	-.2(2)
O2	.7(4)	.4(3)	.0(4)	.0	.0	-.1(2)
O3	.2(3)	.3(3)	.4(4)	.0	.0	.1(2)
O4[b]	.4(2)					
O5	.4(3)	.3(3)	.6(3)	.0	.0	.1(2)
Zn	.51(5)	.47(5)	.35(5)	.0	.0	.0

[a]Anisotropic temperature factors are given in the form $\exp[-1/4(B_{11}h^2a^{*2} + B_{22}k^2b^{*2} + \ldots + 2B_{23}k\ell b^*c^*)]$.

[b]O4 was refined isotropically.

Table 5.11. Bond distances (A) for $ZnMo_8O_{10}$

Mo1-Mo1	2.585(2)	Mo1-O1	2.197(6)
Mo1-Mo2	2.9525(2)	Mo1-O2	2.023(9)
Mo1-Mo3	2.836(1)	Mo1-O5	2.068(2)
Mo1-Mo4	2.760(1)	Mo2-O1	2.154(6)
Mo2-Mo2	2.817(2)	Mo2-O3	2.01(1)
Mo2-Mo3	2.680(1)	Mo2-O4	2.07(2)
Mo2-Mo4	2.734(1)	Mo3-O2	2.085(6)
Mo3-Mo3	2.694(2)	Mo3-O4	2.080(7)
	3.202(2)	Mo3-O5	2.19(2)
Mo4-Mo4	2.651(2)	Mo4-O3	2.037(6)
	3.245(2)	Mo4-O4	2.21(2)
Mo3-Mo4[a]	3.223(1)	Mo4-O5	2.108(6)
Mo1-Mo1[a]	3.311(2)	Zn-O2	1.881(9)
Mo2-Mo2[a]	3.079(2)	Zn-O3	1.93(1)

[a]Interchain distance.

Table 5.12. Bond angles (degree) for $ZnMo_8O_{10}$[a]

Mo1-Mo1-Mo2	92.25(2)	O1-Mo1-O1	82.0(4)
Mo2-Mo1-Mo2	173.73(4)[b]	O1-Mo1-O2	86.7(5)
Mo1-Mo2-Mo2	87.75(2)	O1-Mo1-O5	91.8(5)
Mo4-Mo1-Mo1	62.08(2)	O2-Mo1-O5	178.0(4)
Mo4-Mo2-Mo2	58.99(2)	O1-Mo2-O1	88.8(3)
Mo3-Mo1-Mo1	62.89(2)	O1-Mo2-O3	86.7(5)
Mo3-Mo2-Mo2	58.30(2)	O1-Mo2-O4	87.3(5)
Mo4-Mo1-Mo2	57.08(3)	O3-Mo2-O4	171.7(3)
Mo3-Mo1-Mo2	55.12(3)	O2-Mo3-O2	79.5(4)
Mo1-O1-Mo2	85.45(3)	O2-Mo3-O4	90.6(3)
Mo2-O4-Mo4	177.0(5)	O2-Mo3-O4	167.4(4)
Mo3-O4-Mo4	97.3(5)	O2-Mo3-O5	88.5(3)
Mo1-O5-Mo3	179.8(5)	O4-Mo3-O4	97.9(3)
Mo3-O5-Mo4	97.1(5)	O4-Mo3-O5	83.4(5)
O2-Zn-O2	118.2(6)	O3-Mo4-O3	98.6(3)
O2-Zn-O3	110.6(2)	O3-Mo4-O4	88.7(4)
O3-Zn-O3	93.3(6)	O3-Mo4-O5	91.2(2)
		O3-Mo4-O5	166.5(4)
		O4-Mo4-O5	82.2(5)
		O5-Mo4-O5	77.8(4)

[a]The atom labels refer to Fig. 5.2.

[b]This angle corresponds to the dihedral angle between basal planes of adjacent octahedra.

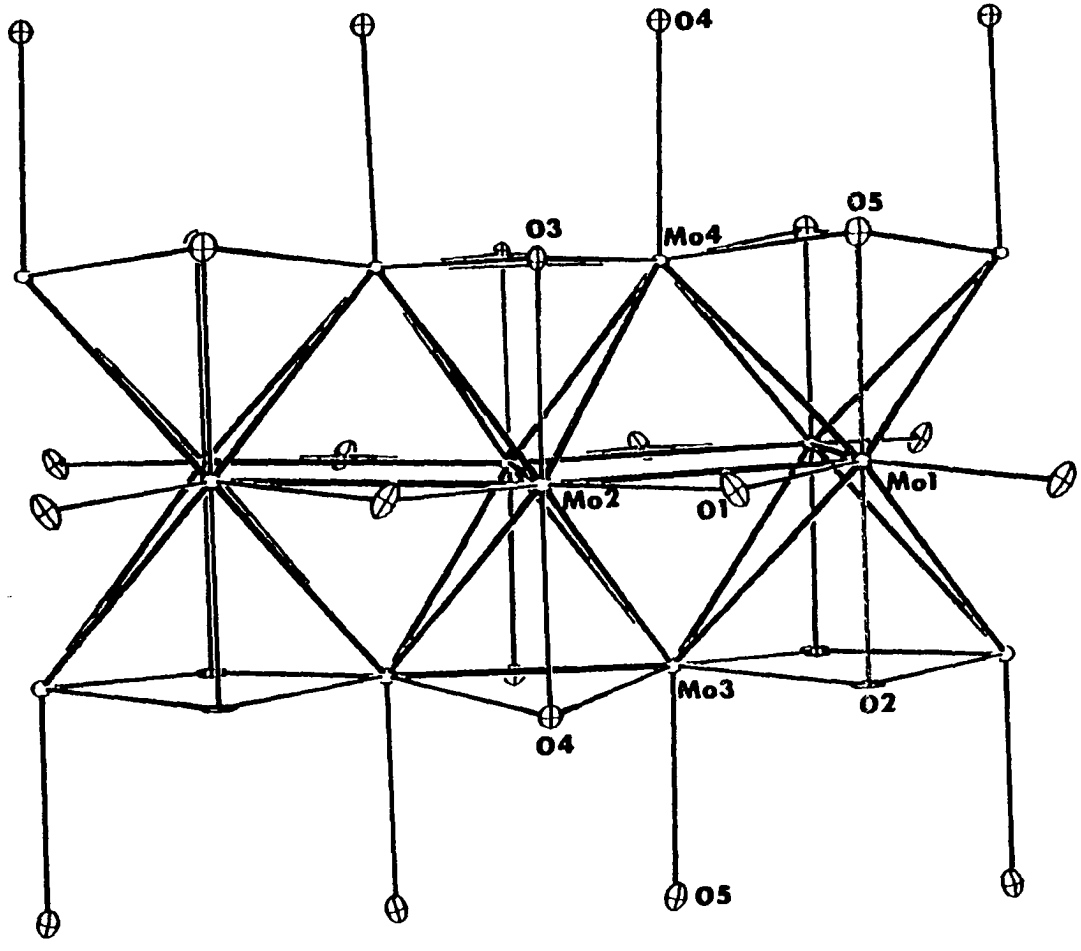

Fig. 5.2. A section of one molybdenum-oxide cluster chain in $ZnMo_8O_{10}$. The Mo-Mo bonds are represented by the thicker lines

Magnetic Susceptibility Studies

Both samples contained a little impurity of molybdenum metal. A very weak line due to MoO_2 was also observed in the x-ray powder pattern for $LiMo_8O_{10}$. Magnetic susceptibility data were measured using the Faraday technique from about 350 to 4 K on 0.2932 g of $LiMo_8O_{10}$ and 0.1864 g of $ZnMo_8O_{10}$ by Dr. F. J. DiSalvo at AT & T Bell Laboratories. Both samples were weakly paramagnetic at room temperature and showed Curie tails at low temperature due to a little magnetic impurities. The data were treated in a similar way as for $InMo_4O_6$ (see SECTION II). The lower curves in Figs. 5.3 and 5.4 represent the susceptibilities with the Curie contributions from impurities subtracted out. There was an obvious anomaly near 200 K for $ZnMo_8O_{10}$. $LiMo_8O_{10}$ was somewhat similar to the zinc compound, but the transition was quite smeared out.

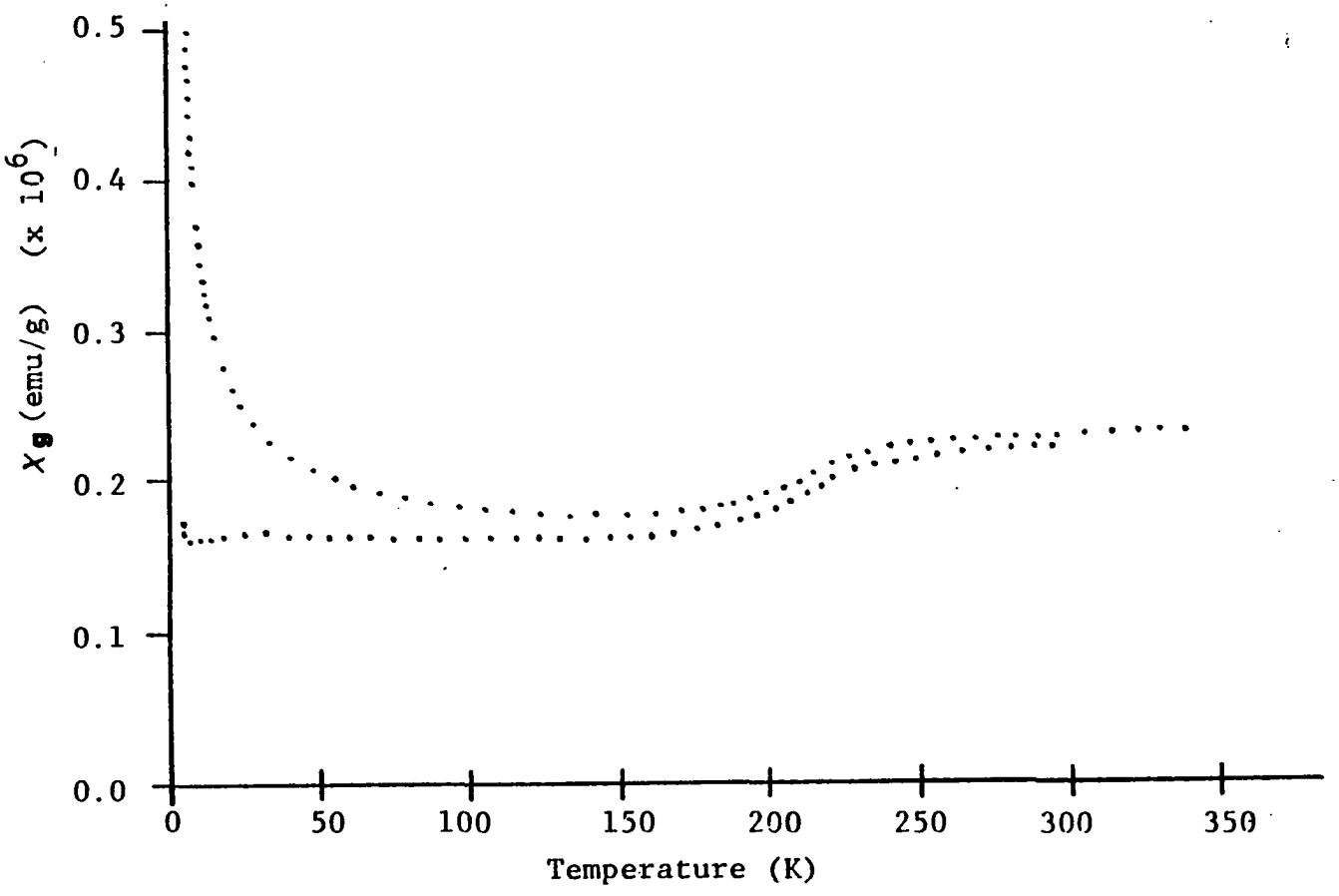

Fig. 5.3. A plot of the gram magnetic susceptibility of $ZnMo_8O_{10}$ powder as a function of temperature. The lower curve represents the susceptibilities with the Curie contribution from impurities subtracted out

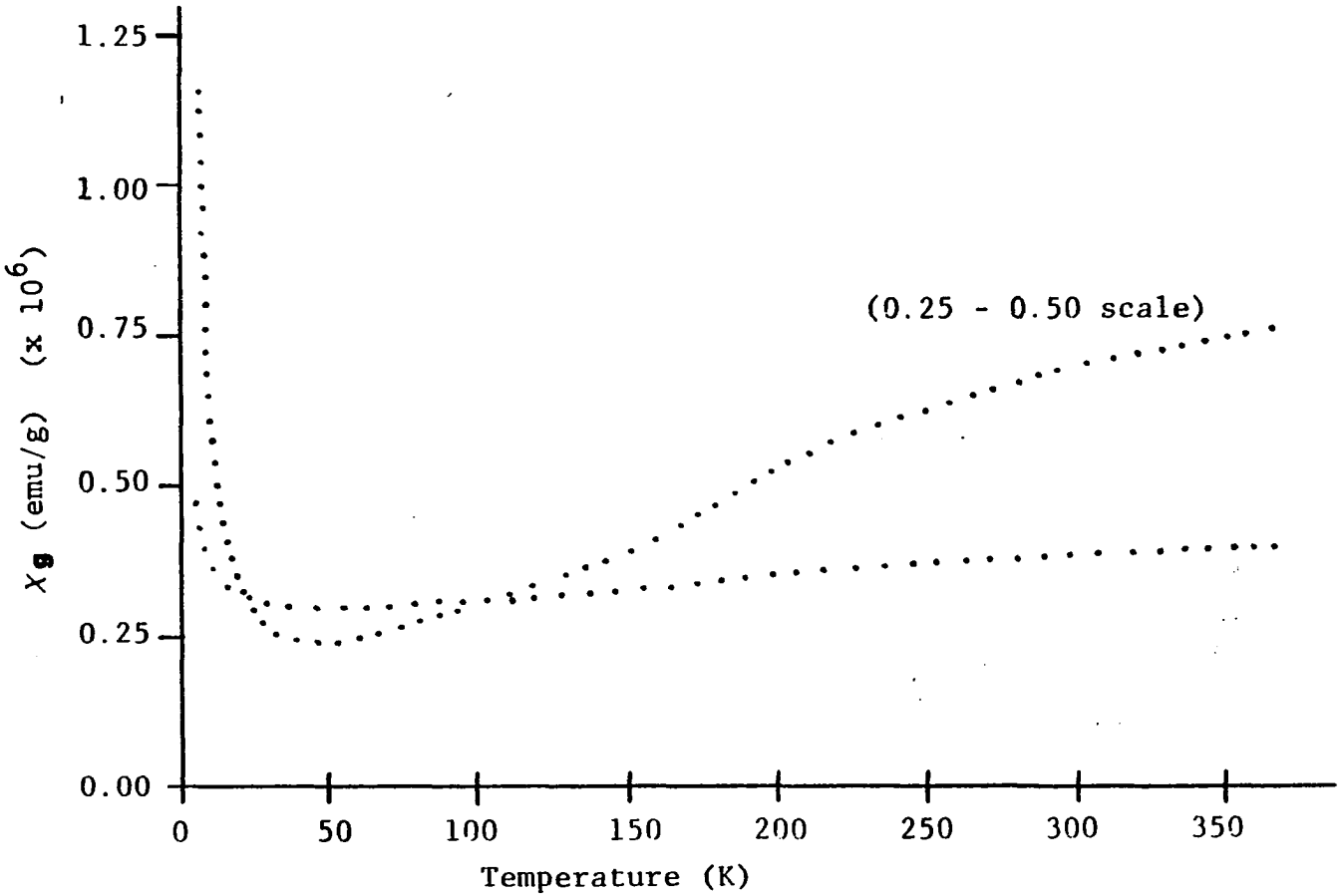

Fig. 5.4. Plots of the gram magnetic susceptibility of $LiMo_8O_{10}$ powder as a function of temperature

DESCRIPTION OF THE CRYSTAL STRUCTURES AND DISCUSSION

The most prominent structural feature of MMo_8O_{10} (M = Li, Zn) is the orthogonal, but nonintersecting molybdenum metal cluster chains. The infinite chains are interlinked in the ab plane by Mo(waist)-O1-Mo(waist) bonding to form layers (Fig. 5.5). In the c direction the layers are connected by Mo-O-M bonding and sharing oxygen atoms. One may regard the infinite chain as a rectangular column. Then, a projection of the MMo_8O_{10} structure along the tetragonal c axis can be represented in Fig. 5.6. In a unit cell, there are four layers of columns with z values equal to 1/8, 3/8, 5/8, and 7/8, respectively. This arrangement can be described in space group $I4_1/amd$ if one disregards the detailed structure in each column. Some of the symmetry elements for space group $I4_1/amd$ are also shown in the figure. Notice that there are glide planes perpendicular to the c axis at z = 1/8 and 3/8 so that the structural features on two sides of a column are glide-plane related. However, for the MMo_8O_{10} structures the a-glide plane does not exist because the hk0 reflections with h odd are present. Thus, the molybdenum metal cluster chains in MMo_8O_{10} are expected to be less symmetric than those in $M_2Mo_4O_7$ (vide infra).

The three space groups Imma, $I4_1/amd$, and Fd3m are related as follows: Imma $\subset$ $I4_1/amd$ $\subset$ Fd3m. Because the ideal spinel

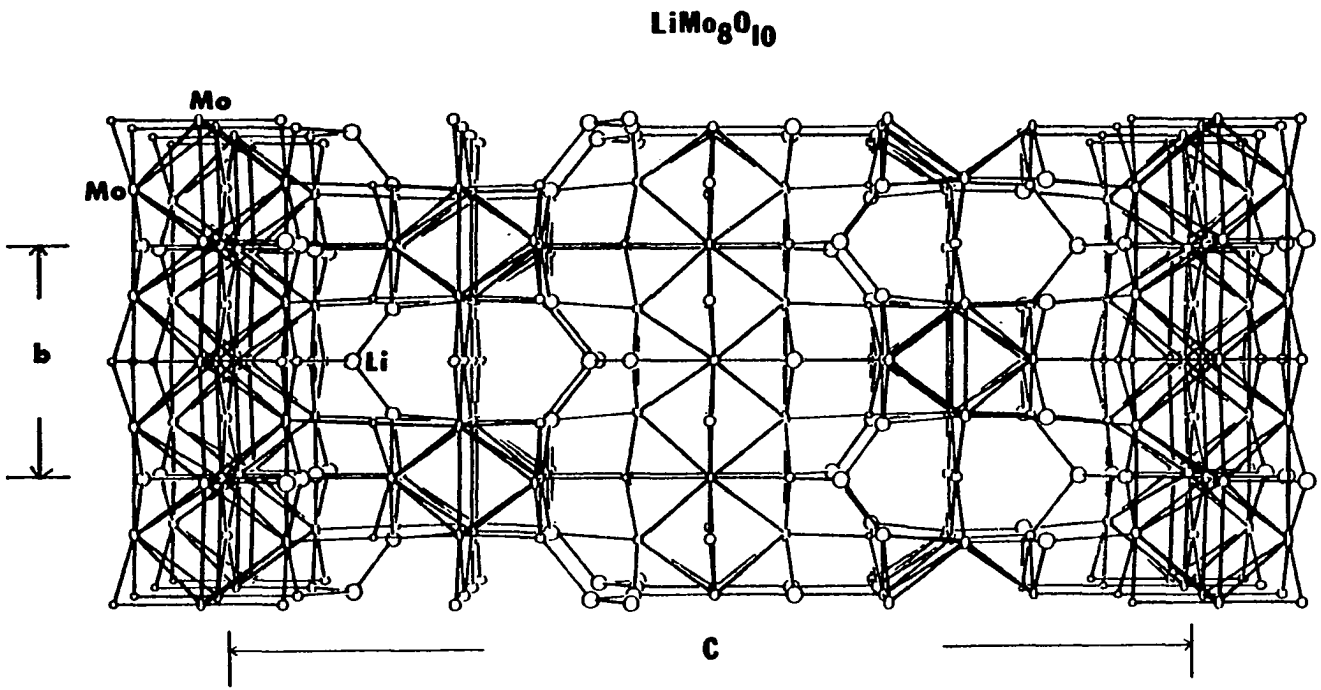

Fig. 5.5. A representation of the structure of $LiMo_8O_{10}$ as viewed down the tetragonal a axis

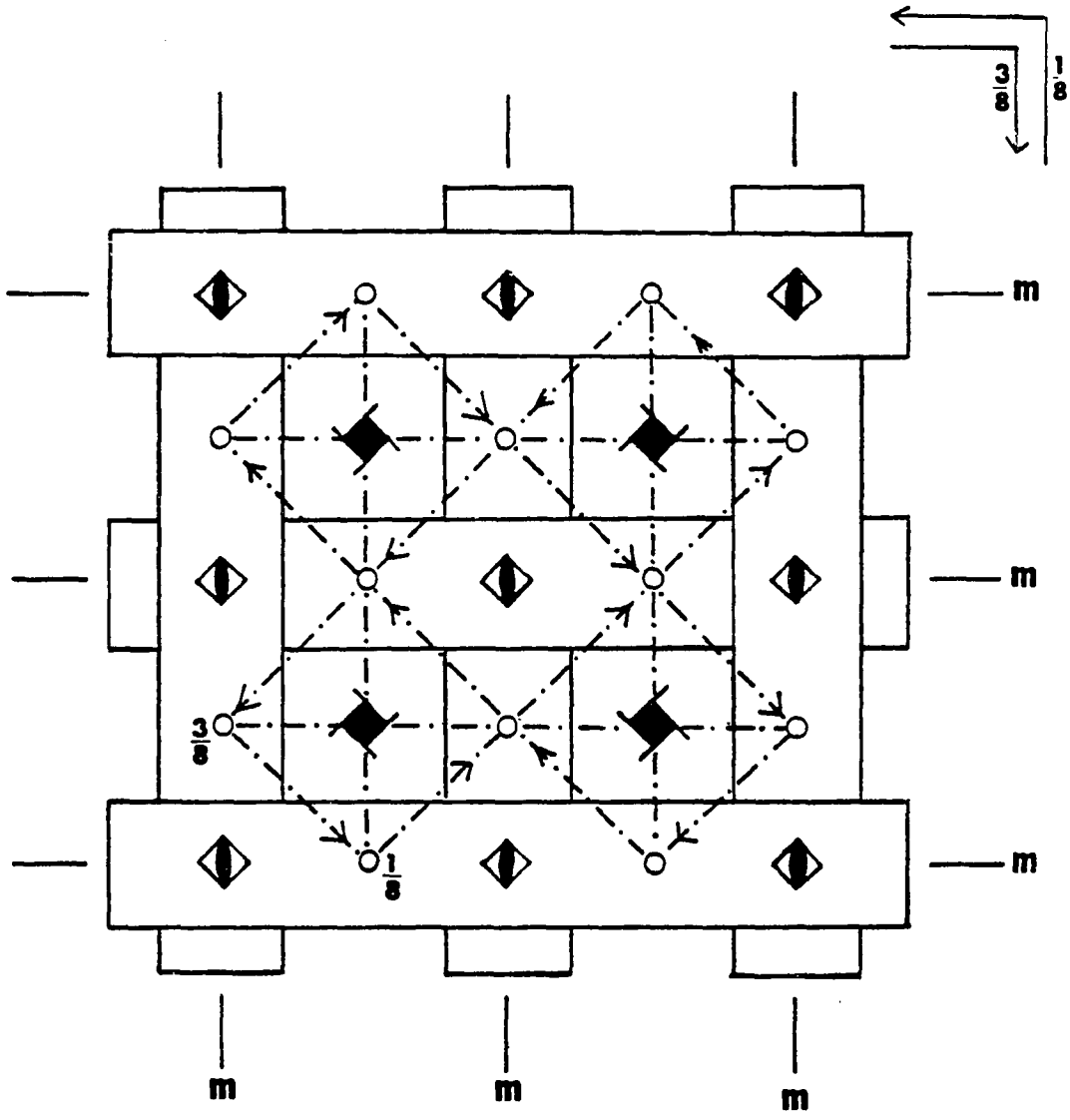

Fig. 5.6. A projection of the MMo_8O_{10} structure along the tetragonal c axis assuming that the molybdenum-oxide chains can be represented by rectangular columns. Positions and directions of the symmetry elements for space group $I4_1/amd$ are indicated

structure has space group Fd3m, one may regard both MMo_8O_{10} and $M_2Mo_4O_7$ as two modifications of the spinel structure. The spinel structure can be considered as a closely packed lattice of oxygen atoms in which half of the octahedral sites and one eighth of the tetrahedral sites are occupied by metal cations. Figure 5.7 shows a projection of the spinel structure on the (001) plane. Four successive layers with z = 1/8, 3/8, 5/8, and 7/8 are shown in the figure. The tetrahedrally coordinated metal cations which are at the 8(a) (0,0,0) special position are not shown in the diagram. Interestingly, the octahedra share trans edges to form infinite ribbons extending parallel to the face diagonals of the cube. The ribbons in one layer are orthogonal to those in the neighboring layers. At this point, one may assume some type of modification on the ideal spinel structure such that the c axis is elongated. Then, the crystal system for the modified structure becomes tetragonal. If one keeps the same axes of reference, the unit cell remains F-centered. Conventionally, one should choose shortest lattice vectors which are indicated by dashed lines in Fig. 5.7. With a conventional choice of axes, the unit cell has space group $I4_1/amd$. In the structure, the orthogonal ribbons in the neighboring layers are still equivalent. One may suppose there is a further modification such that the ribbons in two neighboring layers are not symmetry related. Then, the 4_1 axis no longer exists and the space group lowers to Imma. If the ribbons in the

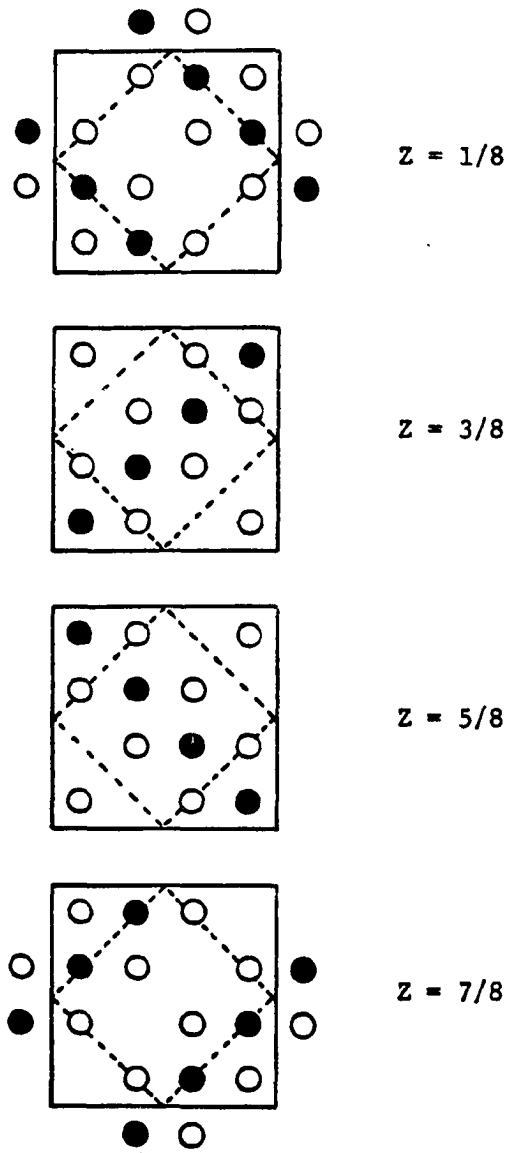

Fig. 5.7. Spinel structure, projected on (001). The four diagrams show successive layers of the structure. The solid and open circles represent octahedral metal and oxygen atoms, respectively. The tetrahedral metal atoms sites are not shown in the figure. A smaller unit cell for space group $I4_1/amd$ is indicated by the dashed lines

tetragonal spinel structure are replaced by the molybdenum metal cluster chains, then the structure becomes essentially the same as MMo_8O_{10}. The orthogonal chains have to be distorted so that the repeat distances along a and b directions are equal. The $M_2Mo_4O_7$ structure has orthorhombic space group Imma because the neighboring layers contain entirely different chains.

These compounds have an ordered defect sodium chloride structure. The unit cell can be divided into twelve sections which are perpendicular to the c axis of the MMo_8O_{10} structure and correspond to the {h00} planes of the rock salt structure. Six of the twelve sections are shown in Fig. 5.8 and the other six sections can be generated by the I-centering operation. The unit cell and the z value for each section are designated in the figure. The solid and open circles represent molybdenum and oxygen atoms, respectively. In fact, both the molybdenum and oxygen atoms are slightly off each section primarily because of the distortion in the chain. The Mo-Mo bonds are not shown for clarity. The ternary metal cations which are not shown in the diagram are located at the sections with z values approximately equal to 0, 1/4, 1/2, and 3/4. Only 1/8 of the tetrahedral sites in each of the sections are occupied by the ternary metal cations. Each section contains four oxygen and four molybdenum atoms if it is fully loaded. Two oxygen or two molybdenum sites are vacant in each section in an ordered way such that there are 4 lithium, 32

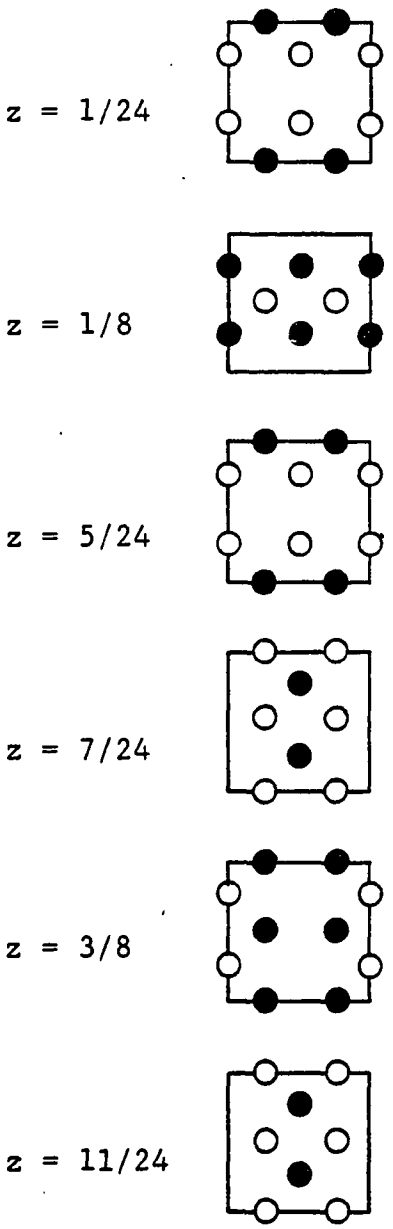

Fig. 5.8. The MMo_8O_{10} structure, projected on (001). The six diagrams show successive layers of the structure. The solid and open circles represent Mo and O atoms, respectively. The ternary metal cation sites are not indicated in the figure

molybdenum, and 40 oxygen atoms in one unit cell. Note that in the first three sections in Fig. 5.8, the vacant sites are along a unit cell edge. In the next three sections, the vacancies are in a perpendicular direction. Both the apex and the waist molybdenum atoms reside on mirror planes. Because there is no symmetry element perpendicular to the tetragonal c axis, the structure contains two crystallographically different apex Mo and two waist Mo atoms. Figure 5.9 shows the molybdenum metal cluster chains of both $LiMo_8O_{10}$ and $ZnMo_8O_{10}$ for comparison. It appears that the octahedral cluster in the zinc-containing compound is even more distorted than the lithium analogue. The waist-waist bond distance in the cluster chain direction in either compound is markedly elongated. There are two different Mo(waist)-Mo(waist) bond distances perpendicular to the chain direction. One of them is significantly longer as the nearest neighboring Mo(apex)-Mo(apex) bonds are shorter. The Mo(apex)-Mo(apex) bond distances on both sides of the cluster chain are alternately short and long. However, the alternation in Mo3-Mo3 distances for $LiMo_8O_{10}$ is considerably less significant.

The ternary metal cations are located on 4a special positions and have a local symmetry of C_{2v}. Therefore, there are two different M-oxygen bond distances. The Li-03 bond distance (1.70 A) is unusually short. The Zn-0 bond lengths are a little shorter than the predicted value (1.98 A) using the effective ionic radii from Shannon (12).

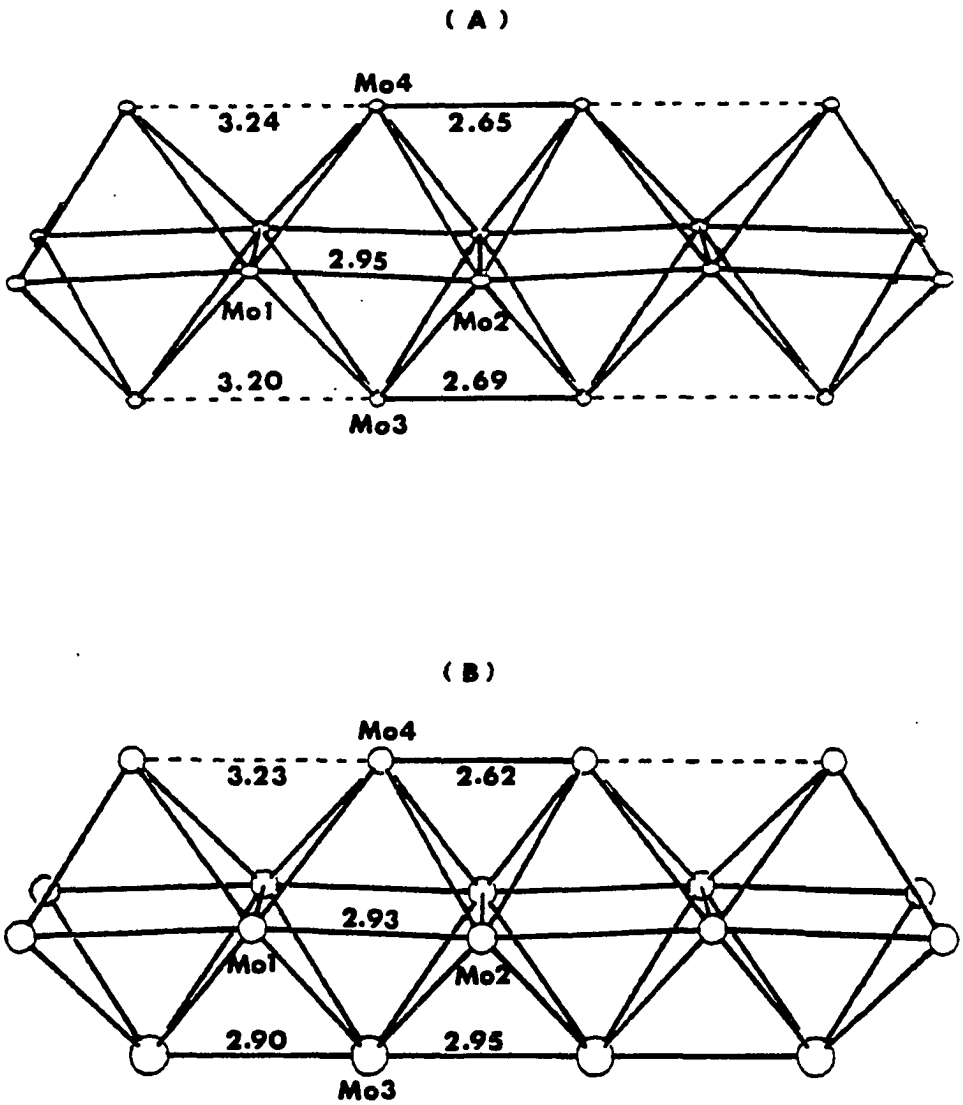

Fig. 5.9. Sections of molybdenum metal cluster chains in (a) $ZnMo_8O_{10}$ and (b) $LiMo_8O_{10}$

The five crystallographically different oxygen atoms can be grouped into three distinct types according to their coordination geometries (Fig. 5.10). Both O2 and O3 are pseudo-tetrahedral. They are coordinated by three molybdenum and one ternary metal atoms. Oxygen 1 is coordinated by four waist Mo atoms in an approximately square-planar symmetry. Oxygen 4 and 5 are each bonded to two apex Mo, one waist Mo, and one apex Mo in the neighboring chain in a sawhorse geometry. In fact, the coordination environments for the oxygen atoms in the MMo_8O_{10} structures are similar to those in the $M_2Mo_4O_7$ structures.

The observed anomalies in magnetic susceptibilities in $ZnMo_8O_{10}$ and $LiMo_8O_{10}$ are mostly likely due to charge density wave (CDW) formations because the crystal structures have low-dimensional character. The opening of the CDW gaps led to a decrease of the density of states at the Fermi level, which in turn results in the decrease of χ below the transition temperature. Similar behaviors were also observed in the two quasi two-dimensional metallic oxides, η-Mo_4O_{11} and γ-Mo_4O_{11} (13). A further study of the transport and magnetic properties on single crystals of MMo_8O_{10} (M = Zn, Li) should provide very interesting and informative results.

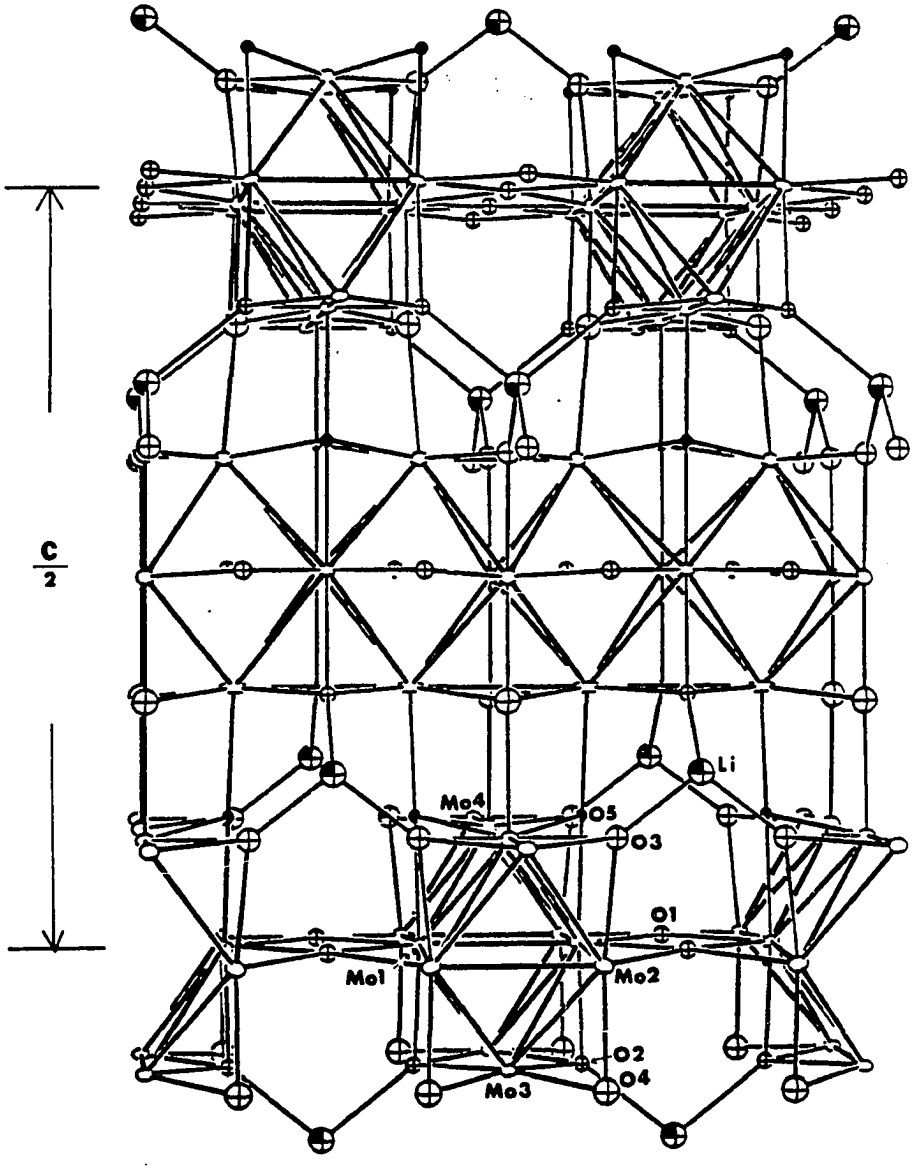

Fig. 5.10. A section of the structure of $LiMo_8O_{10}$ as viewed down the tetragonal a axis. Open ellipsoids are Mo, crossed spheres O, and shaded spheres Li.

REFERENCES

1. Torardi, C. C.; McCarley, R. E. J. Am. Chem. Soc. 1979, 101, 3963.

2. Carlson, C. D.; McCarley, R. E. presented at the 11th Midwest High Temperature Chemistry Conference, Ames, Iowa State University, Iowa, June 1985.

3. Schwartz, K. B.; Prewitt, C. T.; Shannon, R. D.; Corliss, L. M.; Hastings, J. M.; Chamberland, B. L. Acta Crystallogr. 1982, B38, 363.

4. Cahen, D.; Ibers, J. A.; Wagner, J. B., Jr. Inorg. Chem. 1974, 13, 1377.

5. Brown, I. D.; Cutforth, B. D.; Davies, C. G.; Gillespie, R. J.; Ireland, P. R.; Vekris, J. E. Can. J. Chem. 1974, 52, 791.

6. Jacobson, R. A. J. Appl. Crystallogr. 1976, 9, 115.

7. Karcher, B. A. Ph.D. Dissertation, Iowa State University, Ames, Iowa, 1981.

8. Hanson, H. P.; Herman, F.; Lea, J. D.; Skillman, S. Acta Crystallogr. 1964, 17, 1040.

9. Templeton, D. H. In "International Tables for X-Ray Crystallography", 1st ed.; Macgillavry, C. H. and Rieck, G. D., Eds.; Kynoch Press: Birmingham, England, 1962; Vol. III, page 215.

10. Rohrbaugh, W. J.; Jacobson, R. A. Inorg. Chem. 1974, 13, 2535.

11. This E&A four-circle diffractometer was modified in Dr. R. A. Jacobson's laboratory. Stepping motors and encoders were attached and interfaced to a LSI/11 computer, which in turn was interfaced to a VAX11/730 computer. It is equipped with a scintillation counter and incorporates a graphite monochromator in the detection system.

12. Shannon, R. D. Acta Crystallogr. 1976, A32, 751.

13. Guyot, H.; Schlenker, C.; Fourcaudot, G. Lecture Notes in Physics 1985, 217, 133.

SECTION 6. SYNTHESES, CRYSTAL STRUCTURES, AND PROPERTIES OF $Fe_{1.67}Mo_{1.33}O_4$ AND $Gd_4Mo_4O_{11}$

INTRODUCTION

This section reports two different structures. The first one is the spinel $Fe_{1.67}Mo_{1.33}O_4$ which was mentioned in SECTION 4 of this thesis. The second structure which was briefly discussed in SECTION 3 is $Gd_4Mo_4O_{11}$. Their syntheses, x-ray powder data, x-ray single-crystal structures, and properties will be presented.

$Fe_{1.67}Mo_{1.33}O_4$

Experimental and Results

Materials

The materials used were Aldrich Mo powder (99.99%), Thermo-Electron Mo tubing (99.97%), Baker Fe_2O_3 (99.2%), and MoO_3 (99.9%).

Syntheses and analyses

As mentioned in SECTION 4 of this thesis black octahedral crystals were discovered in a reaction to prepare "$FeMo_2O_4$" at 1500°C. Analyses on six octahedral crystals by the electronmicroprobe method gave Mo/Fe (mole ratio) = 0.78(5). Subsequently, a reaction was performed to prepare $Fe_{1.67}Mo_{1.33}O_4$ by heating a pelletized sample containing a stoichiometric mixture of Fe_2O_3, MoO_3, and Mo at 1450°C for 2 days. A Guinier powder pattern of the bulk product showed that a very weak reflection was due to Mo metal and that all other lines could be indexed with a face-centered cubic unit cell with a = 8.5316(7) A. The x-ray powder pattern is given in Table 6.1 with the calculated interplanar d-spacings and intensities.

Table 6.1. X-ray powder diffraction data for $Fe_{1.67}Mo_{1.33}O_4$

d-spacings (A)		intensities		
obsd.	calcd.	obsd.	calcd.[a]	hkℓ
4.931(7)	4.9257	m-s	36	111
3.017(2)	3.0164	m	23	220
2.574(2)	2.5724	vs	100	311
2.463(2)	2.4629	m	22	222
2.133(1)	2.1329	m-s	31	400
1.957(1)	1.9573	w	6	331
1.7416(8)	1.7415	w	5	422
1.6421(7)	1.6419	m-s	41	511, 333
1.5088(5)	1.5082	m-s	46	440
1.4421(5)	1.4421	w	4	531
1.3012(4)	1.3011	w	8	533
1.2856(4)	1.2862	w	11	622

[a]Intensities were calculated with a computer program (1).
$a = b = c = 8.5316(7)$ A, $\alpha = \beta = \gamma = 90^{o}$.

Single crystal x-ray structure determination

One small octahedral crystal was selected and its crystal quality was confirmed by the sharp reflections on the oscillation pictures. The crystal was indexed on the AL four-circle diffractometer (2) as F-centered cubic. The indexing procedures have been described in the previous sections. Three strong, high-angle reflections were used to determine the accurate orientation matrix. Important crystallographic parameters are given in Table 6.2. The intensity data were treated for Lorentz and polarization effects, but the absorption correction was not applied. Scattering factors (3) for neutral atoms were used throughout the calculations. Both the real ($\Delta f'$) and imaginary ($\Delta f''$) components of anomalous dispersion (4) were included for Mo and Fe atoms.

Upon examination of the data set, its was found that all reflections with $h + k + \ell = 2n + 1$ were unobserved and all $h0\ell$, $0k\ell$, and $hk0$ reflections except two weak ones (200, 002) were not observed unless $h + k$, $h + \ell$, or $k + \ell$ is equal to $4n$, respectively. The data were averaged in m3m symmetry with R(int) = 3.06%. Two reflections (200, 002) were eliminated in the data averaging because $|F_o - F_o(ave)| > 6.0\sigma(F_o)$. Thus, space group Fd3m was selected. The structure was initially refined on the basis of "$FeMo_2O_4$". The Mo atoms were at 16d special positions (1/2,1/2,1/2), Fe atoms were at 8a special positions (1/8,1/8,1/8), and oxygen atoms were at 32e special positions (x,x,x). A few cycles of least-squares refinement

with anisotropic thermal parameters for all atoms led to R = 7.6%, R_w = 9.0%. The electronmicroprobe analysis result suggested that there must be some iron atoms at the octahedral sites and the possible stoichiometry was $Fe[Fe_xMo_{2-x-y}\square_y]O_4$, where $\square$ denotes the vacant site. Two extreme compositions were $Fe[Fe_{0.25}Mo\square_{0.75}]O_4$ and $Fe[Fe_{0.67}Mo_{1.33}]O_4$. The weighted average of atomic scattering factors for the octahedral sites were used in the least-squares refinements. The former stoichiometry was not correct because both the temperature factors and R values increased too much. For the latter stoichiometry, R = 7.3%, R_w = 8.4%, and the temperature factors remained about the same. All the intermediate stoichiometries were found to be less likely because their R values were higher than 7.3% and 8.4%, respectively. The results from single-crystal x-ray data were in good agreement with the microprobe analysis results.

The three strongest reflections showed that there is a secondary extinction effect. The secondary extinction factor ($g = 5.7 \times 10^{-6}$) was obtained by plotting F_c/F_o vs I_c. Using the data after extinction correction and based on the stoichiometry of $Fe[Fe_{0.67}Mo_{1.33}]O_4$, a few cycles of least-squares refinement converged at R = 4.9%, R_w = 5.8%, and residual electron density on the final difference map was less than 0.1 e/A^3. The x value for the 32e special position was 0.256(1). The positional and thermal parameters are listed in Table 6.3.

Table 6.2. Crystallographic data for $Fe_{1.67}Mo_{1.33}O_4$

---

crystal system: cubic
space group: Fd3m
a = 8.5316(7) A
V = 621.0(2) A^3
Z = 8
d(calcd) = 6.096 g/cm^3
crystal size: 0.1 x 0.1 x 0.1 mm^3
diffractometer: AL[a]
radiation: Mo Kα (λ = 0.70964 A)
monochromator: oriented graphite
scan type: ω-scan
automatic background detn, max scan half width: 0.5 degree
std reflns: 3 measured every 75 reflns; no significant variation in intensity.
reflns measd: hkℓ
max 2Θ: 50^o
reflns collected: 134 collected (symmetry extinct reflns not included), 127 observed ($I > 3\sigma(I)$)
no. of unique reflns with $I > 3\sigma(I)$: 38
no. of parameters refined: 7
R = 0.049[b], R_w = 0.058[c]
quality-of-fit indicator[d]: 3.06

---

[a]For details of the AL diffractometer, see reference 2.

[b]$R = \Sigma||F_o| - |F_c||/\Sigma|F_o|$.

[c]$R_w = [\Sigma w(|F_o|-|F_c|)^2/\Sigma w|F_o|^2$; $w = 1/\sigma^2(|F_o|)$.

[d]Quality of fit =

$[\Sigma w(|F_o|-|F_c|)^2/(N(observns)-N(parameters))]^{1/2}$.

Table 6.3. Positional and thermal parameters for $Fe_{1.67}Mo_{1.33}O_4$

atom	position	x[a]	B11[a]	B12[a]
O	32e	0.256(1)	2.5(4)	0.2(3)
Fe	8a	1/8	3.1(2)	0.0
Mo/Fe[b]	16d	1/2	2.6(2)	1.4(1)

[a]B11 = B22 = B33; B12 = B13 = B23; x = y = z.

[b]Special positions (16d) are 2/3 and 1/3 occupied by Mo and Fe, respectively.

Magnetic susceptibilities study

The sample was checked for purity by means of an x-ray powder pattern. Magnetic susceptibilities data were obtained using a SQUID instrument from 4 K to 380 K on 13.13 mg of powder by Dr. Robert N. Shelton. Figures 6.1 and 6.2 show the plots of χ_M vs. T and χ_M^{-1} vs. T at H_o = 1.0 KG, indicating a ferrimagnetic material. A least-squares fit to Curie-Weiss law, $\chi_M = C/(T - \Theta)$, in the temperature range 269 - 380 K was performed. The calculation led to $\chi_M = 5.59/(T + 385)$. The effective magnetic moment, calculated from $\mu_{eff} = 2.828(C^{1/2})$ is 6.68 μ_B which is somewhat higher than than the spin only value (6.33 μ_B) for noninteracting high-spin Fe^{2+}, that is $\mu_{eff} = [1.67 \times (\mu_{Fe}{}^{2+})^2]^{1/2}$. The Neel temperature is at about 210 K which is the highest among $Fe_{1.89}Mo_{4.11}O_7$ (190 K), $Sc_{0.5}Fe_{1.5}Mo_4O_7$ (110 K), and $Al_{0.4}Fe_{1.4}Mo_{4.1}O_7$ (80 K) (5). However, the Neel point of Fe_2MoO_4 is at 348 K (6).

Description of the Structure and Discussion

The spinel $Fe_{1.67}Mo_{1.33}O_4$ along with $Fe_{1.89}Mo_4O_7$ (5), $Fe_2Mo_3O_8$ (7), and the spinel Fe_2MoO_4 (8) constitute all the examples in the Fe-Mo-O system with molybdenum atoms in the oxidation states lower than 4+. The spinel structure can be considered as a closely packed lattice of oxygen atoms in which half of the octahedral sites and one eighth of the tetrahedral sites are occupied by metal cations. In

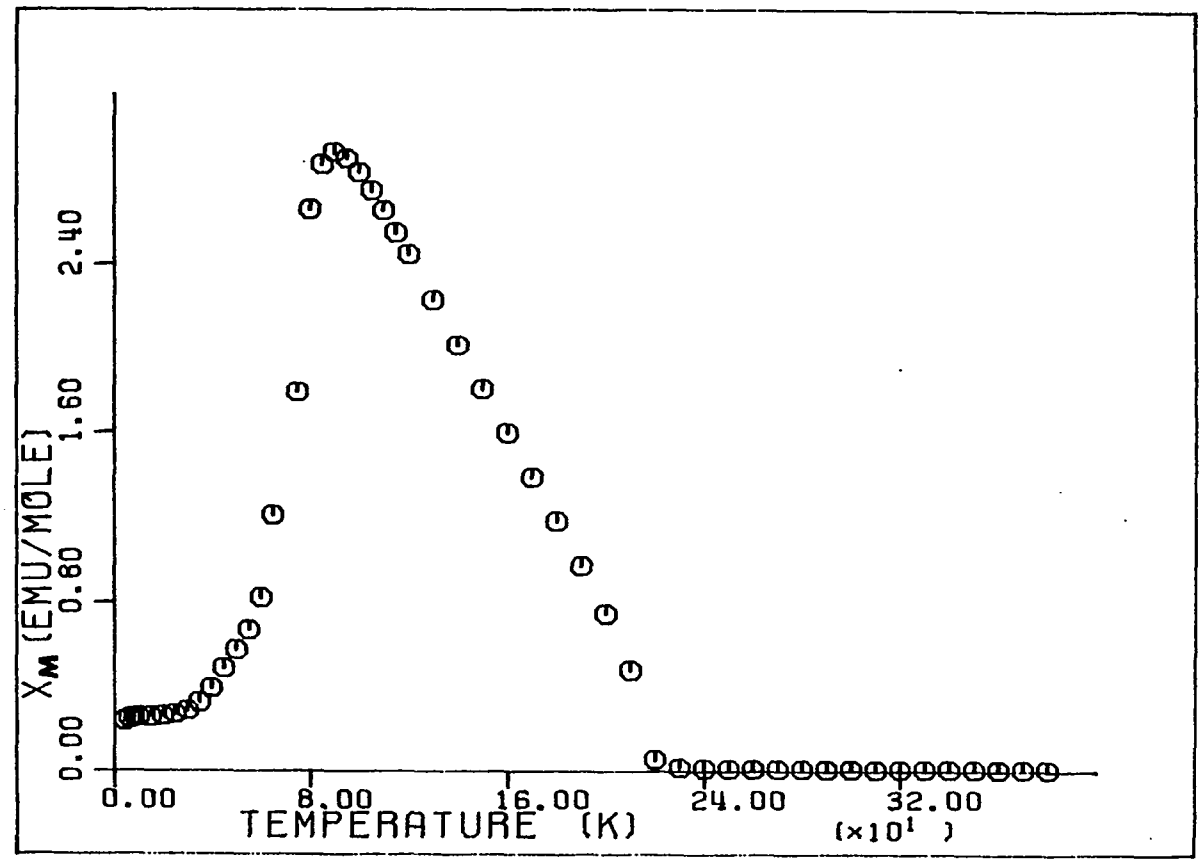

Fig. 6.1. A plot of the molar magnetic susceptibility of $Fe_{1.67}Mo_{1.33}O_4$ powder as a function of temperature

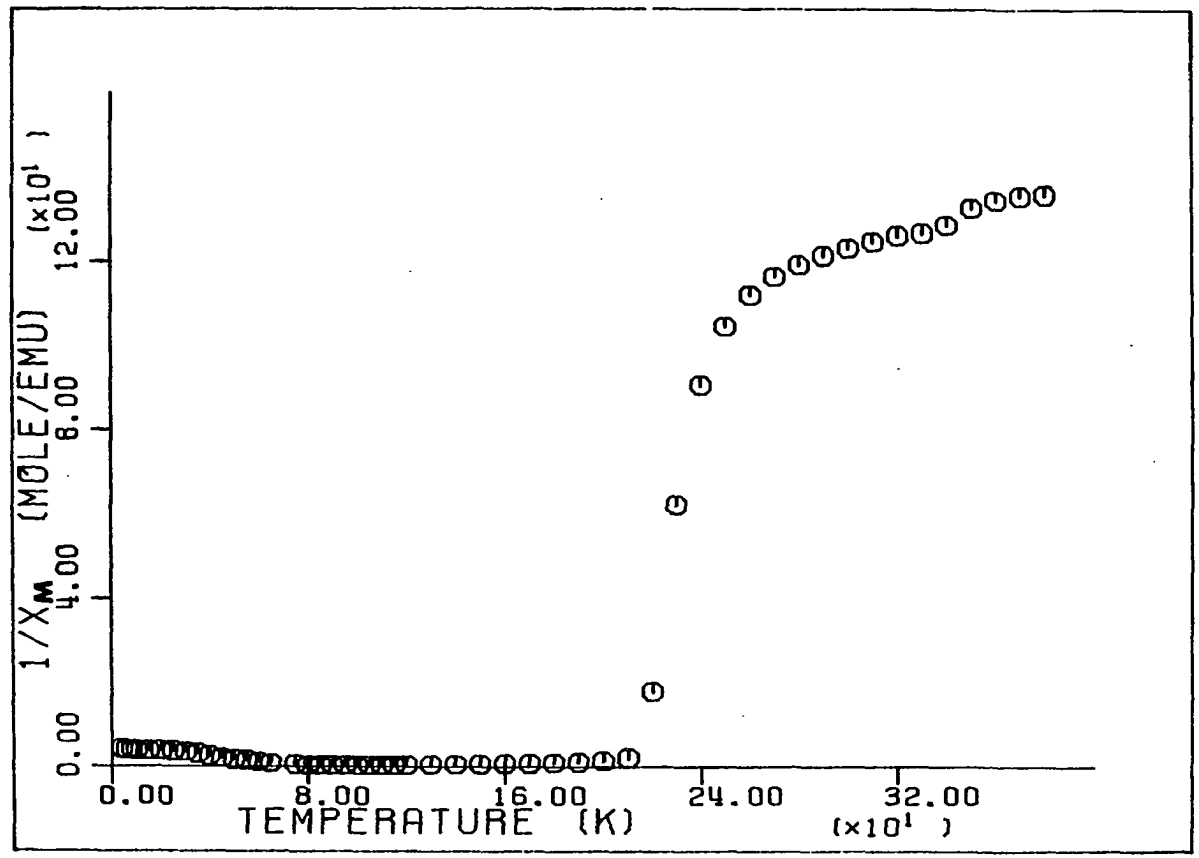

Fig. 6.2. A plot of the inverse molar magnetic susceptibility of $Fe_{1.67}Mo_{1.33}O_4$ powder as a function of temperature

$Fe_{1.67}Mo_{1.33}O_4$, one-third of the molybdenum atoms are replaced by the iron atoms. The exact arrangement of the molybdenum atoms at the octahedral sites is not known so far. Although the x-ray powder pattern did not reveal any superlattice reflections, film work on a single crystal may provide further insight of the crystal structure. The thermal parameters for all three atoms appear somewhat larger than they should be, implying a more complicated structure.

Some important interatomic distances are listed below: d(Mo-O) = 2.086(9), d(Fe-O) = 1.93(2), d(Mo-Mo) = 3.0164(2) A. Using the bond-length bond-strength relationships for Mo-O and Fe-O bonds (9), we have found that the formal oxidation states for the Mo, the tetrahedral Fe, and the octahedral Fe are 3.2, 2.4, and 2.4, respectively. The estimated oxidation states are a little higher than those in $Sc_{0.5}Fe_{1.5}Mo_4O_7$, but slightly lower than those in $Al_{0.4}Fe_{1.5}Mo_{4.1}O_7$. The effective magnetic moment (6.68 μ_B) calculated from the data points in the paramagnetic state is also between the values for ScFeMoO (6.11 μ_B) and AlFeMoO (6.92 μ_B). The molybdenum atoms in $Fe_{1.67}Mo_{1.33}O_4$ should have no resultant spin moment because there is likely bonding interaction among them. The effective charge on the iron atoms in $Fe_{1.67}Mo_{1.33}O_4$ are probably a little higher than 2+. A Mossbauer spectroscopy study on this interesting spinel may provide more conclusive results.

$Gd_4Mo_4O_{11}$

Experimental and Results

Materials

Gd_2O_3 was obtained from Ames Laboratory. Other starting materials used were Aldrich Mo powder (99.99%), Thermo-Electron Mo tubing (99.97%), Alfa Mo foil (99.97%), and Baker MoO_3 (99.9%).

Synthesis

As mentioned in SECTION 3 of this thesis, columnar crystals of $Gd_4Mo_4O_{11}$ were discovered in a reaction to prepare "$Gd_2Mo_8O_{16}$" at 1450°C. The stoichiometry of the crystal was not known until its single crystal x-ray structure was solved. The reaction product was qualitatively analyzed by the method of emission spectroscopy to check the purity of the starting rare earth oxide (10). Subsequently, a reaction to prepare pure $Gd_4Mo_4O_{11}$ was conducted. A pressed pellet containing a stoichiometric amount of Gd_2O_3, MoO_3, and Mo was wrapped with a sheet of molybdenum foil, sealed in an evacuated silica tube, and then fired at 1250°C for 2 days. A Guinier powder pattern of the bulk product indicated that it was essentially pure. No crystals which were big enough for single crystal x-ray structure determination could be obtained at the reaction temperature (1250°C). Considerably higher temperatures are

necessary for the growth of bigger crystals.

Preliminary film work and x-ray powder diffraction

Most of the columnar crystals in the reaction product were either too small or multiple crystals. A small crystal of dimensions 0.10 x 0.04 x 0.02 mm was selected for data collection even though the film work indicated that the crystal was probably a twinned crystal. Axial oscillation and hk0-hkl layer photographs were registered. It has mmm Laue symmetry with the unit cell constants a = 10.7, b =16.0, c = 5.67 A. Systematic absences were h = 2n for h0ℓ and k = 2n for 0kℓ. The possible space groups thus were Pbam and Pba2.

The Guinier powder pattern is listed in Table 6.4 along with the calculated interplanar distances. A least-squares fit of the peak positions of 30 reflections gave a = 10.802(2), b = 15.998(4), c = 5.698(1) A. They will be used in later calculations.

Single crystal x-ray structure determination

The crystal was indexed on the DATEX four-circle diffractometer as primitive orthorhombic. The indexing procedures have been described in the previous sections. Important crystallographic parameters are listed in Table 6.5. The intensity data were treated for Lorentz and polarization effects, and an empirical absorption correction was also applied. Scattering factors (3) for neutral atoms were used.

Table 6.4. X-ray powder diffraction data for $Gd_4Mo_4O_{11}$

d-spcaings (A) observed	d-spcaings (A) calculated	intensities	hkℓ
8.96(2)	8.952	w-m	110
8.01(1)	7.999	w	020
5.400(7)	5.401	vw	200
4.783(5)	4.782	vw	130
4.473(4)	4.476	vw	220
4.266(4)	4.264	vw	121
3.918(3)	3.920	vvw	201
3.805(3)	3.807	vw	211
3.519(3)	3.520	w	221
3.255(2)	3.274, 3.214	vw, br	041, 240
3.158(2)	3.158	s	231
3.073(2)	3.068	vvw	150
2.991(2)	2.990	vvw	311
2.848(2)	2.849	m	002
2.801(2)	2.799	w	241
2.701(2)	2.701	w-m	400
2.665(2)	2.666	m	060
2.605(1)	2.605	w	122
2.559(1)	2.559	vvw	420
2.488(1)	2.489	vw	212
2.423(1)	2.422	vw	341
2.279(1)	2.278	vw	232
2.213(1)	2.213	vw	312
2.0870(9)	2.088	vvw	152
2.0638(9)	2.064	w	450
1.9780(8)	1.980	vvw	252
1.9506(8)	1.951	m	342
1.9462(8)	1.947	m	062, 412
1.8981(8)	1.897	m	460
1.7053(6)	1.706	vvw	630
1.6991(6)	1.698	w-m	233
1.6191(5)	1.619	vw	291
1.4940(4)	1.494	vvw	192
1.4244(4)	1.424	w	004

Both the real ($\Delta f'$) and imaginary ($\Delta f''$) components of anomalous dispersion (4) were included for Gd and Mo.

The data set showed the systematic absences h = 2n for h0ℓ and k = 2n for 0kℓ. Since statistical tests favored a centrosymmetric space group, Pbam was selected. The data were averaged in mmm symmetry with R(int) = 0.061. Thirty-one reflections out of 682 were eliminated in the data averaging.

All the heavy atom positions were determined by a hybrid approach of Patterson superposition/direct methods (11) developed by Sue-Lein Wang in Dr. Jacobson's group. The oxygen atoms were located from a subsequent difference Fourier map. A final full-matrix least-squares refinement varying the positional and anisotropic thermal parameters of gadolinium and Mo3 and positional and isotropic thermal parameters of Mo1, Mo2, and oxygen atoms, converged at R = 4.7% and R_w = 5.1% (12). The positional and isotropic equivalent thermal parameters and selected interatomic bond distances are given in Tables 6.6 and 6.7, respectively.

Description of the Structure and Discussion

$Gd_4Mo_4O_{11}$ was also discovered independently by Patrick Gougeon (14) at about the same time. Only the essential structural feature will be discussed.

The most prominent structural feature of $Gd_4Mo_4O_{11}$ is that the molybdenum metal cluster chains are "diluted" with Gd^{3+}

Table 6.5. Crystallographic data for $Gd_4Mo_4O_{11}$

---

crystal system: orthorhombic

space group: Pbam

a = 10.802(2), b = 15.998(4), c = 5.698(1) A

V = 984.7(4) A^3

Z = 4

d(calcd) = 8.021 g/cm^3

crystal size: 0.10 x 0.04 x 0.02 mm^3

abs coeff: 315.6 cm^{-1}

refln used for empirical absorption correction (hkl, 2θ, T(max)/T(min)): 002, 14.36°, 1.44

diffractometer: DATEX[a]

radiation: Mo Kα (λ = 0.70966 A)

monochromator: oriented graphite

scan type: ω-scan

scan half width: 0.6 degree

std reflns: 3 measured every 50 reflns; no significant variation in intensity.

reflns measd: hkℓ, $\bar{h}\bar{k}\ell$

max 2θ: 50°

reflns collected: 1724 collected (symmetry extinct reflns not included), 1143 observed ($I > 3\sigma(I)$)

no. of unique reflns with $I > 3\sigma(I)$: 651

no. of parameters refined: 67

R = 0.047[b], R_w = 0.051[c]

quality-of-fit indicator[d]: 2.03

---

[a]For details of the DATEX diffractometer, see ref. 13.

[b]$R = \Sigma||F_o| - |F_c||/\Sigma|F_o|$.

[c]$R_w = [\Sigma w(|F_o|-|F_c|)^2/\Sigma w|F_o|^2]^{1/2}$; $w = 1/\sigma^2(|F_o|)$.

[d]Quality of fit = $[\Sigma w(|F_o|-|F_c|)^2/(N(observns)-N(parameters))]^{1/2}$.

Table 6.6. Positional parameters for $Gd_4Mo_4O_{11}$

atom	position	x	y	z	$B(A^2)^a$
Gd1	4h	0.5985(2)	0.2384(1)	0.5	0.46
Gd2	4h	0.3798(2)	0.0771(1)	0.5	0.55
Gd3	4g	0.8142(2)	0.2765(1)	0.0	0.54
Gd4	4g	0.5806(2)	0.0986(1)	0.0	0.56
Mo1	4h	0.0824(3)	0.0594(2)	0.5	0.39
Mo2	4g	0.0906(3)	0.0673(2)	0.0	0.30
Mo3	8i	0.8681(2)	0.0840(1)	0.7731(4)	0.42
O1	4g	0.759(2)	0.012(1)	0.0	0.3
O2	4g	0.963(2)	0.162(1)	0.0	0.5
O3	8i	0.184(1)	0.1351(9)	0.258(3)	0.5
O4	4f	0.5	0.0	0.251(4)	0.1
O5	8i	0.459(1)	0.172(1)	0.251(3)	0.7
O6	8i	0.227(1)	0.3277(9)	0.239(3)	0.6
O7	4h	0.950(2)	0.152(1)	0.5	0.3
O8	4h	0.774(2)	0.025(1)	0.5	0.2

[a]The isotropic equivalent thermal parameter is difined as $B = 4/3\ [a^2\beta_{11} + b^2\beta_{22} + c^2\beta_{33} + 2ab(\cos\gamma)\beta_{12} + 2ac(\cos\beta)\beta_{13} + 2bc(\cos\alpha)\beta_{23}]$.

Table 6.7. Selected bond distances (A) for $Gd_4Mo_4O_{11}$[a]

Mo1-Mo1	2.604(6)	Gd1-03	2.62(2) (2x)
Mo1-Mo2	2.8532(5)	Gd1-05	2.32(2) (2x)
Mo1-Mo3	2.817(3)	Gd1-06	2.29(2) (2x)
	2.823(3)	Gd1-07	2.37(2) (1x)
Mo2-Mo2	2.912(6)	Gd2-03	2.69(2) (2x)
Mo2-Mo3	2.742(3)	Gd2-04	2.29(1) (2x)
	2.781(3)	Gd2-05	2.25(2) (2x)
Mo3-Mo3	2.586(5)	Gd2-08	2.32(2) (1x)
	3.112(5)	Gd3-02	2.44(2) (1x)
Mo1-03	2.14(2)	Gd3-03	2.48(2) (2x)
Mo1-07	2.07(2)	Gd3-05	2.27(2) (2x)
Mo1-08	2.06(2)	Gd3-06	2.35(2) (2x)
Mo2-01	2.06(2)	Gd4-01	2.37(2) (1x)
Mo2-02	2.05(2)	Gd4-04	2.30(1) (2x)
Mo2-03	2.08(2)	Gd4-05	2.28(2) (2x)
Mo3-01	2.10(2)	Gd4-06	2.39(2) (2x)
Mo3-02	2.06(2)		
Mo3-06	2.08(2)		
Mo3-07	2.10(1)		
Mo3-08	2.09(1)		

[a]The atom labels refer to Figs. 6.3 and 6.4.

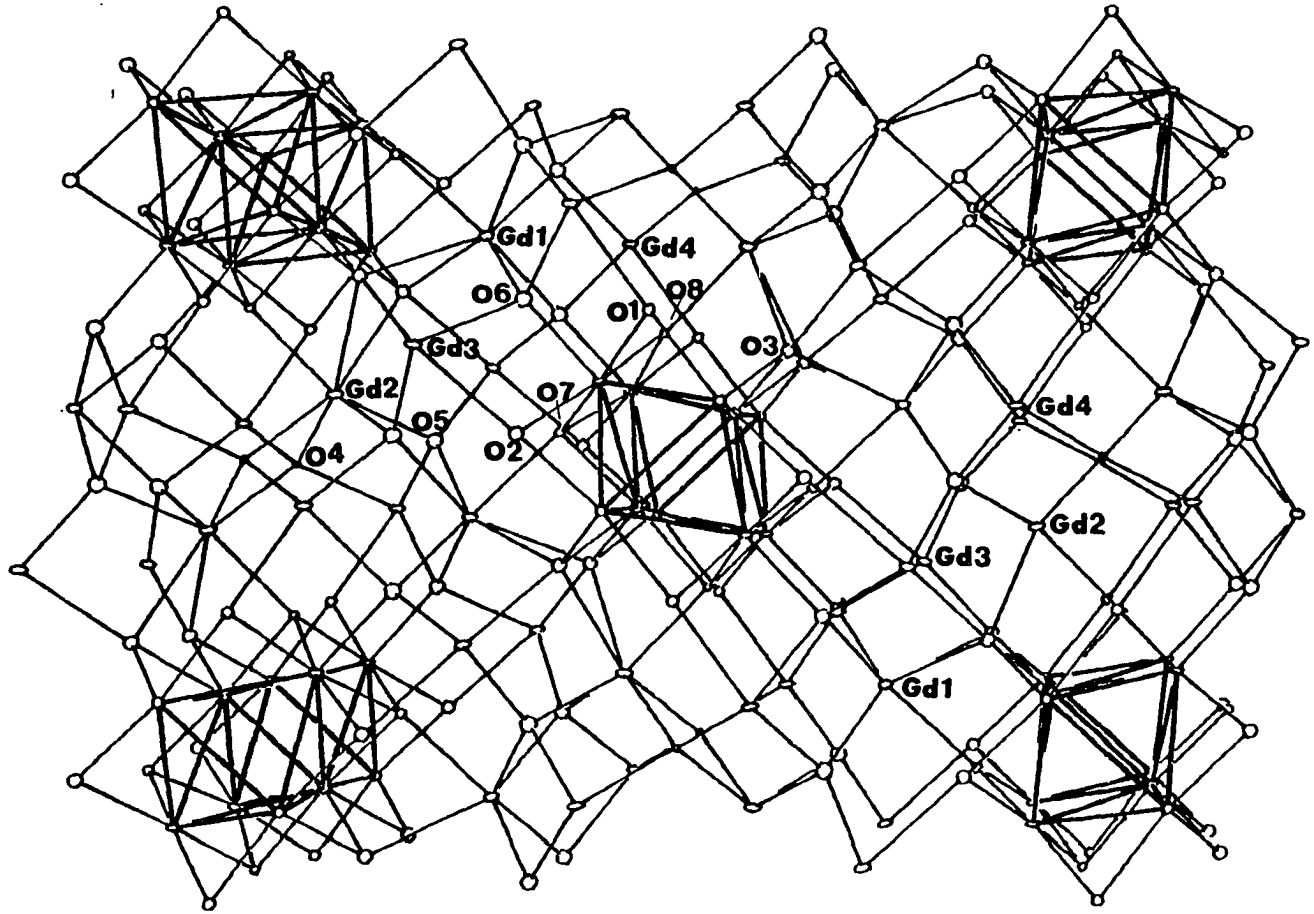

Fig. 6.3. A view of the $Gd_4Mo_4O_{11}$ structure as seen along the c axis. The Mo-Mo bonds are represented by the thicker lines

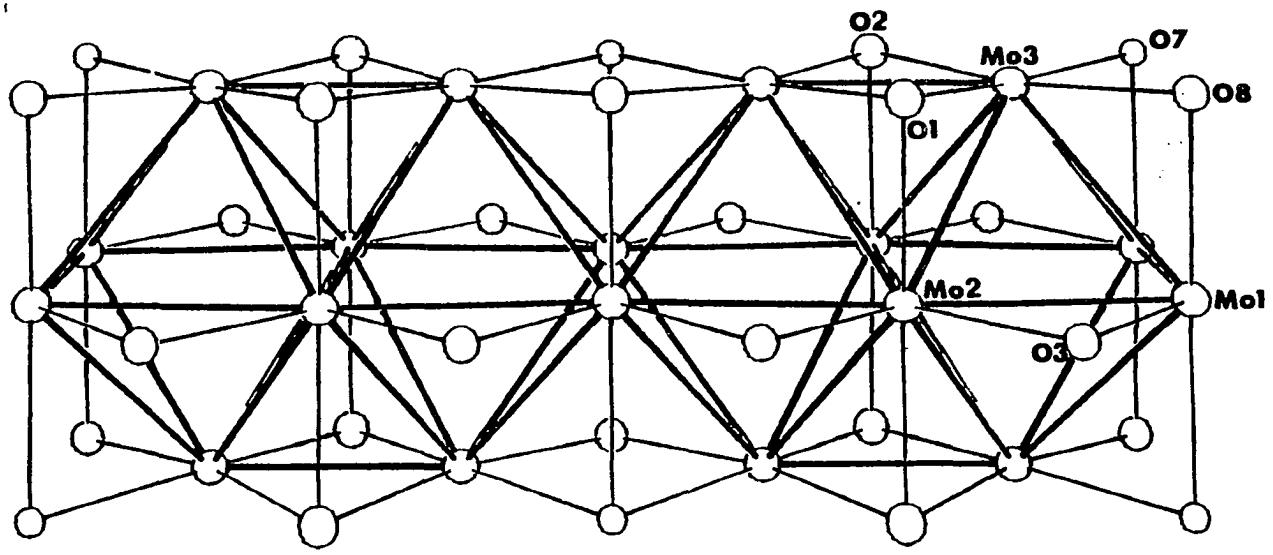

Fig. 6.4. A section of one molybdenum-oxide cluster chain in $Gd_4Mo_4O_{11}$. The Mo-Mo bonds are represented by the thicker lines

cations (Fig. 6.3). The interchain interaction should be negligible. Interestingly enough two crystallographically different oxygen atoms are only bonded to the ternary metal cations. Accordingly, the compound can be formulated as $Gd_4(Mo_4O_8)O_3$ where the Mo_4O_8 repeat unit is the metal cluster chain based on 6-12 building blocks.

The infinite chains (Fig. 6.4) are markedly distorted in a similar way as in $ZnMo_8O_{10}$ (15). The two-fold axes run along the infinite chain direction. The Mo(waist)-Mo(waist) bonds which are shared by adjacent octahedra reside on inversion centers. The basal planes of adjacent octahedra are puckered such that the Mo(apex)-Mo(apex) bond distances are alternately short and long. There are two different Mo(wasit)-Mo(waist) bond distances perpendicular to the chain direction. One of them is significantly longer as the nearest neighboring Mo(apex)-Mo(apex) bond is shorter.

The gadolinium ions are located at 4g and 4h special positions. Each of them is coordinated by seven oxygen atoms in a geometry of monocapped trigonal prism. Using the bond-length bond-strength relationship for Gd-O bond (9), we have found that the effective charges of the four different Gd sites are + 2.90, + 3.11, + 3.00, + 3.35 for Gd1, Gd2, Gd3, and Gd4, respectively. A similar calculation was performed on Mo-O bonds (9). The charges on the three distinct molybdenum atoms are + 2.07, + 2.28, + 2.70 for Mo1, Mo2, and Mo3,

respectively. Then, the total charge on the $Mo_4O_8^{q-}$ repeat unit is equal to -6.2. For the formula $Gd_4(Mo_4O_8)O_3$, $\Sigma q^- = -6.2 - 6 = -12.2$ which is in a good agreement with $\Sigma q^+ = 3 \times 4 = 12$.

The eight crystallographically different oxygen atoms can be classified into five distinct types according to their coordination geometries. Oxygen 1 and 02 are coordinated by three Mo and one Gd in a sawhorse geometry, which has been observed in $M_2Mo_4O_7$ (5), $Mn_{1.5}Mo_8O_{11}$ (16), and MMo_8O_{10} (15). Oxygen 3 is coordinated by two Mo and three Gd. Oxygen 4 and 05 are surrounded by four ternary metal cations only. Oxygen 6 is coordinated by one Mo and three Gd in a pseudo-tetrahedral symmetry. Oxygen 7 and 08 are surrounded by three Mo and one Gd in a very distorted tetrahedral geometry.

Although the MCE count per Mo_4 unit in $Gd_4Mo_4O_{11}$ is considerably lower than that in $ZnMo_8O_{10}$, the extents of distortions are comparable. Evidently, factors other than MCE are important in determining the distortions. Syntheses and characterizations of a series of isostructural compounds may help understand the various competitive factors. On the other hand, the metal cluster chain in $Gd_4Mo_4O_{11}$ is closer to a one-dimensional system which could be a good candidate for charge density wave instabilities. Further studies on electrical resistivity would be interesting.

REFERENCES

1. Clark, C. M.; Smith, D. K.; Johnson, G. J. "A Fortran IV Program for Calculating X-Ray Powder Diffractions Patterns-Version 5", Department of Geosciences, Pennsylvania State University, University Park, PA, 1973.

2. Rohrbaugh, W. J.; Jacobson, R. A. Inorg. Chem. 1974, 13, 2535.

3. Hanson, H. P.; Herman, F.; Lea, J. D.; Skillman, S. Acta Crystallogr. 1964, 17, 1040.

4. Templeton, D. H. In "International Tables for X-Ray Crystallography", 1st ed.; Macgillavry, C. H. and Rieck, G. D., Eds.; Kynoch Press: Birmingham, England, 1962; Vol. III, page 215.

5. Lii, K.-H. Ph.D. Dissertation, Iowa State University, Ames, Iowa, 1985, Section 4.

6. Abe, M.; Kawachi, M.; Nomura, S. J. Phys. Soc. Japan 1972, 33, 1296.

7. McCarroll, W. H.; Katz, L.; Ward, R. J. Am. Chem. Soc. 1957, 79, 5410.

8. Rahmel, A.; Jaergel, W.; Becker, K. Arch Eisenhuettenwes 1959, 30, 351.

9. Brown, I. D.; Wu, K. K. Acta Crystallogr. 1976, B32, 1957.

10. The sample vial containing Gd_2O_3 was mislabeled as La_2O_3. The compound was thought as $La_4Mo_4O_{11}$ until its magnetic susceptibility was measured.

11. Wang, S.-L. Ph.D. Dissertaion, Iowa State University, Ames, Iowa, 1985.

12. Mo1, Mo2, and some of the oxygen atoms gave negative temperature factors as they were anisotropically refined.

13. This E&A four-circle diffractometer was modified in Dr. R. A. Jacobson's laboratory. Stepping motors and encoders were attached and interfaced to a LSI/11 computer, which in turn was interfaced to a VAX11/730 computer. It is equipped with a scintillation counter and incorporates a graphite monochromator in the detection system.

14. Gougeon, P.; McCarley, R. E. unpublished research, Department of Chemistry, Iowa State University, Ames, Iowa, 1985.

15. Lii, K.-H. Ph.D. Dissertation, Iowa State University, Ames, Iowa, 1985, Section 5.

16. Carlson, C. D.; McCarley, R. E. presented at the 11th Midwest High Temperature Chemistry Conference, Ames, Iowa, June 1985.

SUMMARY

Although chains based on M_6X_8-type clusters have been observed in molybdenum chalcogenides and a few halides of early transition and rare earth metals, the structural feature of the highly reduced ternary molybdenum oxides with the average oxidation state of Mo < 3.0 has been dominated by the Mo_4O_6 repeat unit derived by condensation of M_6O_{12} clusters. For small nonmetals such as oxide the Mo_6X_8-type cluster is not favored because the short Mo-O bond distance (ca. 2.1 A) requires a similar bond length for Mo(waist)-Mo(waist), which is evidently too short.

In a few structures, the infinite metal cluster chains are markedly distorted. A common way of distortion is the alternately short and long apex molybdenum atoms. However, the way of distortion on one side of the cluster chain is not necessarily equivalent to that on the opposite side. The extent of distortion does not appear to be solely determined by the metal cluster electron (MCE) count, which has been well exemplified by the $M_2Mo_4O_7$ structures. Other factors such as the nature of the ternary metal cation and the structure type are also important. It seems that the ternary metal cation determines the structure type which in turn decides the way of distortion. So far, only a narrow range of MCE have been observed for each structure type.

Figure 1 shows a plot of the number of valence electrons

(VEC) on the molybdenum atom vs. the oxygen/molybdenum (O/Mo) ratio for some molybdenum oxides (5). VEC is calculated according to: VEC = VEC_o - 2 x (O/Mo), where VEC_o is the number of valence electrons for free metal. A similar plot has been applied to halides of early transition metals in an elegant paper by Professor A. Simon (6). A few conclusions can be drawn from Figure 1. In general, increasing the VEC with simultaneous decrease in the O/Mo ratio lead to larger metal clusters, unidirectional condensed metal cluster chains, and condensed metal cluster chains running in two orthogonal directions. The effect of the nature of the ternary metal cation on the cluster size is revealed in the examples falling on the line with O/Mo = 2. The structure of $NaMo_2O_4$ is in sharp contrast to that of $Ba_{1.14}Mo_8O_{16}$ where similar chains of Mo are broken into discrete rhomboidal cluster units, although their VEC values are rather close. However, $LiMoO_2$ and MoO_2 have basically the same structure. Compounds containing discrete cluster units, such as $Zn_2Mo_3O_8$, appear to be more flexible to change in VEC while keeping the same structure type. So far, all compounds with VEC $>$ 3.0 and O/Mo $<$ 2.0 contains infinite metal cluster chains based on M_6X_{12} cluster units. However, the opposite is not true because the interesting structure $Gd_4Mo_4O_{11}$ (O/Mo = 2.75) consists of the same type of cluster chains which are "diluted" with the rare earth and oxygen atoms. Accordingly, a low VEC value seems more important for the formation of octahedral cluster chains

than special values of O/Mo. The potential for further interesting structures in the system of reduced molybdenum oxides is considerable. The large gap between $ZnMo_8O_{10}$ and Mo metal in Fig. 1 is likely to be filled with compounds with increasing 3-dimensional character. Additional compounds containing smaller cluster units should exit in the gap between MoO_2 and Mo_4O_{11}.

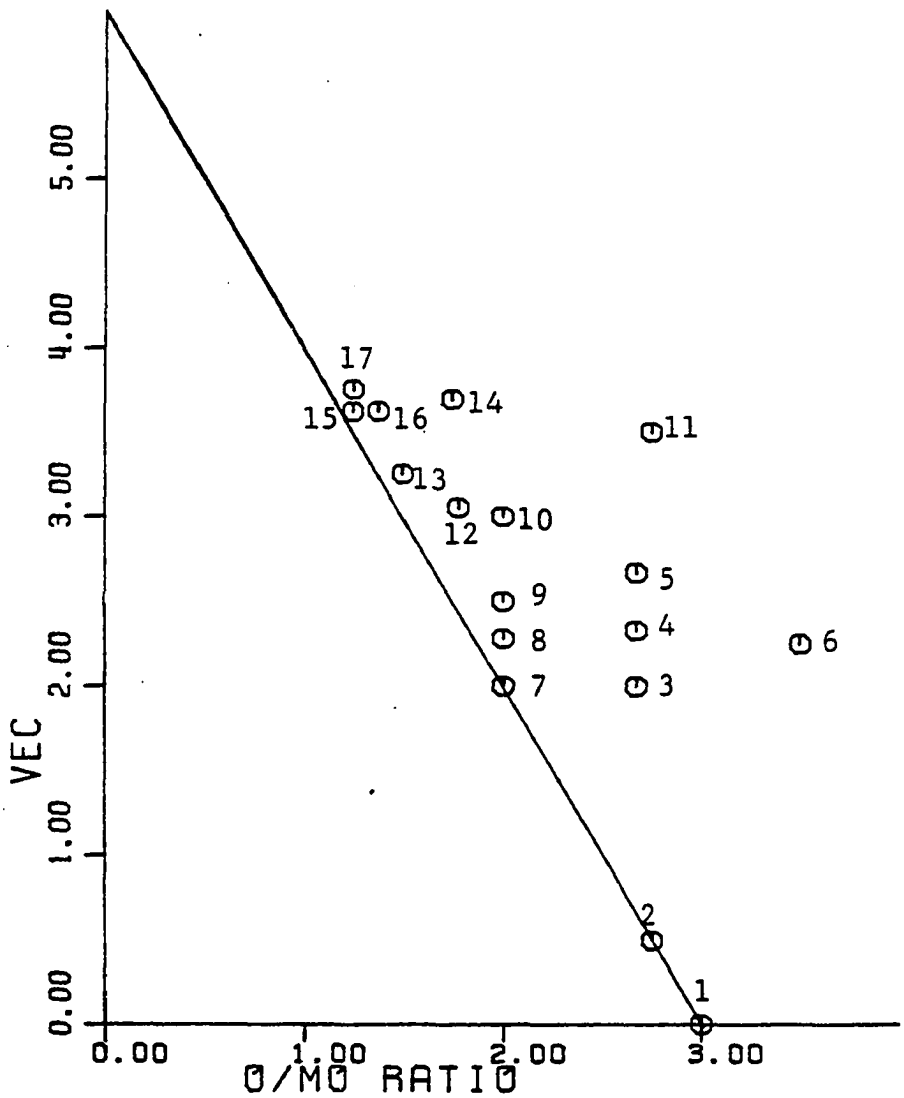

Fig. 1. The number of valence electrons on the Mo atom (VEC) for some molybdenum oxides are plotted vs. O/Mo ratios. 1: MoO_3, 2: Mo_4O_{11}, 3: $Zn_2Mo_3O_8$, 4: $LiZn_2Mo_3O_8$, 5: $Zn_3Mo_3O_8$, 6: $La_3Mo_4SiO_{14}$, 7: MoO_2, 8: $Ba_{1.14}Mo_8O_{16}$, 9: $NaMo_2O_4$, 10: $LiMoO_2$, 11: $Gd_4Mo_4O_{11}$, 12: $Ca_{5.45}Mo_{18}O_{32}$, 13: $NaMo_4O_6$, 14: $Sc_{0.75}Zn_{1.25}Mo_4O_7$, 15: $LiMo_8O_{10}$, 16: $Mn_{1.5}Mo_8O_{11}$, 17: $ZnMo_8O_{10}$

REFERENCES

1. McCarroll, W. H.; Katz, L.; Ward, R. J. Am. Chem. Soc. 1957, 79, 5410.

2. Torardi, C. C.; McCarley, R. E. J. Am. Chem. Soc. 1979, 101, 3963.

3. Torardi, C. C.; McCarley, R. E. J. Solid State Chem. 1981, 37, 393.

4. McCarley, R. E. Phil. Trans. R. Soc. Lond. 1982, A308, 141.

5. $Zn_2Mo_3O_8$: ref. 1.
   $LiZn_2Mo_3O_8$ & $Zn_3Mo_3O_8$: Torardi, C. C.; McCarley, R. E. Inorg. Chem. 1985, 24, 476.
   $La_3Mo_4SiO_{14}$: Betteridge, P. W.; Cheetham, A. K.; Howard, J. A. K.; Jakubicki, G.; McCarroll, W. H. Inorg. Chem. 1984, 23, 737.
   $Ba_{1.14}Mo_8O_{16}$: ref. 3.
   $LiMoO_2$: Cava, R. J.; McWhan, D. B.; Murphy, D. W. J. Phys. Chem. Solids 1982, 43, 657.
   $Ca_{5.45}Mo_{18}O_{32}$ & $NaMo_2O_4$: McCarley, R. E.; Lii, K.-H.; Edwards, P. A.; Brough, L. F. J. Solid State Chem. 1985, 57, 17.
   $Mn_{1.5}Mo_8O_{11}$: Carlson, C. D.; McCarley, R. E. presented at the 11th Midwest High Temperature Chemistry Conference, Ames, Iowa, June 1985.
   $NaMo_4O_6$: ref. 2.
   $Sc_{0.75}Zn_{1.25}Mo_4O_7$: ref. 4.
   $LiMo_8O_{10}$, $ZnMo_8O_{10}$, & $Gd_4Mo_4O_{11}$: Lii, K.-H. Ph.D. Dissertation, Iowa State University, Ames, Iowa, 1985.

6. Simon, A. Angew. Chem. int. Ed. Engl. 1981, 20, 1.

ACKNOWLEDGEMENTS

I am indebted to Dr. Robert E. McCarley for his guidance through the course of this work. His enthusiasm for the work presented in this thesis, patience and understanding during my graduate years have been a constant source of encouragement. The discussions, suggestions, supports, and companionship provided by other members of the group were also appreciated. I learned much from Bill Beers and Larry Brough.

Special thanks are due to the following people in Dr. Robert A. Jacobson's crystallographic group for their valuable assistance during crystal structure determination: Sue-Lein Wang, Sangsoo Kim, Jim Richardson, and Jim Benson.

I wish to thank Dr. Robert N. Shelton, Dr. Frank J. DiSalvo and Dr. William M. Reiff for the magnetic susceptibility and Mossbauer spectroscopy measurements.

I am also grateful to my parents who have encouraged my educational goal.

My deepest appreciation goes to my lovely and capable wife, Sue-Lein, whose love, assistance and encouragement have been infinite.